UNIVERSITY OF Southampton

SHEP Southampton High Energy Physics

Phenomenological Aspects of Beyond the Standard Model Theories at the LHC

In Search of Dark Matter, Supersymmetry and other New Physics

by

Patrick Bernhard Schaefers

Presented for the degree of
Doctor of Philosophy

Faculty of Physical Sciences & Engineering
School of Physics and Astronomy
University of Southampton
United Kingdom

Supervisors:

Prof. Dr. Alexander Belyaev
Prof. Dr. Stephen King

— January 2018 —

UNIVERSITY OF SOUTHAMPTON

ABSTRACT

FACULTY OF PHYSICAL SCIENCES AND ENGINEERING
SCHOOL OF PHYSICS AND ASTRONOMY

Doctor of Philosophy

PHENOMENOLOGICAL ASPECTS OF BEYOND THE STANDARD MODEL THEORIES AT THE LHC - IN SEARCH OF DARK MATTER, SUPERSYMMETRY AND OTHER NEW PHYSICS

Patrick Bernhard Schaefers

In this thesis, we study the phenomenological implications of different Beyond the Standard Model (BSM) theories at the Large Hadron Collider (LHC) with a focus on the anomalous magnetic moment of the muon Δa_μ and dark matter (DM). We consider two Grand Unified Theory (GUT) scale models, namely a Pati-Salam model with $A_4 \times Z_5$ family symmetry as well as an $SU(5)$ with A_4 family symmetry. After both models break down to the Minimal Supersymmetric Standard Model (MSSM), we study their capabilities of explaining Δa_μ, DM and further collider and non-collider constraints. We find that both models comprise a viable set of parameters leading to distinctive solutions, provided the gaugino masses are non-universal. We also explore the capability of models with extra vector resonances Z' to account for DM when combined with a coloured vector-like top partner sector. We find that the presence of a Z' boson may greatly improve the sensibility of the LHC to such models, especially in regions where non-collider searches are considerably less sensitive. Finally, we study the potential of current and future hadron colliders to narrow down the nature of the 2012 discovered scalar particle at the LHC, which matches the Standard Model (SM) Higgs boson astonishingly well so far. To further determine whether this scalar may belong to a different BSM theory, we use an effective field theory to study the unitarity violations arising from Higgs couplings to vector bosons slightly different as compared to the SM. We find that triple Higgs production substantially benefits from non-SM couplings and can be probed effectively at a 100 TeV future collider with high precision.

Contents

List of Figures

List of Tables

Declaration of Authorship

I, **Patrick Schaefers**, declare that this thesis entitled **Phenomenological Aspects of Beyond the Standard Model Theories at the LHC - In Search of Dark Matter, Supersymmetry and other New Physics** and the work presented in it are my own and has been generated by me as the result of my own original research. I confirm that:

1. This work was done wholly or mainly while in candidature for a research degree at this University;

2. Where any part of this thesis has previously been submitted for a degree or any other qualification at this University or any other institution, this has been clearly stated;

3. Where I have consulted the published work of others, this is always clearly attributed;

4. Where I have quoted from the work of others, the source is always given. With the exception of such quotations, this thesis is entirely my own work;

5. I have acknowledged all main sources of help;

6. Where the thesis is based on work done by myself jointly with others, I have made clear exactly what was done by others and what I have contributed myself;

7. Parts of this work have been published as:

    - A. S. Belyaev, J. E. Camargo-Molina, S. F. King, D. J. Miller, A. P. Morais and P. B. Schaefers, *"A to Z of the Muon Anomalous Magnetic Moment in the MSSM with Pati-Salam at the GUT scale"*, JHEP **1606** (2016) 142

- A. S. Belyaev, S. F. King, P. B. Schaefers, *"Muon $g-2$ and Dark Matter suggest Non-Universal Gaugino Masses: $SU(5) \times A_4$ case study at the LHC"*, arXiv:1801.00514, currently being reviewed by PRD
- A. S. Belyaev, T. Flacke, B. Jain, P. S. Schaefers, *"Dark Matter Signatures from Vector Resonances of Composite Higgs Models with top partners"*, arXiv:1707.07000, currently being reviewed by PRD
- A. S. Belyaev, M. C. Thomas, P. B. Schaefers, *"Precise test of Higgs properties via triple Higgs production in VBF at future colliders"*, arXiv:1801.10157, currently being reviewed by PRD

Signed:.....

Date:.....

Acknowledgements

First, I would like to thank my supervisor Professor Alexander Belyaev for his guidance and the inspiration he passed on to me during the last three years. His support and encouragement allowed me to learn more about physics than I could have ever dreamed of and enabled me to connect to a network of outstanding researchers around the world to work with and present my work to.

I also want to thank Professor Stephen King for the countless fruitful discussions and his valuable advice on so many physics and non-physics related topics.

During my time in Southampton, I was very fortunate to get to spend my time with the best colleagues imaginable: Daniel Locke, Marc Thomas and Hugo Prager. Especially the frequent lunch breaks with Daniel at the Chinese helped me to stay motivated and work efficiently.

A very special thanks goes to Semir Vrana, who helped me with a lot of things and has always been a good friend to me.

I am also very grateful for the support of my family. Without my parents and my grandfather, I would not have had the possibility to study physics and get to the point I am standing at now.

Completing this work would also not have been possible without the funding provided by the SHEP group and I would like to thank them for this opportunity.

Finally, I want to thank my wife Kathy for her encouragement and everlasting patience, which helped me to successfully tackle all the obstacles I had to face in the last years.

Abbreviations

The following table (continued on the next page) lists all abbreviations used in this thesis in alphabetical order.

Abbreviation	Meaning
BR	Branching Ratio
BSM	Beyond the Standard Model
CM	Center of Mass
c.c.	Charge Conjugation
CCB	Charge or Coloure Breaking
CCWZ	Callan–Coleman–Wess–Zumino
cMSSM	constrained Minimal Supersymmetric Standard Model
CH	Composite Higgs
CP	Charge-Parity
DM	Dark Matter
DM DD	Dark Matter Direct Detection
DM ID	Dark Matter Indirect Detection
e.g.	exempli gratia (for example)
$\not{E}_T$	Missing Transverse Energy
EW	Electroweak
EWSB	Electroweak Symmetry Breaking
FCC	Future Circular Collider
FSR	Final State Radiation
FCNC	Flavour Changing Neutral Current
GIM	Glashow-Iliopoulos-Maiani
GR	General Relativity
GUT	Grand Unification Theory (or Grand Unified Theory)
h.c.	Hermitian Conjugation

Abbreviation	Meaning
i.e.	id est (that is)
ISR	Initial State Radiation
LEP	Large Electron-Positron Collider
LHC	Large Hadron Collider
LO	Leading Order
LSP	Lightest Supersymmetric Particle
MSSM	Minimal Supersymmetric Standard Model
mSUGRA	minimal Supergravity
NLO	Next-to-Leading Order
NLσM	Non-Linear σ Model
NLSP	Next-to-lightest Supersymmetric Particle
NWA	Narrow Width Approximation
PDF	Parton Distribution Function
pMSSM	phenomenological Minimal Supersymmetric Standard Model
PS	Pati-Salam
QFT	Quantum Field Fheory
QED	Quantum Electrodynamics
QCD	Quantum Chromodynamics
SB	Symmetry Breaking
SM	Standard Model
sparticle	Supersymmetric Particle
SSB	Spontaneous Symmetry Breaking
SUSY	Supersymmetry
TC	Technicolor
UV	Ultraviolet
VBF	Vector Boson Fusion
vev	Vacuum Expectation Value
WIMP	Weak Interacting Massive Particle

Conventions and Symbols

- For all calculations, $\hbar = c = 1$.
- The commutation relation for two elements A and B is defined as

  $$[A, B] = AB - BA\,,$$

  whereas the anticommutation relation of these elements is defined as

  $$\{A, B\} = AB + BA\,.$$

- The metric tensor is set as

  $$g_{\mu\nu} = g^{\mu\nu} = \mathrm{diag}(+1, -1, -1, -1)\,,$$

  with the usual spacetime indices $\mu\,, \nu = 0{,}1{,}2{,}3$.
- Covariant four-vectors are written with lower indices, contravariant four-vectors appear with upper indices.
- The Einstein notation is used, implying summation over indices appearing twice in a single term.
- The Dirac matrices are a set of matrices obeying the following anticommutation relation

  $$\{\gamma^\mu, \gamma^\nu\} = \gamma^\mu\gamma^\nu + \gamma^\nu\gamma^\mu = 2\,g^{\mu\nu}\,\mathbb{1}\,,$$

  implying that

  $$\gamma_\mu\gamma^\mu = 4 \cdot \mathbb{1}\,,$$

  where $\mathbb{1}$ is the four-dimensional unit matrix.
- The Feynman Slash notation is used, implying

  $$\not{\partial} \equiv \gamma^\mu\,\partial_\mu\,.$$

1 | Introduction

Whenever scientists discover a new physical phenomenon, they are eager to explain it in accordance with already existing theories and observations made before. In the not-too-uncommon case where this is not possible, the existing theories have to be modified or completely new theories need to be developed in order to yield an explanation for the new phenomenon. Additionally, any new theories of course need to comprise the well studied and verified parts of older, until then established theories.

A historical event of such kind worth mentioning took place in the 19^{th} and early 20^{th} century. Isaac Newton's theory of gravity was well established and able to describe many astrophysical phenomena precisely, among others also the trajectories of planets in our solar system. However, in 1846 the French astronomer Urbain le Verrier discovered an irregular movement of the Uranus that disagreed with the prediction Newton's theory gave for its orbit. Instead of enhancing or falsifying Newton's theory of gravity, le Verrier postulated a yet unobserved planet to be responsible for his observations. This planet was observed later the same year and should become known as Neptune. Around the same time, le Verrier also studied the anomalous orbit of Mercury and suggested once again a yet unknown planet (called Vulcan) to be responsible for the disagreement with the Newtonian orbit prediction [1]. This time, le Verrier's postulate turned out to be false with Vulcan never being found and eventually not being the reason for the anomalous orbit of Mercury. The solution to this problem had to wait for more than 25 years, until Albert Einstein's theory of general relativity (GR), which comprises Newtonian gravity as a limit of weak gravity and small velocities, was finally able to predict the precessive movement of Mercury correctly.

A century later, the game is still the same, only the theories and experiments have changed. With the rise and triumph of quantum field theory (QFT) in the 20^{th} century, describing the

physics of subatomic scales and particles, we now have a powerful and experimentally well tested theory to describe three of the four fundamental forces of nature simultaneously (electromagnetism, the weak force and the strong force). This theory is known as the *Standard Model of Particle Physics* (SM) and to this day, there is almost no experimentally observed phenomenon in particle physics the SM cannot explain. However, it is not all roses and there are some significant flaws in the SM which seem to demand for more than just a modification to compensate for. For example, one of the more obvious flaws of such kind lies in the fact that the SM is not describing gravity. Modifying the SM to include gravity also seems unlikely due to the highly different natures of the SM as a QFT and GR as a classical theory. With several more such issues of the SM, the game repeats and new theories addressing them are in high demand. Fortunately, a variety of most diverse theories have already been developed, with some of them probably (and hopefully) at the brink of discovery (or exclusion) in the upcoming years.

Before focussing on these new theories, let us briefly review the SM and its aforementioned flaws.

1.1 The Standard Model of Particle Physics

The SM currently is one of the best tested physical theories in the world and describes the electromagnetic, weak and strong forces relativistically at quantum level. As a gauge theory, the SM is based on the gauge groups $\mathrm{SU}(3)_C \otimes \mathrm{SU}(2)_L \otimes \mathrm{U}(1)_Y$, where the $\mathrm{SU}(3)_C$ describes the quark sector (quantum chromodynamics, QCD) and the $\mathrm{SU}(2)_L \otimes \mathrm{U}(1)_Y$ describes the electroweak interactions before eventually breaking down to the $\mathrm{U}(1)_{\mathrm{EM}}$. The SM has been developed over several decades in the 20^{th} century before reaching its current form in the 1970s. An essential part in validating the SM experimentally thereby came from the Large Electron-Positron Collider (LEP) at CERN. After the discovery of the W [2, 3] and Z [4] bosons in 1983 by the UA1 and UA2 collaborations at the CERN Super Proton Synchrotron, LEP measured their masses and further electroweak parameters with an outstanding accuracy (see Ref. [5] for a summary of all LEP experiments and results). Thanks to this data, the electroweak theory and its high-precision predictions based on radiative corrections e.g. to the Z boson mass were tested and beautifully validated and marked a major success in establishing the SM. Furthermore, the lower mass limit

LEP set on the then undiscovered Higgs boson mass, $m_h \geq 114.4$ GeV [6], was just slightly below the mass of the Higgs boson discovered in 2012 by the ATLAS and CMS collaborations at the CERN Large Hadron Collider (LHC) [7, 8]. Together with the Higgs boson, all of the particles predicted by the SM have been found, with other noteworthy discoveries being the discovery of the tau neutrino in 2000 by the DONUT collaboration [9] and the top quark in 1995 by the D0 collaboration [10] at Fermilab. It should be stressed, however, that even though the 2012 discovered Higgs boson matches the SM Higgs boson quite well so far, its properties are not fully determined yet and it might still be based in theories other than the SM.

The reason to expect all of these particles in the first place usually is to either not lose certain (gauge) symmetries of the theory or due to observations in nature requiring or suggesting such particles. Exemplarily, the charm quark was predicted as a consequence of the so called GIM mechanism, named after Sheldon Lee Glashow, John Iliopoulos, and Luciano Maiani [11]. The GIM mechanism successfully describes the suppression of flavour changing neutral currents (FCNC) in weak interactions and implies that quarks should be arranged in $SU(2)$ doublets. This, in turn, had further consequences, as the discovery of the bottom quark in 1977 by the E288 experiment at Fermilab [12] strongly suggested the existence of a sixth quark, the top quark, which eventually was found eighteen years later.

Besides just predicting physical phenomena, the SM can also be extremely accurate. For example, the SM prediction of the anomalous magnetic moment of the electron matches the experimentally measured value up to 10 decimals [13]. For completeness, the particle content of the SM together with some basic particle properties is given below in table 1.1.

1.2 Problems of the Standard Model

While the SM is able to explain a variety of observations with incredible accuracy, there are still numerous problems the SM is not able to resolve. These problems are of very different nature, including observations made in nature the SM cannot explain, theoretical considerations not compatible or explainable within the SM and a general arbitrariness of SM parameters and assumptions. A general overview over some of the problems the SM is currently facing is given below.

		Particle	Symbol	Mass [GeV]	Charge [e]	Spin
Fermions	Quarks	up	u	0.002	$\frac{2}{3}$	$\frac{1}{2}$
		down	d	0.005	$-\frac{1}{3}$	$\frac{1}{2}$
		charm	c	1.28	$\frac{2}{3}$	$\frac{1}{2}$
		strange	s	0.10	$-\frac{1}{3}$	$\frac{1}{2}$
		top	t	173.21	$\frac{2}{3}$	$\frac{1}{2}$
		bottom	b	4.18	$-\frac{1}{3}$	$\frac{1}{2}$
	Leptons	electron	e	0.511	-1	$\frac{1}{2}$
		muon	μ	0.11	-1	$\frac{1}{2}$
		tauon	τ	1.78	-1	$\frac{1}{2}$
		electron neutrino	ν_e	$> 0^*$	0	$\frac{1}{2}$
		muon neutrino	ν_μ	$> 0^*$	0	$\frac{1}{2}$
		tau neutrino	ν_τ	$> 0^*$	0	$\frac{1}{2}$
Bosons		gluon	g	0	0	1
		photon	γ	0	0	1
		W boson	$W^\pm$	80.39	± 1	1
		Z boson	Z	91.19	0	1
		Higgs boson	h	125.09	0	0

Table 1.1: Particle content and some of their properties in the Standard Model. *In the SM, neutrinos are predicted to be massless. However, experiments have shown that neutrinos are actually massive (see also section 1.2 below).

Arbitrariness of SM parameters and assumptions: While the general idea of the SM and most of its assumptions are very well motivated, it still remains a mystery why e.g. there are exactly three colours. Or why there are three different quark and lepton families. Might there be even more? Why are the particles arranged in multiplets and why are they arranged in these multiplets just the way they are? The SM offers no solution to any of these fundamental questions and most likely never will.

Hierarchy Problem: The hierarchy problem, sometimes also referred to as fine tuning problem, addresses the large discrepancy between the value of a fundamental parameter of a theory and its effective, experimentally measured value. In case of the SM, this usually relates to the vast discrepancy between the Higgs mass ($m_h \sim 125$ GeV) and the Planck Mass ($M_P \sim 10^{19}$ GeV). Due to radiative corrections (see Appendix A), the Higgs mass in the SM is expected to be around the Planck mass, but experiment has shown otherwise with the discovery of a particle consistent with the SM Higgs boson in 2012 [7, 8]. Now the

only way to resolve this mismatch is to either require a large amount of fine tuning of the radiative corrections to the Higgs mass and its bare mass, or to have some new physics arising at a scale much lower than the Planck scale and not much larger than the Higgs vacuum expectation value (vev), i.e. at the order of a few TeV. While the first solution is usually disfavoured, the second solution offers a more general (and possibly more natural) perspective to solve the hierarchy problem.

Dark Matter: Dark matter (DM) is a form of matter first mentioned in the 1930s by astronomer and physicist Fritz Zwicky [14]. While examining the Coma cluster, he noticed a much bigger velocity dispersion of the cluster than was expected at that time, leading to a mass of the cluster much larger than what gravity alone would be able to hold together. As a solution, Zwicky suggested some form of invisible or *dark* matter to be responsible for this discrepancy in mass. Over the following decades, evidence of dark matter was found in many more astronomical observations, e.g. in observations of the Bullet cluster [15] or via gravitational lensing. The amount of dark matter present in the universe was estimated by the Planck experiment to be 26.8 %, whereas all matter and antimatter ever observed by humans make up only 4.9 % [16]. Despite the large amounts of dark matter out there in the universe, no dark matter has ever been observed directly. This is mainly due to the fact that dark matter must be neutral, massive and non-baryonic (like neutrinos) and is mostly of non-relativistic nature (unlike neutrinos), while the latter characteristic is important to explain the structure formation in the universe as we observe it today. This type of dark matter is often referred to as *cold* (or *warm* in case of semi-relativistic) dark matter [17]. The only possible DM candidates the SM could provide are the neutrinos. However, since neutrinos would not be *cold* but *hot* dark matter due to their relativistic nature, they cannot be the major part of dark matter and therefore render the SM unable to explain dark matter.

Dark Energy: Similar to dark matter, there seems to be a yet unknown form of energy present in the universe, called *dark energy*. It is expected to be responsible for the accelerated expansion of the universe and is consistent with having a nonzero cosmological constant in the Einstein field equations. Dark energy makes up for the remaining 68.3 % of our universe [16] and, if the SM is assumed to be valid up to the Planck scale (see Hierarchy

problem), it would overestimate this energy by a factor of 10^{120}.

Neutrinos: While the SM actually contains neutrinos, all of them are constrained to be massless. However, experiments such as the Super-Kamiokande for example have shown that neutrinos oscillate [18], which is only possible if they are massive particles. The SM is neither able to explain these oscillations nor any neutrino masses.

Gravity: Gravity and the SM are not and cannot be combined simply based on the Einstein field equations. This is due to the fact that general relativity as a quantum theory would be unrenormalisable. Different approaches to make GR a renormalisable quantum theory have been attempted with the more famous ones being string theory and loop quantum gravity. These theories, however, follow different concepts of quantisation and are not merged with the SM. Therefore, it is safe to say for the time being that the SM is incapable of explaining gravity.

Strong CP Problem: The SM allows for a term in its Lagrangian proportional to

$$\mathcal{L} \sim \frac{\theta}{16\,\pi^2}\, G^a_{\mu\nu} \tilde{G}^{\mu\nu,a} \tag{1.1}$$

that breaks CP symmetry. Although experiments on the electric dipole moment of the neutron suggest $\theta < 10^{-9}$ [19], the SM is not able to give any prediction about whether θ should be zero or nonzero at all.

Inflation: Very shortly after the big bang, the universe was undergoing a massive expansion, increasing in size by at least a factor of 10^{26} [20]. This expansion is what is known as *inflation* and different models exist describing inflation successfully. For example, inflation can arise as a consequence of discretised spacetime in loop quantum gravity, whereas other theories suggest a new scalar field responsible for inflation, usually called the inflaton (field). None of the SM scalars has properties as required by an inflaton to explain inflation, and neither does the SM have a discretised spacetime, therefore rendering the SM incapable of giving an explanation for inflation.

Matter-Antimatter Asymmetry: In the early stages of the universe, matter and antimatter

should have been produced in identical amounts. Nowadays, however, we only observe matter – be it on earth, the milky way or even beyond. It is unknown what has caused this asymmetry in matter and antimatter, but it is at least possible to specify when baryogenesis occurs thanks to the so called Sakharov conditions [21]. The three Sakharov conditions require

1. at least one baryon-number violating process,
2. C as well as CP violation,
3. particle interactions outside the thermal equilibrium.

Without further specifying conditions 1 and 3 and besides the unobserved and heavily constrained strong CP violation discussed above, the SM features another source of CP violation in the electroweak sector, first observed in Kaon decays in 1964 [22]. However, the amount of CP violation coming from the SM is small and therefore insufficient to explain the full matter-antimatter asymmetry regardless of the first and third condition.

Anomalous Magnetic Moment of the Muon: Charged elementary particles have a magnetic moment $\vec{M}$, given as

$$\vec{M} = g\,\frac{q}{2m}\,\vec{S} \tag{1.2}$$

with the gyromagnetic ratio g, the spin $\vec{S}$, the charge q and the mass m of the corresponding particle. Non-relativistically, the gyromagnetic ratio of any charged particle with semi-integer spin equals exactly two[1], but quantum corrections change this value. While for the electron, the SM prediction of g_e including quantum corrections matches the experimentally measured value with unrivalled accuracy, there is a tension of roughly 3σ between the SM prediction of g_μ and its experimental value. This discrepancy exists for several decades already and, provided that it persists, is unresolvable by the SM.

While some of the above mentioned issues are of fundamental nature and it is uncertain how, when or if it all any of these issues will be solved, other problems can be and are already addressed by

[1] This is a prediction by the Pauli equation, which directly emerges as the non-relativistic limit of the Dirac equation under the presence of an electromagnetic field. Therein, a term $\sim \frac{e}{2m}\vec{\sigma}\cdot\vec{B}$ with charge e and mass m of the fermion as well as the magnetic field $\vec{B}$ and the Pauli matrices σ appears. Identifying the Bohr magneton $\mu_B = \frac{e}{2m}$ and the spin of the fermion $\vec{S} = \frac{1}{2}\vec{\sigma}$ results in the above term to read $\vec{\mu}\cdot\vec{B} = g\,\mu_B\vec{S}\cdot\vec{B}$ with $g = 2$.

a variety of theories. These theories are usually denoted as *Beyond the Standard Model* (BSM) theories and we will give an overview on some of the more relevant theories for this thesis in the following section.

1.3 Going Beyond the Standard Model

While there exists a plethora of highly diverse BSM theories addressing different issues of the SM, they all include the SM as some limit in order to reproduce its well tested predictions. For a large class of theories, the SM reappears as the low energy limit of the BSM theory, which typically lives at an energy scale close to the Planck mass, however it can also live very well just a few orders of magnitude above the SM or, in fact, anywhere between the electroweak and the Planck scale. As an example, a class of BSM theories usually situated at very large energy scales are the so called *Grand Unified Theories* or *Grand Unification Theories* (GUT), which unify all forces of nature but gravity at the so called GUT scale, typically around $M_{\text{GUT}} \sim 10^{16}$ GeV.

Most BSM theories simply extend the SM by additional fields or symmetries, which makes it comparatively easy to recreate the SM in some limit. However, there are also approaches developing or relying on completely different mathematical frameworks beyond QFT, such as string theory and loop quantum gravity. In this thesis, we will not focus on such new frameworks but instead focus mainly on two sets of BSM theories known as *supersymmetry* (SUSY) and *effective field theories* (EFTs). The latter one, however, is rather a framework suitable to do BSM physics than an actual BSM theory, as EFTs can also be used to describe the SM, just parts of it or completely different areas of physics.

1.3.1 Supersymmetry

Before considering supersymmetric models in detail, it is worth to briefly recap the history of SUSY, which is closely related to the S-matrix[2] and the Poincaré group. The full symmetry of the S matrix consists of the direct products of the Poincaré group and all internal symmetries, where 'internal' means that a symmetry transformation does not act on the spacetime coordinates

[2]The S-matrix denotes the scattering matrix, given as $S = 1 - \mathrm{i}(2\pi)^4\,\delta^{(4)}(p_\mu - p'_\mu)\,\mathcal{M}$ with the scattering amplitudes collected in the matrix $\mathcal{M}$.

x^μ. The SM gauge group $SU(3)_C \otimes SU(2)_L \otimes U(1)_Y$ is such an internal symmetry under the S matrix. Now in case one wants to extend the symmetry of the S-matrix in a non-trivial way — e.g. to include gravity, which clearly acts on x^μ and thus cannot be an internal symmetry — the Coleman-Mandula theorem has to be taken into account. This theorem mainly states that all new generators of a new symmetry of the S-matrix must commute with the generators of the Poincaré group [23], which is only possible if the Poincaré group and the new symmetry are connected trivially, i.e. via a direct product. While this first seemed to be the end of the story, there actually is a way to non-trivially extend the symmetries of the S-matrix, namely by relaxing Coleman and Mandula's assumption of considering only commuting (or bosonic) generators and also allow for anticommuting (fermionic) generators Q. This idea of anticommuting or fermionic generators was picked up and realised by Haag, Łopuszański and Sohnius [24] and allowed them to embed the Poincaré group in a larger, not trivially connected symmetry group. The new fermionic generators thereby have the property of transforming a boson into a fermion and vice versa, schematically depicted as

$$Q\ |\text{fermion}\rangle = |\text{boson}\rangle\ , \qquad\qquad Q\ |\text{boson}\rangle = |\text{fermion}\rangle\ . \tag{1.3}$$

Altogether, the regular spacetime with its four coordinates x^μ is extended to the so called superspace, which contains an additional fermionic spacetime with four Grassmann coordinates θ_α and $\bar{\theta}^{\dot{\beta}}$ with $\alpha, \dot{\beta} = 1, 2$. This extension of the spacetime to superspace further allows us to construct supermultiplets or superfields[3], which contain a bosonic, a fermionic and an auxiliary field. The latter, unphysical field can be removed via the Euler-Lagrange equations of motion[4].

With the ability to construct superfields, we can now successfully build supersymmetric Lagrangians and therefore supersymmetric models or theories. Almost regardless of the particular model, SUSY is able to address and solve a variety of problems of the SM (see section 1.2) which are worth showing again, but this time with the respective solution SUSY may offer.

Hierarchy Problem: The hierarchy problem is solved by SUSY due to new supersymmetric

[3]The supermultiplets or superfields are the irreducible representations of the new so called Super Poincaré group.

[4]Using the equations of motion, one can identify the auxiliary field $\mathcal{F} = \frac{\partial \mathcal{W}^\dagger}{\partial \Phi}$ with the superpotential $\mathcal{W}$ and a superfield Φ.

particle (sparticle) loops contributing to the Higgs self energy. In particular and if SUSY is exact (or unbroken), for each loop with SM fermions f, there is also a loop with its supersymmetric scalar partner $\tilde{f}$, leading to a perfect cancellation between the two and thus a naturally light Higgs mass without the need of fine tuning (see figure 1.1 below).

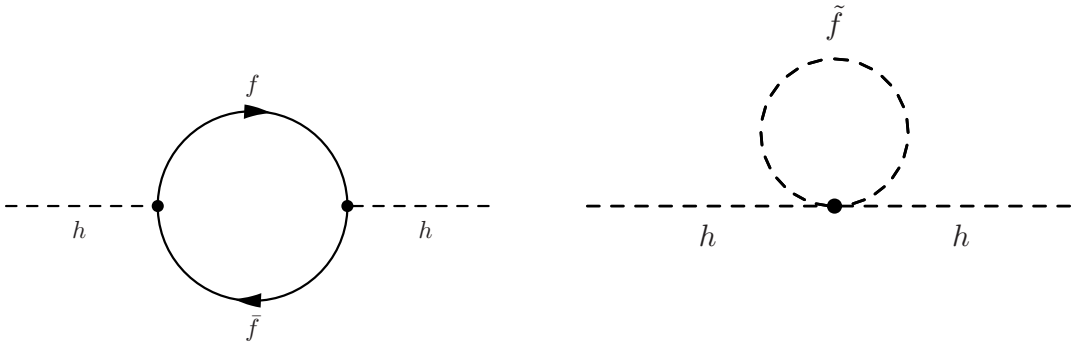

Figure 1.1: Corrections to the Higgs mass by fermions (left) and their supersymmetric scalar partners (right).

E.g. for the top quark with Yukawa coupling y_t, the fermion loop of figure 1.1 (left diagram) contributes a factor[5]

$$\delta m_h^2 \sim -\frac{|y_t|^2}{8\pi^2}\left(\Lambda^2 - m_t^2 \ln\frac{\Lambda^2}{m_t^2}\right), \tag{1.4}$$

whereas the stop quark appearing in the diagram on the right contributes

$$\delta m_h^2 \sim +\frac{|y_t|^2}{8\pi^2}\left(\Lambda^2 - m_{\tilde{t}}^2 \ln\frac{\Lambda^2}{m_{\tilde{t}}^2}\right), \tag{1.5}$$

therefore perfectly cancelling both contributions. If SUSY is broken (see section 1.3.1.1 below), the cancellation is not perfect any longer due to $m_t \neq m_{\tilde{t}}$ and instead logarithmic divergences proportional to

$$\delta m_h^2 \sim \frac{|y_t|^2}{8\pi^2}\left(m_t^2 - m_{\tilde{t}}^2\right)\ln\Lambda^2 \tag{1.6}$$

arise. However, compared to the quadratic divergences, the logarithmic divergences are much smaller, as long as the respective sparticle masses (in this case $m_{\tilde{t}}$) are small enough.

[5]The minus sign for fermionic loops is a consequene of the spin-statistics theorem.

Dark Matter: The supersymmetric partners of the neutral gauge bosons and the Higgs boson mix and form the so called neutralinos. The lightest of these neutralinos is weakly interacting, massive and can be stable, thus making it a viable DM candidate.

Anomalous Magnetic Moment of the Muon: The anomalous magnetic moment of the muon can be partially or even fully resolved in supersymmetric theories, as new SUSY particles provide further one-loop contributions, accounting for the large observed deviation. This topic will be discussed in far more detail in chapters 2 and 3.

Additionally, SUSY allows for gauge coupling unification at about 10^{16} GeV (which is desirable for naturalness reasons) and SUSY is necessary for the description of fermions in string theory.

In the next subchapter, we will focus on a particularly well studied SUSY model, namely the Minimal Supersymmetric Standard Model (MSSM).

1.3.1.1 The Minimal Supersymmetric Standard Model

The Minimal Supersymmetric Standard Model (MSSM) is the minimal supersymmetric extension to the SM, such that each SM particle has exactly one superpartner. This is not true for the Higgs, however, as two Higgs doublets (rather than just one as in the SM) are required. One of the main reasons for a second Higgs doublet is that the superpotential needs to be holomorphic, hence the complex conjugate of the Higgs field cannot give mass to the up-type quarks, as realised in the SM. Additionally, a single Higgs doublet would result in a triangle gauge and Witten anomaly caused by its superpartner (called higgsino). This anomaly can be cancelled by the higgsino of a second Higgs doublet with opposite hypercharge. The full particle content of the MSSM is shown in table 1.2 below. To fully specify the MSSM, the aforementioned superpotential still needs to be chosen. With R-parity conserved (see below), the superpotential reads

$$\mathcal{W} = y_u^{ij}\, U_i^c Q_j H_u - y_d^{ij}\, \bar{D}_i^c Q_j H_d - y_e^{ij}\, \bar{E}_i^c L_j H_d + \mu H_u H_d \tag{1.7}$$

with the fields being the left-chiral superfields from table 1.2 and suppressed colour indices. The Yukawa couplings are organised in 3×3 matrices $\mathbf{y}$ with components y^{ij} and the indices i and j running from one to three, labelling the respective generation. μ is the higgsino mass parameter.

Superfields	$SU(3)_C$	$SU(2)_L$	$U(1)_Y$	Particles	Particle Names
$L = \begin{pmatrix} \nu_{e,L} \\ e_L \end{pmatrix}$	$\mathbf{1}$	$\mathbf{2}$	-1	$\begin{pmatrix} \nu_{e,L} \\ e_L \end{pmatrix}, \begin{pmatrix} \widetilde{\nu}_{e,L} \\ \widetilde{e}_L \end{pmatrix}$	leptons, sleptons
E^c	$\mathbf{1}$	$\mathbf{1}$	2	$\bar{e}_R,\ \widetilde{e}^*_R$	
$Q = \begin{pmatrix} u_L \\ d_L \end{pmatrix}$	$\mathbf{3}$	$\mathbf{2}$	$\frac{1}{3}$	$\begin{pmatrix} u_L \\ d_L \end{pmatrix}, \begin{pmatrix} \widetilde{u}_L \\ \widetilde{d}_L \end{pmatrix}$	quarks, squarks
U^c	$\bar{\mathbf{3}}$	$\mathbf{1}$	$-\frac{4}{3}$	$\bar{u}_R,\ \widetilde{u}^*_R$	
D^c	$\bar{\mathbf{3}}$	$\mathbf{1}$	$\frac{2}{3}$	$\bar{d}_R,\ \widetilde{d}^*_R$	
$H_u = \begin{pmatrix} h_u^+ \\ h_u^0 \end{pmatrix}$	$\mathbf{1}$	$\mathbf{2}$	1	$\begin{pmatrix} H_u \\ \widetilde{h}_u \end{pmatrix}$	Higgs bosons, higgsinos
$H_d = \begin{pmatrix} h_d^{0*} \\ -h_d^- \end{pmatrix}$	$\mathbf{1}$	$\bar{\mathbf{2}}$	-1	$\begin{pmatrix} H_d \\ \widetilde{h}_d \end{pmatrix}$	
G^a	$\mathbf{8}$	$\mathbf{1}$	0	$G^\mu,\ \widetilde{g}$	gauge bosons, gauginos
W^i	$\mathbf{1}$	$\mathbf{3}$	0	$W_i^\mu,\ \widetilde{w}_i$	
B	$\mathbf{1}$	$\mathbf{1}$	0	$B^\mu,\ \widetilde{b}$	

Table 1.2: The particle content of the MSSM for one generation. Particles denoted with a tilde refer to the supersymmetric particles and the superscript ^{c} denotes charge conjugation. The second, third and fourth column refer to the gauge transformation properties and the weak hypercharge of the corresponding superfields.

It is worth noting that all fermion masses are generated by $\mathcal{W}$, as a fermionic mass term in the Lagrangian would explicitely break $SU(2)_L$.

The superpotential in equation (1.7) is not complete in the sense that more gauge-invariant and renormalisable terms exist, namely

$$\mathcal{W}_{\Delta L=1} = \lambda_e^{ijk}\, L_i L_j E_k^c + \lambda_L^{ijk}\, L_i Q_j D_k^c + \mu_L^i\, L_i H_u\,, \tag{1.8}$$

$$\mathcal{W}_{\Delta B=1} = \lambda_B^{ijk}\, U_i^c D_j^c D_k^c\,. \tag{1.9}$$

Here, the superfield Q carries baryon number $B = +\frac{1}{3}$, U^c and D^c carry $B = -\frac{1}{3}$, L carries lepton number $L = +1$ and finally E^c carries $L = -1$. By counting B and L, it becomes apparent that

these terms all violate baryon and lepton number conservation by one unit. This is problematic, as such terms would give rise to proton decay and further introduce B- and L-violating processes, which are not observed experimentally[6]. A possible solution to this problem is to introduce a new symmetry, commonly denoted as R-parity. R-parity is multiplicatively conserved and is defined as

$$R = (-1)^{3B+L+2s}\,, \tag{1.10}$$

with s being the particle's spin. Inserting the quantum numbers quickly shows that all SM particles have $R = +1$, whereas all SUSY particles carry $R = -1$. Furthermore, the superpotential in equation (1.7) conserves R-parity, whereas equations (1.8) and (1.9) do not, thus forbidding these terms in the superpotential. Additional important features of R-parity arise, when noting that each vertex in the superpotential (1.7) features an even number of SUSY particles. As a consequence, the lightest supersymmetric particle (LSP) is absolutely stable and SUSY particles can only be produced in pairs at colliders.

Down to some energy scale, each supersymmetric particle has the same mass as its corresponding SM particle. However, we never observed any SUSY particle, thus indicating that SUSY is not an exact symmetry but must be broken at some energy scale larger than the electroweak scale of the SM. SUSY breaking is considered to happen spontaneously, however the exact mechanism is unknown and presumably intricate, as the massless (fermionic) Goldstone mode — the so called goldstino — of spontaneous SUSY breaking is not observed and therefore has to be evaded somehow. This can be achieved e.g. by assuming a flavour-blind hidden sector, in which SUSY is broken spontaneously and which couples to the chiral superfields. In practice, it turns out to be convenient to parametrise our ignorance of this hidden sector and simply add terms to the Lagrangian that explicitely break SUSY. The SUSY-breaking couplings of these terms thereby should have a positive mass dimension (so called 'soft' couplings, or 'soft' SUSY breaking), as otherwise the hierarchy problem would be reintroduced [25]. With soft SUSY breaking, the quadratic divergences still cancel and the much smaller logarithmic corrections become dominant.

[6] Apart from some non-perturbative electroweak effects which are non-negligible only at energy scales as in the early universe, no B- and L-violating processes were observed.

There are only a few terms that lead to soft SUSY breaking, reading [26]

$$\begin{aligned}\mathcal{L}_{\text{soft}} = &-\frac{1}{2}\left(M_1\tilde{B}\tilde{B} + M_2\tilde{W}\tilde{W} + M_3\tilde{g}\tilde{g} + \text{c.c.}\right)\\ &-\left(\tilde{\bar{u}}\mathbf{a_u}\tilde{Q}H_u - \tilde{\bar{d}}\mathbf{a_d}\tilde{Q}H_d - \tilde{\bar{e}}\mathbf{a_e}\tilde{L}H_d + \text{c.c.}\right)\\ &-\tilde{Q}^\dagger\mathbf{m}^{\mathbf{2}}_{\tilde{\mathbf{Q}}}\tilde{Q} - \tilde{L}^\dagger\mathbf{m}^{\mathbf{2}}_{\tilde{\mathbf{L}}}\tilde{L} - \tilde{\bar{u}}\mathbf{m}^{\mathbf{2}}_{\tilde{\bar{\mathbf{u}}}}\tilde{\bar{u}}^\dagger - \tilde{\bar{d}}\mathbf{m}^{\mathbf{2}}_{\tilde{\bar{\mathbf{d}}}}\tilde{\bar{d}}^\dagger - \tilde{\bar{e}}\mathbf{m}^{\mathbf{2}}_{\tilde{\bar{\mathbf{e}}}}\tilde{\bar{e}}^\dagger\\ &-m^2_{H_u}H^*_uH_u - m^2_{H_d}H^*_dH_d - (bH_uH_d + \text{c.c.})\ . \end{aligned} \tag{1.11}$$

The parameters M_1, M_2 and M_3 correspond to the bino, wino and gluino masses respectively, whereas $\mathbf{a_u}$, $\mathbf{a_d}$ and $\mathbf{a_e}$ are complex 3×3 matrices in family space. $\tilde{Q}$, $\tilde{u}$, $\tilde{d}$, $\tilde{L}$ and $\tilde{e}$ are the SUSY partners of the quarks and leptons as defined in table 1.2 in form of family triplets. Subsequently, $\mathbf{m^2_{\tilde{Q}}}$, $\mathbf{m^2_{\tilde{\bar{u}}}}$, $\mathbf{m^2_{\tilde{\bar{d}}}}$, $\mathbf{m^2_{\tilde{L}}}$ and $\mathbf{m^2_{\tilde{\bar{e}}}}$ are 3×3 Hermitian matrices in family space. H_u and H_d correspond to the scalar up- and down-type Higgs fields, while the last line of equation (1.11) is responsible for the soft SUSY breaking of the Higgs potential.

While the unbroken MSSM may seem attractive due to its comparably small number of free parameters, the softly broken MSSM drastically changes this picture by adding a total of 105 new paramters in the form of masses, mixing angles and phases [27]. Although this looks discouraging at first, a large fraction of these parameters is heavily constrained or has to be zero in order to be in agreement with experimental observations. As an example, some of the softly broken MSSM parameters introduce FCNC or CP-violation at levels already ruled out by experiments (see e.g. [28]). Lastly, many phenomenological studies involve more constrained versions of the MSSM with just a few free parameters. As an example, the models known as minimal Supergravity (mSUGRA) or constrained MSSM (cMSSM) are very popular and one of their core features is the gauge coupling unification at the GUT[7] scale. As a consequence, only five free parameters remain, namely

$$m_0\,, \qquad M_{1/2}\,, \qquad A_0\,, \qquad \tan\beta\,, \qquad \operatorname{sgn}\mu\,, \tag{1.12}$$

with m_0 being the unified soft scalar mass, $M_{1/2}$ the unified gaugino mass and A_0 the unified trilinear coupling. $\tan\beta = \frac{v_2}{v_1}$ is defined as the ratio of the Higgs vev's and $\operatorname{sgn}\mu$ is the sign of the higgsino mass parameter.

[7] GUT stands for *Grand Unified Theory* or *Grand Unification Theory*.

In this thesis, we will consider two GUT scale models breaking down to the MSSM with a specific set of parameters — less constrained than in the cMSSM, but more constrained than the full MSSM — in chapters 2 and 3.

1.3.2 Effective Field Theories

In nature, different physical phenomena are observed on extremely small distances (as small as 10^{-18} m, corresponding to high energies), but also on incredibly large distances (such as e.g. 10^{10} m, corresponding to low energies). As we can see from everyday life and the history of physics, we do not need to know about all effects on all scales to describe a given phenomenon with precision. In fact, to explain a phenomenon of interest, it usually is sufficient to focus on just the energy scales small enough to comprise the phenomenon — without any knowledge of other possible high energy effects. This is the basic idea of what is called an *effective field theory* (EFT): to describe given quantities at some low energy scale without having to know or care about possible high energy effects. In terms of quantum field theories, the high energy effects are considered to take place at some energy scale Λ and refer e.g. to the mediation of some heavy particles with masses around Λ, whereas the low energy phenomena involve only particles with masses much smaller than Λ. To get rid of the high energy effects in the action of the EFT, the heavy particles will be *integrated out* and replaced by an infinite series of local interactions between the light particles, expanded in powers of Λ^{-1}. While just integrating out the heavy particles results in the action to be non-local, further developing the infinite series restores the locality of the action. Hence, apart from kinetic terms and mass terms, the general Lagrangian of an EFT can be written as

$$\mathcal{L}_{\text{EFT}} \sim \sum_i \frac{c_i}{\Lambda^{D_i - d}} \mathcal{O}_i \,, \tag{1.13}$$

where $\mathcal{O}_i$ is an operator of the EFT consisting of local combinations or interactions of the low energy fields, D_i is the mass dimension of $\mathcal{O}_i$, d is the number of spacetime dimensions[8], c_i are the so called Wilson coefficients (containing information about the high energy effects, see also below), Λ is the cut-off scale up to which the EFT is valid and the sum runs over the amount i of all possible operators. While in general an EFT is not renormalisable, in practice only some

[8] Usually, but not necessarily, $d = 4$.

terms of the infinite series are considered, up to some desired accuracy.

An important property of an EFT is that all high energy effects that are relevant once the energy of a given process E is similar to the cut-off scale, $E \approx \Lambda$, are contained within the Wilson coefficients c_i. Therefore, as long as models describing the high energy effects both contain the same low energy particle spectrum and symmetries, they share the exact same EFT with the only difference being different values for the c_i. In reverse, this means that just one EFT is able to provide limits for a variety of high energy models, if the c_i are constrained experimentally e.g. by LHC searches. This feature is also reflected in the way EFTs can be constructed. In the so called *top-down* approach, the theory at the high energy scale Λ is fully specified. The EFT is then constructed by first integrating out the high energy particles and then developing the infinite series shown in equation (1.13). Regarding the latter, first the desired accuracy of any computation is chosen and then all operators $\mathcal{O}$ that are necessary to achieve this accuracy are constructed. The advantage of the top-down approach on the one hand is that the Wilson coefficients c_i are known due to the knowledge of the full high energy theory and, on the other hand, lead to a simpler Lagrangian for further calculations.

The more commonly used *bottom-up* approach is independent of any high energy theory, as here the EFT Lagrangian based on equation (1.13) is constructed up to some desired accuracy without any knowledge on possible high energy effects or the c_i, but only based on a chosen set of symmetries and the particle content at the considered low energy. Together with experimental searches constraining the Wilson coefficients in a model-independent way, this approach is very often favoured due to its ability to set limits on several high energy models at once.

EFTs are also important tools in studying BSM physics. As such, the unknown BSM physics is taken to be the high energy theory with its low energy limit being the SM. The SM is incredibly well tested and its particle content and symmetries precisely known, thus the Wilson coefficients of various EFTs can be strongly constrained. When further focussing on experiments, this implies that e.g. the LHC phenomenology of theories with particles too heavy to be produced during collisions can be explored with an EFT. It should be noted, however, that even though the SM is very well tested and it is likely that any new physics arise at energy scales much larger than the ones directly testable at the LHC, there is still the possibility of yet undiscovered light, very

weakly interacting particles existing at about the same energy scale as the SM. These particles cannot be described by an EFT, as a necessary requirement for an EFT to be valid is the existence of a scale hierarchy.

For the work carried out in Chapter 5, we use an EFT based on a bottom-up approach to explore the potential of colliders to test the Higgs couplings to other gauge bosons.

1.4 Aim and Structure of this Thesis

With the issues of the SM raised in section 1.2, new physics clearly become a necessity to successfully explain what we observe in nature. Various theoretical models and frameworks have been proposed to address these issues and it is nearly impossible to study all of them at once. Furthermore, some models and frameworks make predictions out of the scope of current experiments such as the LHC. In this thesis, we will not focus on yet untestable theories (or theories with very little phenomenological implications for current experiments), but will focus on two classes of models that might be discovered (or excluded) by current or future LHC searches. In particular, we consider two models involving supersymmetry and two models based on an EFT. The first model involving supersymmetry is a GUT scale Pati-Salam model with an $A_4 \otimes Z_5$ family symmetry, which breaks down to the MSSM with special constraints on the soft GUT scale masses. We study the capabilities of this model to account for the anomalous magnetic moment of the muon, dark matter and further experimental constraints in the next Chapter 2 based on work published in Ref. [29]. Additionally, we perform an analysis on the vacuum stability for a given set of benchmark points, as this is necessary for some (but not necessarily all) solutions we find.

In Chapter 3, we explore similar BSM aspects for the well studied GUT scale model $SU(5)$, however also considering an A_4 family symmetry, as was done in Ref. [30]. While the $SU(5) \otimes A_4$ also breaks down to the MSSM, the newly imposed GUT scale constraints differ from the Pati-Salam ones and allow us to perform a completely different explorative study with a larger focus on LHC phenomenology. In particular, the $SU(5) \otimes A_4$ provides an excellent opportunity to investigate the influence of gaugino mass universality and non-universality on the model predictions for both cosmological and collider searches.

In Chapter 4, we study the phenomenological implications of theories such as Composite Higgs (CH) models as an alternative to SUSY. In such theories, the electroweak (EW) symmetry is broken by strong dynamics in analogy to QCD and the Higgs boson arises as a bound state of these strong dynamics. In particular and based on Ref. [31], we provide a simplified effective model containing a heavy vector resonance Z', a coloured vector-like top partner sector and a possible DM candidate. We study the coverage of the model parameter space by various LHC searches with a special focus on the expected model-specific signature of a top quark pair and missing transverse energy, $t\bar{t} + \not{E}_T$. Furthermore, we investigate whether such a model is able to successfully describe DM.

Due to the yet unknown nature of the Higgs boson and the resulting fact that it may still be part of a BSM theory (such as a CH model) rather than the SM, we explore the potential of current and future hadron colliders to determine the nature of the Higgs by using an EFT based on a non-linear σ model in Chapter 5. In this model, the couplings of the Higgs boson to other gauge bosons may differ by a multiplicative factor (anomalous Higgs couplings), therefore potentially leading to a violation of unitarity, which in turn marks the beginning of new physics. The unitarity violation is expected to be visible in form of a large increase in cross section, which we study in detail for different LHC final states containing W and Higgs bosons. Finally, we investigate the capability of the LHC to observe such new physics by comparing the predicted signal to the estimated background for various collider energies and anomalous Higgs couplings. This chapter is based on Ref. [32].

Lastly, we summarise and conclude the findings of this thesis in Chapter 6.

2 | MSSM $(g-2)_\mu$ and DM from GUT scale Pati-Salam

2.1 Introduction

An attractive theory for BSM physics is SUSY (for a review, see e.g. [28]), even if to date no evidence for it was found at experiments, especially not at colliders such as the LHC. However, SUSY remains an attractive BSM theory for several reasons worth repeating here. Not only allows SUSY for gauge coupling unification, which is absent in the SM, but also provides viable DM candidates such as the R parity stable lightest neutralino and it also addresses the hierarchy problem of the SM. Even if no evidence for SUSY has been found yet (including the lack of non-standard flavour signals in the LHCb detector), there remains one puzzling experimental discrepancy in the SM that exists for more than two decades. This discrepancy comes from the anomalous magnetic moment of the muon, which is often neglected or ignored for different reasons. Contrary to the SM, SUSY is able to fully account for this discrepancy in case light sleptons and charginos are provided. While this condition alone is not in tension with current LHC constraints on new coloured supersymmetric particles, it remains an exciting question whether a well motivated unified SUSY model is able to account not only for the anomalous magnetic moment of the muon, but also for various more collider and non-collider constraints including DM. Addressing this question is the aim of this chapter.

The discrepancy between the SM and experimental values for the anomalous magnetic moment

of the muon[1], Δa_μ, is given by

$$\Delta a_\mu = a_\mu^{\text{exp}} - a_\mu^{\text{SM}} = 288(80) \times 10^{-11}\,, \tag{2.1}$$

which is a $3.6\,\sigma$ tension. In case Δa_μ does not vanish when measured more precisely by upcoming experiments and/or once improvements to the SM (hadronic)contributions are available, it may become a sign of new physics beyond the SM.

As mentioned before, SUSY is able to account for Δa_μ, however the situation can be very tricky depending on the particular SUSY model considered. For example, it is known that within the framework of the constrained Minimal Supersymmetric Standard Model (cMSSM), it is difficult to achieve Δa_μ due to the few soft mass parameters available [33–35]. In the full MSSM with its many parameters, however, Δa_μ can be accounted for more easily (see e.g. [36, 37]). There is also the possibility to only partially account for Δa_μ with supersymmetric effects and thus making simple Grand Unified Theory (GUT) models viable (see e.g. [38, 39]), however these models then are no more attractive for explaining Δa_μ than the SM.

Other possible SUSY GUT models to explain Δa_μ are models with normal mass hierarchy and non-universal scalar masses for the first two and the third generation of sfermions [40] as well as the phenomenological MSSM (pMSSM) [41], which is based on the following simplifying assumptions:

- First and second generation universality for low energy soft masses $m_{Q_i}, m_{U_i}, m_{D_i}, m_{L_i}, m_{E_i}$ with $i = 1, 2$
- Separate low energy soft masses for third generation scalar masses $m_{Q_3}, m_{U_3}, m_{D_3}, m_{L_3}, m_{E_3}$
- Separate low energy gaugino masses M_1, M_2, M_3
- Separate trilinear parameters A_t, A_b, A_τ

The model cosidered in this chapter is a conceptually different MSSM model based on a GUT scale Pati-Salam gauge group together with an $A_4 \times Z_5$ family symmetry [42]. While the initial purpose of the model was to describe the quark and lepton masses and mixings (which it does

[1]It is also common to refer to Δa_μ as $(g-2)_\mu$ or in less common cases just $g-2$.

excellently) with a focus on the neutrino sector, here the capabilities of the model to additionally explain Δa_μ as well as further experimental observations are studied. The model is set up by the following GUT scale parameters:

- A universal high energy soft scalar mass for all left-handed squarks and sleptons of all three families $m_0 = m_{Q_i} = m_{L_i}$ for $i = 1, 2, 3$
- Three high energy soft mass parameters for the right-handed squarks and leptons, one for each family $m_i = m_{U_i} = m_{D_i} = m_{E_i}$ for $i = 1, 2, 3$
- Separate high energy gaugino masses M_1, M_2, M_3
- Separate trilinear parameters A_t, A_b, A_τ

We will show that this model is able to fully explain Δa_μ while simultaneously providing a viable DM candidate, a stable vacuum and being in agreement with all remaining dark matter and collider constraints.

The remainder of this chapter is organised as follows. In section 2.2 we describe the model with a focus on phenomenological aspects. In section 2.3, we highlight some key aspects of the anomalous magnetic moment of the muon and clarify its leading contributions. We will discuss experimental constraints, including collider constraints and those on the dark matter relic density, in section 2.4. We present our results, including some example scenarios, in section 2.5. Finally, we investigate the vacuum stability for these example scenarios in section 2.6, before concluding in section 2.7.

2.2 The Model

The model we consider is based on the Pati-Salam (PS) gauge group $SU(4)_C \otimes SU(2)_L \otimes SU(2)_R$ together with an $A_4 \otimes Z_5$ family symmetry and has been proposed in Ref. [42]. In a PS model, leptons are considered as a fourth colour (historically denoted as *lilac*) and unify quarks and

leptons in the following PS representations

$$F = (4,2,1)_i = \begin{pmatrix} u & u & u & \nu \\ d & d & d & e \end{pmatrix}_i \rightarrow (Q_i, L_i)\,, \tag{2.2}$$

$$F_i^c = (\bar{4},1,2)_i = \begin{pmatrix} u^c & u^c & u^c & \nu^c \\ d^c & d^c & d^c & e^c \end{pmatrix}_i \rightarrow (u_i^c, d_i^c, \nu_i^c, e_i^c)\,, \tag{2.3}$$

where the subscript i $(= 1,2,3)$ denotes the family index and the SM multiplets Q_i, L_i, u_i^c, d_i^c, ν_i^c and e_i^c arising after PS breaking are also shown. When the PS model also comprises an $A_4 \otimes Z_5$ symmetry (see Appendix B), the left and right-handed sectors transform differently under them. The full representations together with their A_4 structure are shown pictorially in figure 2.1. The left-handed quarks and leptons form an A_4 triplet F, whereas the right-handed fields F_i^c

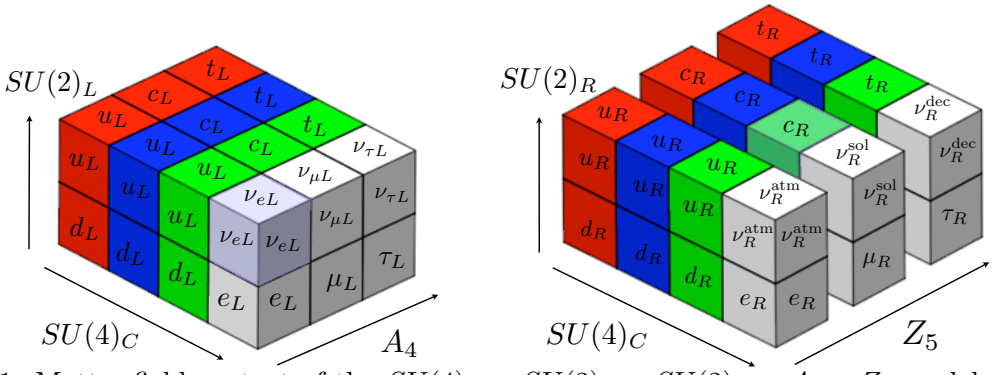

Figure 2.1: Matter field content of the $SU(4)_C \otimes SU(2)_L \otimes SU(2)_R \otimes A_4 \otimes Z_5$ model. The left-handed families form a triplet of A_4 and are doublets of $SU(2)_L$. The right-handed families are singlets under A_4 distinguished by Z_5 charges and are doublets of $SU(2)_R$. The $SU(4)_C$ unifies the quarks and leptons with leptons as the fourth colour, shown here as white blocks.

are singlets under the A_4, distinguished by the Z_5 charges $\alpha, \alpha^3, 1$ for $i = 1,2,3$ respectively. Therefore, the model contains four different matter multiplets at the GUT scale, namely F, F_1^c, F_2^c and F_3^c, which acquire soft masses labelled with m_0, m_1, m_2 and m_3 respectively.

The beforementioned breaking of the PS gauge group to the SM at the GUT scale is initiated

by the PS Higgs fields H^c and $\bar{H}^c$, where

$$H^c = (u_H^c, d_H^c, \nu_H^c, e_H^c) \in (\bar{4}, 1, 2)\,, \tag{2.4}$$

$$\bar{H}^c = (\bar{u}_H^c, \bar{d}_H^c, \bar{\nu}_H^c, \bar{e}_H^c) \in (4, 1, 2)\,. \tag{2.5}$$

To maintain supersymmetric gauge coupling unification, the PS Higgs fields acquire vacuum expectation values (vev's) close to the GUT scale $2 \cdot 10^{16}$ GeV in the direction of ν_H^c, i.e.

$$\langle H^c \rangle = \langle \nu_H^c \rangle = \langle \bar{H}^c \rangle = \langle \bar{\nu}_H^c \rangle \sim 2 \cdot 10^{16} \text{ GeV}, \tag{2.6}$$

Besides the PS Higgs, the model involves three kinds of Higgs bi-doublets: h_u, h_d and h_3. While h_u (h_d) is responsible for the up-type (down-type) quark and neutrino (charged lepton) Yukawa couplings, h_3 — which is also an A_4 triplet — gives rise to the Yukawa couplings of the third family. After PS and A_4 breaking, the majority of these bi-doublets will get high-scale masses and therefore does not appear in the low-energy mass spectrum. The only doublets with masses in the TeV range are H_u and H_d, which are linear combinations of h_u and h_3 or h_d and h_3 respectively. H_u has a hypercharge of $Y = +\frac{1}{2}$ and couples to up-type quarks and neutrinos, whereas H_d has a hypercharge of $Y = -\frac{1}{2}$ and couples to down-type quarks and charged leptons.

With this, the model reduces to the usual MSSM below the GUT scale, however with novel boundary conditions for the soft scalar masses. In particular, we have four different soft masses, namely m_0 for the left-handed fields of all generations and m_1, m_2, m_3 for the right-handed fields for each generation. These boundary conditions result in the model being more constrained than the general MSSM, but less so than the cMSSM.

Although the initial focus of the model is set on neutrino physics[2], we shall see that, thanks to the just explained new boundary conditions, it is also able to explain several phenomenological aspects, including Δa_μ, the Dark Matter relic density as well as a variety of collider constraints, and also leads to a distinctive and novel low energy sparticle mass spectrum with characteristic signatures at the LHC.

[2] Among other features, it predicts a normal neutrino mass hierarchy with $\theta_{13} \approx 9^\circ$, $\theta_{23} \approx 45^\circ$ and $\delta \approx 260^\circ$ [42].

2.3 The Anomalous Magnetic Moment of the Muon

2.3.1 Overview

The magnetic moment of the muon (or any charged massive particle) is related to its spin $\vec{S}$ by

$$\vec{M} = g_\mu \frac{e}{2m_\mu} \vec{S}\,, \tag{2.7}$$

where g_μ is the gyromagnetic ratio. In the non-relativisitc limit, g_μ equals two exactly for any massive charged particle with semi-integer spin. Deviations from this classical value emerge once quantum level effects (loop corrections) are considered, where — besides SM corrections — new physics contributions may also be relevant. The corrections to g_μ can be parametrised by the so called anomalous magnetic moment

$$a_\mu = \frac{g_\mu - 2}{2} \tag{2.8}$$

and a_μ is one of the most precisely measured quantities in modern particle physics. In 2006, the E821 experiment at the Brookhaven National Laboratory measured a_μ with an accuracy of 0.54 ppm [43, 44] to

$$a_\mu^{\text{exp}} = 116592091(63) \times 10^{-11} \tag{2.9}$$

and future experiments at Fermilab [45] and J-PARC [46] aim to improve this result by a factor of four. On the other side, there is the SM theory prediction for a_μ of similar accuracy (for useful reviews, see [47–50]), consisting of QED corrections up to five loops [51] (see also [52–55]), electroweak corrections up to two loops [56, 57] and hadronic corrections [58–68] (for lattice QCD evaluations, see also [69–73]). Due to varying theoretical uncertainties between the authors for the hadronic corrections, the difference $\Delta a_\mu = a_\mu^{\text{exp}} - a_\mu^{\text{SM}}$ ranges from

$$\Delta a_\mu = a_\mu^{\text{exp}} - a_\mu^{\text{SM}} = 237(86) \times 10^{-11} \tag{2.10}$$

to

$$\Delta a_\mu = a_\mu^{\text{exp}} - a_\mu^{\text{SM}} = 278(80) \times 10^{-11}, \tag{2.11}$$

which are $2.8\,\sigma$ and $3.4\,\sigma$ tensions respectively [50]. To allow for an easier comparison with other studies, here we will use the value for Δa_μ as quoted in Ref. [44], reading

$$\Delta a_\mu = a_\mu^{\text{exp}} - a_\mu^{\text{SM}} = 288(80) \times 10^{-11}\,. \tag{2.12}$$

There are various theories that can account for the discrepancy in a_μ and we shall focus on a supersymmetric approach within this chapter, explained in detail in the following section 2.3.2.

2.3.2 MSSM One-Loop Contributions

In supersymmetric models, Δa_μ can fully or at least partially be attributed by smuon-neutralino and sneutrino-chargino loops [36,37,74–103], shown in figure 2.2 below. The respective analytical

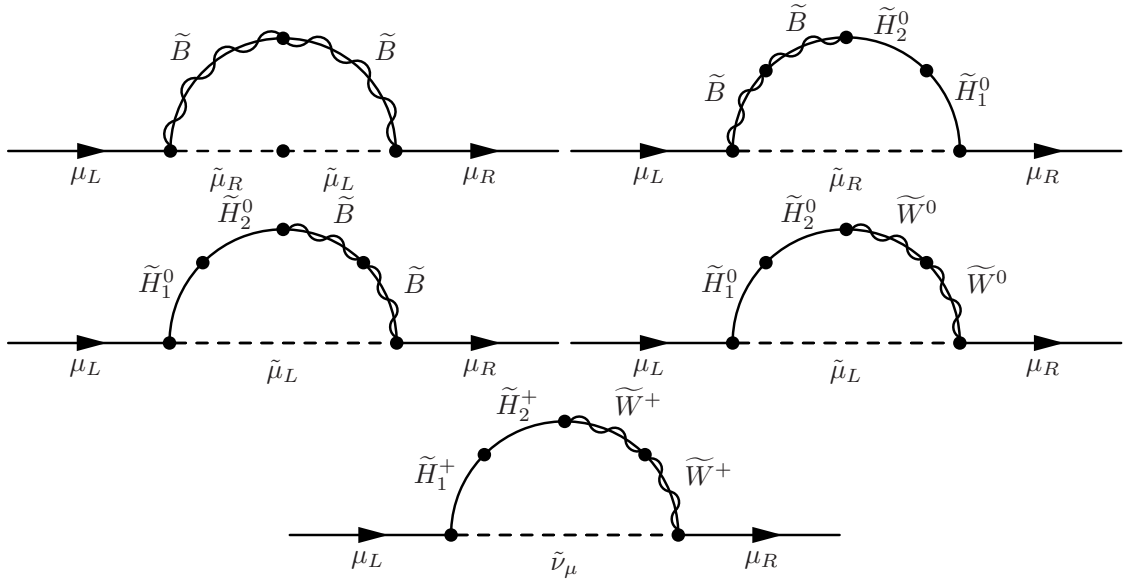

Figure 2.2: One-loop contributions to the anomalous magnetic moment of the muon for supersymmetric models with low-scale MSSM.

expressions for the above diagrams were computed in Refs. [37, 83] and read

$$\Delta a_\mu^{(A)} = \left(\frac{M_1\mu}{m^2_{\tilde{\mu}_L} m^2_{\tilde{\mu}_R}}\right) \frac{\alpha_1}{4\pi} m_\mu^2 \tan\beta \cdot f_{\mathrm{N}}^{(A)} \left(\frac{m^2_{\tilde{\mu}_L}}{M_1^2}, \frac{m^2_{\tilde{\mu}_R}}{M_1^2}\right), \tag{2.13a}$$

$$\Delta a_\mu^{(B)} = -\left(\frac{1}{M_1\mu}\right) \frac{\alpha_1}{4\pi} m_\mu^2 \tan\beta \cdot f_{\mathrm{N}}^{(B)} \left(\frac{M_1^2}{m^2_{\tilde{\mu}_R}}, \frac{\mu^2}{m^2_{\tilde{\mu}_R}}\right), \tag{2.13b}$$

$$\Delta a_\mu^{(C)} = \left(\frac{1}{M_1\mu}\right) \frac{\alpha_1}{8\pi} m_\mu^2 \tan\beta \cdot f_{\mathrm{N}}^{(C)} \left(\frac{M_1^2}{m^2_{\tilde{\mu}_L}}, \frac{\mu^2}{m^2_{\tilde{\mu}_L}}\right), \tag{2.13c}$$

$$\Delta a_\mu^{(D)} = -\left(\frac{1}{M_2\mu}\right) \frac{\alpha_2}{8\pi} m_\mu^2 \tan\beta \cdot f_{\mathrm{N}}^{(D)} \left(\frac{M_2^2}{m^2_{\tilde{\mu}_L}}, \frac{\mu^2}{m^2_{\tilde{\mu}_L}}\right), \tag{2.13d}$$

$$\Delta a_\mu^{(E)} = \left(\frac{1}{M_2\mu}\right) \frac{\alpha_2}{4\pi} m_\mu^2 \tan\beta \cdot f_{\mathrm{C}}^{(E)} \left(\frac{M_2^2}{m^2_{\tilde{\nu}_\mu}}, \frac{\mu^2}{m^2_{\tilde{\nu}_\mu}}\right), \tag{2.13e}$$

with α_1 and α_2 being the $U(1)_Y$ and $SU(2)_L$ fine structure constants respectively. The loop functions $f_{\mathrm{N}}^{(A,B,C,D)}(x,y)$ and $f_{\mathrm{C}}^{(E)}(x,y)$ are given by

$$f_{\mathrm{N}}^{(A,B,C,D)}(x,y) = xy\left[\frac{-3+x+y+xy}{(x-1)^2(y-1)^2} + \frac{2x\log x}{(x-y)(x-1)^3} - \frac{2y\log y}{(x-y)(y-1)^3}\right], \tag{2.14a}$$

$$f_{\mathrm{C}}^{(E)}(x,y) = xy\left[\frac{5-3(x+y)+xy}{(x-1)^2(y-1)^2} - \frac{2\log x}{(x-y)(x-1)^3} + \frac{2\log y}{(x-y)(y-1)^3}\right], \tag{2.14b}$$

where we use the superscripts (A,B,C,D) and (E) as a short notation to allow omission of the mass ratio arguments. Both f_N and f_C are monotonically increasing for all $0 \leq x, y < \infty$ and are defined in $0 \leq f_{N,C} \leq 1$ [37]. Figure 2.3 shows contour plots of $f_N(x,y)$ (left) and $f_C(x,y)$ (right) and it is worth noting that, for most x and y, $f_N(x,y) < f_C(x,y)$. E.g. for $x = y = 0.2$, f_N is roughly ten times smaller then f_C. The importance of this behaviour towards explaining Δa_μ will become relevant in section 2.5.

While investigating equation (2.13) in detail, it is apparent that major contributions to Δa_μ come from the prefactors in brackets on the right-hand side. Thus, having large, positive μ together with light smuon masses $m_{\tilde{\mu}_{L/R}}$ greatly enhances diagram (A) while simultaneously suppressing diagrams (B) to (E). Also, as long as M_1 does not get too large, the loop functions are nearly neglegible within this setup.

The solution for large μ is not unique, however, and small values of μ can also lead to the

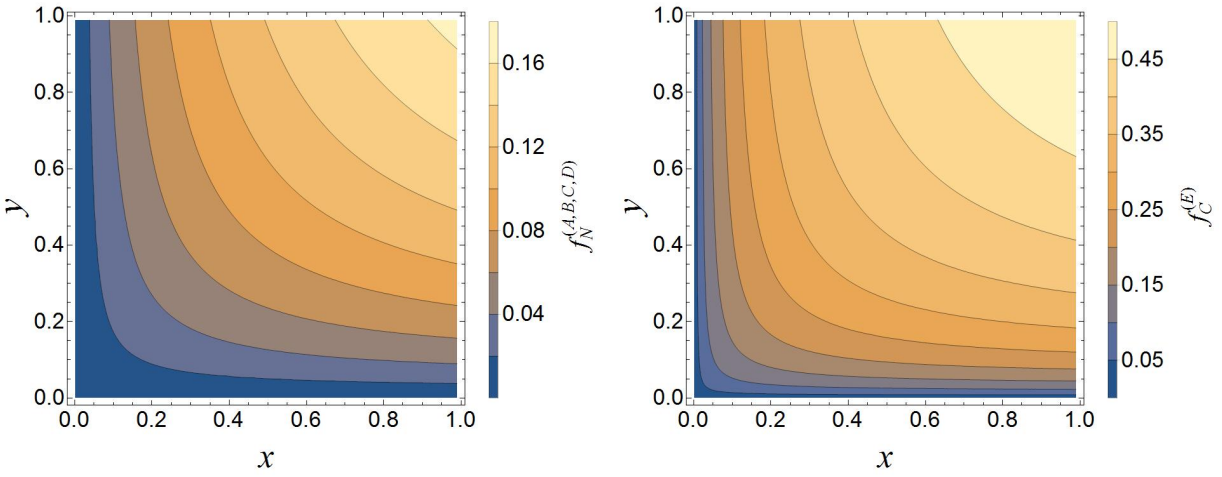

Figure 2.3: Contour plots for $f_{\mathrm{N}}(x, y)$ (left) and $f_{\mathrm{C}}(x, y)$ (right).

desired Δa_μ. Now, large contributions arise from diagrams (B) and (E) or (C) and (D) (depending on $\mathrm{sgn}(\mu)$), while diagram (A) is suppressed. In this scenario, the loop functions become important and may distinguish the dominant contributions among diagrams (B) to (E).

2.4 Experimental Constraints

Any successful high energy theory completing the SM should also comprise all known low-energy experimental constraints. In particular, we require our model to be in conformity with the dark matter relic density, limits coming from DM direct detection (DD) experiments, the Higgs boson mass and the branching ratios for $\mathrm{BR}(B_s \to \mu^+\mu^-)$ and $\mathrm{BR}(b \to s\gamma)$. The current combined best fit of the DM relic density to data from Planck and Wmap is $\Omega h^2 = 0.1198 \pm 0.0026$ [104]. However, we also consider the possibility that our model only partially accounts for the relic density, thus opening up the bound to $\Omega h^2 \in [0.06, 0.1224]$. Regarding the DM DD limits, we consider data from the Lux collaboration on the 90 % upper confidence level cross sections for spin-independent models. At a WIMP mass of 33 GeV, the limit reads $\sigma^{\text{DD-SI}} \leq 7.6 \times 10^{-46}\ \mathrm{cm}^{-2} = 7.6 \times 10^{-10}$ pb [105]. For smaller or larger WIMP masses, the limits are weaker, therefore making our choice conservative. Concerning the Higgs mass m_H, the current best combined measurement was performed by the ATLAS and CMS collaborations, yielding $m_H =$

$(125.09 \pm 0.21\,(\text{stat.}) \pm 0.11\,(\text{sys.}))$ GeV [106]. However, due to much larger theoretical uncertainties arising in the computation of radiative corrections to the Higgs mass in the current state of the art spectrum generators, we relax this constraint to $m_H = (125.09 \pm 1.50)$ GeV. The branching ratios $\text{Br}(b \to s\gamma) = (3.29 \pm 0.19 \pm 0.48) \times 10^{-4}$ [107] and $\text{Br}(B_s \to \mu^+\mu^-) = 3.0^{+1.0}_{-0.9} \times 10^{-9}$ [108] are directly applied to our results.

While the above experimental constraints are fixed, we still have the possibility to further adapt our model parameter space in order to aim for some useful features. Light sleptons and especially light smuons are one such feature due to the consequent large contribution to $\Delta a_\mu^{(A)}$ (see equation (2.13a)). Additionally, light smuons provide a suitably higher possibility to explore them in experimental studies as currently performed at the LHC because of their comparably clean muonic signals. The smuon masses $m_{\tilde{\mu}_L}$ and $m_{\tilde{\mu}_R}$ are controlled by m_0 and m_2 respectively, and in order to get both smuons to be light, both m_0 and m_2 have to be light. Another useful feature related to the smuon masses is a large mass gap between at least one of them and the LSP (denoted by $\tilde{\chi}$). This prevents muons coming from smuon decays $\tilde{\mu}^\pm \to \tilde{\chi}\,\mu^\pm$ to be soft and hence nearly undedectable by any collider. Finally, having a bino-like LSP is desirable as it helps providing the correct DM relic density. Light LSPs can be aimed at by choosing $M_1 < M_2, \mu$, but not controlled directly. Therefore, different scans with different such parameter choices need to be performed for an ideal choice of the gaugino mass parameters.

Lastly, we verified that none of our proposed benchmarks violate any of the 8 TeV ATLAS and CMS analyses. This step is necessary as one set of our solutions, namely the small μ scenario, includes light $\tilde{\chi}_1^0$, $\tilde{\chi}_2^0$ and $\tilde{\chi}_1^\pm$ with comparatively low mass splittings (of order 100 GeV), leading to potential di or tri-lepton signatures unobserved at the LHC and thus ruling out the respective parameter space. The verification was done using `MadGraph 5.2.2.3` [109] to generate events for all relevant combinations of chargino-neutralino pair production, `PYTHIA 6.4` [110] linked to `MadGraph` to perform the parton[3] showering[4] and hadronisation, `DELPHES 3.0` [111] linked to `CheckMATE 1.2.1` [112] for fast detector simulations and `CheckMATE` itself for the final event

[3] Historically, *partons* were the then unkown constituents of hadrons. Nowadays, we know hadrons consist of quarks and gluons and the name parton can be used to address both.

[4] *Showering* or *parton showering* is the process of simulating initial and final state radiation for some underlying, usually hard scattering event. Partons participating in this scattering can radiate gluons, for example, which themselves can emit further radiation. This eventually leads to a cascade of particles, hence the name *showering*.

analysis. The event analysis relies on the data provided by both ATLAS and CMS and is validated against it in `CheckMATE`. Furthermore, the same experimental cuts as used by either collaboration are applied, thus allowing us to establish whether a point in parameter space is ruled out or still unexplored.

As a result, we found that tri-lepton signatures explored in Refs. [113, 114] are the most constraining ones for the small μ region. Di-lepton signatures, although turning out to be less constraining for the parameter space under study, are also worth mentioning.

2.5 Results

To begin with, a point in parameter space is chosen by setting all relevant model parameters (cf. section 2.1 and 2.2). Next, `SoftSUSY 3.5.2` [115] is used to generate the associated mass spectrum and any point with a Higgs mass out of the bounds chosen in section 2.4 is discarded. If the Higgs mass is in bounds, `micrOMEGAs_3.6.9.2` [116] is employed to compute the relic density as well as all remaining constraints described in section 2.4.

2.5.1 An Inclusive Scan

Due to the lack of evidence for any strongly interacting SUSY particle at the LHC, the masses of gluinos and squarks of the first two generations must be $\gtrsim 1.5$ TeV and thus be rather heavy. However, the electroweak searches are much less sensitive and consequently, less stringent bounds on the sleptons and gauginos arise. As Δa_μ benefits from light smuons and gauginos, we perform a first inclusive scan taking this as well as the stronger bounds on coloured sparticles into account. An overview of the parameter space we consider is shown in table 2.1, where for simplicity we assume $A_{\text{tri}} \equiv A_t = A_b = A_\tau$. In particular, we allow the $SU(3)_C$ gaugino mass, M_3, and the third

Parameter	Range	Parameter	Range
$\lvert A_{\text{tri}}\rvert$	$1 - 3000$	$\lvert M_1\rvert$, $\lvert M_2\rvert$	$1 - 600$
m_0, m_1, m_2	$1 - 500$	$\lvert M_3\rvert$	$1 - 6000$
m_3	$1 - 3000$	$\tan\beta$	$5 - 50$
m_{H_1}, m_{H_2}	$1 - 3000$	$\text{sgn}\,(\mu)$	± 1

Table 2.1: Model parameters at the GUT scale. Dimensionful parameters are in GeV.

generation right-handed scalar mass, m_3, to be very heavy so that the stop loops may provide a significant contribution to the Higgs mass. Also, the smuons, controlled by m_0 and m_2 are kept rather light to enhance Δa_μ contributions. All other parameters remain fairly unconstrained.

In figure 2.4, we present viable portions of parameter space in the Δa_μ-μ (top), Δa_μ-M_1 (bottom-left) and Δa_μ-M_2 (bottom-right) planes. Here, the light green and orange triangles have too low relic density, the turquoise and salmon circles have only the relic density in bounds and the dark blue and red diamonds have Δa_μ as well as the relic density in bounds. From the top

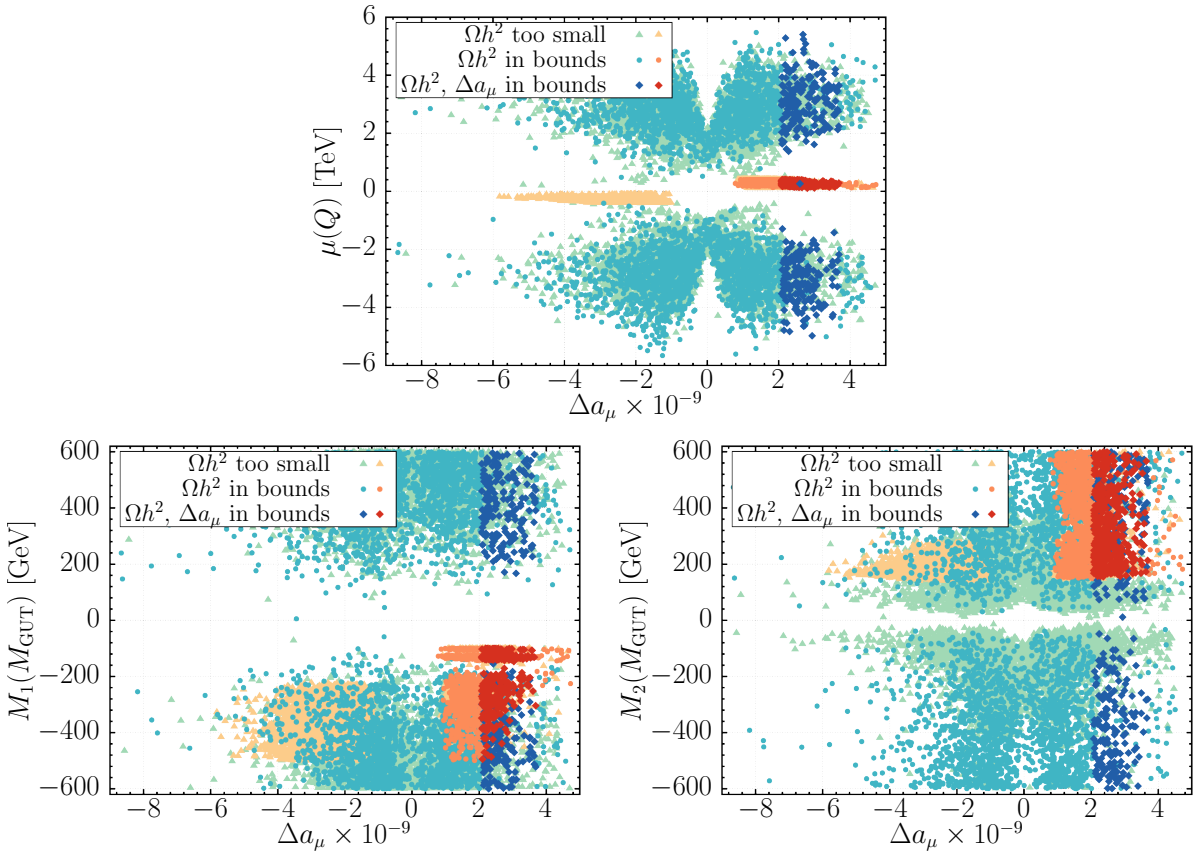

Figure 2.4: Viable scenarios in the Δa_μ-μ (top) and Δa_μ-M_1 (bottom-left) as well as Δa_μ-M_2 (bottom-right) planes. Dark blue and red diamonds correspond to scenarios with bino-like DM, whereas light green and orange triangles as well as turquoise and salmon circles correspond to scenarios with mainly wino and partially higgsino-like DM. The reddish points correspond to a separate scan around the isolated dark blue point at small μ in the top panel. The input parameters are shown in table 2.2.

panel, it is apparent that there are two classes of solutions for viable Δa_μ. These are namely

solutions with small μ (the isolated blue diamond at $\mu \approx 0$ GeV and the red band around it) as well as solutions with large μ (the two blue bands with $|\mu| \gtrsim 2$ TeV). Additionally to a large SUSY-preserving mass parameter $|\mu| \gtrsim 2$ TeV, these solutions also prefer the bino mass paramter $|M_1| \gtrsim 100$ GeV and at first glance do not differentiate between $\operatorname{sgn} M_1$ or $\operatorname{sgn} M_2$. For the solutions with small μ, the situation is different, as viable Δa_μ can only be achieved if $\operatorname{sgn} M_1 = -1$ and $\operatorname{sgn} M_1 = -\operatorname{sgn} M_2$. The isolated blue diamond around $\mu \approx 0$ and $\Delta a_\mu \approx 2.6 \cdot 10^{-9}$ has $\mu = 262.5$ GeV, $\mathrm{M}_1 = -475.8$ GeV and $\mathrm{M}_2 = 588.9$ GeV and predicts a bino-like LSP with mass $m_{\tilde{\chi}} = 200.1$ GeV.

In figure 2.5, we show the μ-M_1 parameter space with points where the lightest neutralino $\tilde{\chi}_1^0$ is predominantly composed of the bino component. In the left panel, the colour-coding is the same as in figure 2.4, while in the right panel, brighter colours correspond to heavier $m_{\tilde{\chi}_1^0}$. As can be expected, it turns out that smaller values of the $U(1)_Y$ gaugino mass M_1 at the GUT scale strengthen the bino character of the LSP.

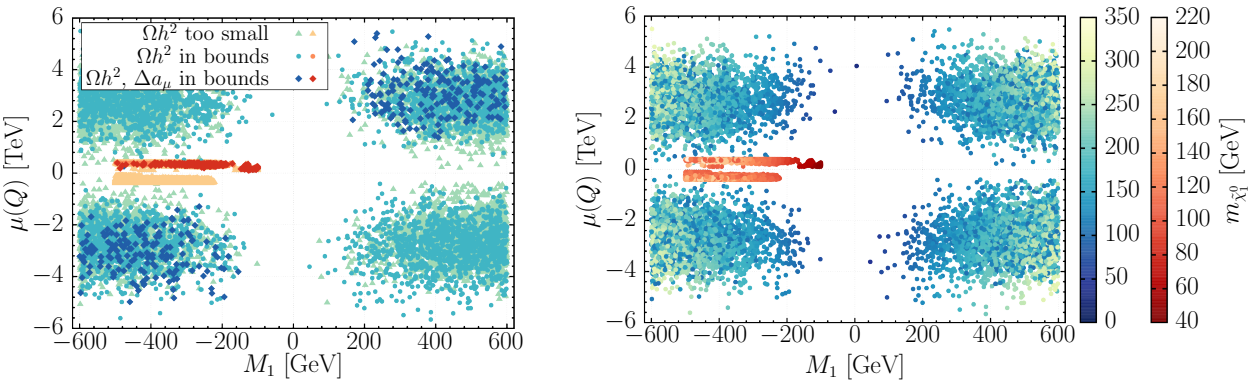

Figure 2.5: Correlation between $\mu(Q)$ and M_1. The left panel holds points satisfying the experimental constraints from section 2.4, where the dark blue and red diamonds fulfil both the relic density and Δa_μ constraints, turquoise and salmon circles only have the relic density in bounds (but not Δa_μ), and light green and orange triangles refer to points with neither the relic density nor Δa_μ in bounds. The panel on the right shows the same data, but with colour-coded LSP mass $m_{\tilde{\chi}_1^0}$ for the inclusive scan (blue points, see table 2.1) and the small μ scan (red points, see table 2.2).

2.5.2 Small μ Solutions

In this section, we investigate the solutions with small μ from the narrow band in figure 2.4. For this, a dedicated scan was performed with the GUT scale parameters chosen as shown in table 2.2 below. In figure 2.6, we show an overview over the scan results in the $m_{\tilde{\chi}_1^0}$-$m_{\tilde{\mu}_{L/R}}$ plane,

Parameter	Range			Parameter	Range		
A_{tri}	-4000	–	-2300	M_1	-500	–	-100
m_0	400	–	700	M_2	100	–	600
m_1	300	–	500	M_3	5	–	50
m_2	200	–	400	$\tan\beta$	15	–	35
m_3	200	–	2000	$\operatorname{sgn}\mu$		$+1$	
m_{H_1}, m_{H_2}	1500	–	2500				

Table 2.2: Model parameters at the GUT scale. Dimensionful parameters are in GeV.

including only those points which have a positive contribution towards Δa_μ. For both smuons,

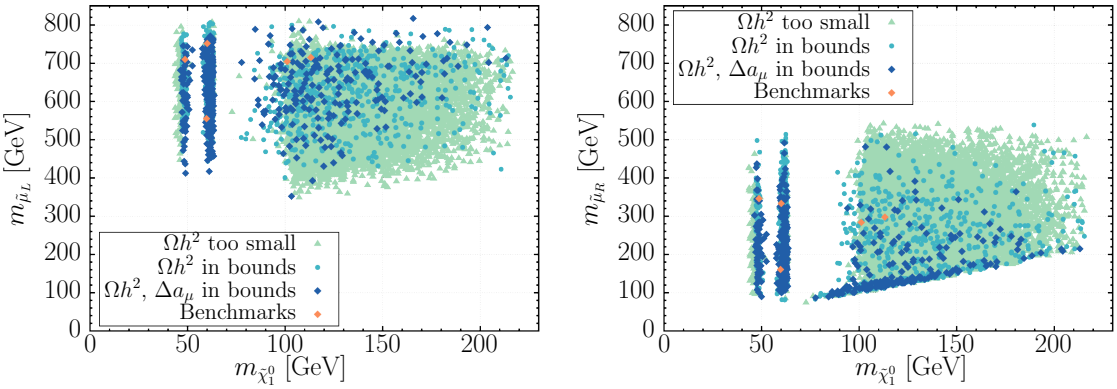

Figure 2.6: Lightest neutralino mass vs. smuon masses. All dark blue diamonds are bino-like, whereas the light green triangles and turquoise circles are wino-like. The orange pentagons represent the benchmark points defined in table 2.3.

three distinguishable regions can be identified. Two vertical bands around $m_{\tilde{\chi}_1^0} \approx 50$ and 60 GeV as well as a broad bulk for larger $m_{\tilde{\chi}_1^0}$. The first two bands correspond to the situation where the LSP annihilates via resonant Z and Higgs boson decays. In the bulk region, one has to differentiate between $\tilde{\mu}_L$ and $\tilde{\mu}_R$. In case of right-handed smuons, we observe a diagonal stripe at the bottom of the bulk corresponding to an effective co-annihilation between $\tilde{\mu}_R$ and $\tilde{\chi}_1^0$. The bulk

above this stripe and the entire bulk for left-handed smuons then corresponds to the situation where DM co-annihilates with non-smuonic next-to-lightest supersymmetric particles (NLSPs).

In figure 2.7, we show the same data, however this time for the mass differences $m_{\tilde{\mu}_{L/R}} - m_{\tilde{\chi}_1^0}$ versus the LSP mass. As could already be estimated from figure 2.6, the mass difference in case of left-handed smuons is quite large and never deceeds 200 GeV. For right-handed smuons, this is not the case and mass gaps as small as 1 GeV or less are possible, although not exclusively. If there were only such small mass gaps, any muons arising from smuon decays would be nearly invisible at the LHC. To allow for harder muons and thus possibly detectable signatures at the LHC, we chose benchmark points with a mass gap to either smuon $\gtrsim$ 100 GeV (see orange pentagons in figure 2.7).

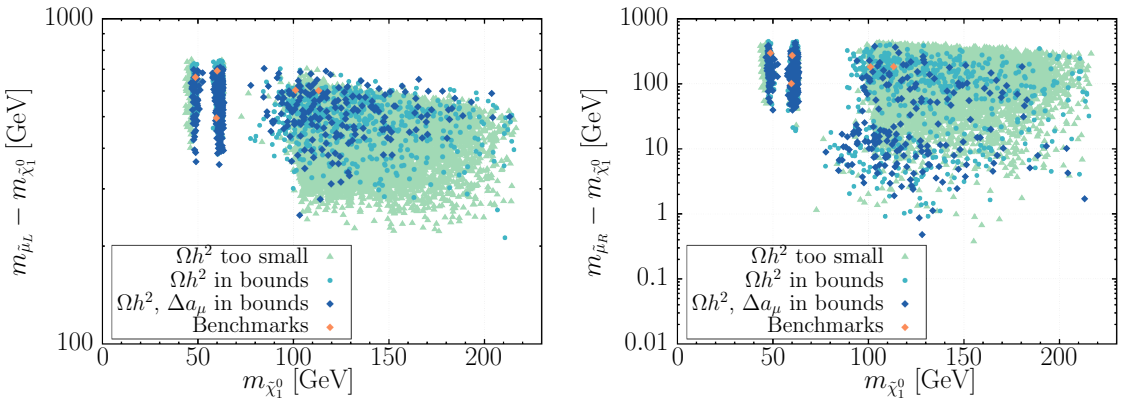

Figure 2.7: Mass gaps between the smuon and lightest neutralino masses, $m_{\tilde{\mu}_{L/R}}$ and $m_{\tilde{\chi}_1^0}$. All dark blue diamonds are bino-like, whereas the light green triangles and turquoise circles are wino-like. The orange pentagons represent the benchmark points defined in table 2.3.

Due to the smallness of μ in this scenario, contributions to Δa_μ are expected to arise from diagrams (B), (C), (D) and (E) $\propto \mu^{-1}$ of equations (2.13b) to (2.13e), whereas only minor contributions from diagram (A) $\propto \mu$ of equation (2.13a) are expected. As mentioned earlier, in case of small μ the loop functions $f_{\mathrm{N}}^{(A,B,C,D)}(x,y)$ and $f_{\mathrm{C}}^{(E)}(x,y)$ can have a significant impact on the overall contributions to Δa_μ. We therefore analysed each individual loop contribution from figure 2.2 (or equation (2.13) respectively) to understand how the total Δa_μ is put together in this situation. This is shown in the following figure 2.8, where we plot each contribution $\Delta a_\mu^{(X)}$ for $X = A, B, C, D, E$ versus the corresponding loop function $f_{N,C}(x,y)$ with the total

value of Δa_μ for each point being colour-coded. It turns out that the only relevant positive contributions are coming from diagrams (B) and (E). By noting that we chose M_1 negative and μ and M_2 positive (see table 2.2), this makes perfect sense, as only equations (2.13b) and (2.13e) yield positive contributions to Δa_μ under these assumptions. Both diagrams (B) and (E) also contribute the major part to the total Δa_μ, as a closer look at the loop functions reveals. Since, in this scenario, the left-handed smuon is always heavier than the right-handed smuon, the loop functions for diagrams (C) and (D) are suppressed compared to the one from diagram (B): $f_{\mathrm{N}}^{(C,D)}\left(\frac{M_{1,2}^2}{m_{\tilde{\mu}_L}^2}, \frac{\mu^2}{m_{\tilde{\mu}_L}^2}\right) \ll f_{\mathrm{N}}^{(B)}\left(\frac{M_1^2}{m_{\tilde{\mu}_R}^2}, \frac{\mu^2}{m_{\tilde{\mu}_R}^2}\right)$. With this reasoning, one could expect that diagram (E) is also suppressed, as the muon sneutrino and the left-handed smuon are similar in mass and both loop functions $f_{N,C}(x,y)$ share the same asymptotic limits. This is not the case, however, as for fixed (x,y), $f_C(x,y) \gg f_N(x,y)$ (see discussion in section 2.3.2 and figure 2.3 therein.). Thus, diagram (E) is driven mainly by its loop function $f_{\mathrm{C}}^{(E)}\left(\frac{M_2^2}{m_{\tilde{\nu}_\mu}^2}, \frac{\mu^2}{m_{\tilde{\nu}_\mu}^2}\right)$, which allows for a significant contribution to the total Δa_μ.

Based on the above findings in the small μ scenario, we provide a set of benchmarks listed in table 2.3.

2.5.3 Large μ Solutions

The second set of solutions for viable Δa_μ we found requires a quite large higgsino mass parameter $|\mu| \gtrsim 2$ TeV. Analogue to the small μ scenario, we performed a dedicated scan around the points with the correct Δa_μ from figure 2.4 with a GUT scale parameter choice as shown in table 2.4 below. As μ now is large, we expect major contributions to Δa_μ only from diagram (A) (see equation (2.13a)) due its proportionality to μ, whereas contributions from diagrams (B) to (E) (see equations (2.13b) to (2.13e)) should be suppressed due to their proportionality to μ^{-1}. Additionally, diagram (A) benefits greatly from having small smuon masses due to their appearance in the prefactor of equation (2.13a). Analogue to figure 2.8, we show each contribution $\Delta a_\mu^{(X)}$ for $X = A, B, C, D, E$ versus $\mu(Q)$ in figure 2.9, which confirms our above assumptions.

Regarding the relic density, it is possible to fully account for it in the large μ scenario in case dark matter is entirely bino-dominated. There are several points fulfilling this condition, which we show as dark blue diamonds in figure 2.10.

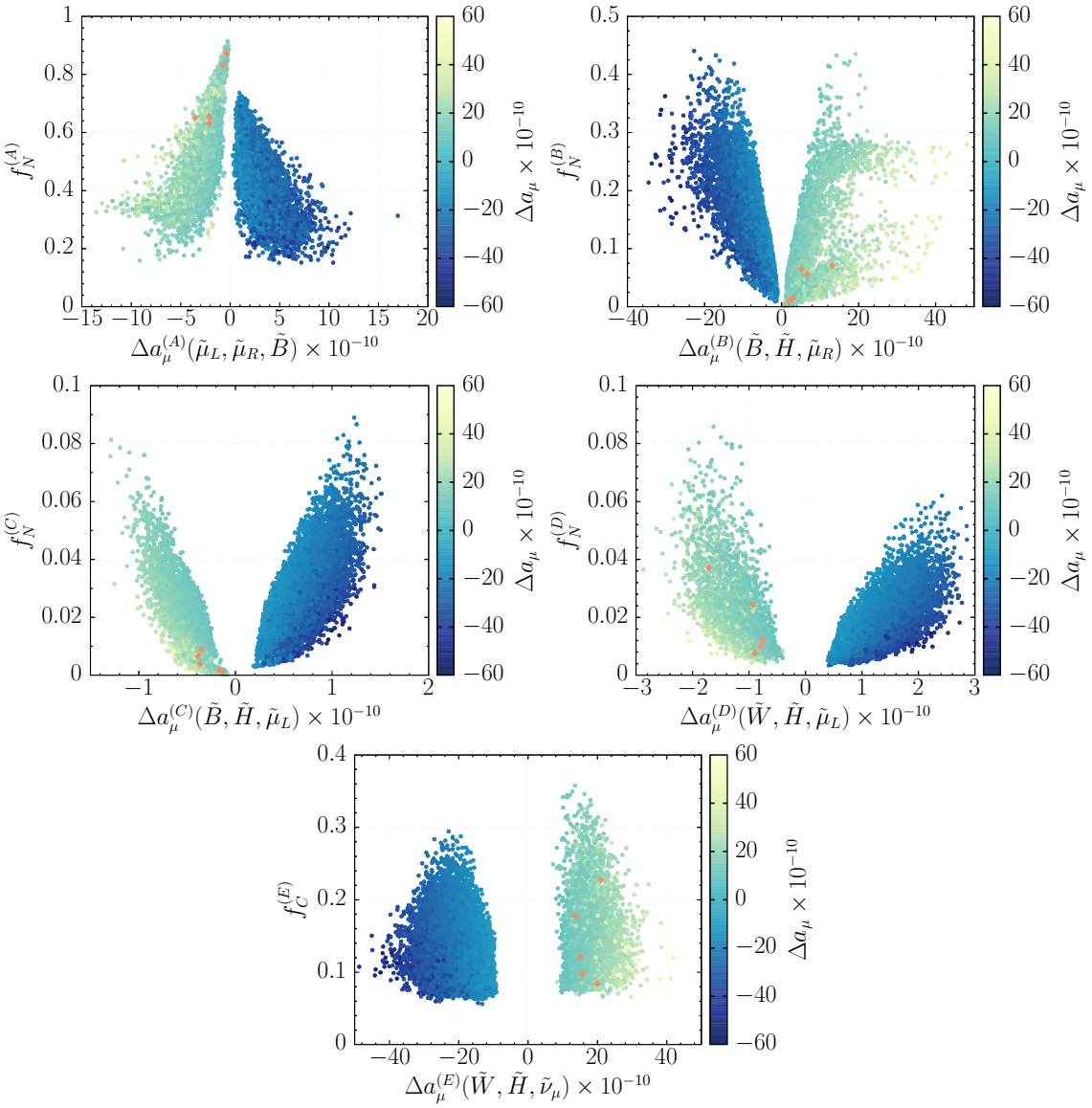

Figure 2.8: Individual contributions $\Delta a_\mu^{(i)}$ with $i = \{A, B, C, D, E\}$ of equation (2.13) versus the loop functions $f_{N,C}(x, y)$. The colour scale indicates the total value value of Δa_μ. The orange pentagons represent the benchmark points defined in table 2.3.

	Benchmark:	BP1	BP2	BP3	BP4	BP5	
Input at GUT scale	$\tan\beta$	26.48	21.20	22.89	29.52	25.88	
	$\mathrm{sgn}(\mu)$	+	+	+	+	+	
	m_0	681.1	490.4	689.0	691.4	688.4	
	m_1	402.0	327.5	447.0	364.4	417.9	
	m_2	397.4	273.0	394.2	342.2	390.7	
	m_3	1204.7	871.8	1085.4	987.4	1192.3	
	M_1	-100.1	-124.1	-123.8	-224.9	-255.1	
	M_2	294.9	367.5	449.9	168.6	177.9	[GeV]
	M_3	1004.6	1085.7	1109.8	1066.5	947.6	
	M_{h_1}	2204.8	2108.4	2246.6	2127.3	2007.2	
	M_{h_2}	2385.7	2350.9	2455.7	2330.2	2344.7	
	A_{tri}	-2839.1	-2762.5	-2838.5	-2764.0	-3090.0	
Masses	m_{h_0}	125.2	125.2	125.2	125.1	125.1	
	$m_{\tilde{g}}$	2220.9	2373.5	2427.3	2349.4	2108.5	
	$m_{\tilde{q}_L^{1,2}}$	2040.6	2122.7	2220.1	2149.1	1949.0	
	$m_{\tilde{b}_1}$	1424.1	1537.5	1592.3	1506.8	1234.0	
	$m_{\tilde{t}_1}$	1120.3	1117.4	1207.9	1184.6	962.3	
	$m_{\tilde{q}_R^1}$	1963.9	2086.2	2149.9	2070.3	1872.7	
	$m_{\tilde{q}_R^2}$	1962.9	2078.1	2136.3	2066.3	1866.5	
	$m_{\tilde{b}_2}$	2164.4	2108.7	2209.8	2026.6	1984.0	
	$m_{\tilde{t}_2}$	1488.6	1584.3	1641.0	1561.4	1323.4	
	$m_{\tilde{e}_L}$	710.5	555.8	752.4	705.3	715.6	
	$m_{\tilde{e}_R}$	352.7	244.2	396.3	313.5	335.2	
	$m_{\tilde{\mu}_L}$	710.1	555.2	751.8	704.5	714.9	
	$m_{\tilde{\mu}_R}$	346.1	160.7	333.5	283.9	297.6	[GeV]
	$m_{\tilde{\tau}_1}$	594.8	375.0	589.5	424.9	483.8	
	$m_{\tilde{\tau}_2}$	1054.1	612.5	834.6	560.1	894.9	
	$m_{\tilde{\chi}_1^0}$	-48.58	-59.58	-60.00	-101.0	-113.2	
	$m_{\tilde{\chi}_2^0}$	169.5	215.5	243.3	115.9	127.9	
	$m_{\tilde{\chi}_3^0}$	-228.2	-265.1	-277.4	-350.7	-411.9	
	$m_{\tilde{\chi}_4^0}$	287.7	337.3	391.5	357.2	416.9	
	$m_{\tilde{\chi}_1^\pm}$	171.3	217.3	245.0	116.3	128.2	
	$m_{\tilde{\chi}_2^\pm}$	287.4	336.9	390.8	360.4	419.9	
	$m_{\tilde{\nu}_L^e}$	705.8	549.9	747.9	700.5	711.0	
	$m_{\tilde{\nu}_L^\mu}$	705.5	549.4	747.5	704.5	710.4	
	$m_{\tilde{\nu}_L^\tau}$	589.5	367.5	584.5	421.6	478.1	
	Q	1293.4	1337.0	1409.0	1360.4	1143.6	
	$\mu(Q)$	212.3	250.5	263.2	335.2	397.9	
Constraints	$\mathrm{Br}(b\to s\gamma)$	2.89×10^{-4}	2.91×10^{-4}	2.91×10^{-4}	3.25×10^{-4}	3.25×10^{-4}	
	$\mathrm{Br}(B_s\to\mu^+\mu^-)$	2.69×10^{-9}	2.97×10^{-9}	2.97×10^{-9}	3.06×10^{-9}	3.11×10^{-9}	
	$\sigma^{\mathrm{DD\ SI}}$	1.31×10^{-11}	1.28×10^{-11}	1.18×10^{-11}	2.42×10^{-11}	1.06×10^{-11}	[pb]
	Ωh^2	1.05×10^{-1}	1.25×10^{-1}	1.23×10^{-1}	8.32×10^{-2}	8.47×10^{-2}	
	Δa_μ	1.37×10^{-9}	2.28×10^{-9}	1.30×10^{-9}	1.99×10^{-9}	1.52×10^{-9}	

Table 2.3: Input and Output parameters for the small μ benchmark points with the most accurate Δa_μ and Ωh^2 and all other experimental constraints fulfilled. $\tilde{q}^i$ labels the i-th generation of squarks.

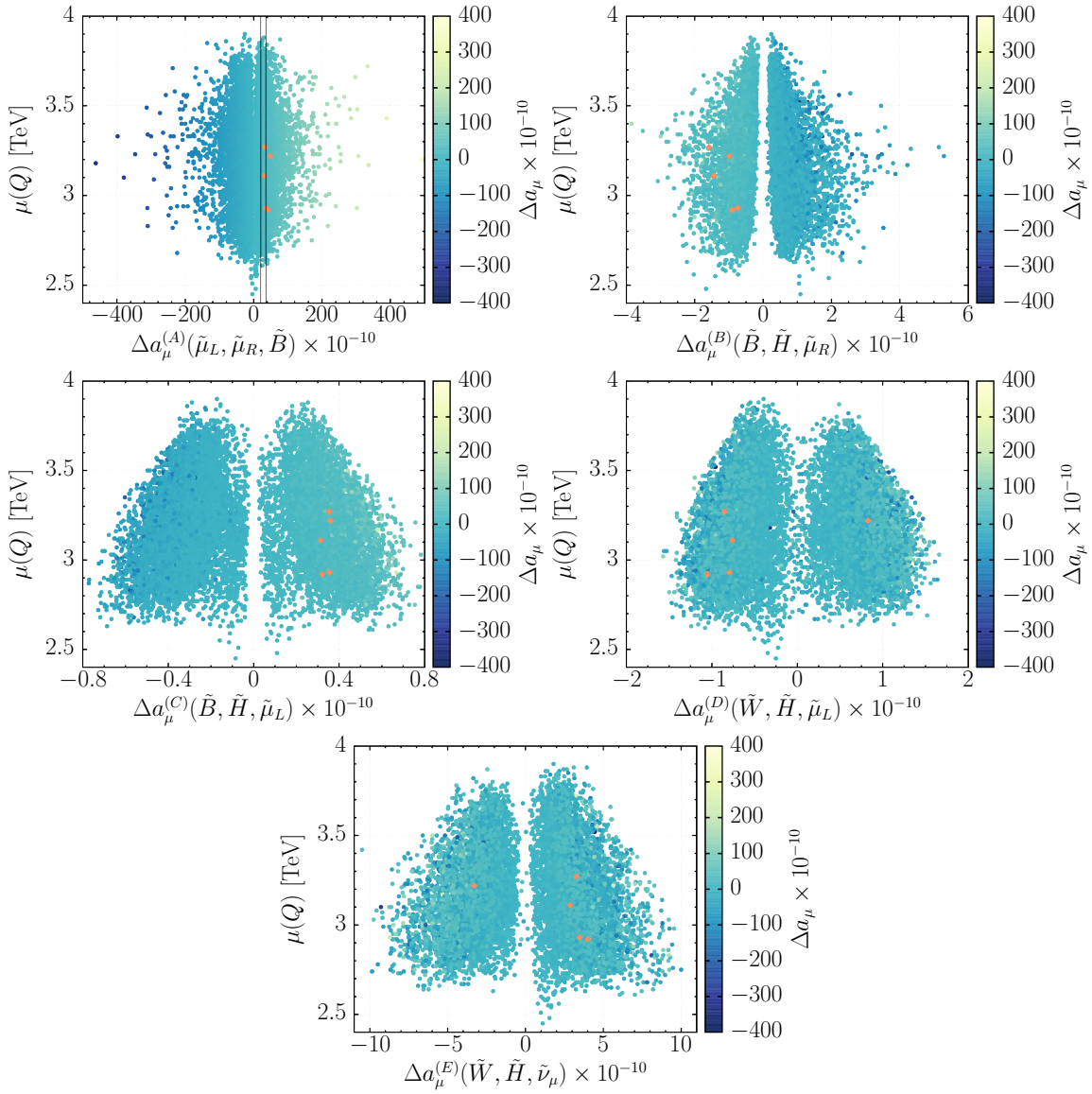

Figure 2.9: Individual contributions $\Delta a_\mu^{(i)}$ with $i = \{A, B, C, D, E\}$ of equation (2.13) versus $\mu(Q)$. The colour scale indicates the total value value of Δa_μ, while the black bars in the top left panel show the $1\,\sigma$ bound of Δa_μ. The orange pentagons represent the benchmark points defined in table 2.5.

Parameter	Range		Parameter	Range	
A_{tri}	-3000	0	M_1	-1000	1000
m_0	100	300	M_2	-2000	2000
m_1	500	1500	M_3	2000	3000
m_2	100	400	$\tan\beta$	5	50
m_3	1000	2000	$\operatorname{sgn}\mu$	$+1$	
m_{H_1}, m_{H_2}	100	3000			

Table 2.4: Theory parameters at the GUT scale. The soft-SUSY breaking parameters are given in GeV.

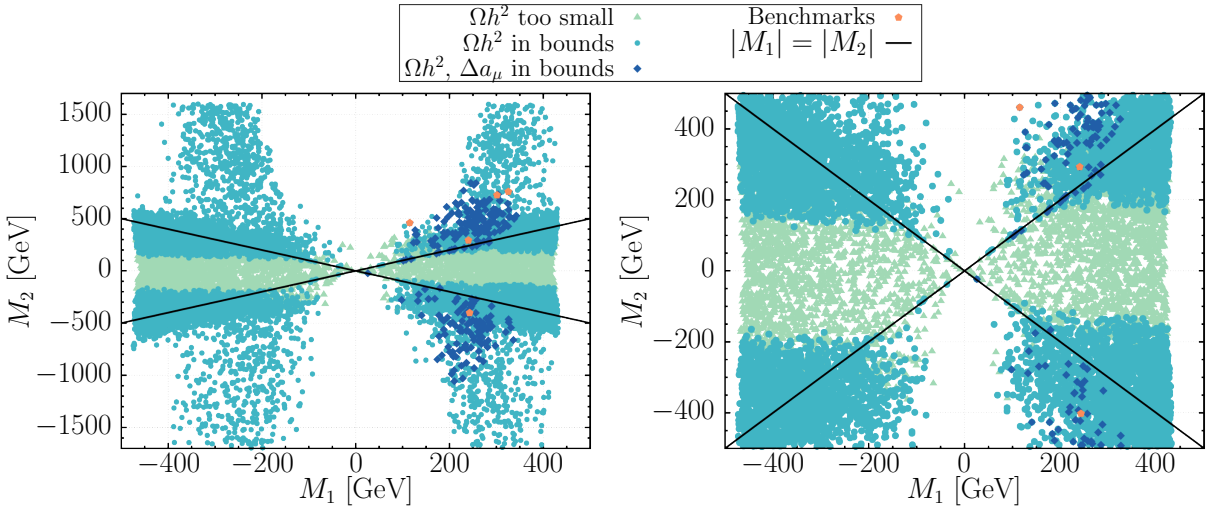

Figure 2.10: $M_1(Q)$ vs. $M_2(Q)$ (left) and a smaller excerpt of it (right). All dark blue diamonds are bino-like, whereas the light green triangles and turquoise circles are wino-like. The orange pentagons represent the benchmark points defined in table 2.5.

In figure 2.11, we show the mass gaps between both left and right-handed smuons and the lightest neutralino, which always is the LSP in this scenario. Other than in the small μ scenario, the mass gaps for left-handed smuons now can be as light as 50 GeV (if both the relic density and Δa_μ are required to be viable), whereas the mass gap between the right-handed smuons and the LSP ranges down even further up to 0.01 GeV. As mentioned before, mass gaps that small would render muons from smuon decays nearly undetectable, thus we aimed for choosing benchmarks with larger mass gaps. While this is always possible for left-handed smuons, some right-handed smuons are degenerate in mass with the LSP up to 10 GeV, however as long as at least one smuon offers a larger mass gap, this is not problematic.

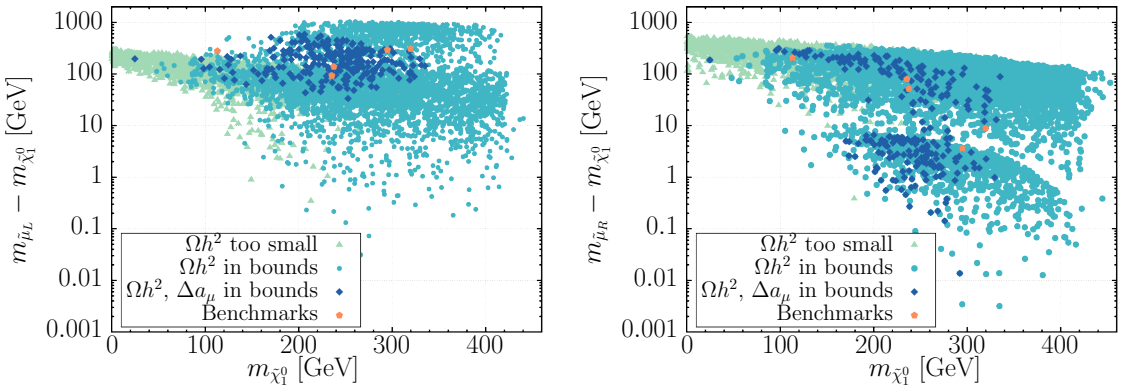

Figure 2.11: Mass gaps between the smuon and lightest neutralino masses, $m_{\tilde{\mu}_{L/R}}$ and $m_{\tilde{\chi}_1^0}$. All dark blue diamonds are bino-like, whereas the light green triangles and turquoise circles are wino-like. The orange pentagons represent the benchmark points defined in table 2.5.

Next, we examine the various possible NLSPs arising in this scenario by analysing the mass gaps between the NLSP and LSP versus the LSP mass for different experimental bounds on Δa_μ and the relic density in figure 2.12. In the top left panel, the relic density is too small, which is characterised by a first chargino NLSP, which is almost exactly mass-degenerate with the LSP. In case the relic density is required to be in bounds, but not necessarily having the correct Δa_μ, we observe the NLSP spectrum in the top right panel. The chargino NLSPs almost entirely vanished and the right-handed smuon took its place instead, however the $\tilde{\tau}_1$ and τ-sneutrino also appear as NLSPs in non-negligible amounts. All $\tilde{\mu}_R$, $\tilde{\tau}_1$ and $\tilde{\nu}_\tau$ thereby can be mass-degenerate with the LSP up to about 10 GeV. In case both the relic density and Δa_μ are required to be correct (bottom panel), the picture does not change much in terms of NLSP distributions and is just a subset of the top right panel. A noteworthy change however is that for right-handed smuon NLSPs, the LSP mass is now favoured to lie between 200–300 GeV instead of 100–400 GeV. In case of stau or tau-sneutrino NLSPs, the LSP mass range is only slightly reduced.

Lastly in figure 2.13, we show the Δa_μ-Ωh^2 plane and the respective experimental 1σ bounds as grey shaded rectangle. There a numerous points in the vicinity of the desired relic density and still several points in both the relic density and Δa_μ $1\,\sigma$ reference bounds. From these points, we chose the most interesting ones for a second set of benchmarks, listed in table 2.5 below.

	Benchmark:	BP6	BP7	BP8	BP9	BP10	
Input at GUT scale	$\tan\beta$	16.96	26.88	32.15	22.21	40.22	
	$\mathrm{sgn}(\mu)$	+	+	+	+	+	
	m_0	238.8	149.6	106.5	271.5	137.5	
	m_1	1426.7	1131.1	626.5	508.9	1470.7	
	m_2	239.2	302.7	125.3	193.5	178.4	
	m_3	1458.7	1631.9	1076.3	1434.2	1847.8	
	M_1	577.9	292.3	711.6	579.8	760.7	[GeV]
	M_2	412.8	612.4	948.8	-436.4	982.8	
	M_3	2195.7	2055.2	2680.5	2456.0	2524.6	
	M_{h_1}	670.6	2924.4	577.0	1512.8	1577.3	
	M_{h_2}	814.9	925.9	918.8	1306.2	1362.7	
	A_{tri}	-2244.8	-2776.6	-1113.2	-2896.2	-2370.1	
Masses	m_{h_0}	124.1	124.1	123.5	124.5	123.6	
	$m_{\tilde{g}}$	4595.1	4308.9	5497.4	5089.9	5201.7	
	$m_{\tilde{q}_L^{1,2}}$	3931.0	3697.9	4709.6	4356.0	4468.8	
	$m_{\tilde{b}_1}$	3527.8	3216.6	4257.5	3893.5	3878.2	
	$m_{\tilde{t}_1}$	3412.9	3154.1	4068.0	3743.2	3842.3	
	$m_{\tilde{q}_R^1}$	4183.9	3859.4	4731.4	4378.0	4683.5	
	$m_{\tilde{q}_R^2}$	3936.0	3699.4	4690.4	4352.2	4445.5	
	$m_{\tilde{b}_2}$	4137.3	3891.1	4637.2	4478.3	4510.4	
	$m_{\tilde{t}_2}$	3586.5	3334.7	4286.0	3936.8	4038.8	
	$m_{\tilde{e}_L}$	328.2	393.0	588.3	375.9	627.6	
	$m_{\tilde{e}_R}$	1442.2	1136.2	684.3	552.4	1497.9	
	$m_{\tilde{\mu}_L}$	328.2	393.0	588.1	375.9	627.7	
	$m_{\tilde{\mu}_R}$	315.0	318.7	298.4	289.1	328.5	[GeV]
	$m_{\tilde{\tau}_1}$	248.1	120.0	485.0	244.9	328.2	
	$m_{\tilde{\tau}_2}$	1445.0	1553.8	1052.4	1399.6	1720.5	
	$m_{\tilde{\chi}_1^0}$	235.5	113.0	294.8	237.6	319.7	
	$m_{\tilde{\chi}_2^0}$	310.4	483.2	758.4	-426.1	792.1	
	$m_{\tilde{\chi}_3^0}$	-2942.2	-2921.4	-3116.3	3226.7	-3273.1	
	$m_{\tilde{\chi}_4^0}$	2942.6	2921.6	3116.9	-3226.9	3273.5	
	$m_{\tilde{\chi}_1^\pm}$	310.6	483.4	758.5	426.3	792.2	
	$m_{\tilde{\chi}_2^\pm}$	2943.5	2922.6	3117.6	3227.8	3274.3	
	$m_{\tilde{\nu}_L^e}$	318.5	384.8	582.7	367.4	622.4	
	$m_{\tilde{\nu}_L^\mu}$	318.5	384.8	582.7	367.4	622.5	
	$m_{\tilde{\nu}_L^\tau}$	243.3	129.8	517.2	247.0	350.5	
	Q	3409.7	3163.2	4072.1	3742.4	3845.1	
	$\mu(Q)$	2932.7	2917.6	3105.9	3217.7	3271.1	
Constraints	$\mathrm{Br}(b\to s\gamma)$	3.32×10^{-4}	3.29×10^{-4}	3.30×10^{-4}	3.32×10^{-4}	3.28×10^{-4}	
	$\mathrm{Br}(B_s\to\mu^+\mu^-)$	3.07×10^{-9}	3.13×10^{-9}	3.14×10^{-9}	3.08×10^{-9}	3.32×10^{-9}	
	$\sigma^{\mathrm{DD\ SI}}$	9.69×10^{-13}	4.44×10^{-13}	6.65×10^{-13}	5.50×10^{-13}	6.31×10^{-13}	[pb]
	Ωh^2	1.20×10^{-1}	1.22×10^{-1}	1.20×10^{-1}	1.20×10^{-1}	1.19×10^{-1}	
	Δa_μ	2.71×10^{-9}	3.06×10^{-9}	2.23×10^{-9}	2.98×10^{-9}	2.36×10^{-9}	

Table 2.5: Input and Output parameters for the large μ benchmark points with the most accurate Δa_μ and Ωh^2 and all other experimental constraints fulfilled. $\tilde{q}^i$ labels the i-th generation of squarks.

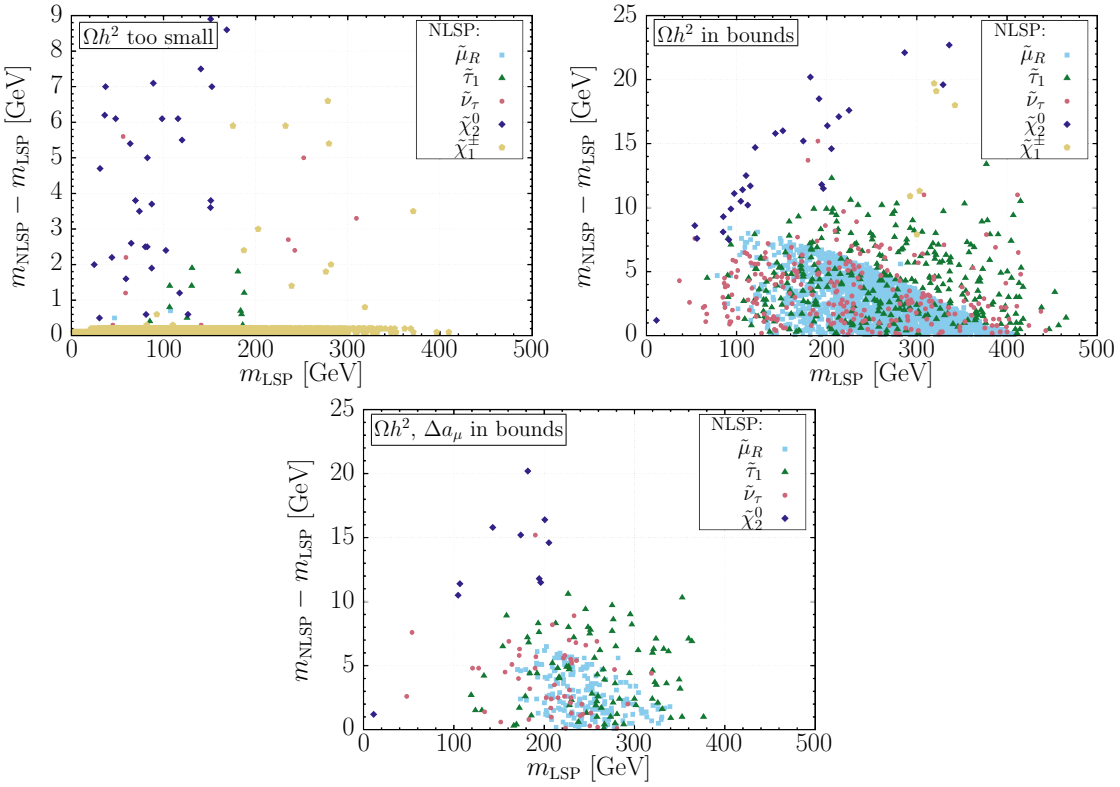

Figure 2.12: Mass differences between the LSP and NLSP compared to the LSP mass. In the top left panel, the relic density is too small, whereas it is in bounds in the top right panel. In the bottom panel, the relic density as well as Δa_μ are in bounds. For the entire figure, the LSP always is the lightest neutralino $\tilde{\chi}_1^0$.

2.6 Vacuum Stability

To ensure elecrtoweak symmetry breaking (EWSB) is caused by the Higgs vev's, `SoftSUSY` applies two-loop tadpole contributions in its minimisation conditions. These are then used to fix theory parameters such that the desired vacuum is a minimum of the scalar potential. While this approach in general is convenient, it usually does not take into account all possible solutions to the minimisation conditions and hence there might exist solutions lying lower in the scalar potential of the theory. Additonally, charge and colour-breaking (CCB) vev's, which might also lie lower than the desired vacuum, are typically ignored as well.

To exclude the possibility of providing benchmarks that suffer from CCB minima, minima lying lower than the desired vacuum or vacua that are not long-lived (meta-stable), we performed

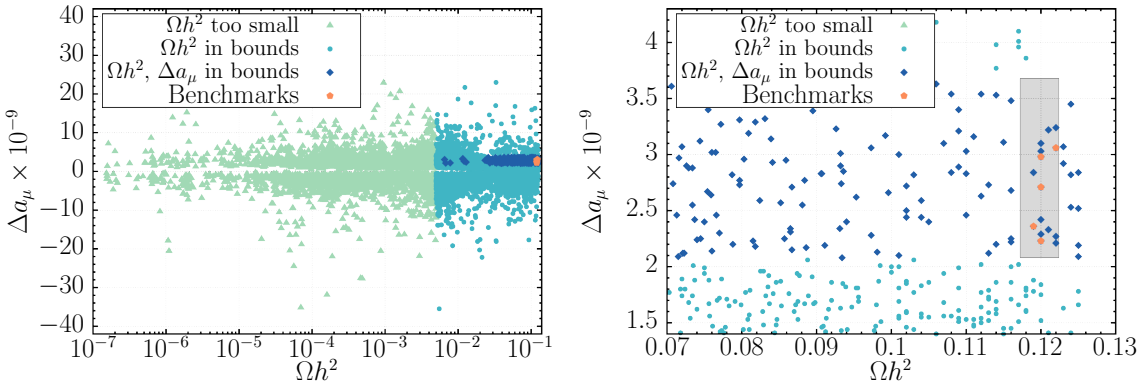

Figure 2.13: Δa_μ vs. Ωh^2. The top left panel holds the full parameter spectrum while the top right panel holds a smaller excerpt of it with the grey shaded area being the $1\,\sigma$ bound of Δa_μ and Ωh^2. All dark blue diamonds are bino-like, whereas the light green triangles and turquoise circles are wino-like. The orange pentagons represent the benchmark points defined in table 2.5.

a numerical analysis of the tree and one-loop effective potential for a set of handpicked possible benchmarks[5] using `Vevacious` [117]. Although approximate analytical conditions for the avoidance of CCB minima exist for the MSSM, a full numerical study of the one-loop effective potential is often needed as the conditions are neither sufficient nor necessary to ensure the absence of such minima [118]. Additionally, such analytical rules are based on a tree-level analysis and are thus irrelevant for points where the symmetry breaking occurs only at one-loop.

The numerical analysis showed that the points considered can be classified by mainly two different aspects. First, quite often the EWSB minimum appears only after two-loop contributions to the effective potential have been considered[6] and for such points, `Vevacious` is not able to investigate the vacuum stability due to its current restriction to one-loop effective potentials. Second, there are also several points where the EWSB minimum develops at tree or one-loop level and `Vevacious` can be used to investigate the stability of these points.

In the small μ scenario (see section 2.5.2), all studied points had the desired vacuum matching the global minimum of the one-loop effective potential. We then picked five of these points as benchmarks, shown in table 2.3. In the large μ scenario, the situation is not as clear as in the small μ case and different points yield different minima. An overview of the studied points and

[5] A point is considered a potential benchmark if it satisfies all constraints from section 2.4.

[6] This can be attributed to the fact that the desired vacuum arises as a solution of two-loop minimisation conditions.

their characteristic minimum is shown in figure 2.14. In the left panel, it strikes that points with

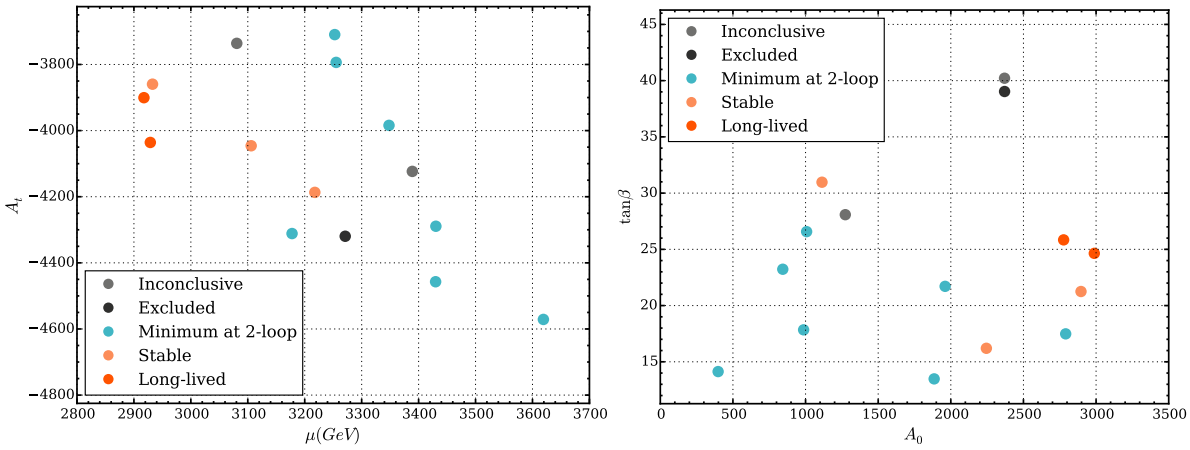

Figure 2.14: Vacuum stability analysis for a set of points in the large-μ region fulfilling all experimental constraints. Orange and red points correspond to the final benchmark points, for which the desired vacua are either stable or long-lived. Light blue points (labelled 'Minimum at two-loop') lead to the desired vacuum only when two-loop corrections are included and thus could not be studied with current tools. Black points show CCB minima deeper than the desired vacuum with the latter having a survival probability of < 1 %. Grey points (labelled *inconclusive*) show CCB minima at 1-loop, but the desired vacua appear only after two-loop corrections are included.

larger μ tend to develop the desired vacuum once two-loop corrections are taken into account. Additionally, points that have a stable or long-lived vacuum tend to larger values of $|A_t|$ (left panel) as well as larger A_0 and lower $\tan\beta$ (right panel). This is due the fact that larger $\tan\beta$ result in smaller $m^2_{\tilde{\tau}_R}$, thus increasing the probability for $\tilde{\tau}$ vev's. In return, lower values of $\tan\beta$ allow for higher A_0 and $|A_t|$, making this a combination that satisfies both all constraints from section 2.4 as well as vacuum stability. The points for which the desired vacuum is either the global or long-lived minimum (red and orange points in figure 2.14) correspond to the benchmark points shown in table 2.5.

2.7 Conclusions

The anomalous magnetic moment of the muon is still a prime target of study for new physics at a relatively low mass scale due to its large tension with the SM. One of the most promising theories to explain these new physics is the MSSM with light sleptons as well as light charginos

and neutralinos, which is able to fully account for the experimentally measured Δa_μ at one-loop level. A SUSY spectrum as light as the one required to explain Δa_μ contrasts the absence of coloured sparticle discoveries (squarks and gluinos) at the LHC and hence leads to strict bounds on such sparticles with their masses typically required to be at the TeV scale. Furthermore, the Higgs mass also requires at least some stop masses in the multi-TeV range within the scope of the MSSM.

Although spectra with light sleptons and gauginos together with strong constraints on coloured sparticles may naïvely look inconsistent, there actually are not many experimental limitations on such spectra. This is due to the LHC being significantly less sensitive to colour singlets than to coloured particles. Simultaneously, from the theory side, accomodating light sleptons together with heavy squarks for all generations at the weak scale is highly challenging within the cMSSM or mSUGRA models with universal sfermion masses at the GUT scale. This task gets even more difficult if several collider and non-collider constraints such as the DM relic density are taken into account as well.

Due to this tension, MSSM models with non-universal sfermion masses at the GUT scale are strongly favoured, as long as they do not introduce excessive flavour changing neutral currents or a plethora of new parameters (like the MSSM with its more than 100 parameters). While the pMSSM falls into this category, it still contains 19 SUSY parameters and is not particularly well theoretically motivated. In this chapter, we use a more constrained model than the pMSSM, but less constrained than the cMSSM. In particular, we consider a model with four scalar soft masses at the GUT scale, namely m_0 (a universal left-handed scalar mass) and m_i for $i = 1, 2, 3$ (a universal right-handed scalar mass for each family i) together with non-universal gaugino and trilinear soft masses. This enables us to have the first and second family sleptons light in order to successfully explain Δa_μ while at the same time having m_3 large enough to provide enough mass for the Higgs boson and to keep the agreement of further observables such as $\mathrm{Br}(b \to s\gamma)$ and $\mathrm{Br}(B_s \to \mu^+\mu^-)$ valid.

In a comprehensive scan over the soft parameter space of the model, we confirmed the existence of viable points in two distinguishable regions satisfying both Δa_μ as well as dark matter constraints , i.e. in regions of small μ and regions of large μ, which we subsequently investigated in

detail separately. For both regions, we were able to understand the dominant contributions leading to Δa_μ as well as the characteristics of the DM candidate, all while being in conformity with all other experimental constraints. Exemplarily, we pinned down the responsible SUSY particle for the effective co-annihilation by investigating the NLSP and also investigated the LSP-NLSP mass splitting, which is of high importance e.g. for collider experiments. For each solution scenario, we then proposed a set of benchmarks and checked their vacuum stability, which is especially important in the large μ scenario due to possible two-loop effects.

In case μ is small ($\mu \lesssim 400$ GeV), the LSP is a bino-like neutralino annihilating in the early universe either resonantly, if its mass is around half the Z or Higgs boson mass, or via co-annihilation with the higgsino states, if μ is approximately 15 GeV larger than the LSP mass. All benchmarks provided are chosen with a large mass gap of about 100 GeV between the LSP and the right-handed smuon. This allows for hard muons arising from smuon decays at the LHC, resulting in comparably clear signals. For all points with small μ, Δa_μ is dominated by diagrams (B) and (E) of figure 2.2. In case of large $\mu \lesssim 3$ TeV, the LSP again is a bino-like neutralino, co-annihilating in the early universe with NLSPs either $\tilde{\tau}_1$, $\tilde{\nu}_\tau$, $\tilde{\chi}_2$ or $\tilde{\mu}$ depending on the precise parameters. Δa_μ, in contrary, comes entirely and dominantly from diagram (A) of figure 2.2. Both scenarios contain heavy gluinos (above 2 TeV), which result in heavy squark masses satisfying current LHC bounds. Likewise, both scenarios contain light smuons (100 – 300 GeV), which can be accessible via leptonic signatures at the LHC. In addition, the small μ scenario comprises light and almost mass-degenerate charginos and next-to-lightest neutralinos, which exhibit di or tri-lepton signatures that can be accessible in the near future as well.

In conclusion, the MSSM with a Pati-Salam gauge group broken at the GUT scale and flavour symmetries A_4 and Z_5 unifying the soft masses of the left-handed (but not right-handed) squarks and sleptons, provides a well motivated framework with a relatively low number of input soft masses. The model is capable of accounting for Δa_μ and provides a well suited bino-like neutralino as dark matter candidate, all while being consistent with all other experimental and theoretical constraints. It is also very worth stressing that the A to Z of Pati-Salam model was not designed to explain Δa_μ (unlike some other models), but focussed on flavour mass and mixing of quarks and leptons, but especially neutrinos. Nonetheless, the model is very well capable of explaining

the experimentally observed Δa_μ and provides characteristic SUSY spectra different enough to be distinguished from other less well motivated models such as the pMSSM.

3 | LHC Implications of MSSM $(g-2)_\mu$ and DM from $SU(5) \otimes A_4$

3.1 Introduction

While the Pati-Salam model studied in chapter 2 offers viable solutions for Δa_μ and DM, its LHC signatures are currently not being probed. This is not a problem in general, however there exist other variations of the MSSM explaining Δa_μ and DM that may lead to signatures the LHC is more sensitive to, as will be discussed below. In particular, such models could comprise light gauginos and light sleptons (especially smuons, if Δa_μ shall be explained), however with a sufficiently large mass gap between the LSP and the next heavier particles in order to avoid soft particles arising from NLSP decays. It is possible to account for these features in models with non-universal gaugino masses, e.g. in GUT scale models (such as $SU(5)$ and $SO(10)$), where the non-universality can be achieved by non-singlet F-terms or a linear combination of such terms [119–126]. In the most general situation of having all gaugino masses as independent parameters, a recent work showed that it is possible to explain both Δa_μ as well as DM successfully within an $SU(5)$ framework [127]. Apart from the independent gaugino masses, two soft masses m_F and m_T accommodating the $\overline{\mathbf{5}}$ and $\mathbf{10}$ representations respectively, were considered therein, while the soft Higgs masses were set equal to m_F.

In this chapter, we also consider an $SU(5)$ model, but with an additional A_4 family symmetry. This results in the three $\overline{\mathbf{5}}$ representations to form a single triplet of A_4 with mass m_F, whereas the three $\mathbf{10}$ representations are singlets of A_4 with soft masses m_{T1}, m_{T2} and m_{T3} instead of

one universal mass m_T. We will show that even with such family-non-universality, Δa_μ cannot be explained with universal gaugino masses. Fully non-universal gaugino masses $(M_1, M_2) \ll M_3$, on the other hand, may lead to viable Δa_μ with $\mu \simeq -300$ GeV, while further providing a stable, bino-dominated neutralino as DM candidate and fulfilling all other experimental constraints. We will also provide a set of benchmarks this region of parameter space and explore their LHC phenomenology, which is more exciting compared to Chapter 2 due to the respectively lighter mass spectra comprising a right-handed smuon around 100 GeV and all other neutralinos and charginos below about 300 GeV. All other masses lie in the multi-TeV range.

The layout of the remainder of this chapter is as follows: In section 3.2, we present the $SU(5) \otimes A_4$ model and its symmetry breaking to the MSSM. In section 3.3, the MSSM one-loop contributions to Δa_μ are briefly summarised and we give first predictions for viable regions of parameter space of the model. Any experimental limits we consider from both collider and cosmological side are listed and explained in section 3.4. Scans of the model parameter space for universal, partially non-universal and fully non-universal gaugino masses are shown in section 3.5. Lastly, we draw our conclusions in section 3.6.

3.2 The Model

The model under study is an $SU(5)$ with A_4 family symmetry. The former is a rank 4 group and comprises 24 gauge bosons, which transform in the **24** adjoint representation. Left-handed quark and lepton families are neatly accommodated into the $\overline{\mathbf{5}}$ and **10** representations (which we label as F and T respectively) and read

$$F = \begin{pmatrix} d_r^c \\ d_b^c \\ d_g^c \\ e^- \\ -\nu_e \end{pmatrix}_L , \qquad T = \begin{pmatrix} 0 & u_g^c & -u_b^c & u_r & d_r \\ . & 0 & u_r^c & u_b & d_b \\ . & . & 0 & u_g & d_g \\ . & . & . & 0 & e^c \\ . & . & . & . & 0 \end{pmatrix}_L \tag{3.1}$$

with r, b, g being the quark colours, c denoting CP conjugation and T being antisymmetric as expressed by the dots in the lower triagonal part.

The $SU(5)$ gauge group may be broken to the SM by a Higgs multiplet in the **24** representation,

$$SU(5) \to SU(3)_C \otimes SU(2)_L \otimes U(1)_Y \,. \tag{3.2}$$

The $\overline{\mathbf{5}}$ and **10** representations then transform as

$$\overline{\mathbf{5}} \to d^c(\overline{\mathbf{3}}, \mathbf{1}, 1/3) \oplus L(\mathbf{1}, \overline{\mathbf{2}}, -1/2) \,, \tag{3.3}$$

$$\mathbf{10} \to u^c(\overline{\mathbf{3}}, \mathbf{1}, -2/3) \oplus Q(\mathbf{3}, \mathbf{2}, 1/6) \oplus e^c(\mathbf{1}, \mathbf{1}, 1) \,, \tag{3.4}$$

and (Q, u^c, d^c, L, e^c) corresponds to a complete quark and lepton SM family.

Furthermore, the electroweak symmetry can be broken by Higgs doublets H_u and H_d (as appearing in two Higgs doublet models), which may arise from the $SU(5)$ multiplets $H_{\mathbf{5}}$ and $H_{\overline{\mathbf{5}}}$, if their colour triplet components can be made heavy. This is known as the doublet-triplet splitting problem.

Once the A_4 is combined with the $SU(5)$, it is common to unify the three families $\bar{\mathbf{5}} \equiv F \equiv (d^c, L)$ into a triplet of A_4 with mass m_F. The three **10** representations $T_i \equiv (Q, u^c, e^c)_i$, on the other hand, are singlets of A_4 and have independent soft masses m_{T1}, m_{T2}, m_{T3} [128–132]. The Higgs doublet masses m_{H_u} and m_{H_d} are unconstrained, however we will assume for simplicity $m_F = m_{H_u} = m_{H_d}$.

Finally, we have the following soft scalar masses in the $SU(5) \otimes A_4$ model:

$$\begin{aligned}
m_F &= m_{\tilde{D}_i^c} = m_{\tilde{L}_i} = m_{H_u} = m_{H_d} \,, \\
m_{T1} &= m_{\tilde{Q}_1} = m_{\tilde{U_1}^c} = m_{\tilde{E_1}^c} \,, \\
m_{T2} &= m_{\tilde{Q}_2} = m_{\tilde{U_2}^c} = m_{\tilde{E_2}^c} \,, \\
m_{T3} &= m_{\tilde{Q}_3} = m_{\tilde{U_3}^c} = m_{\tilde{E_3}^c} \,,
\end{aligned} \tag{3.5}$$

where it is worth mentioning that e.g. the stop masses are completely contained in m_{T3} and the right-handed smuon mass comes from m_{T2}.

3.3 MSSM One-loop Contributions to Δa_μ

Since the $SU(5) \otimes A_4$ breaks down to the MSSM, the one-loop contributions to Δa_μ are the same as already explained in section 2.3.2 and no new contributions arise. For convenience and comparability, we will therefore take over the same short notation as introduced in section 2.3.2, i.e. referring to equations (2.13a) to (2.13e) as diagrams (A) to (E).

Even though the Pati-Salam model from chapter 2 and the $SU(5) \otimes A_4$ model both break down to the MSSM, they feature completely different GUT scale boundary conditions and hence may lead to entirely different phenomenological implications. In the following, we qualitatively estimate the relevant contributions to Δa_μ coming from the $SU(5) \otimes A_4$ with its different GUT scale boundary conditions and motivate the different sign choices of the higgsino mass parameter μ.

One of the most important parameters in any MSSM scenario to provide viable Δa_μ is μ, or rather $\operatorname{sgn}\mu$. Positive μ results in positive contributions from diagrams (A), (C) and (E), whereas negative μ results in diagrams (B) and (E) positively contributing to Δa_μ. The particular case of negative μ thereby is especially hard to accommodate in models such as the cMSSM and it has been shown that the cMSSM cannot account for Δa_μ and further experimental limits simultaneously, regardless of $\operatorname{sgn}\mu$ (see e.g. [36, 37, 83]). If the cMSSM is extended or its constraints relaxed, the above statement is not true any longer and new solutions without the need for fine tuning arise — all while being in conformity with all other low energy observations [29, 36, 37, 74–103].

In this chapter, we have found regions in the model parameter space that lead to viable Δa_μ with a particularly light mass spectrum for negative μ, whereas solutions with large positive $\mu \simeq 2$–5 TeV are possible in general, but with a slightly heavier mass spectrum (see e.g. Ref. [102]). With negative μ, at least one of the smuons (either left or right-handed) is required to be light to provide the desired Δa_μ from diagrams (B) and (D) while keeping the gaugino mass parameters positive and small as well. Contributions from diagrams (A), (C) and (E) yield negative contributions to Δa_μ, so they need to be small or suppressed in another way to provide the correct Δa_μ. The suppression of diagram (A) and (C) can be achieved by having a heavy $\tilde{\mu}_L$, however at the cost of also suppressing diagram (D). This is fine as long as the right-handed smuon can be made

light, which is possible within the scope of our model thanks to $m_{\tilde{\mu}_L}$ and $m_{\tilde{\mu}_R}$ being controlled by two different GUT scale parameters, m_F and m_{T2} respectively. Choosing a heavy $m_{\tilde{\mu}_L}$ based on a heavy m_F effectively suppresses diagram (E) as well, as the muon sneutrino mass appearing therein (see equation (2.13e)) is also controlled by m_F and will acquire a mass similar to $m_{\tilde{\mu}_L}$.

Overall, to fully account for Δa_μ we therefore desire negative μ, light $m_{\tilde{\mu}_R}$, light gaugino mass parameters $M_{1/2}$ (or M_1 and M_2 in case of non-universality) and heavy $m_{\tilde{\mu}_L}$. Finally, before actually scanning the parameter space for such solutions in section 3.5, we briefly summarise the experimental constraints considered for this chapter in section 3.4 below.

3.4 Experimental Constraints

In analogy to the Pati-Salam model studied in chapter 2, the $SU(5) \otimes A_4$ model also needs to explain any low-energy observations coming from various experiments. These include all observations listed in section 2.4, but with updated DM DD limits coming from the Xenon1T experiment. In particular, the Xenon1T data provides the current best limit on DM direct detection with $\sigma_{\text{DD-SI}} \leq 7.64 \times 10^{-47}$ cm^2 $= 7.64 \times 10^{-11}$ pb [133] for spin-independent models and a WIMP-mass of 36 GeV. WIMP masses smaller or larger than 36 GeV lead to weaker limits, hence making this choice conservative.

For convenience, all considered experimental limits are summarised once more below in table 3.1, while a more detailed explanation can be read again in section 2.4. Regarding the relic density,

Constraint	Ref. Value	Ref.	Allowed Bound
DM relic density	$\Omega h^2 = 0.1198 \pm 0.0026$	[104]	$\Omega h^2 \lesssim 0.1224$
DM DD cross section	$\sigma_{\text{DD-SI}} \leq 7.64 \times 10^{-47}$ cm^2 $= 7.64 \times 10^{-11}$ pb	[133]	same
Higgs Mass	$m_h = (125.09 \pm 0.21\,(\text{stat.}) \pm 0.11\,(\text{sys.}))$ GeV	[106]	$m_h = 125.09 \pm 1.5$ GeV
BR($b \to s\gamma$)	$(3.29 \pm 0.19 \pm 0.48) \times 10^{-4}$	[107]	same
Br($B_S \to \mu^+\mu^-$)	$3.0^{+1.0}_{-0.9} \times 10^{-9}$	[108]	same

Table 3.1: Summary of the experimental constraints considered for the $SU(5) \otimes A_4$ model. For a more comprehensive description of these limits, see section 2.4.

we allow the possibility of our model not fully accounting for it, thus choosing $\Omega h^2 \lesssim 0.1224$. The Higgs boson again is plagued by theoretical errors in the radiative corrections to its mass inherent in the existing state of the art SUSY spectrum generators and we therefore allow Higgs masses of

$m_h = 125.09 \pm 1.5$ GeV

Lastly, we also take into account several 8 and 13 TeV ATLAS and CMS searches at the LHC, which will be discussed in detail in the following section 3.5 below.

3.5 Results

Based on the previous thoughts in section 3.3 on enhancing Δa_μ with the available GUT scale parameters, we desire the following parameter choices:

- m_F large for large $m_{\tilde{\mu}_L}$ and $m_{\tilde{\nu}^\mu_L}$,
- m_{T2} small for light $m_{\tilde{\mu}_R}$,
- m_{T1} and m_{T3} large for large squark masses,
- M_1 small for light $\tilde{\chi}^0_1$,
- $\tan\beta$ large (affects all diagrams).

All other parameters are in principle unconstrained, but in practice will be constrained by the experimental constraints from section 3.4 and from further LHC searches.

The data for this work was acquired as follows: First, a GUT scale input point was chosen either randomly or on a fixed grid (with variable grid spacing) and its corresponding mass spectrum and decay table were computed using `SPheno_v4.0.3` [134, 135]. In the next step, we used `micrOMEGAs_v3.6.9.2` [116] to compute Δa_μ and all low-energy constraints listed in section 3.4. Other than in chapter 2, we did not discard points not fulfilling certain constraints, but kept all data in order to also acquire some information on possibly excluded parts of the parameter space.

In the following two subsections, we present scans where the above considerations have been taken into account. In particular, subsection 3.5.1 refers to the case of universal gaugino masses (commonly labelled as $M_{1/2}$) and subsection 3.5.2 refers to the case of partially non-universal gaugino masses, i.e. $M_{1,2}$ and M_3. The last case of fully non-universal gaugino masses M_1, M_2 and M_3 is addressed in subsection 3.5.3.

3.5.1 Universal Gaugino Masses

In case of universal gaugino masses, we scanned over

$$m_{T3} \in [200, 7000] \text{ GeV},$$
$$M_{1/2} \in [200, 7000] \text{ GeV}$$

with all other parameters fixed to values as shown in table 3.2 below. All scanned points in the

Parameter	m_F	m_{T1}	m_{T2}	m_{T3}	$M_{1/2}$	A_{tri}	$m_{H_{1,2}}$	$\tan\beta$	$\text{sgn}\,\mu$
Value	6000	7000	300	free	free	-6000	6000	30	-1

Table 3.2: Input parameters at the GUT scale in GeV (apart for $\tan\beta$ and $\text{sgn}\,\mu$) for universal gaugino masses $M_{1/2}$.

m_{T3}-$M_{1/2}$ plane are shown in figure 3.1, where the colour coding indicates the value of Δa_μ.

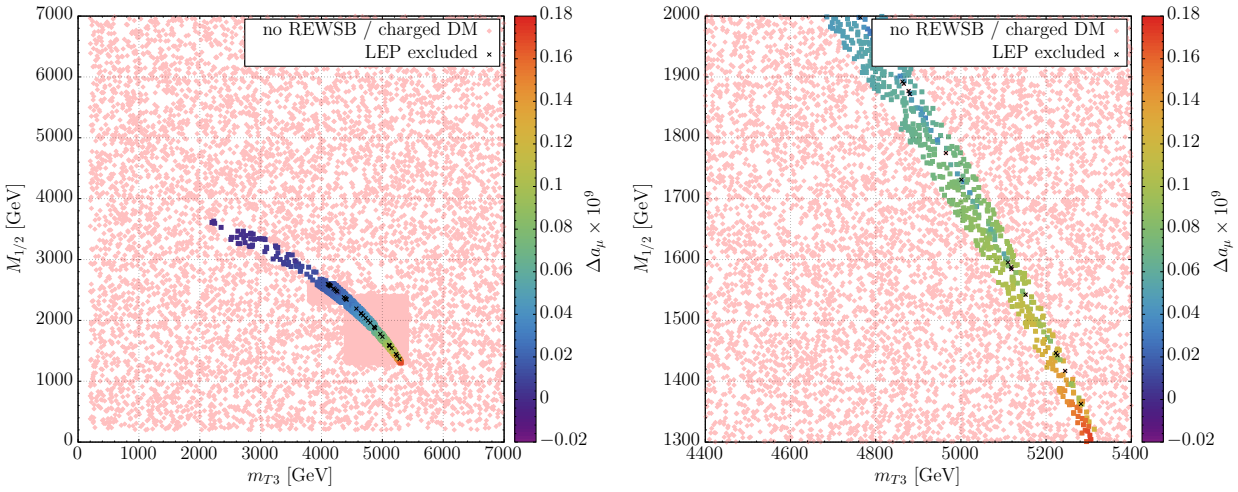

Figure 3.1: m_{T3}-$M_{1/2}$ plane with colour-coded Δa_μ with universal gaugino masses. The right panel is an excerpt of the full scan shown in the left panel.

As it turns out, the vast majority of the m_{T3}-$M_{1/2}$ plane leads to either no radiative EWSB or charged DM, leaving only a narrow stripe of physical solutions at the low scale. This stripe is characterised by increasing Δa_μ and a narrower cone of solutions when followed to larger m_{T3} and smaller $M_{1/2}$. Around $(m_{T3}, M_3) = (5.3, 1.3)$ TeV, the points leading to non-zero Δa_μ vanish and

the region of no radiative EWSB is entered. When having a closer look at Δa_μ, we observe that it ranges from 0 to a maximum of $1.8 \cdot 10^{-10}$ in the bottom right peak, which is about 10–20 times smaller than experimentally observed. This behaviour is actually expected and can be explained by the structure of the Δa_μ one-loop contributions from equation (2.13) and the assumptions made earlier in section 3.3. With negative μ, diagrams (B) and (D) yield the only positively contributing terms to Δa_μ and differ only in the exchange of M_1 and M_2 as well as $m_{\tilde{\mu}_R}$ and $m_{\tilde{\mu}_L}$ (the difference of the fine structure constants α_1 and α_2 is negligible for the following argument). The loop functions (2.14), defined only between 0 and 1, are also rather a factor of suppression than an enhancement to Δa_μ and will be irrelevant for the following argument. For a moment, we therefore make the conservative assumption of all loop functions equalling 1 — independent of their arguments x and y. In this particular case, we see that Δa_μ is governed by the prefactors of equations (2.13b) and (2.13d), which are proportional to M_1^{-1} and M_2^{-1} respectively. Now with universal gaugino masses at the GUT scale, the low scale M_1 and M_2 will not be much different, therefore allowing us to focus on just one diagram, e.g. diagram (B). Suitable Δa_μ now can only be achieved if M_1 is small and of order 200 GeV. This, however, is in strong tension with current ATLAS [136] and CMS [137] gluino searches at the LHC, excluding gluino masses below about 1.6 TeV and thus requiring a large gluino mass parameter M_3. With $M_1 \sim \mathcal{O}(200)$ GeV at the GUT scale, however, M_3 at the low scale will be larger, but not large enough to escape the gluino mass limits, hence leading to a contradiction and eventually to the statement that universal gaugino masses (in case of negative μ) cannot lead to viable Δa_μ. A supporting, but secondary argument lies in the observation of too light $M_{1/2}$ preventing radiative electroweak symmetry breaking from occuring, as can be seen in figure 3.1.

While the discussion above already is enough to rule out universal gaugino masses when requiring Δa_μ and collider and non-collider constraints to be fulfilled, it is nevertheless worth to have a look at the DM aspects (i.e. the relic density Ωh^2 and the DM DD limits) and the μ dependence of Δa_μ. This is shown in the following figure 3.2.

The relic density, shown in the left panel of figure 3.2, is well situated compared to the experimental limit and exceeds it only for very small Δa_μ close to zero. With increasing Δa_μ, the relic density slightly converges to some value between its minimum and maximum reach, which

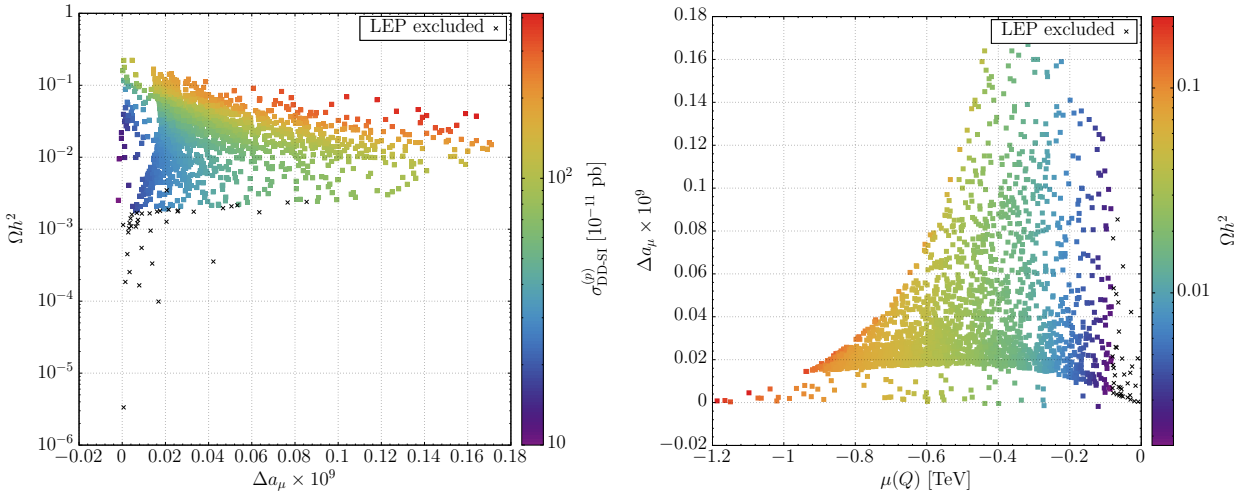

Figure 3.2: Left: Relic density vs. Δa_μ with colour-coded $\sigma_{\text{DD-SI}}$ with universal gaugino masses. Right: Δa_μ vs. μ with colour-coded relic density Ωh^2 with universal gaugino masses.

is spread out by at most two orders of magnitude. While this shows that the relic density is not an issue and can be easily accounted for with universal gaugino masses, the picture changes drastically when including the DM DD limits (see colour-coding in figure 3.2). For any point in parameter space and any relic density, $\sigma_{\text{DD-SI}} \geq 10^{-10}$ pb and thus fully excluded by the Xenon1T data. This is no surprise, as dark matter in this setup is dominantly higgsino-like (due to $\mu \ll M_{1/2}$) and couples significantly to the Higgs boson, further resulting in large DM DD cross sections. The latter is true, since DM can interact with nuclei only via squark or Higgs exchange in case of spin-independent direct detection. While the squark contributions to $\sigma_{\text{DD-SI}}$ are small due to the large squark masses, the Higgs contributions are much larger due to the comparably much lighter Higgs mass. Therefore, the stronger the DM coupling to the Higgs, the larger $\sigma_{\text{DD-SI}}$ becomes.

In the right panel of figure 3.2, the change of Δa_μ as a function of μ is shown. As anticipated, smaller values of $|\mu|$ lead to an enhancement of Δa_μ, while the relic density decreases simultaneously due to DM in form of the lightest neutralino $\tilde{\chi}_1^0$ becoming more higgsino-like.

In summary, we did not find a region in the model parameter space explaining both Δa_μ as well as all other experimental constraints with universal gaugino masses $M_{1/2}$. On the other hand, relaxing this unification by allowing for partially non-universal gaugino masses $M_1 = M_2 \equiv M_{1,2}$

and M_3 may lead to viable results, as then the gluino can be made heavy enough to escape LHC bounds while keeping $M_{1,2}$ sufficiently light to provide the desired Δa_μ. This setup is studied in detail in the following section 3.5.2.

3.5.2 Partially Non-Universal Gaugino Masses

With partially non-universal gaugino masses, we can fix $M_{1,2}$ to some value light enough to enhance Δa_μ while keeping M_3 heavy to escape gluino mass bounds. In particular, we scanned over the m_{T3}-M_3 plane with

$$m_{T3} \in [500, 7000] \text{ GeV}\,,$$
$$M_3 \in [500, 7000] \text{ GeV}$$

and all other parameters fixed as shown in table 3.3 below. To be able to compare the two cases

Parameter	m_F	m_{T1}	m_{T2}	m_{T3}	$M_{1,2}$	M_3	A_{tri}	$m_{H_{1,2}}$	$\tan\beta$	$\text{sgn}\,\mu$
Value	6000	7000	300	free	250	free	-5000	6000	30	-1

Table 3.3: Input parameters at the GUT scale in GeV for non-universal gaugino masses $M_{1,2}$ and M_3.

of universal and partially non-universal gaugino masses more easily, we first present the m_{T3}-M_3 plane (analogue to figure 3.1) in figure 3.3 in case of split gaugino masses.

While the overall shape of solutions for non-zero Δa_μ in parameter space looks similar, there are far more solutions yielding small Δa_μ in the band around and especially below the elliptic stripe (purple area). The characteristic stripe itself now ends at $(m_{T3}, M_3) \simeq (4.5, 2.48)$ TeV with $\Delta a_\mu \sim 3 \cdot 10^{-9}$ at its peak, hence perfectly matching the experimental observation. This can be seen in detail in the right panel of figure 3.3, which shows a zoomed excerpt of the left panel. In this excerpt, we also note that the stripe with large Δa_μ extends slightly into the 'unphysical' region without radiative EWSB or where DM is charged. These points however are excluded by LEP searches due to too light charginos or smuons [138]. A second set of solutions now shown in figure 3.3 arises for $M_3 \gtrsim 3$ TeV and $m_{T3} \gtrsim 6.5$ TeV, however with vanishingly small Δa_μ.

Comparing these results to figure 3.1 with universal gaugino masses, we see that splitting the

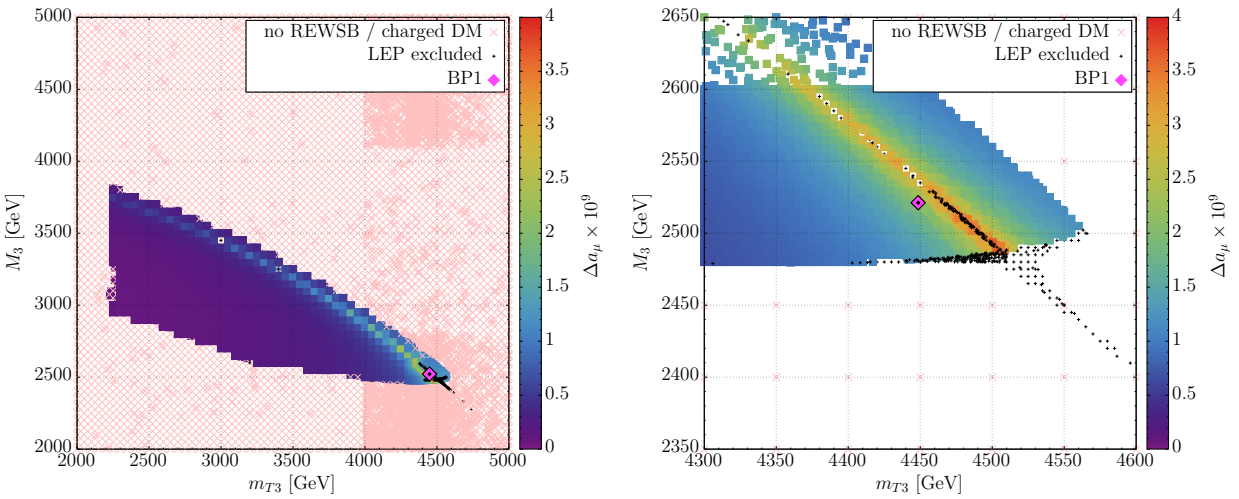

Figure 3.3: m_{T3}-M_3 plane with colour-coded Δa_μ with non-universal gaugino masses. The panel at the right is an excerpt of the full scan shown in the left panel.

gaugino masses indeed allows us to achieve the desired Δa_μ. However, we still have to check the other experimental constraints such as the relic density and DM DD limits. In figure 3.4, we therefore show the relic density-Δa_μ plane with colour-coded DM direct detection cross sections, analogue to figure 3.2, left.

Unlike with universal gaugino masses, where due to the smallness of μ DM was mainly higgsino-like, it predominantly consists of the bino component now. The relic density also is distributed similar, while at the same time being about one order of magnitude larger. The direct detection cross sections on the other hand have been reduced significantly, but they decrease with increasing Δa_μ, which in general is in tension with what would be desirable. To further investigate $\sigma_{\text{DD-SI}}$, we show a zoomed excerpt of the rectangle in the left panel of figure 3.4 in its right panel. Also note that the logarithmic scaling of $\sigma_{\text{DD-SI}}$ was removed and values with $\sigma_{\text{DD-SI}} > 10 \cdot 10^{-11}$ pb are also shown in red to enhance comparability with the experimental reference bound (reading $\sigma^{\text{exp}}_{\text{DD-SI}} = 7.64 \cdot 10^{-11}$ pb). It turns out that most points in the $1\,\sigma$ reference bounds of Δa_μ and Ωh^2 are excluded by the DM DD limits and only a small fraction of points with Δa_μ at the bottom of the $1\,\sigma$ bound survives.

While the tension between Δa_μ and $\sigma_{\text{DD-SI}}$ already becomes clear from figure 3.4, it is worth showing $\sigma_{\text{DD-SI}}$ directly as a function of Δa_μ, which corresponds to replotting figure 3.4 with

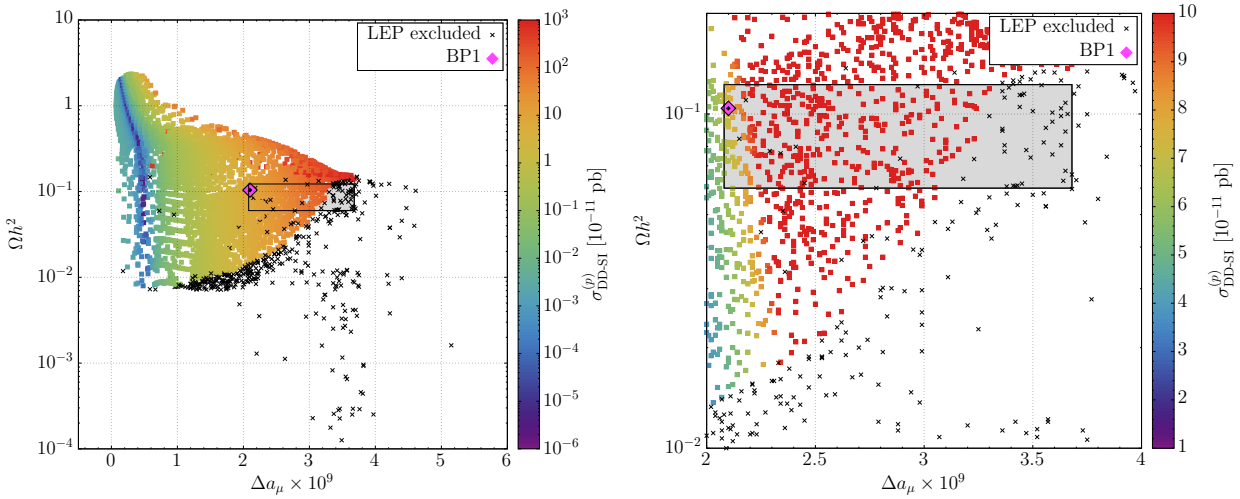

Figure 3.4: Relic density vs. Δa_μ with colour-coded $\sigma_{\text{DD-SI}}$ with non-universal gaugino masses. The grey shaded rectangle shows the (extended) 1σ bound for Δa_μ (Ωh^2). The panel at the right is an excerpt of the full scan shown in the left panel.

switched relic density and $\sigma_{\text{DD-SI}}$. This is shown in figure 3.5 below and it becomes clear again, that larger values of Δa_μ lead to massively increasing $\sigma_{\text{DD-SI}}$. The main reason for this is that with increasing Δa_μ, μ acquires smaller and smaller negative values (approaching zero, see figure 3.6 below) and hence DM is not dominantly bino-like any longer, but contains a significant higgsino component again. This in turn leads to a larger relic density and also a larger DM DD cross section due to larger couplings of DM to the Higgs boson and subsequently an increased probability of DM recoiling of a nucleus via Higgs boson exchange.

The aforementioned dependence of Δa_μ on μ is shown in figure 3.6 below, where it turns out that viable Δa_μ requires $\mu \in [-300, -100]$ GeV. Having μ even closer to zero will result on the one hand in the just explained large higgsino component of DM — leading to an unwanted large relic density and DM DD cross section — and on the other hand will eventually lead to too light charginos already ruled out by LEP searches [138].

In figure 3.7, we show the $m_{\tilde{\mu}_R}$-$m_{\tilde{\chi}^0_1}$ plane with colour-coded relic density. As can be seen for the benchmark BP1 (introduced later in table 3.4 below), it sits well above the line where the right-handed smuon and LSP are mass-degenerate. This together with a non-vanishing higgsino component of DM results in the correct relic density, since in addition to contributions from the dominant $\tilde{\mu}_R$-$\tilde{\chi}^0_1$ co-annihilation (which just by itself would lead to too small Ωh^2), the relic

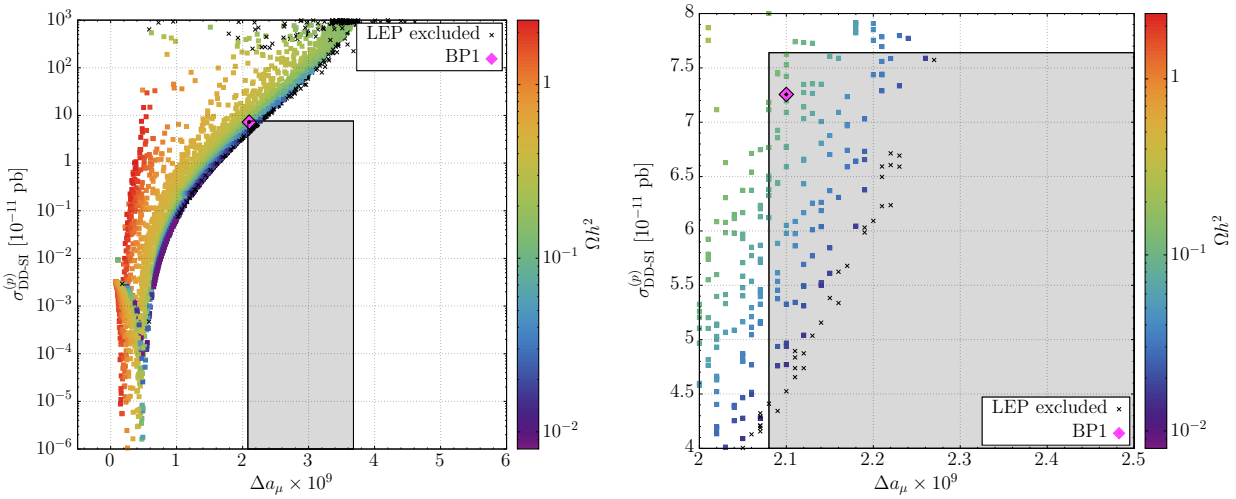

Figure 3.5: $\sigma_{\text{DD-SI}}$ vs. Δa_μ with colour-coded relic density Ωh^2 with non-universal gaugino masses. The grey shaded rectangle shows the 1σ bound for Δa_μ and the upper limit for $\sigma_{\text{DD-SI}}$. The panel at the right is an excerpt of the full scan shown in the left panel.

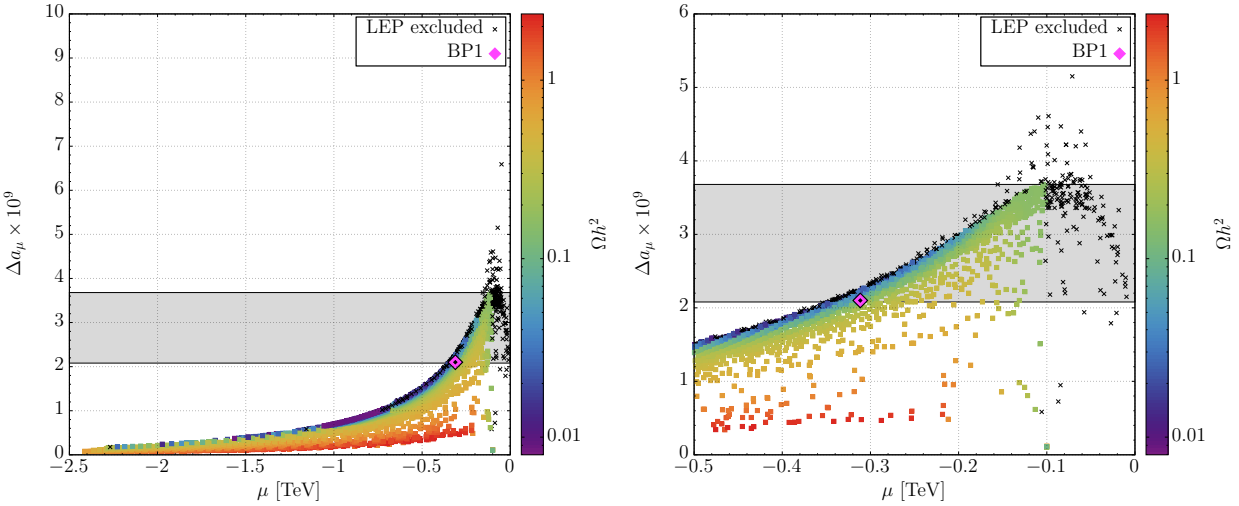

Figure 3.6: Δa_μ vs. μ with colour-coded relic density Ωh^2 with non-universal gaugino masses. The grey shaded rectangle shows the 1σ bound for Δa_μ. The panel at the right is an excerpt of the full scan shown in the left panel.

density also obtains contributions from $\tilde{\chi}_1^0$-$\tilde{\chi}_1^0$ annihilation.

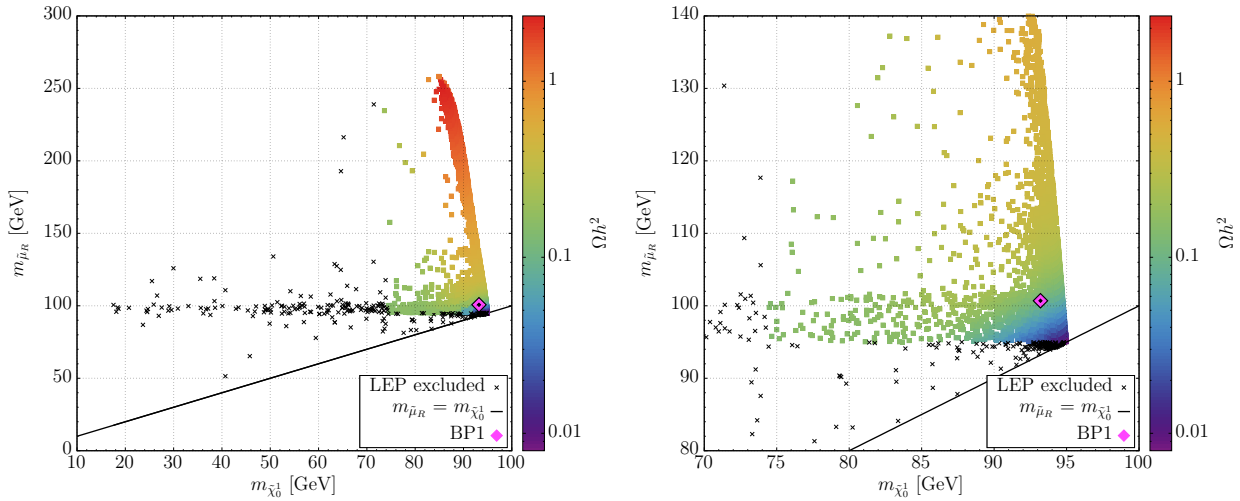

Figure 3.7: $m_{\tilde{\mu}_R}$ vs. $m_{\tilde{\chi}_1^0}$ with colour-coded relic density Ωh^2 with non-universal gaugino masses. The panel at the right is an excerpt of the full scan shown in the left panel.

Next, in figure 3.8, the Higgs mass m_h is shown as a function of Δa_μ with colour-coded relic density (left) and DM DD cross sections (right). Within this fixed set of GUT scale parameters as defined in table 3.3 and free m_{T3} and M_3, Δa_μ peaks for Higgs masses around 126.5 GeV. Smaller values of Δa_μ open up the Higgs mass window, however it should be noted that the behaviour depicted in figure 3.8 only represents one fixed set of GUT scale parameters. Different choices of these parameters will lead to very similar distributions, but shifted along the m_h-axis, thus allowing for further Higgs masses to be accessible at large Δa_μ.

To finish this discussion, we compare our findings with respect to Δa_μ in figure 3.9 in case of partially non-universal gaugino masses (orange squares) with those of universal gaugino masses (purple diamonds). The lower horizontal axis thereby shows M_3 at the low energy scale, whereas the top horizontal axis refers to the gluino mass $m_{\tilde{g}}$. It becomes obvious that universal gaugino masses do not lead to viable Δa_μ and would potentially violate exisiting gluino mass bounds, if Δa_μ were to somehow be increased any further. On the other hand, partially non-universal gaugino masses lead to a good amount of points in the $1\,\sigma$ reference bound of Δa_μ (grey band) and also exhibit a slightly squeezed Δa_μ spectrum with respect to M_3.

After the above discussion, we see that partially non-universal gaugino masses allow for points

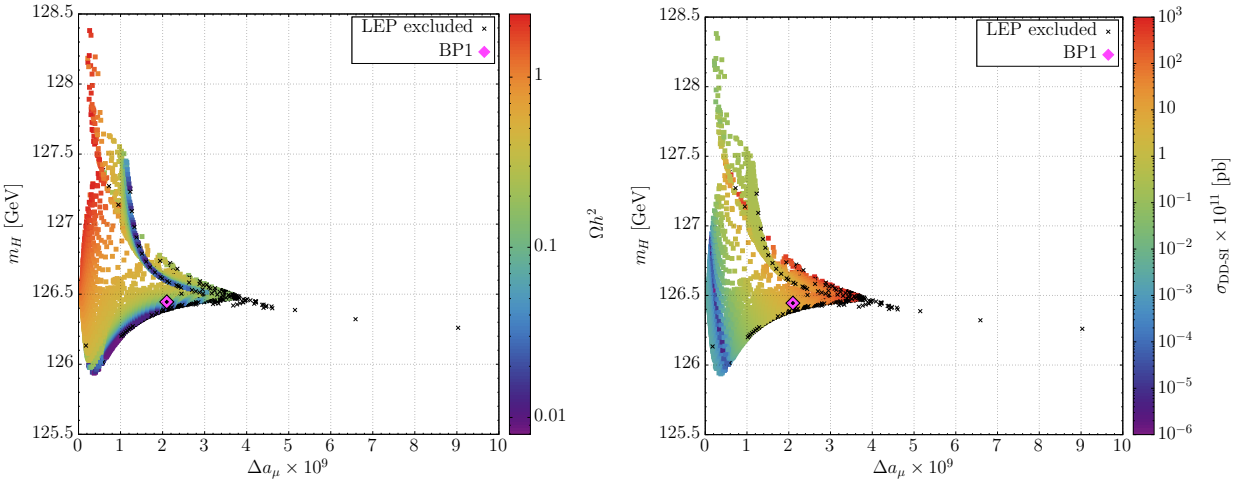

Figure 3.8: m_h vs. Δa_μ with colour-coded Ωh^2 (left) and $\sigma_{\text{DD-SI}}$ (right) with non-universal gaugino masses.

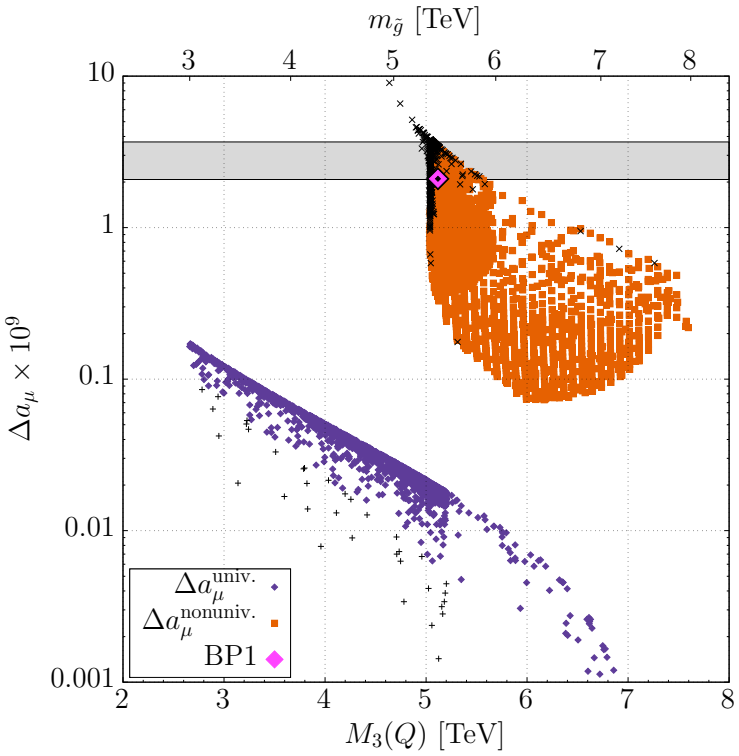

Figure 3.9: Influence of having universal (non-universal) gaugino masses $M_{1/2}$ ($M_{1,2}, M_3$) on Δa_μ. The purple (orange) points represent the universal (non-universal) case. The grey shaded rectangle shows the 1σ bound for Δa_μ. Note that, to allow for an easier comparison, the non-universal points were gathered with $A_{\text{tri}} = -6$ TeV instead of $A_{\text{tri}} = -5$ TeV as shown in figures 3.3 - 3.7.

fulfilling both Δa_μ as well as all other experimental constraints as listed in table 3.1. The next step therefore will be to check whether these points can be or already are probed at the LHC. To do so, we first chose a set of characteristic benchmark points for that region of parameter space, listed in detail in table 3.4 below. Therein, BP2 differs from BP1 mainly in having $\tan\beta = 28$ and $A_{\text{tri}} = 0$, whereas BP3 has a non-vanishing negative A_{tri} and split m_F and m_{T1}.

Further characteristics of the benchmark include a bino-dominated $\tilde{\chi}_1^0$ LSP being the DM candidate with mass below about 100 GeV, a right-handed smuon $\tilde{\mu}_R$ a few GeV heavier and wino-dominated $\tilde{\chi}_2^0$ and $\tilde{\chi}_1^\pm$ with mass gaps between them and the LSP of less than the Z or W boson masses. The heavier neutralinos and charginos $\tilde{\chi}_3^0$ and $\tilde{\chi}_2^\pm$ are higgsino-dominated and feature masses below 400 GeV, while the remaining SUSY particle masses lie in the multi-TeV range.

A SUSY spectrum with such a light electroweak sector usually predicts some characteristic signals at the LHC. In our case, this will be a di- or tri-lepton signal coming from chargino and second-lightest neutralino decays, i.e. from $\tilde{\chi}_1^\pm \tilde{\chi}_2^0$ and $\tilde{\chi}_1^+ \tilde{\chi}_1^-$-pair production. The neutralino decays as $\tilde{\chi}_2^0 \to \tilde{\mu}_R^\pm \mu^\mp$ with the smuon decaying $\tilde{\mu}_R \to \tilde{\chi}_1^0 \mu$. The chargino, on the other hand, will decay dominantly via virtual W bosons as $\tilde{\chi}_1^\pm \to f \bar{f} \tilde{\chi}_1^0$. Due to a non-zero mixing between the left and right-handed smuon, however, smuonic decays $\tilde{\chi}_1^\pm \to \tilde{\mu}_R^\pm \nu_\mu$ are almost as likely and therefore cannot be neglected. The signal strength strongly depends on the mass gap $\Delta m(\tilde{\mu}_R, \tilde{\chi}_1^0) \equiv \tilde{\mu}_R$-$\tilde{\chi}_1^0$ and can be comparably small, if $\Delta m(\tilde{\mu}_R, \tilde{\chi}_1^0)$ is small and thus the muons arising from smuon decays are soft. The $\tilde{\chi}_2^0$ decays are expected to yield a better signal strength, as they will dominantly decay to smuons and muons with a large mass gap $\Delta m(\tilde{\chi}_2^0, \tilde{\mu}_R) \equiv \tilde{\chi}_2^0 - \tilde{\mu}_R$ and thus at least one not-so-soft muon.

To study these considerations for our benchmarks at the LHC, we performed a `CheckMATE 2.0.11` [139] analysis including all implemented 8 and 13 TeV ATLAS and CMS analysises on chargino and neutralino searches with light smuons. First, `MadGraph 5.2.3.3` [109] linked to `CheckMATE` is used to generate 50000 events for SUSY final states consisting of $\tilde{\mu}_R^\pm$, $\tilde{\chi}_1^0$, $\tilde{\chi}_2^0$ as well as $\tilde{\chi}_1^\pm$. Next, `PYTHIA 8.2.30` [140] was used for parton showering and hadronisation of the events. The fast detector simulation was perfomed using `Delphes 3.3.3` [111] linked to `CheckMATE`. Finally (and making sure the same experimental cuts are applied to our simulation),

	Benchmark:	BP1	BP2	BP3	
Input at GUT scale	$\tan\beta$	30	28	28	
	$\mathrm{sgn}(\mu)$	-	-	-	
	m_F	6000.0	6000.0	6200.0	
	m_{T1}	7000.0	6000.0	5700.0	
	m_{T2}	300.0	300.0	290.0	
	m_{T3}	4448.6	5572.0	5518.0	
	$M_{1,2}$	250.0	250.0	250.0	[GeV]
	M_3	2521.2	2446.0	2790.0	
	M_{h_1}	6000.0	6000.0	6200.0	
	M_{h_2}	6000.0	6000.0	6200.0	
	A_{tri}	-5000.0	0	-500.0	
Masses	m_h	126.4	124.3	124.7	
	$m_{\tilde{g}}$	5457.7	5280.9	5963.4	
	$m_{\tilde{q}_L^1}$	8248.5	7312.5	7433.2	
	$m_{\tilde{u}_R}$	8250.1	7316.9	7439.2	
	$m_{\tilde{q}_L^2}$	4350.1	4173.2	4764.6	
	$m_{\tilde{c}_R}$	4377.1	4198.9	4788.7	
	$m_{\tilde{b}_1}$	4866.7	5884.2	6162.0	
	$m_{\tilde{t}_1}$	3944.4	5068.5	5340.8	
	$m_{\tilde{t}_2}$	4875.0	5887.4	6165.7	
	$m_{\tilde{d}_R}$	7423.9	7320.6	7832.1	
	$m_{\tilde{s}_R}$	7423.8	7320.5	7831.9	
	$m_{\tilde{b}_2}$	6934.5	6947.4	7453.3	
	$m_{\tilde{e}_L}$	5987.1	5988.4	6188.8	
	$m_{\tilde{e}_R}$	7001.2	5999.3	5699.4	
	$m_{\tilde{\mu}_L}$	5986.5	5988.0	6188.3	[GeV]
	$m_{\tilde{\mu}_R}$	100.7	95.6	95.4	
	$m_{\tilde{\tau}_1}$	3731.8	5175.0	5057.0	
	$m_{\tilde{\tau}_2}$	5737.5	5789.7	5989.0	
	$m_{\tilde{\chi}_1^0}$	93.2	91.1	89.2	
	$m_{\tilde{\chi}_2^0}$	169.4	163.6	158.7	
	$m_{\tilde{\chi}_3^0}$	-341.9	-336.2	-337.8	
	$m_{\tilde{\chi}_4^0}$	353.9	347.8	348.6	
	$m_{\tilde{\chi}_1^\pm}$	169.6	163.7	158.9	
	$m_{\tilde{\chi}_2^\pm}$	356.8	350.7	351.5	
	$m_{\tilde{\nu}_L^e}$	5986.1	5987.5	6187.8	
	$m_{\tilde{\nu}_L^\mu}$	5985.6	5987.0	6187.3	
	$m_{\tilde{\nu}_L^\tau}$	5736.8	5788.7	5988.1	
	Q	4287.9	5353.0	5609.8	
	μ	-311.5	-302.1	-299.5	
Constraints	$\mathrm{Br}(b\to s\gamma)$	3.40×10^{-4}	3.35×10^{-4}	3.34×10^{-4}	
	$\mathrm{Br}(B_s\to\mu^+\mu^-)$	3.03×10^{-9}	3.04×10^{-9}	3.04×10^{-9}	
	$\sigma^{\mathrm{DD\ SI}}$	7.23×10^{-11}	7.59×10^{-11}	6.89×10^{-11}	[pb]
	Ωh^2	1.04×10^{-1}	4.65×10^{-2}	7.55×10^{-2}	
	Δa_μ	2.10×10^{-9}	2.09×10^{-9}	2.09×10^{-9}	

Table 3.4: Input and output parameters for the benchmark points with partial gaugino non-universality $M_1 = M_2 \ll M_3$. These points have good Δa_μ as well as Ωh^2, but the wino dominated charginos $\tilde{\chi}_1^\pm$ and neutralinos $\tilde{\chi}_2^0$ are too light to avoid 8 TeV LHC searches as discussed below in the text. $\tilde{q}^i$ labels the i-th generation of squarks.

`CheckMATE` itself was used to analyse the prepared events and state whether the benchmark under study is ruled out by experimental searches or still allowed. The rate of exclusion or potential discovery thereby is given as the so called r-value, defined as [139]

$$r = \frac{S - 1.64 \cdot \Delta S}{S95},$$

where S is the number of predicted signal events with its uncertainty ΔS and $S95$ is the experimental 95 % upper limit on the number of signal events[1]. In case $r \geq 1$, the signal is excluded, whereas $r < 1$ indicates that the signal is not excluded or probed yet.

All three benchmarks are strongly excluded by the 8 TeV ATLAS search `ATLAS_1402_7029` [113], which is aimed at three leptons plus $\not{E}_T$. The reason why this 8 TeV analysis sets stronger bounds on our signal than the respective 13 TeV analysis is due to well designed asymmetric p_T cuts for the final state leptons, allowing for a sensitivity to a second or third lepton with p_T as low as 10 GeV. To the best of our knowledge, such low p_T leptons are currently out of reach for analogue 13 TeV searches.

A summary of this benchmark study including the r-values and further properties of the chargino and second-lightest neutralino is given below in table 3.5.

While it seemed that with partially non-universal gaugino masses, we would be able to find physical spectra obeying all experimental constraints, the predicted light electroweak sector of the model leads to a strong exclusion by corresponding LHC searches[2]. However, this is not necessarily the end of the story, as we still have the freedom to further split $M_{1,2}$ into M_1 and M_2 separately. The idea then is to slightly increase M_2 and hence get heavier winos ($\tilde{\chi}_2^0$, $\tilde{\chi}_1^\pm$) while keeping M_1 constant. This idea is studied in detail in the following section 3.5.3.

3.5.3 Fully Non-Universal Gaugino Masses

Based on the previous results, we found that viable Δa_μ and DM require a light neutralino $\tilde{\chi}_1^0$ of order 100 GeV together with a slightly heavier right-handed smuon. This scenario, however, stands in tension with universal GUT scale gaugino masses due to LHC gluino mass bounds

[1] Potential k-factors from next-to-leading-order (NLO) corrections have not been taken into account.

[2] In case of solutions with large, positive μ, the 8 TeV LHC is not sensitive to such points due to the heavier mass spectrum [102]

Quantity	Unit	Benchmark		
		BP1	BP2	BP3
r		7.38	9.16	9.30
$\sqrt{s}$	TeV	8	8	8
Analysis		ATLAS_1402_7029	ATLAS_1402_7029	ATLAS_1402_7029
Signal Region		SR0taua06	SR0taua02	SR0taua02
Ref.		[113]	[113]	[113]
σ_{LO}	pb	1.65	1.85	2.14
$\text{BR}(\tilde{\chi}_2^0 \to \tilde{\mu}_R^\pm \mu^\mp)$	%	99.4	99.4	99.7
$\text{BR}(\tilde{\chi}_2^0 \to \bar{q}\, q\, \tilde{\chi}_1^0)$	%	0.4	0.4	0.2
$\text{BR}(\tilde{\chi}_2^0 \to \ell^\pm \ell^\mp \tilde{\chi}_1^0)$	%	0.1	0.1	< 0.1
$\text{BR}(\tilde{\chi}_2^0 \to \bar{\nu}_\ell \nu_\ell \tilde{\chi}_1^0)$	%	< 0.1	< 0.1	< 0.1
$\text{BR}(\tilde{\chi}_1^\pm \to \bar{d}^{1,2} u^{1,2} \tilde{\chi}_1^0)$	%	45.4	40.2	47.9
$\text{BR}(\tilde{\chi}_1^\pm \to \tilde{\mu}_R^\pm \nu_\mu)$	%	31.9	39.8	34.7
$\text{BR}(\tilde{\chi}_1^\pm \to \ell^\pm \nu_\ell \tilde{\chi}_1^0)$	%	22.7	20.0	17.4
$\Delta m(\tilde{\chi}_1^\pm, \tilde{\mu}_R)$	GeV	68.9	67.9	63.5
$\Delta m(\tilde{\chi}_2^0, \tilde{\mu}_R)$	GeV	68.7	67.7	63.3
$\Delta m(\tilde{\mu}_R, \tilde{\chi}_1^0)$	GeV	7.5	6.6	6.2

Table 3.5: CheckMATE analysis results for the benchmarks of table 3.4 with partial gaugino non-universality $M_1 = M_2 \ll M_3$.

and also stands in tension with partially non-universal GUT scale gaugino masses due to lighter wino-dominated charginos and neutralinos than allowed by several 8 TeV di and tri-lepton LHC searches.

By further relaxing the gaugino non-universality to $M_1 < M_2 \ll M_3$, we will show that the chargino and second-lightest neutralino can be made heavy enough to satisfy current LHC constraints. As a side effect, M_2 now can be larger than $|\mu| \sim 300$ GeV, hence resulting in higgsino-dominated charginos and second-lightest neutralinos. Since this change of parameters has only minor effects on the physics as shown in figures 3.3 to 3.8, we will not show further scans, but limit ourselves to the more interesting LHC phenomenology by providing three new benchmarks with $M_1 < M_2 \ll M_3$. These benchmarks, listed as BP4, BP5 and BP6 in table 3.6, are very similar to the benchmarks BP1–BP3 from table 3.4, however differ in now having higgsino dominated $\tilde{\chi}_2^0$ and $\tilde{\chi}_1^\pm$ with masses governed by $|\mu| \sim 300$ GeV and wino dominated $\tilde{\chi}_3^0$ and $\tilde{\chi}_2^\pm$ with masses governed by M_2.

	Benchmark:	BP4	BP5	BP6	
Input at GUT scale	$\tan\beta$	30	28	30	
	$\mathrm{sgn}(\mu)$	-	-	-	
	m_F	5000.0	6200.0	5000.0	
	m_{T1}	5000.0	5700.0	5000.0	
	m_{T2}	200.0	280.0	200.0	
	m_{T3}	2995.0	5430.0	3005.0	
	M_1	250.0	250.0	250.0	[GeV]
	M_2	400.0	550.0	500.0	
	M_3	2600.0	2945.0	2595.0	
	M_{h_1}	5000.0	6200.0	5000.0	
	M_{h_2}	5000.0	6200.0	5000.0	
	A_{tri}	-4000.0	-500.0	-4000.0	
Masses	m_h	126.3	124.7	126.2	
	$m_{\tilde{g}}$	5531.7	6235.3	5516.5	
	$m_{\tilde{q}^1_L}$	6743.0	7589.2	6735.7	
	$m_{\tilde{u}_R}$	6743.7	7589.9	6734.1	
	$m_{\tilde{q}^2_L}$	4516.4	5003.3	4505.7	
	$m_{\tilde{c}_R}$	4529.2	5018.0	4514.9	
	$m_{\tilde{b}_1}$	4312.4	6262.8	4306.4	
	$m_{\tilde{t}_1}$	3601.6	5443.3	3588.2	
	$m_{\tilde{t}_2}$	4324.0	6266.7	4318.0	
	$m_{\tilde{d}_R}$	6748.0	7975.4	6738.4	
	$m_{\tilde{s}_R}$	6747.9	7975.3	6738.3	
	$m_{\tilde{b}_2}$	6348.2	7597.3	6337.5	
	$m_{\tilde{e}_L}$	4994.9	6196.1	4998.5	
	$m_{\tilde{e}_R}$	5002.1	5699.9	5002.1	
	$m_{\tilde{\mu}_L}$	4994.4	6195.6	4998.0	[GeV]
	$m_{\tilde{\mu}_R}$	98.9	96.8	99.4	
	$m_{\tilde{\tau}_1}$	2282.9	4968.1	2293.7	
	$m_{\tilde{\tau}_2}$	4802.1	5999.4	4805.3	
	$m_{\tilde{\chi}^0_1}$	91.7	89.0	92.0	
	$m_{\tilde{\chi}^0_2}$	266.9	303.3	302.2	
	$m_{\tilde{\chi}^0_3}$	-335.1	-327.8	-335.9	
	$m_{\tilde{\chi}^0_4}$	376.8	458.9	430.4	
	$m_{\tilde{\chi}^\pm_1}$	267.4	303.7	302.8	
	$m_{\tilde{\chi}^\pm_2}$	378.2	459.0	430.7	
	$m_{\tilde{\nu}^e_L}$	4993.8	6195.1	4997.4	
	$m_{\tilde{\nu}^\mu_L}$	4993.4	6194.6	4997.0	
	$m_{\tilde{\nu}^\tau_L}$	4800.9	5998.4	4804.1	
	Q	3866.1	5705.8	3856.5	
	μ	-313.0	-293.3	-314.3	
Constraints	$\mathrm{Br}(b\to s\gamma)$	3.43×10^{-4}	3.34×10^{-4}	3.43×10^{-4}	
	$\mathrm{Br}(B_s\to\mu^+\mu^-)$	3.01×10^{-9}	3.04×10^{-9}	3.01×10^{-9}	
	$\sigma^{\mathrm{DD\ SI}}$	6.72×10^{-11}	6.81×10^{-11}	6.52×10^{-11}	[pb]
	Ωh^2	9.67×10^{-2}	1.10×10^{-1}	1.03×10^{-1}	
	Δa_μ	2.17×10^{-9}	2.14×10^{-9}	2.16×10^{-9}	

Table 3.6: Input and output parameters for the benchmark points with full gaugino non-universality $M_1 < M_2 \ll M_3$. These points have good Δa_μ as well as Ωh^2 with all other constraints being fulfilled. In particular the higgsino dominated charginos $\tilde{\chi}^\pm_1$ and neutralinos $\tilde{\chi}^0_2$ are heavy enough to avoid current LHC searches, but remain a target for future searches, as discussed below in the text. $\tilde{q}^i$ labels the i-th generation of squarks.

Comparing the low scale mass spectrum to BP1 – BP3 from table 3.4, we note that the main difference lies in the now heavier $\tilde{\chi}_1^\pm$ and $\tilde{\chi}_2^0$ due to the larger M_2, as was anticipated. The respective $\tilde{\chi}_1^\pm$ and $\tilde{\chi}_2^0$ masses thereby cannot be increased much further, as they are governed by $|\mu| \sim 300$ GeV, which is necessary to account for Δa_μ. Therefore, both $\tilde{\chi}_1^\pm$ and $\tilde{\chi}_2^0$ remain in target range for the LHC.

To study the actual reach of the LHC regarding the benchmarks BP4 – BP6, we again performed a `CheckMATE` analysis exactly as described at the end of section 3.5.2 and a summary of this study is shown in table 3.7 below (analogue to table 3.5 for partially non-universal gaugino masses).

Quantity	Unit	Benchmark		
		BP4	BP5	BP6
r		0.88	0.12	0.13
$\sqrt{s}$	TeV	13	13	13
Analysis		ATLAS_CONF_2016_096	ATLAS_CONF_2016_096	ATLAS_CONF_2016_096
Signal Region		3LI	2LADF	3LI
Ref.		[141]	[141]	[141]
σ_{LO}	pb	0.54	0.24	0.26
$\text{BR}(\tilde{\chi}_2^0 \to h\,\tilde{\chi}_1^0)$	%	51.0	55.5	55.4
$\text{BR}(\tilde{\chi}_2^0 \to Z\,\tilde{\chi}_1^0)$	%	30.5	30.2	30.1
$\text{BR}(\tilde{\chi}_2^0 \to \tilde{\mu}_R^\pm\,\mu^\mp)$	%	18.5	14.3	14.5
$\text{BR}(\tilde{\chi}_1^\pm \to W^\pm\,\tilde{\chi}_1^0)$	%	99.4	99.5	99.5
$\text{BR}(\tilde{\chi}_1^\pm \to \tilde{\mu}_R^\pm\,\nu_\mu)$	%	0.6	0.5	0.5
$\Delta m(\tilde{\chi}_1^\pm, \tilde{\mu}_R)$	GeV	168.5	207.0	203.4
$\Delta m(\tilde{\chi}_2^0, \tilde{\mu}_R)$	GeV	168.0	206.5	202.7
$\Delta m(\tilde{\mu}_R, \tilde{\chi}_1^0)$	GeV	7.2	7.8	7.5

Table 3.7: `CheckMATE` analysis results for the benchmarks of table 3.6 with full gaugino non-universality $M_1 < M_2 \ll M_3$.

In contrast to the results for partially non-universal gaugino masses, we now observe that all benchmarks BP4 – BP6 satisfy current LHC bounds, however it is worth noting that BP4 is on the verge of exclusion with an r-value of 0.88. BP5 and BP6 are safer due to $r \approx 0.12$, hence requiring a significant increase in luminosity to be probed. The most sensitive analysis now is not the 8 TeV analysis `ATLAS_1402_7029` [113], but its 13 TeV successor `ATLAS_CONF_2016_096` [141] aimed at chargino and neutralino production resulting in two or three leptons and $\not{E}_T$. Reasons

for this loss of sensitivity lie in the overall smaller cross sections due to the larger neutralino and chargino masses (see table 3.7), but also in the highly different branching ratios of $\tilde{\chi}_2^0$ and $\tilde{\chi}_1^\pm$. Due to the large mass gap between the right-handed smuon and $\tilde{\chi}_2^0$ as well as $\tilde{\chi}_1^\pm$, decays to on-shell Z and W bosons are now possible and especially the $\tilde{\chi}_2^0$ can decay as $\tilde{\chi}_2^0 \to h\,\tilde{\chi}_1^0$ with a significant branching ratio of more than 50 %, thus further reducing the LHC sensitivity.

While BP5 and BP6 are currently farthest from being probed at the LHC, future colliders with a total integrated luminosity of about 3 ab^{-1} will be able to effectively probe also these parts of the model parameter space with di and tri-lepton signatures from higgsino production. Furthermore, with the expected increase in sensitivity by a factor of two of DM direct detection experiments in the next few years, the model parameter space under study can be probed entirely and independently of any LHC constraints.

3.6 Conclusions

In this chapter, we explored a region in parameter space not studied before, which is characterised by a small, negative higgsino mass parameter $\mu \simeq -300$ GeV. In this region, we argue that the anomalous magnetic moment of the muon, Δa_μ, and dark matter can only be accommodated in GUT scale models breaking to the MSSM at the high scale in case of non-universal gaugino masses $M_1 \simeq 250 \text{ GeV} < M_2 \ll M_3$. Furthermore, a light right-handed smuon of order 100 GeV slightly heavier than the lightest neutralino $\tilde{\chi}_1^0$ (which is also the LSP) is required to satisfy current LHC searches. The bino-dominance of the LSP together with the almost mass-degenerate $\tilde{\mu}_R$ make the $\tilde{\chi}_1^0$ a good DM candidate, as it thus can effectively co-annihilate in the early universe and provides the observed relic density. The DM direct detection limits by Xenon1T, on the other hand, set strong constraints on this scenario.

The particular model we considered was the well studied $SU(5)$, together with an A_4 family symmetry. The three $\overline{\mathbf{5}}$ representations of the $SU(5)$ form a single triplet of A_4 with a unified soft mass m_F, whereas the three **10** representations are singlets under A_4 with independent soft masses m_{T1}, m_{T2} and m_{T3}. While it is possible to have light $\tilde{\mu}_R$ based on light m_{T2}, Δa_μ further requires $M_1 \simeq 250$ GeV. This is in contrast to LHC searches for gluinos and gauginos and hence we extended the $SU(5) \otimes A_4$ model parameter space to include non-universal gaugino masses,

which is theoretically possible by having non-singlet F-terms in the $SU(5)$. With this, it is worth noting that the $SU(5)\otimes A_4$ stands representative for a larger class of GUT scale models comprising similar non-universal MSSM scenarios, where the left and right-handed sfermions are split and where an especially light right-handed smuon is allowed.

After explicitly showing that universal gaugino masses $M_{1/2}$ at the GUT scale are excluded by LHC gluino searches, we performed benchmark studies on the cases of partially and fully non-universal gaugino masses to find that the former case is excluded by LHC gaugino searches, whereas the latter is still unprobed. However — and independent of the non-universality of the gaugino masses — the model inevitably predicts $\mu \approx -300$ GeV, which leads to higgsino-dominated gaugino masses of the same order posing an attractive target for future LHC searches. In particular, di and tri-lepton searches with missing transverse energy are expected to fully explore this region of parameter space, once the LHC or another future collider reaches a luminosity of about 3 ab^{-1}. The wino-dominated gauginos are expected to be slightly heavier than the higgsinos, while the rest of the spectrum lies in the multi-TeV range and hence evades current LHC bounds. Completely independent of the LHC searches, DM direct detection experiments also provide an excellent way to further explore the model parameter space. If the current limits are enhanced by a factor of about two (which is expected to happen in the following years), the entire parameter space of the scenario we studied can be probed.

In conclusion, if the anomalous magnetic moment of the muon persists, we expect the $SU(5)\otimes A_4$ to comprise a right-handed smuon with mass around 100 GeV and a bino-dominated neutralino $\tilde{\chi}_1^0$ only a few GeV lighter, thus representing a good DM candidate. Furthermore, the higgsino mass parameter in this scenario is expected to be $\mu \approx -300$ GeV, leading to a light gaugino mass spectrum that may be probed entirely and independently in the near future by the LHC and DM direct detection experiments.

4 | DM Signals from Vector Resonances and Top Partners at the LHC

4.1 Introduction

After exploring the phenomenology of two supersymmetric models in Chapters 2 and 3, we now turn towards an alternative set of BSM theories addressing the issues of the SM discussed in section 1.2. In particular, we focus on models able to explain DM that also agree with the requirement of a 125 GeV Higgs boson. As explained in the first Chapter 1, it is not completely known yet whether the discovered Higgs boson really is the SM one and hence, this discovery opened up a window in the exploration of BSM physics. As such, the Higgs boson can be a fundamental particle as in SUSY or the SM, but can also arise e.g. as the bound state of new fundamental particles with some new strong dynamics, as realised in a theory called Technicolor (TC) [142,143]. These strong dynamics then are responsible for breaking the electroweak symmetry (analogue to QCD) and, although the nature of the Higgs boson here is completely different as compared to SUSY, its properties can be similar to the SM Higgs and consistent with LHC data [144]. Besides TC, another class of theories addressing the issues of the SM with a fundamentally different Higgs boson are Composite Higgs (CH) models [145–147] (see also recent developments starting from [148]), where instead of electroweak symmetry, a global symmetry of the high energy model is broken by the new gauge dynamics[1]. Further alternatives include Randall-Sundrum models [150, 151], Little Higgs models [152–154], as well as Twin-Higgs models [155], also known

[1]It should be noted that CH models require UV completion with some new strong dynamics and therefore, TC and CH models can appear as different limits of strongly coupled theories [149].

as neutral naturalness [156].

An important aspect of both TC and CH models is the prediction of integer spin bound states, which we will minimally incorporate in our model in form of a Z' boson. Besides these BSM resonances (typically lying at the TeV scale), many models apart from SUSY also include a top partner sector, which can be important to keep the model technically natural. In case of TC and CH models in particular, the top partners are bound states of new strong dynamics and thus provide an attractive solution to the hierarchy problem without the use of supersymmetry. Lastly, these models usually also address DM together with a parity (or a larger symmetry group) keeping dark matter stable as well as a parity-odd dark matter sector.

In this chapter, we consider a simplified model incorporating the above mentioned ingredients, i.e. both a vector resonance Z' as a consequence of the TC and CH predictions of integer spin bound states, a fermionic vector-like coloured partner of the top quark T' as well as a scalar dark matter candidate ϕ arising via minimal gauge-invariant Yukawa interactions[2] $\lambda_{\phi T' t}$. We explore the phenomenology of this model with a focus on the process $pp \to Z' \to T'\overline{T'} \to t\bar{t}\phi\phi$, which gives rise to a $t\bar{t}$ + missing transverse energy signature ($t\bar{t} + \not{E}_T$) signature due to the Z' decays into two top partners $T'\overline{T'}$. This signature has not been studied before when initiated by Z' decays and we show that due to the extra Z', different kinematical distributions as compared to sole QCD production of $T'\overline{T'}$ (see Refs. [157–159]) emerge. Another effect of the Z' is a — potentially even dominant — enhancement of $T'\overline{T'}$-pair production without conflicting with existing bounds from Z' searches with di-jet[3] and di-lepton final states. A similar observation has been made before in the context of pair production enhancement of charge 5/3 top partners through $SU(2)$ triplet vector resonances [160]. We will show in this chapter that the Z', T' and DM masses can be probed well beyond the reach coming only from QCD production, if the $t\bar{t} + \not{E}_T$ signature is considered.

The remainder of this chapter is organised as follows. In section 4.2, we present the model and

[2] As a consequence of this coupling and the desired DM stability, both ϕ and the top partners have the same parity, which we assume to be negative DM parity.

[3] A *jet* in particle physics is a set of hadrons travelling along the same direction in a narrow cone. The jet forms as a consequence of quark (or colour) confinement, which states that isolated quarks (or colour charges) cannot exist freely, but are bound into colourless states. For example, after some high energy scattering process, partons escaping the scattering center will undergo parton showering and eventually start to form colourless hadrons, which is also known as hadronisation. The newly created hadrons travel in a similar direction as the initial hard parton and therefore lead to a spray of hadrons within a narrow cone, which is what is referred to as a jet.

discuss its parameter space in detail. In section 4.3, we first describe the analysis setup and present a parton-level analysis as well as study gluon-Z' interference effects. We then explore the model constraints from di-jet and di-lepton LHC searches before eventually investigating the potential of the LHC to probe our model parameter space via its typical signature $t\bar{t} + \not{E}_T$, which arises once Z', top partners and DM are considered simultaneously. Lastly, we draw our conclusions in section 4.4.

4.2 The Model

The model under study is a simplified effective model containing a vector resonance Z', a fermionic vector-like coloured top partner sector and a neutral scalar dark matter candidate ϕ. The Z' can couple to both SM quarks and leptons as well as to top partners T'_s ($SU(2)$ singlet) or $Q' = (T'_d, B'_d)$ ($SU(2)$ doublet)[4]. DM and the top partners are further assumed to carry negative DM parity and $M_{T'} > m_\phi$, whereas all SM particles and the Z' carry positive DM parity. This results in ϕ being a stable DM candidate coupling to both top quarks and top partners. For completeness of the model, the remaining renormalisable DM couplings consist of a so called Higgs-portal coupling $HH^\dagger\phi^2$ and DM self-interactions ϕ^4. The full Lagrangian for this model (which we abbreviate as ZP-TP-DM model) then reads

$$\mathcal{L} = \mathcal{L}_{SM} + \mathcal{L}_{kin} + \mathcal{L}_{Z'q} + \mathcal{L}_{Z'\ell} + \mathcal{L}_{Z'Q'} + \mathcal{L}_{\phi Q'} - V_\phi \,, \tag{4.1}$$

where

$$\begin{aligned}
\mathcal{L}_{kin} = &-\frac{1}{4}\left(\partial_\mu Z'_\nu - \partial_\nu Z'_\mu\right)\left(\partial^\mu Z'^\nu - \partial_\nu Z'^\mu\right) + \frac{M^2_{Z'}}{2} Z'_\mu Z'^\mu \\
&+ \frac{1}{2}\partial_\mu\phi\,\partial^\mu\phi - \frac{m^2_\phi}{2}\phi^2 \\
&+ \overline{T'_s}\left(i\not{D} - M_{T'_s}\right) T'_s + \overline{Q'_d}\left(i\not{D} - M_{T'_d}\right) Q'_d \,, \qquad (4.2a) \\
\mathcal{L}_{Z'q} = &\,\lambda_{Z'q\bar{q},L/R}\, Z'_\mu \left(\bar{q}_{L/R}\,\gamma^\mu\, q_{L/R}\right) \,, \qquad (4.2b) \\
\mathcal{L}_{Z'\ell} = &\,\lambda_{Z'\ell^+\ell^-,L/R}\, Z'_\mu \left(\bar{\ell}_{L/R}\,\gamma^\mu\, \ell_{L/R}\right) \,, \qquad (4.2c)
\end{aligned}$$

[4]For earlier work on top partner models in the presence of coloured vector resonances, see e.g. Ref. [161].

$$\begin{aligned}\mathcal{L}_{Z'Q'} &= \lambda_{Z'T'_s\overline{T'_s},L/R}\, Z'_\mu \left(\overline{T'}_{s,L/R}\,\gamma^\mu\, q_{L/R}\right) \\ &\quad + \lambda_{Z'T'_d\overline{T'_d},L/R}\, Z'_\mu \left(\overline{T'}_{d,L/R}\,\gamma^\mu\, T'_{d,L/R}\right) \\ &\quad + \lambda_{Z'T'_d\overline{T'_d},L/R}\, Z'_\mu \left(\overline{B'}_{d,L/R}\,\gamma^\mu\, B'_{d,L/R}\right)\,, \end{aligned} \tag{4.2d}$$

$$\mathcal{L}_{\phi Q'} = \left(\lambda_{\phi T'_s t}\,\phi\,\bar{t}_R\, T'_{s,R} + \lambda_{\phi T'_d t}\,\phi\,\bar{t}_L\, T'_{d,L} + \lambda_{\phi T'_d t}\,\phi\,\bar{b}_L\, B'_{d,L}\right) + \text{h.c.}\,, \tag{4.2e}$$

$$V_\phi = \frac{\lambda_\phi}{4!}\phi^4 + \frac{\lambda_{\phi H}}{2}\phi^2\left(|H|^2 - \frac{v^2}{2}\right)\,. \tag{4.2f}$$

In general, the Z' must not necessarily be associated to a gauge symmetry, in which case its couplings are 'current-couplings' unrestricted by gauge-invariance. For this reason, we treat the Z' couplings to quarks, leptons and top partners as free parameters. Regarding the DM mass m_ϕ, we write the DM interaction with the Higgs doublet such that the electroweak contribution to m_ϕ is absorbed and m_ϕ is the physical mass of ϕ. We would like to stress here that the DM-Higgs interactions do not affect the $t\bar{t}+\not{E}_T$ signature at the LHC in any way, however they are important when considering constraints on the model coming from the relic density, DM direct (DD) and indirect (ID) detection experiments as well as LHC constraints coming from invisible Higgs boson decays $H \to \phi\phi$.

Although even this simplified model comprises a wealth of parameters, we shall show in the following that the number of actually relevant parameters for the LHC and DM experimental studies is much smaller.

4.2.1 The Model Parameter Space and Analysis Setup

In this chapter, we focus on the $t\bar{t}+\not{E}_T$ final state, which can be produced via T'-pair production through QCD interactions or through resonant Z' decays. In case of just QCD interactions, the relevant parameter space to fully describe the $t\bar{t}+\not{E}_T$ signature reduces to $M_{T'}$ and m_ϕ. If also the Z' is considered, its mass $M_{Z'}$ as well as the Z' couplings to SM quarks, leptons (which we will choose equal to the Z'-quark coupling to be able to infer the results for other coupling ratios) and the top partners further become relevant. Since the phenomenology between the top partner singlet and doublet states is expected to be similar[5], we consider only the singlets for this work,

[5] As a main difference to T'_s-pair production, T'_d-pair production also gets contributions from $Z^* \to T'_d\overline{T'_d}$, which however is highly suppressed. The kinematical distributions are nevertheless expected to be almost identical. As

i. e. T'_s.

As we will show in section 4.3.1 below, the effects of the chiralities of the Z' couplings are negligible when studying the $t\bar{t} + \not{E}_T$ signature, thus allowing us to choose just one specific set of chiral couplings. In particular, we choose all left-handed couplings, i.e. $\lambda_{Z'q\bar{q},L}$ and $\lambda_{Z'T'_s\overline{T'_s},L}$ (abbreviated as LL), to be non-zero and all other chiral combinations to vanish.

The entirety of model parameters relevant to our study of the $t\bar{t} + \not{E}_T$ signature at the LHC hence comprises the following five parameters:

$$M_{T'_s}, \quad m_\phi, \quad M_{Z'}, \quad \lambda_{Z'q\bar{q},L}, \quad \lambda_{Z'T'_s\overline{T'_s},L}\,. \tag{4.3}$$

The DM phenomenology — with a focus on the DM relic density as well as DM direct and indirect detection — depends on two more parameters

$$\lambda_{\phi H} \quad \text{and} \quad \lambda_{\phi T'_s t}\,, \tag{4.4}$$

whose effects in combination with the top partners and Z' boson within this new model will be illustrated below. Before doing so, however, we give a full description of our analysis setup used to gather all results within the scope of this work. In particular, we used `LanHEP` [163–165] and `FeynRules` [166, 167] to implement the model described by the Lagrangian (4.2) in `CalcHEP` [168] and `MadGraph5_aMC@NLO` [109], respectively. Both implementations have been cross-checked against each other for scattering and decay processes and are available at HEPMDB [169] under hepmdb:0717.0253 [170] for `CalcHEP` and hepmdb:0717.0253 [171] for `MadGraph`. Among other features, HEPMDB allows to generate events using nothing more than the web-interface. All respective parton level analyses have been carried out using `MadGraph5_aMCNLO 2.3.3` and `CalcHEP 3.6.27` with the `NNPDF2.3QED` PDF [172]. The QCD renormalisation and PDF factorisation scales were set to $Q = M_{Z'}$.

After the event generation, we use `Pythia v8.219` [140] for parton showering and hadronisation

a side note, it is also worth mentioning that the T'_d comes along its doublet partner B'_d, which has a charge of $-\frac{1}{3}$ and can also be pair-produced via QCD or Z' interactions. The expected signature then is $b\bar{b} + \not{E}_T$ and is similar to $jj + \not{E}_T$, which has been studied in the context of QCD production of vector-like quarks followed by their decay to light quarks and DM [162].

and subsequently perform a fast detector simulation using `Delphes 3` [111] as well as `FastJet v.3.1.3` [173, 174] with a cone radius $\Delta R = 0.4$ for the jet reconstruction. The final detector level analysis to probe the $t\bar{t} + \not{E}_T$ signature against current $\sqrt{s} = 13$ TeV ATLAS and CMS constraints [175–186] was performed using `CheckMATE 2.0.0` [112, 139].

To study the DM phenomenology at an illustrative level, we use `micrOMEGAs v4.3.5` [116,187, 188] (together with the directly read-in `CalcHEP` model file) to compute the relic density Ωh^2 and the DM direct (DD) and indirect (ID) detection cross sections. Regarding the latter, `micrOMEGAs` computes the spin-independent cross sections $\sigma_{\rm SI}$ for DM scattering off a proton at one-loop level. The cross sections are then compared to the latest and currently strongest bounds for DM DD limits, coming from the Xenon1T experiment [133]. As this data was not available in digitised form, we digitised the limits ourselves and uploaded them to the PhenoData database [189].

In figure 4.1, we present LHC, DM DD and relic density constraints on the parameter space of the ZP-TP-DM model in the $\frac{M_{T'_s}}{m_\phi}$-m_ϕ plane without Higgs portal couplings ($\lambda_{\phi H} = 0$), i.e. for the case in which the relic density is fully determined by co-annihilation of ϕ with the T'_s. The current reach of the LHC for $t\bar{t}+\not{E}_T$ coming from both Z' and QCD mediated T'_s-pair production is shown as green area and will be discussed in detail in section 4.3.4. The thin dashed lines with the respective labels indicate the iso-levels of $M_{T'_s}$ in GeV. While the green exclusion area quantitatively agrees with the one from Ref. [159], we observe a larger exclusion range for small T'_s due to the fact that we not only considered the ATLAS search `ATLAS_CONF_2016_050` [185], but also considered limits coming from `ATLAS_1604_07773` [177], which is more sensitive to smaller mass gaps between the T'_s and DM. Besides the LHC limits, in figure 4.1 we also show the exclusion limits from the Xenon1T data for $\lambda_{\phi T'_s t} = 10$ as grey-shaded area. It should be noted that with smaller values of $\lambda_{\phi T'_s t}$ (e.g. 0.3, 0.5 or 1.0), the Xenon1T data does not set constraints on the parameter space yet, due to the DM DD cross sections scaling quadratically with $\lambda_{\phi T'_s t}$ and hence becoming too small. Lastly, the blue, red, grey and yellow contours correspond to the T'_s and DM masses resulting in a relic density of $\Omega h^2 = 0.12$ as observed by PLANCK [104, 190] for $\lambda_{\phi T'_s t} = 0.3$, 0.5, 1 and 10, respectively. Any mass choices lying above these contours yield a relic density larger than 0.12 and are thus excluded.

In summary, from figure 4.1 it becomes obvious that the LHC plays an important and com-

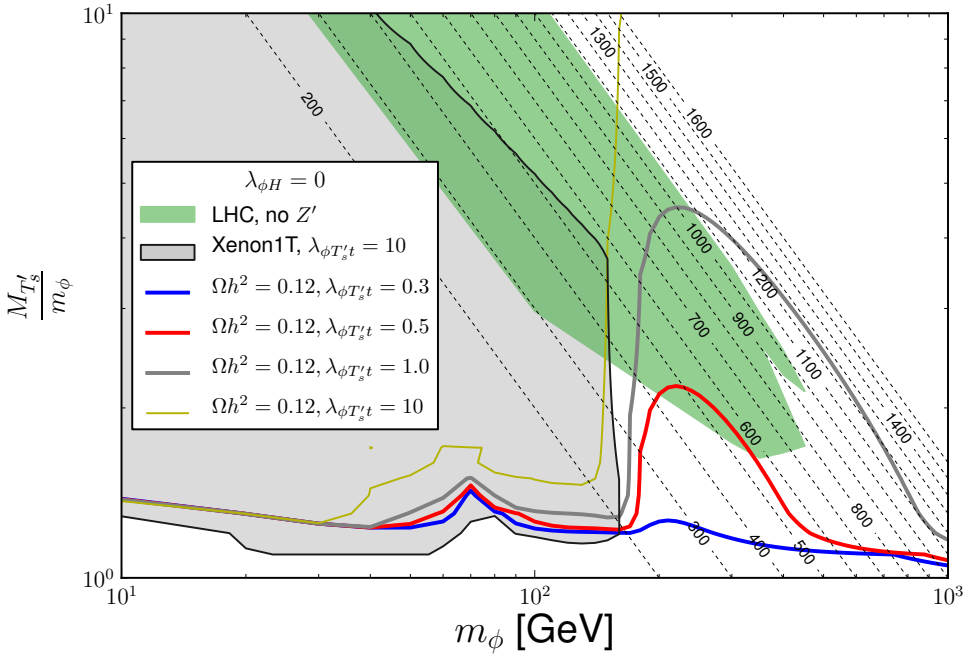

Figure 4.1: LHC, DM Direct Detection and relic density constraints in the $(M_{T'_s}/m_\phi\ ,\ m_\phi)$ plane for $\lambda_{\phi H} = 0$. The green-shaded area indicates the current LHC exclusion region for the $t\bar{t} + \not{E}_T$ signature coming from the process $pp \to T'\overline{T'} \to t\bar{t}\,\phi\phi$, mediated only by gluon exchange (i.e. without Z' exchange). The grey-shaded area indicates the DM DD exclusion region based on the latest Xenon1T data [133] for $\lambda_{\phi T'_s t} = 10$. The parameter space above the blue, red, grey and yellow contours is excluded due to too large relic density for $\lambda_{\phi T'_s t} = 0.3$, 0.5, 1 and 10 respectively, and each contour corresponding to the $\Omega h^2 = 0.12$ iso-level. The thin dashed lines with the respective labels indicate the iso-levels of $M_{T'_s}$ in GeV.

plementary role to the dark matter constraints in covering the $m_\phi > m_t$ region, which is not fully constrained by non-collider experiments, especially not for larger values of $\lambda_{\phi T'_s t}$.

As a side note, it should be mentioned that the available parameter space can be greatly enhanced if a Higgs portal is considered (i.e. $\lambda_{\phi H} > 0$). In this case (and depending on the actual value of $\lambda_{\phi H}$), the relic density gets contributions from DM annihilating through the Higgs boson and thus larger T'_s masses (also for smaller m_ϕ) remain allowed. Furthermore, a Higgs portal also leads to a change of the DM DD cross sections, as now interactions of DM with nuclei via Higgs exchange are possible. Finally, a non-zero $\lambda_{\phi H}$ also results in Higgs decays to DM, if DM is sufficiently light, and hence provides further limits on the parameter space from LHC Higgs measurements.

In figure 4.2, we show the influence of an active Higgs portal on the parameter space for $\lambda_{\phi H} = 0.1$ (top) and 0.3 (bottom) and with fixed $\lambda_{\phi T'_s t} = 1$.

It turns out that even for non-zero $\lambda_{\phi T'_s t}$, the narrow region around $m_\phi = \frac{m_H}{2}$ is unconstrained by non-collider searches due to the relic density being strongly reduced by a resonant DM annihilation to the Higgs. The DM DD cross sections are also suppressed due to the rescaling with the relic density, therefore rendering non-collider searches incapable of constraining the parameter space at $m_\phi \simeq \frac{m_H}{2}$. At the same timer, however, the LHC is able to effectively probe this region. Exemplarily, the pink-shaded area corresponds to the LHC limit on invisibly decaying Higgs bosons coming from ATLAS [191], which excludes BR($H \to$ invisible) < 28 % at 95 % CL. The limit itself is relevant only for $m_\phi \leq 62.5$ GeV and for sufficiently large $\lambda_{\phi H} \gtrsim 0.015$.

As mentioned earlier, these non-collider constraints are meant for illustration purposes only and a more detailed discussion on this topic can be found in Refs. [159,162], where a similar model, but without a Z', has been studied. Comparing these results to ours is still possible, however, as the Z' does not affect the non-collider DM phenomenology.

4.3 Analysis of $pp \to Z' \to T'_s \overline{T'_s} \to t\bar{t}\phi\phi$ for the LHC

The relevant physics of our model with a Z' decaying to a T'_s-pair further decaying to a top quark and DM, i.e. $t\bar{t}\,\phi\phi$ can be summarised by the Feynman diagrams in figure 4.3. The same final state can also be produced from QCD alone without a Z' boson, which we will study later in section 4.3.4 in detail. Before that, we perform several short studies to investigate the impact chiral couplings will have on kinematic distributions, possible interference effects between the Z' and QCD induced final states as well as the validity of the Narrow Width Approximation (NWA) or finite width effects of the Z'. To briefly summarise the findings of these pre-studies already here, we first find that the couplings $\lambda_{Z' q\bar{q}}$, $\lambda_{Z' T'_s \overline{T'}_s}$ and $\lambda_{\phi' T'_s \bar{t}}$ only have minor influence on the kinematics at parton level, thus allowing us to choose one specific chiral combination for all further studies, which will be $\lambda_{Z' q\bar{q},L}$ and $\lambda_{Z' T'_s \overline{T'}_{s,L}}$. Further, the aforementioned interference effects turn out to be negligible and the NWA remains acceptably valid up to a ratio of 5 % of the Z' width over its mass $M_{Z'}$, $\frac{\Gamma_{Z'}}{M_{Z'}}$.

After these pre-studies, we determine the constraints on our model parameter space coming

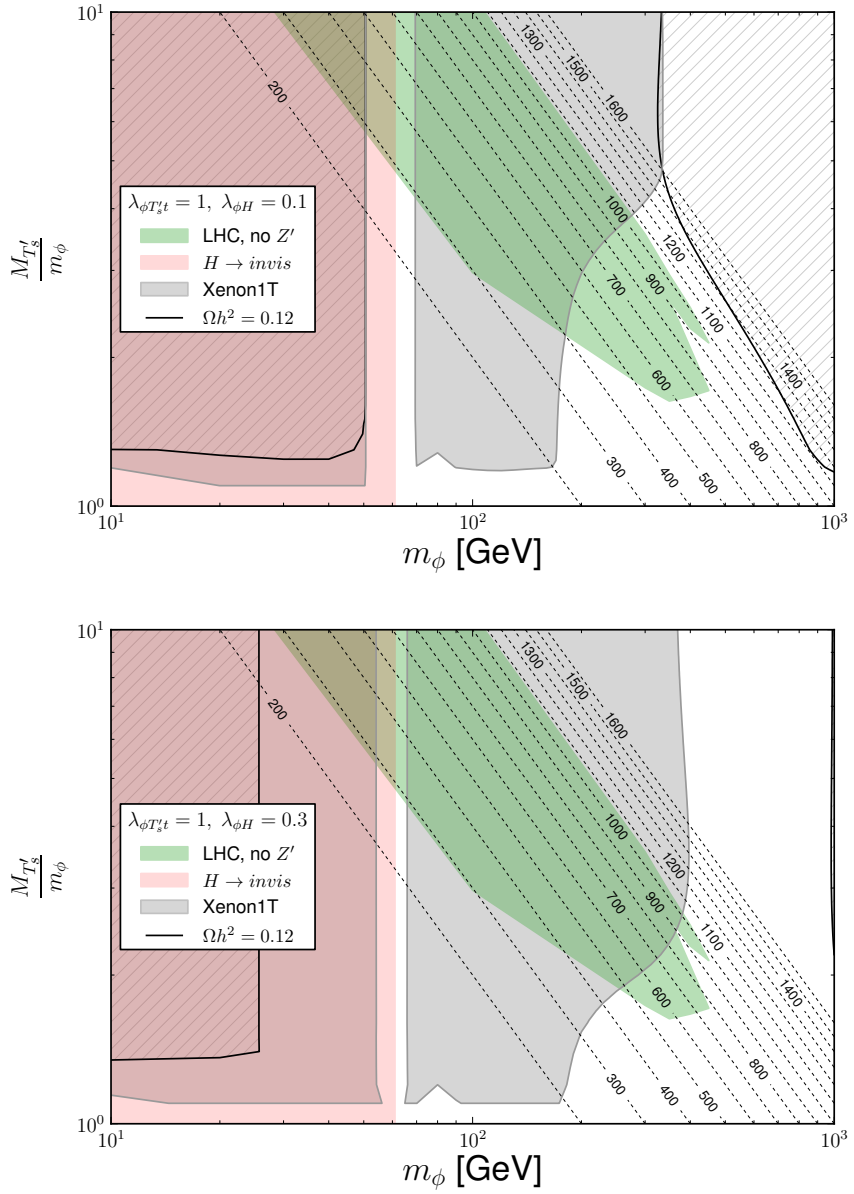

Figure 4.2: LHC, DM Direct Detection and relic density constraints in the $(M_{T'_s}/m_\phi\ ,\ m_\phi)$ plane for $\lambda_{\phi T'_s t} = 1$ and $\lambda_{\phi H} = 0.1$ (top) and 0.3 (bottom). The green-shaded area indicates the current LHC exclusion region from the process $pp \to T'\overline{T'} \to t\bar{t}\phi\phi$ without Z' exchange and the grey-shaded area indicates the DM DD exclusion region based on the latest Xenon1T data [133]. The hatched parameter space is excluded due to too large relic density and the pink-shaded area indicates the experimental limit from the invisible Higgs decay searches. The thin dashed lines indicate the iso-levels of $M_{T'_s}$ in GeV.

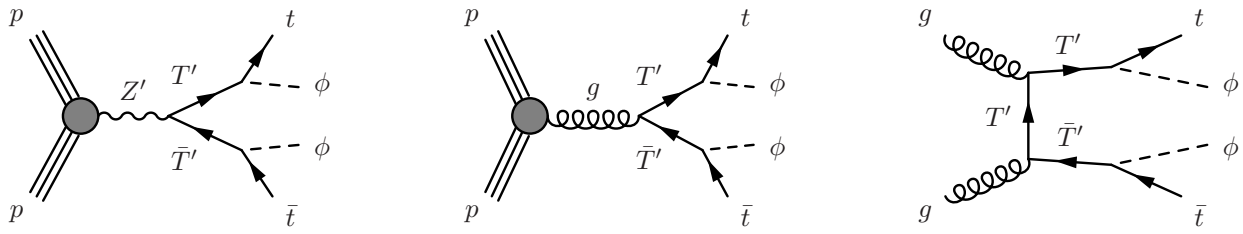

Figure 4.3: Feynman diagrams for $t\bar{t}\,\phi\phi$ production via T_s' decays from Z' bosons (left) and gluons (center and right).

from the LHC for QCD T_s' pair production in section 4.3.4, for the couplings $\lambda_{Z'q\bar{q}}$ and $\lambda_{Z'T_s'\overline{T_s'}}$ via di-jet and di-lepton resonance searches in section 4.3.5 and finally for the full model based on the process $pp \to Z' \to T_s'\overline{T_s'} \to t\bar{t}\,\phi\phi$ in section 4.3.6. In section 4.3.7, we then perform a detailed benchmark analysis.

4.3.1 Impact of Chiral Couplings on Kinematical Distributions

Since the Z' couplings appearing in the Lagrangian (4.2) are chiral, different coupling combinations could lead to different kinematics of the involved particles. To determine the influence of these coupling choices, we have used `MadGraph5_aMCNLO 2.3.3` in conjunction with `MadAnalysis` to generate and analyse several parton level distributions shown in figures 4.4 and 4.5 below. Therein, we refer to the four possible chiral combinations as LL, LR, RL and RR, where the first letter indicates the chirality of $\lambda_{Z'q\bar{q}}$ and the second letter indicates the chirality of $\lambda_{Z'T_s'\overline{T_s'}}$. Furthermore, we fix the couplings to $\lambda_{Z'q\bar{q}} = 0.25$ and $\lambda_{Z'T_s'\overline{T_s'}} = 2.5$ and the respective masses to $M_{Z'} = 3$ TeV, $M_{T_s'} = 1$ TeV and $m_\phi = 500$ GeV. Lastly, all events were generated based on a Z' decaying to a $T_s'\overline{T_s'}$-pair.

At first glance, all distributions (regardless of the coupling choices) appear to be nearly identical. On closer inspection, this remains true for the largest part of the di-top invariant mass (top left panel), the $\not{E}_T$ spectrum (top right panel, evaluated for DM only) and the p_T distribution of the top or anti-top quark respectively (bottom right panel) with slight differences only in the high-energy tails. As we shall show later in section 4.3.7, the difference between the most extreme cases LL and RR is just about 1–2 %, therefore quantitatively justifying our point of choosing just one chiral coupling combination for the remainder of this chapter. Regarding

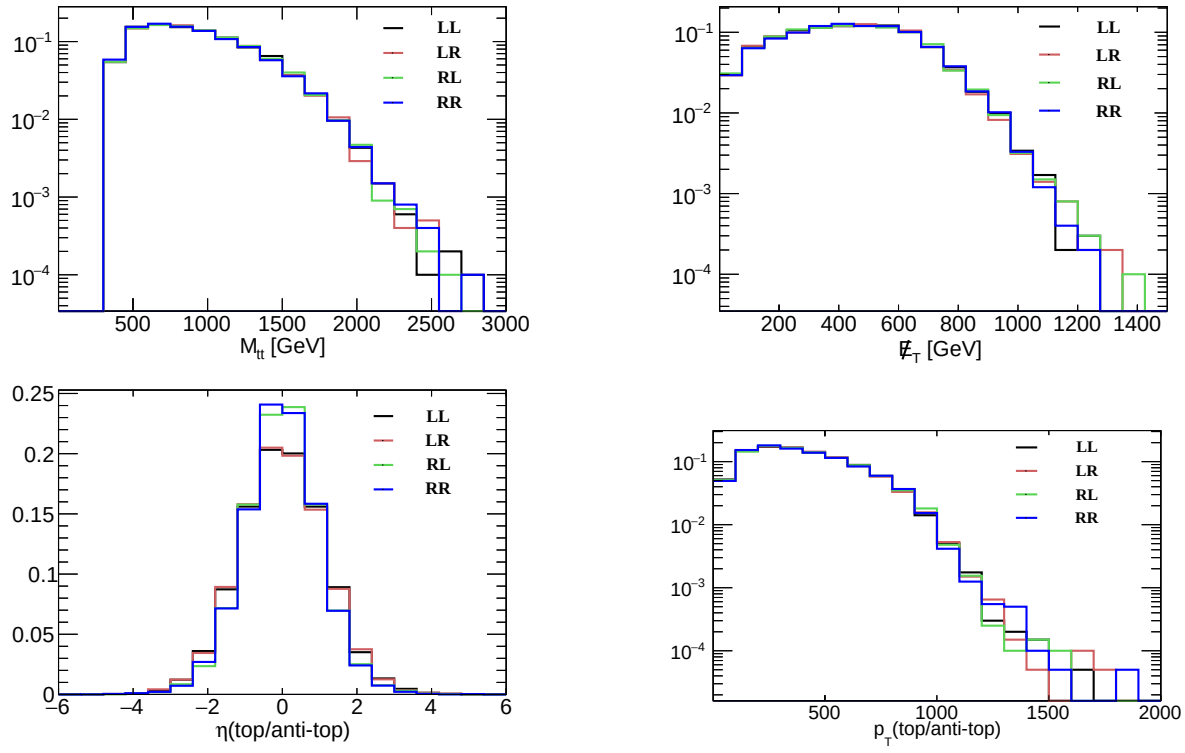

Figure 4.4: Differential distributions (normalised to one) for different chiral choices of $\lambda_{Z'q\bar{q},L/R}$ (first letter) and $\lambda_{Z'T_s'\overline{T_s'},L/R}$ (second letter), when top partner production only via Z' bosons is considered. The top partners decay further to top quarks and dark matter. LL is shown in black, LR in red, RL in green, and RR in blue. The BSM particle masses are chosen as $M_{Z'} = 3$ TeV, $M_{T_s'} = 1$ TeV and $m_\phi = 500$ GeV.

the pseudorapidity η distributions of the top and anti-top quark[6], LL and LR lead to similar distributions as do RL and RR. However in case of left-handed $\lambda_{Z'q\bar{q}}$, the distributions are slightly smaller and broader compared to the case of right-handed $\lambda_{Z'q\bar{q}}$.

Although the distributions in figure 4.4 are not directly observable, they nevertheless define and shape the distributions of the observable top quark decay products, shown in figure 4.5 below. As an example, the lepton p_T from W boson decays of a decaying top quark varies depending on the top quark polarisation (see e.g. Ref. [158] and figure 4.5, bottom right panel).

In case the W bosons arising from the decaying top quarks further decay leptonically, we observe slightly different p_T distributions for different $\lambda_{Z'T_s'\overline{T_s'}}$, but independently of the choice of

[6]More precisely, we plot the η distribution of the top quark added to the η distribution of the anti-top.

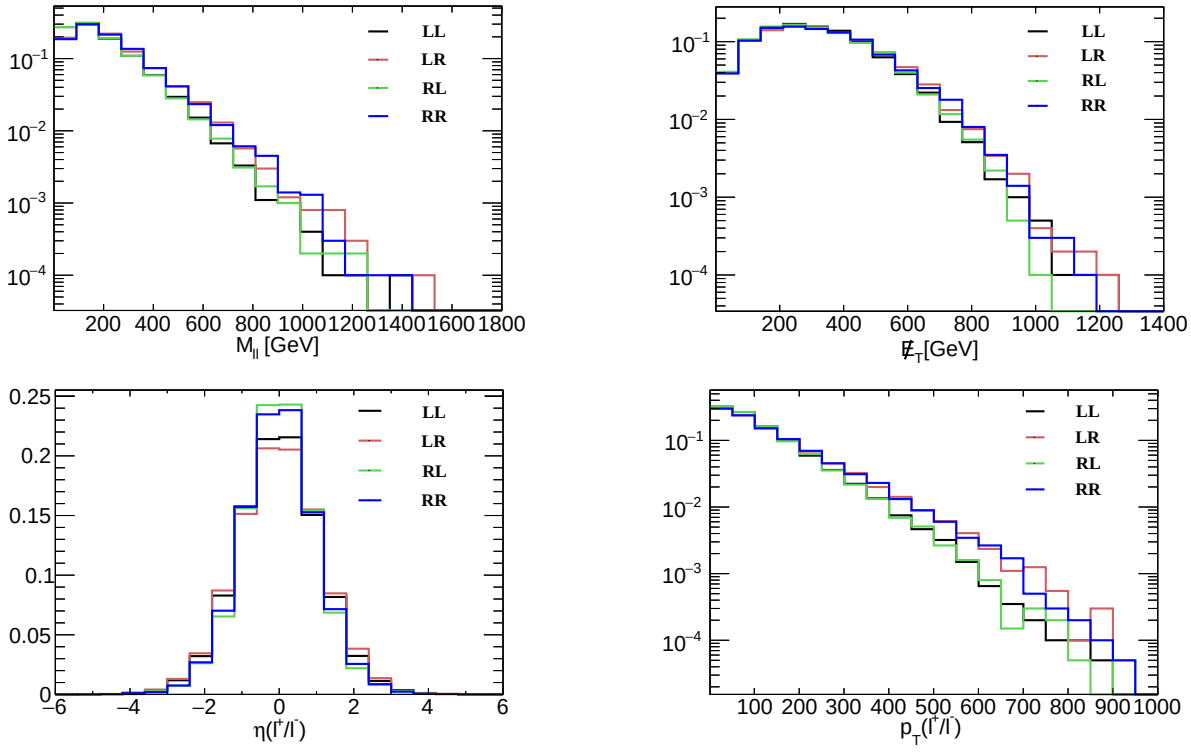

Figure 4.5: Differential distributions (normalised to one) for different chiral choices of $\lambda_{Z'q\bar{q},L/R}$ (first letter) and $\lambda_{Z'T_s'\overline{T_s'},L/R}$ (second letter) when top partner production only via Z' bosons is considered. The top partners decay to top quarks and dark matter and the top quarks further decays into bW with a leptonically decaying W boson. LL is shown in black, LR in red, RL in green, and RR in blue. The BSM particle masses are chosen as $M_{Z'} = 3$ TeV, $M_{T_s'} = 1$ TeV and $m_\phi = 500$ GeV.

$\lambda_{Z'q\bar{q}}$. In other words, RR and LR show a different behaviour than RL and LL. In particular, the *R distributions are slightly harder, which has been observed previously (see Ref. [158]) and is due to the influence of the polarisation of the top quark on the transverse momentum of its subsequent decay products. However, this difference in p_T only occurs for large p_T and thus is not influencing the efficiency of the cuts for the signature we study. The same observation can be made for the $M_{\ell\ell}$ and $\not{E}_T$ distributions, while it is also worth noting that the $\not{E}_T$ distribution before and after the top quark decays are quite similar. The η_ℓ distribution shows the same characteristics and differences as the η_t distribution.

Based on these findings, in the following we will consider for simplicity the case where both

$\lambda_{Z'q\bar{q}}$ and $\lambda_{Z'T'_s\overline{T'_s}}$ are left-handed (LL). This choice is also reasoned by the slightly softer lepton p_T, which results in turn in slightly lower cut-efficiencies compared to LR and RR and hence makes this choice conservative.

Besides the influence of the chiralities, it is also instructive to explore the impact of the T' production channel on the kinematics, i.e. when the T'-pairs are produced via QCD mediation alone or when produced via QCD and Z' mediation. This difference directly relates to the main point of this chapter: the role of a Z' boson in exploring the $t\bar{t} + \not{E}_T$ signature at the LHC. In figure 4.6, we present similar kinematical distributions as before for the cases of no Z', a Z' with mass $M_{Z'} = 2.5$ TeV and $M_{Z'} = 3$ TeV. The couplings (which always are left-handed from now on, i.e. LL) are chosen as $\lambda_{Z'q\bar{q}} = 0.25$ and $\lambda_{Z'T'_s\bar{T}'_s} = 2.5$.

One can observe that for ℓ^-, the p_T distributions are identical no matter whether a Z' is included or not. For ℓ^+, however, the p_T distribution is harder when a Z' is included in the theory, especially for larger p_T. The same holds for the $\not{E}_T$ distribution, which benefits from the Z' especially the larger $\not{E}_T$ gets.

4.3.2 Interference Effects

T'_s-pairs can not only be produced via Z' bosons, but also via QCD interactions (see figure 4.3). This results in possible interference effects, which we determine by comparing cross sections for each production channel alone as well as for the combined channel, where the T'_s-pair can be produced via either Z' or QCD interactions. We computed the cross sections using `MadGraph5 2.3.3` [109] while thereby trying to maximise the interference effects by choosing the couplings and masses such that the Z'-mediated and gluon-only cross sections are nearly identical. Lastly, the Z' width might also affect interference effects, and we take this into account by studying two parameter points: one with a narrow Z' width ($M_{Z'} = 2.5$ TeV, $M_{T'_s} = 1$ TeV, $\lambda_{Z'q\bar{q}} = 0.3$, $\lambda_{Z'T'_s\bar{T}'_s} = 0.58$) and one with a very broad Z' width ($M_{Z'} = 2.5$ TeV, $M_{T'_s} = 1$ TeV, $\lambda_{Z'q\bar{q}} = 0.21$, $\lambda_{Z'T'_s\bar{T}'_s} = 4.7$). The results are summarised in table 4.1. Overall, we find the interference effects to be small with a 2.5 % (3.6 %) gain in cross section for the case of a narrow (broad) Z' width respectively and the interference is always constructive.

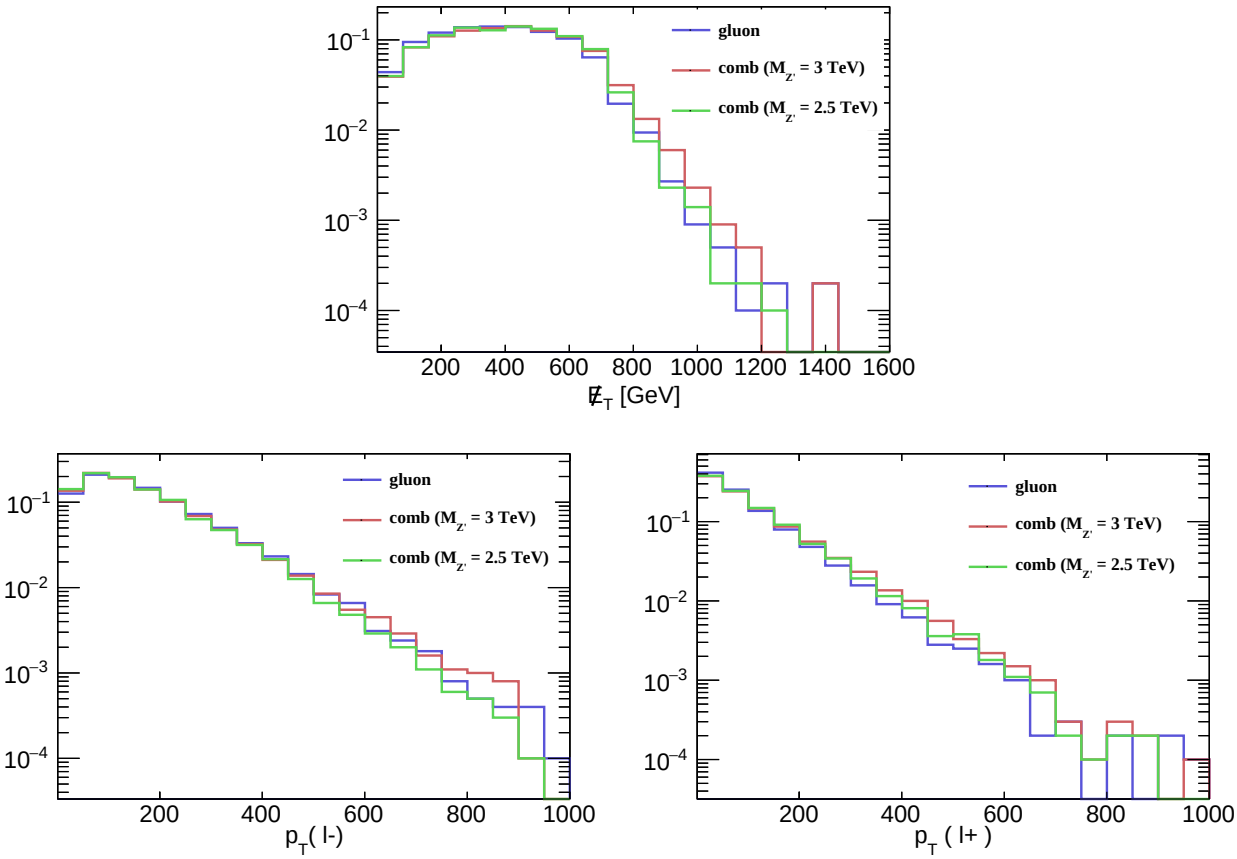

Figure 4.6: Differential distributions (normalised to one) specifically for the chiral choice LL, when top partner-pair production occurs via QCD and for the combined production, i.e with QCD and Z' mediation for $M_{Z'} = 2.5$ and 3 TeV. The top partners decay to top quarks and dark matter. Distributions without Z' mediation are shown in green, while the distributions with Z' mediation are shown in blue for $M_{Z'} = 2.5$ TeV and in red for $M_{Z'} = 3$ TeV. Here, $\lambda_{Z'T'_s\overline{T'_s},L} = 2.5$, $\lambda_{Z'q\bar{q},L} = 0.25$, $M_{T'_s} = 1$ TeV and $m_\phi = 500$ GeV.

4.3.3 Narrow Width Approximation and Corrections

The NWA is a powerful tool to estimate cross sections for different model parameters quite precisely, as long as the relevant resonance width is small. To be able to give precise predictions based on the NWA also for larger widths, the NWA needs to be corrected. In figure 4.7, we show the cross sections for $pp \to Z' \to T'_s\overline{T'_s}$[7] in the NWA (black line) and computed with `CalcHEP` [168] (red '+') for $M_{Z'} = 3$ TeV, $M_{T'_s} = 1.2$ TeV, $\lambda_{Z'q\bar{q}} = 0.1$, $\lambda_{Z'\ell^+\ell^-} = 0$ and varying $\lambda_{Z'T'_s\overline{T'_s}}$. The relative difference between the two (normalised to the `CalcHEP` result) is shown as blue crosses.

[7]For simplicity, we do not consider finite width effects arising from the T'_s decays.

$\Gamma_{Z'}$ [GeV]	production channel	σ [fb]	difference [fb] (rel. difference [%])
70.5	Z'	30.9	+1.6 (+2.5 %)
	QCD	32.4	
	combined	64.9	
1134	Z'	31.3	+2.4 (+3.6 %)
	QCD	32.5	
	combined	66.2	

Table 4.1: Cross sections for T_s' pair production for different production channels with $M_{Z'} = 2.5$ TeV. The difference is computed as 'combined - (Z' + gluon)' and the relative difference as '$1 - \frac{Z'+\text{gluon}}{\text{combined}}$'.

In case $\Gamma_{Z'}/M_{Z'}$ is as small as 1 %, the NWA perfectly estimates the real cross section σ. When

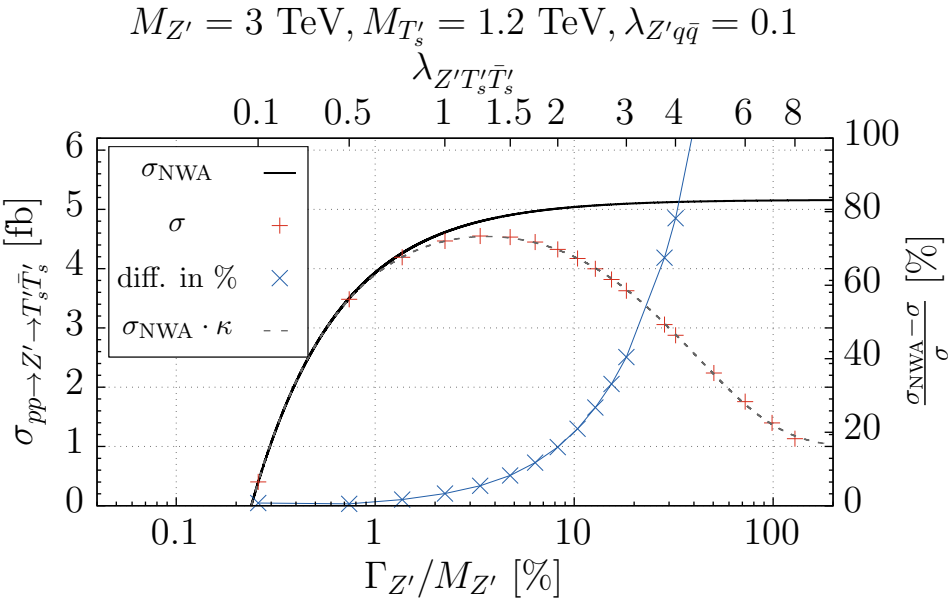

Figure 4.7: Comparison of $pp \to Z' \to T_s'\overline{T_s'}$ in the NWA (black line) and without NWA (red '+') for $M_{Z'} = 3$ TeV. The blue crosses show the difference in % between the two based on σ. The blue curve shows the fitting function equation (4.6) with fit parameters given in equation (4.7).

increasing $\Gamma_{Z'}/M_{Z'}$ up to about 5 %, the NWA gets less accurate and the estimated cross section only matches the real cross section up to a 10 % difference. Increasing $\Gamma_{Z'}/M_{Z'}$ even further results in leaving the scope of application of the NWA and an exponentially fast increasing difference in cross sections. As such, $\Gamma_{Z'}/M_{Z'}$ of about 20 % results in a difference in cross sections of roughly 40 %. It should also be noted that the NWA always overestimates the real cross section, which

would lead to over-optimistic limits. However, this issue can easily be tackled by adapting the NWA with a correction factor $\kappa\left(\lambda^2_{Z'T'_s\overline{T'_s}}\right)$ defined as

$$\kappa\left(\lambda^2_{Z'T'_s\overline{T'_s}}\right) \equiv \frac{\sigma}{\sigma_{\text{NWA}}}. \tag{4.5}$$

With the ansatz function

$$\kappa\left(\lambda^2_{Z'T'_s\overline{T'_s}}\right) = c_0 + c_1 \cdot \exp\left(-c_2\, \lambda^2_{Z'T'_s\overline{T'_s}}\right) \tag{4.6}$$

we obtain

$$c_0 = 0.193(4)\,, \quad c_1 = 0.812(4)\,, \quad c_2 = 0.049(1) \tag{4.7}$$

for $M_{Z'} = 3$ TeV, $M_{T'_s} = 1.2$ TeV (cf. the grey dashed curve in figure 4.7 for the quality of the fit). For different mass choices, these fitting coefficients vary due to cutoff effects appearing for large $\Gamma_{Z'}$ and due to PDF effects. For a fixed mass pair, however, $\kappa\left(\lambda^2_{Z'T'_s\overline{T'_s}}\right)$ is universal in the $\left(\lambda_{Z'T'_s\overline{T'_s}}, \lambda_{Z'q\bar{q}}\right)$ coupling space. Therefore, whenever we make use of the NWA in the following, we rescale

$$\sigma_{\text{NWA}} \mapsto \sigma_{\text{NWA}} \cdot \kappa_{(M_{Z'}, M_{T'_s})}\left(\lambda^2_{Z'T'_s\overline{T'_s}}\right)\,, \tag{4.8}$$

with the fitting function $\kappa_{(M_{Z'}, M_{T'_s})}\left(\lambda^2_{Z'T'_s\overline{T'_s}}\right)$.

4.3.4 QCD-induced T'_s Pair Production

With the preliminaries in place, we now move on to study the 13 TeV LHC limits on QCD-induced T'_s-pair production, i.e. without considering the Z' boson. We use `CheckMATE` to simulate 50000 events for the process $pp \to T'_s\overline{T'_s} \to t\bar{t}\,\phi\phi$ which are compared to current ATLAS and CMS analyses [175–186]. The majority of these searches focusses on SUSY-like final states with jets and $\not{E}_T$, thus matching our proposed sigature $t\bar{t} + \not{E}_T$. Furthermore, the limits for T'_s-pair production only depend on the top partner and DM masses $M_{T'_s}$ and m_ϕ, as these parameters fully fix the relevant kinematics and cross sections. The limits themselves are computed by `CheckMATE` in form of the r value from equation (3.6), where again k-factors from NLO corrections have not been taken into account. Rearranging equation (3.6) allows to estimate the experimental limit in form

of a cross section, which we show in figure 4.8 for various DM masses as coloured lines together with the theoretically predicted signal cross section in black.

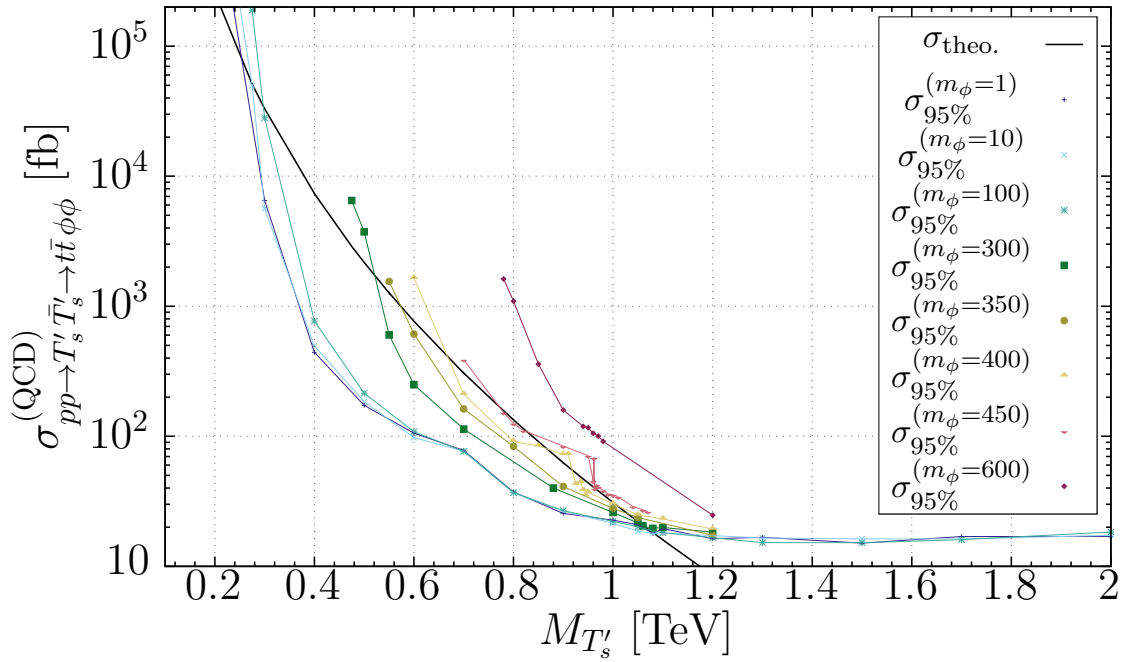

Figure 4.8: Theoretical (black) and experimental (coloured) cross sections for $pp \to T_s'\overline{T_s'} \to t\bar{t}\,\phi\phi$ in fb without Z' mediation in dependence of $M_{T_s'}$ and m_ϕ. m_ϕ is given in GeV.

As it turns out, most limits come from the analysis `ATLAS_CONF_2016_050` [185], which aims at top squarks in final states together with one isolated lepton, jets and $\not{E}_T$ at $\sqrt{s} = 13$ TeV. The most sensitive signal regions therein are `tN_high` and `SR1`, where the first (latter) one is aimed at high (low) mass splittings between $\tilde{t}_1$ and $\tilde{\chi}_1^0$. A large mass split results in highly boosted top quarks, whereas a small mass split is responsible for all decay products to be fully resolved [185]. If this mass split gets very small such that the top quark coming from the T_s' decay is just on-shell (i.e. when $M_{T_s'} \gtrsim m_t + m_\phi$), `ATLAS_1604_07773` [177] yields the best limits.

The first thing to note is that for $M_{T_s'} \gtrsim 1.1$ TeV, the experimental limits are nearly constant at about 20 fb, which is due to the top quarks now always being heavily boosted. At the same time, the signal cross section drops well below this limit due to the high suppression in cross section coming from the heavy T_s'-pair. For top partner masses smaller than 1.1 TeV, an exclusion window that heavily depends on the particular DM mass opens up. Smaller DM masses result in

a larger exclusion range, whereas for DM masses $\gtrsim 450$ GeV, the exclusion window vanishes. The window also closes once $M_{T_s'} \gtrsim m_t + m_\phi$, whereas even smaller top partner masses would result in off-shell top quarks with highly different kinematical distributions not studied in this thesis.

As a side note, the small portions of non-excluded $M_{T_s'}$ for $m_\phi = 400$ and 450 GeV in the otherwise excluded area have no physical meaning, but correspond to a gap (or missing overlap) between the signal regions `tN_high` and `SR1` from `ATLAS_CONF_2016_050`. As an example, `SR1` is most sensitive to $m_\phi = 400$ GeV and $M_{T_s'} \lesssim 920$ GeV, whereas for $M_{T_s'} \gtrsim 920$ GeV, `tN_high` immediately becomes most sensible. Due to the missing overlap between the two signal regions, a kink or step is visible in the eperimental limits.

Based on the above findings, we will investigate the current experimental di-jet and di-lepton limits in the $\left(\lambda_{Z'T_s'\overline{T_s'}}, \lambda_{Z'q\bar{q}}\right)$ plane for $M_{T_s'} \geq 1.1$ TeV, which are generally safe for any m_ϕ.

4.3.5 Di-jet and Di-Lepton Constraints

To determine the LHC di-jet and di-lepton limits on the $\left(\lambda_{Z'T_s'\overline{T_s'}}, \lambda_{Z'q\bar{q}}\right)$ coupling space, we have to extract and isolate the theoretical expression e.g. for $\lambda_{Z'q\bar{q}}$. This can be done via the Z' width, which reads

$$\Gamma_{\text{tot}}\left(Z'\right) = \frac{1}{8\,\pi\,M_{Z'}^2} \sum_{\text{final states}} |\mathcal{M}|^2\,|p_1| \tag{4.9}$$

with the 4-momentum of the first final-state particle

$$|p_1| = \frac{\sqrt{\left[M_{Z'}^2 - (m_1+m_2)^2\right]\left[M_{Z'}^2 - (m_1-m_2)^2\right]}}{2\,M_{Z'}} = \begin{cases} \dfrac{\sqrt{M_{Z'}^2 - 4m^2}}{2} & , m_1 = m_2 \equiv m \\ \dfrac{M_{Z'}}{2} & , m_1 = m_2 = 0 \end{cases}$$

and already having integrated over the solid angle of the first final-state particle $\int \mathrm{d}\Omega = \iint \sin(\theta_1)\,\mathrm{d}\theta_1\,\mathrm{d}\phi_1 = 4\pi$. We further assume

$$\Gamma_{\text{tot}}\left(Z'\right) < \frac{M_{Z'}}{2}\,, \tag{4.10}$$

in order to ensure perturbativity of the Z'-to-fermion couplings.

The remaining squared matrix element for a Z' decaying into its possible decay products times

$|p_1|$ reads

$$\begin{aligned}\sum_{\text{final states}} |\mathcal{M}|^2 |p_1| = & \underbrace{2\left[\sum_{\{q\}} \left(M_{Z'}^2 - m_q^2\right) \cdot |p_1(m_q)|\right]}_{\equiv A_q} \lambda_{Z'q\bar{q}}^2 \\ & + \underbrace{2\left(M_{Z'}^2 - M_{T_s'}^2\right) \cdot |p_1(M_{T_s'})|}_{\equiv A_{T_s'}} \lambda_{Z'T_s'\overline{T_s'}}^2 \\ & + \underbrace{\frac{2}{3}\left[\sum_{\{\ell\}} \left(M_{Z'}^2 - m_\ell^2\right) \cdot |p_1(m_\ell)|\right]}_{\equiv A_\ell} \lambda_{Z'\ell^+\ell^-}^2 \,.\end{aligned} \tag{4.11}$$

Finally, plugging equation (4.11) into (4.9) and (4.10) yields a combined upper bound on $\lambda_{Z'q\bar{q}}$, $\lambda_{Z'T_s'\overline{T_s'}}$ and $\lambda_{Z'\ell^+\ell^-}$. Together with the experimental limits from ATLAS and CMS for di-jet [192, 193] and di-lepton [194, 195] searches, we show this bound in figures 4.9 ($\lambda_{Z'\ell^+\ell^-} = 0$) and 4.10 ($\lambda_{Z'\ell^+\ell^-} = \lambda_{Z'q\bar{q}}$) for various combinations of $M_{Z'}$ and $M_{T_s'}$. The limits for $\lambda_{Z'T_s'\overline{T_s'}} > 0$ were acquired with help of the NWA

$$\begin{aligned}\sigma_{pp\to Z'\to jj}\left(\lambda_{Z'q\bar{q}}(0)\right) = & \sigma_{pp\to Z'}\left(\lambda_{Z'q\bar{q}}\left(\lambda_{Z'T_s'\overline{T_s'}}\right)\right) \\ & \cdot \mathrm{BR}\left(Z' \to q\bar{q}\right) \,, \end{aligned} \tag{4.12a}$$

$$\begin{aligned}\sigma_{pp\to Z'\to \ell^+\ell^-}\left(\lambda_{Z'q\bar{q}}(0)\right) = & \sigma_{pp\to Z'}\left(\lambda_{Z'q\bar{q}}\left(\lambda_{Z'T_s'\overline{T_s'}}\right)\right) \\ & \cdot \mathrm{BR}\left(Z' \to \ell^+\ell^-\right) \,, \end{aligned} \tag{4.12b}$$

with $\lambda_{Z'q\bar{q}}(0)$ being the experimental limit for $\lambda_{Z'T_s'\overline{T_s'}} = 0$.

It can be seen that the di-jet bounds already put rather strong limits on $\lambda_{Z'q\bar{q}}$, however when also considering the di-lepton limits, the latter clearly become dominant. While this observation is nearly independent of $M_{T_s'}$, going to smaller $M_{Z'}$ will increase the experimental limits quite visibly. In case $M_{Z'}$ is close to $2M_{T_s'}$ (see figure 4.9 and 4.10, top left and bottom right), the parameter space opens up in the direction of $\lambda_{Z'T_s'\overline{T_s'}}$ and hence allows larger values of $\lambda_{Z'T_s'\overline{T_s'}}$ to be realised without being in conflict with perturbativity. This is reasoned by the fact that $A_{T_s'}$ becomes smaller the closer $2M_{T_s'}$ approaches $M_{Z'}$ (see equation (4.11)), thus allowing for larger

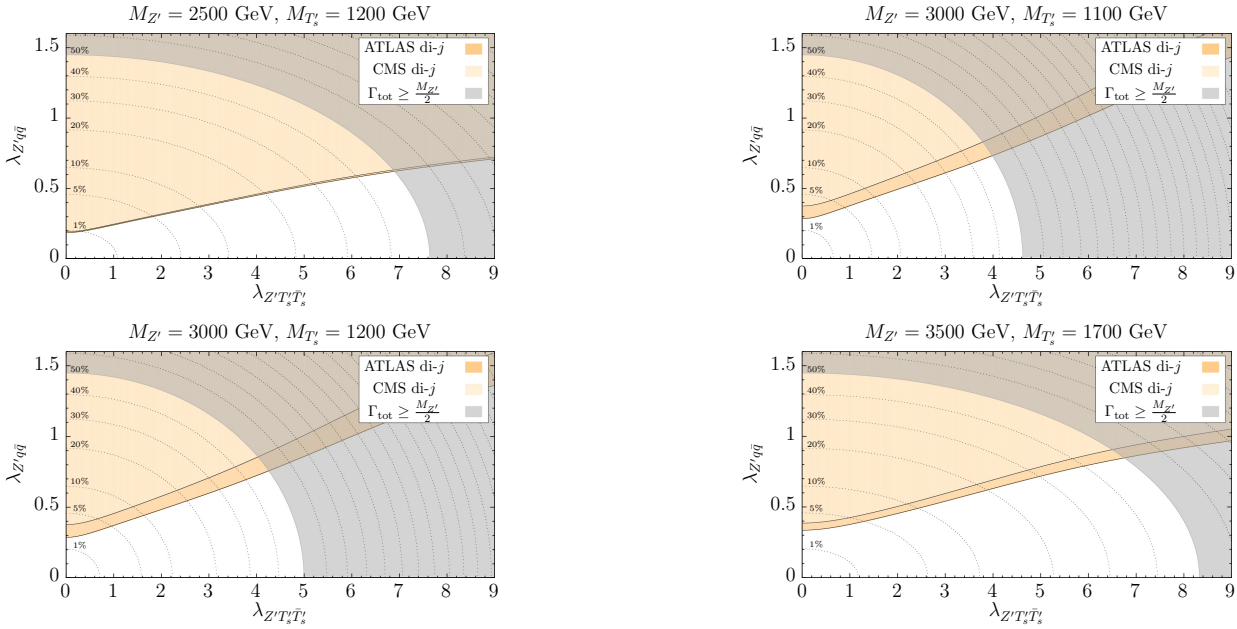

Figure 4.9: $\left(\lambda_{Z'T'_s\overline{T'_s}}, \lambda_{Z'q\bar{q}}\right)$ parameter space for $\lambda_{Z'\ell^+\ell^-} = 0$ as well as different $M_{Z'}$ and $M_{T'_s}$ with di-jet and di-lepton bounds. The dotted lines from bottom to top show when the Z' width is $(1, 5, 10, 20, \ldots)\%$ of its mass.

$\lambda_{Z'T'_s\overline{T'_s}}$ to be realised.

In summary, the di-jet and di-lepton limits alone already constrain large portions of parameter space, however mainly in the $\lambda_{Z'q\bar{q}}$ direction. Nevertheless, the fraction of parameter space surviving, especially in the $\lambda_{Z'T'_s\overline{T'_s}}$ direction, is still large enough to motivate further studies.

4.3.6 LHC Reach Including Z' Bosons

The next step after investigating the di-jet and di-lepton bounds is to check our model parameter space against the proposed $t\bar{t} + \not{E}_T$ signature. Before doing this for the full set of possible Feynman diagrams, we focus on the Z' mediated part (left diagram of figure 4.3). We generated 50000 events for this process with all considered on-shell $(M_{Z'}, M_{T'_s})$ combinations as well as $m_\phi = (10, 62.5, 100, 300, 600)$ GeV together with $\lambda_{Z'q\bar{q}} = 0.2$ and $\lambda_{Z'T'_s\overline{T'_s}} = 2$ and employ `CheckMATE` to analyse these events. As a result, the vast majority of points is constrained by the search `ATLAS_CONF_2016_050` [185] in the `tN_high` signal region and only a small set of points is constrained by marginally stronger limits coming from `ATLAS_1605_03814` [178] in the `2jt` signal

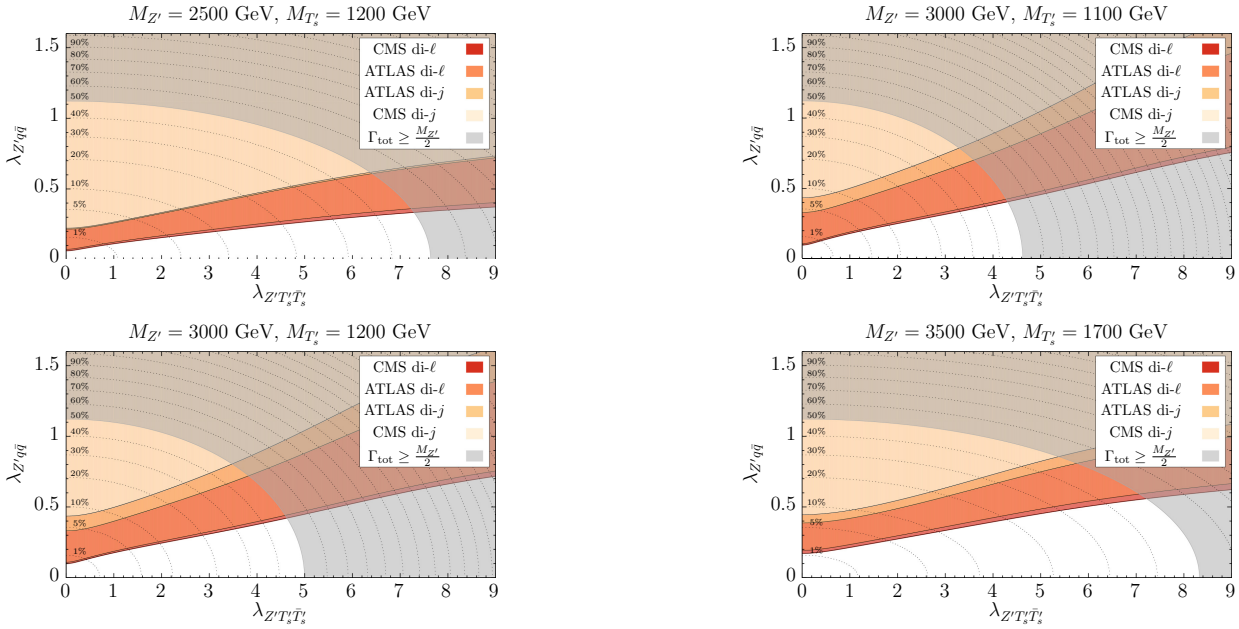

Figure 4.10: $\left(\lambda_{Z'T'_s\overline{T'_s}}, \lambda_{Z'q\bar{q}}\right)$ parameter space for $\lambda_{Z'\ell^+\ell^-} = \lambda_{Z'q\bar{q}}$ as well as different $M_{Z'}$ and $M_{T'_s}$ with di-jet and di-lepton bounds. The dotted lines from bottom to top show when the Z' width is $(1, 5, 10, 20, \ldots)\%$ of its mass.

region. Due to this nearly homogeneous picture, we can make use of the NWA once more in order to rescale the detection/exclusion limits computed by `CheckMATE` via

$$\begin{aligned}\sigma_{95\%} \overset{!}{=} \sigma_{\text{signal}} &= \sigma_{pp\to Z'} \cdot \text{BR}\left(Z' \to T'_s\overline{T'_s}\right) \\ &= \mathcal{P}\,\lambda^2_{Z'q\bar{q}} \cdot \frac{A_{T'_s}\,\lambda^2_{Z'T'_s\overline{T'_s}}}{A_{T'_s}\,\lambda^2_{Z'T'_s\overline{T'_s}} + A_q\,\lambda^2_{Z'q\bar{q}} + A_\ell\,\lambda^2_{Z'\ell^+\ell^-}}\,,\end{aligned} \tag{4.13}$$

where $\sigma_{95\%}$ indicates the bound (at 95% C.L.) on the observed production cross section from the most constraining search and parameter region and $\mathcal{P} = \mathcal{P}(M_{Z'}) = \frac{\sigma_{pp\to Z'}}{\lambda^2_{Z'q\bar{q}}}$ is the prefactor of the Z' production cross section and only depends on $M_{Z'}$. Rearranging equation (4.13) then yields $\lambda_{Z'q\bar{q}}$ as a function of $\lambda_{Z'T'_s\overline{T'_s}}$, which allows us to identify the excluded parts of the respective coupling space. Figures 4.11 ($\lambda_{Z'\ell^+\ell^-} = 0$) and 4.12 ($\lambda_{Z'\ell^+\ell^-} = \lambda_{Z'q\bar{q}}$) show these excluded regions for the same $(M_{Z'}, M_{T'_s})$ mass pairs and various m_ϕ (black lines at the bottom of the blue bands) as in figures 4.9 and 4.10.

The $t\bar{t} + \not{E}_T$ limits are quite complementary to the di-jet and di-lepton limits and constrain

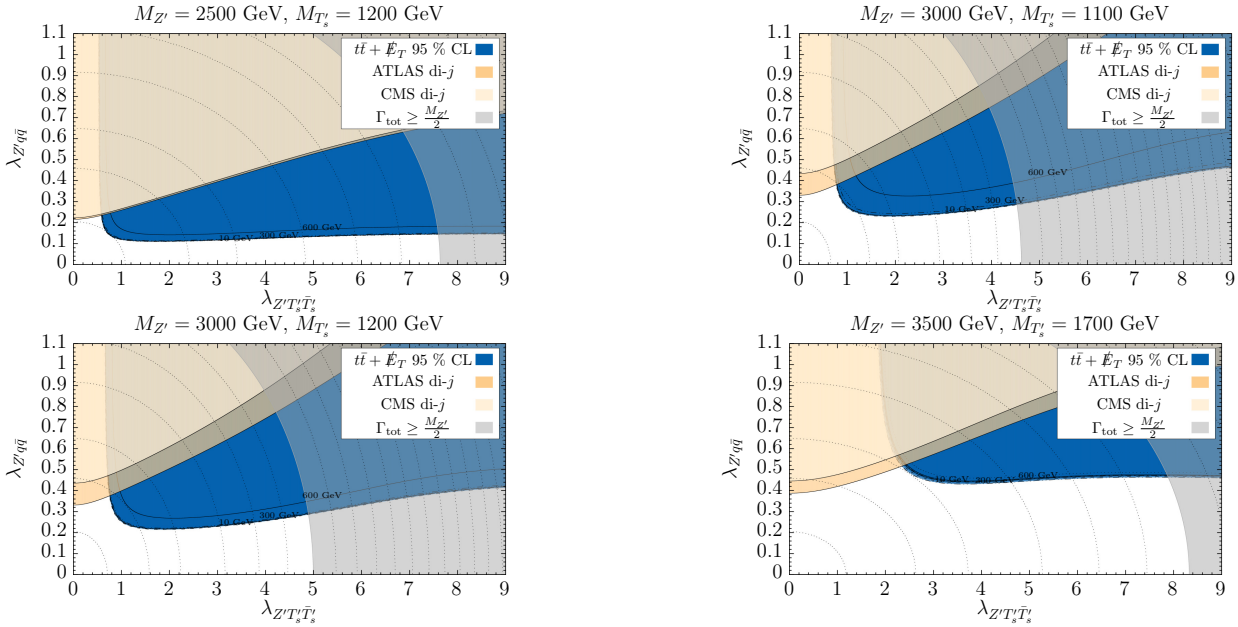

Figure 4.11: Di-jet and di-lepton bounds together with the most constraining $t\bar{t} + \not{E}_T$ bounds coming from `ATLAS_CONF_2016_050` for $\lambda_{Z'\ell^+\ell^-} = 0$. The parameter space below the coloured bands is not excluded and available for study. The labels '10', '300' and '600' on the black lines refer to m_ϕ in GeV for the blue $t\bar{t} + \not{E}_T$ bound.

a large fraction of parameter space with large $\lambda_{Z'T'_s\overline{T'_s}}$, whereas for small $\lambda_{Z'T'_s\overline{T'_s}}$, the di-jet and di-lepton bounds become strong again. In general, the $t\bar{t} + \not{E}_T$ limit abruptly starts and steeply grows before very soon after hitting its maximum. Then, the limit slowly gets weaker with the slope of this decrease depending on the mass gap $\Delta M = M_{Z'} - 2M_{T'_s}$. If ΔM is small, the limit is almost saturated and only slowly decreases with increasing $\lambda_{Z'T'_s\overline{T'_s}}$ (see top left and bottom right panels of figures 4.11 and 4.12). If it gets larger, the limit decreases faster and the overall shape of the exclusion lines gets smoother. While this behaviour for large $\lambda_{Z'T'_s\overline{T'_s}}$ can be reasoned by the fact that $\text{BR}(Z' \to T'_s\overline{T'_s}) \gg \text{BR}(Z' \to q\bar{q})$ and therefore the production of a sufficient amount of T'_s-pairs surviving the experimental cuts is ensured, the fast drop for small $\lambda_{Z'T'_s\overline{T'_s}}$ is due to $\text{BR}(Z' \to T'_s\overline{T'_s}) \lesssim \text{BR}(Z' \to q\bar{q})$ and the subsequent suppression of T'_s-pair production. Lastly, the $t\bar{t} + \not{E}_T$ limits decrease substantially with increasing $M_{Z'}$ and for $M_{Z'} \gtrsim 4$ TeV, the limit becomes weaker than the di-jet and di-lepton limits (not shown here). As long as $M_{Z'} \lesssim 3$ TeV, however, the $t\bar{t} + \not{E}_T$ limits are the strongest in terms of parameter space coverage and yield complementary limits to the di-jet and di-lepton limits.

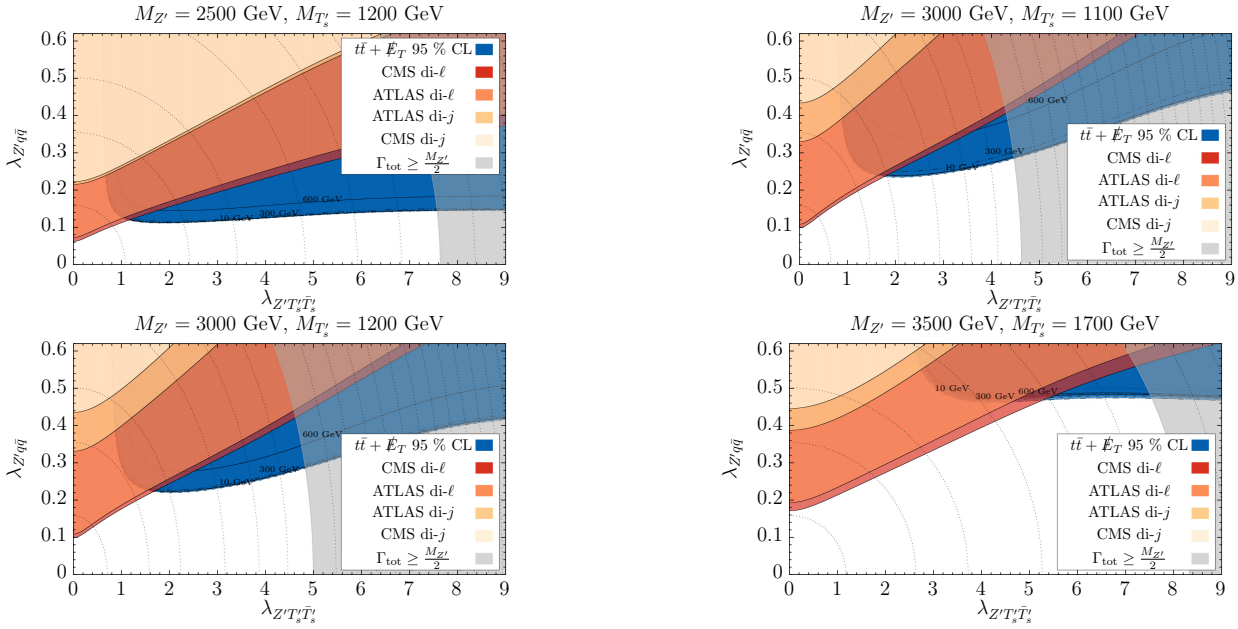

Figure 4.12: Di-jet and di-lepton bounds together with the most constraining $t\bar{t} + \not{E}_T$ bounds coming from `ATLAS_CONF_2016_050` for $\lambda_{Z'\ell^+\ell^-} = \lambda_{Z'q\bar{q}}$. The parameter space below the coloured bands is not excluded and available for study. The labels '10', '300' and '600' on the black lines refer to m_ϕ in GeV for the blue $t\bar{t} + \not{E}_T$ bound.

Overall, the $t\bar{t} + \not{E}_T$ signature therefore is an efficient tool to constrain the parameter space of models with Z' bosons, top partners and DM.

4.3.7 Detailed Benchmark Analysis

Based on the above studies, we now choose a specific benchmark point for further detailed investigation. This benchmark is set in the $\left(\lambda_{Z'T'_s\overline{T'_s}}, \lambda_{Z'q\bar{q}}\right)$ plane and includes all T'_s production processes as shown in figure 4.3. After a quantitative analysis of this benchmark, we will also provide a qualitative discussion for other coupling choices. The benchmark we choose has

$$\lambda_{Z'q\bar{q}} = 0.25\,, \qquad \lambda_{Z'T'_s\overline{T'_s}} = 2.5\,, \qquad \lambda_{Z'\ell^+\ell^-} = \lambda_{Z'q\bar{q}}\,, \tag{4.14}$$

and is chosen such that it covers all interesting states of exclusion depending on the chosen Z' masses. This means being fully excluded, excluded only by our $t\bar{t}+\not{E}_T$ signature and not excluded at all.

An overview of the related cross sections for a variety of Z' and T_s' masses is shown in figure 4.13[8]. Therein, the top three numbers from left to right in each rectangle correspond to the

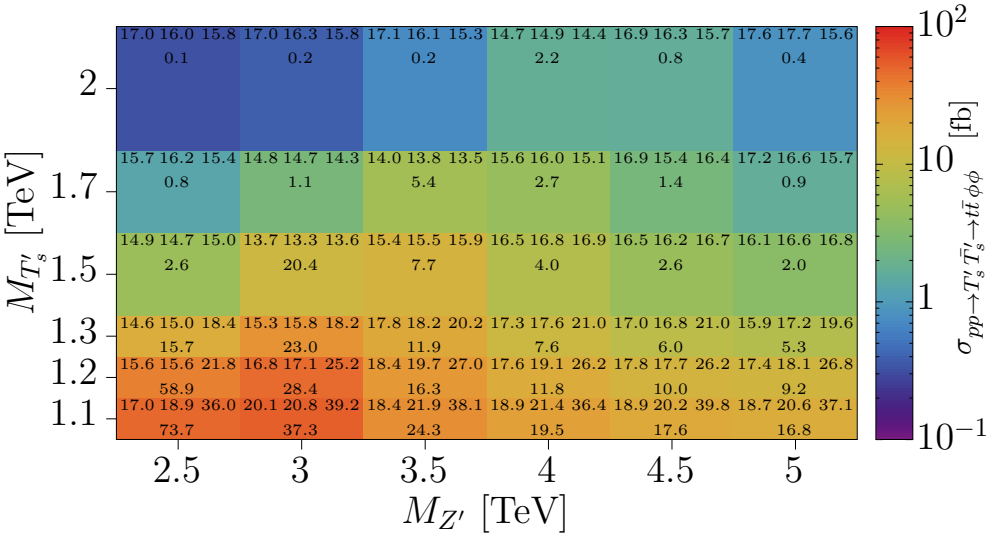

Figure 4.13: Cross sections for $pp \to T_s'\overline{T_s'} \to t\bar{t}\phi\phi$ in fb in dependence of $M_{Z'}$ and $M_{T_s'}$. The top three numbers in each cell show the experimental limit on the cross section in fb for $m_\phi = 10, 300, 600$ GeV from left to right, whereas the central number below marks the theoretical prediction coinciding with the colour-coding. The couplings are chosen as $\lambda_{Z'q\bar{q}} = 0.25 = \lambda_{Z'\ell^+\ell^-}$ and $\lambda_{Z'T_s'\overline{T_s'}} = 2.5$.

experimental limits for $m_\phi = 10$, 300 and 600 GeV respectively, whereas the number in the center corresponds to our signal cross section coinciding with the colour coding. The various exclusion limits can be cross-checked by pinning down the benchmark-couplings in the $\left(\lambda_{Z'T_s'\overline{T_s'}}, \lambda_{Z'q\bar{q}}\right)$ plane from figures 4.11 and 4.12 and then comparing with the numbers from figure 4.13. Exemplarily, the mass pairs $(M_{Z'}, M_{T_s'}) = (2.5, 1.2)$ TeV and $(3, 1.2)$ TeV are strongly excluded, even without the QCD contributions to T_s'-pair production, while $(3.5, 1.7)$ TeV is currently not being probed by neither limit due to its small cross section coming from the large Z' and T_s' masses.

To make the above picture more clear, we show the same data as in figure 4.13 again in figure 4.14, however this time for constant $M_{Z'}$ as well as variable $M_{T_s'}$ and m_ϕ up to 600 GeV. The red curves resemble the signal cross section, whereas the black symbols correspond to the experimental cross section for $m_\phi = 10$, 300 and 600 GeV, respectively.

The advantage of the one-dimensional representation of the cross sections is the ability to spot

[8]For further illustration, details on four extra benchmarks from figure 4.13 are shown in tables A1 and A2.

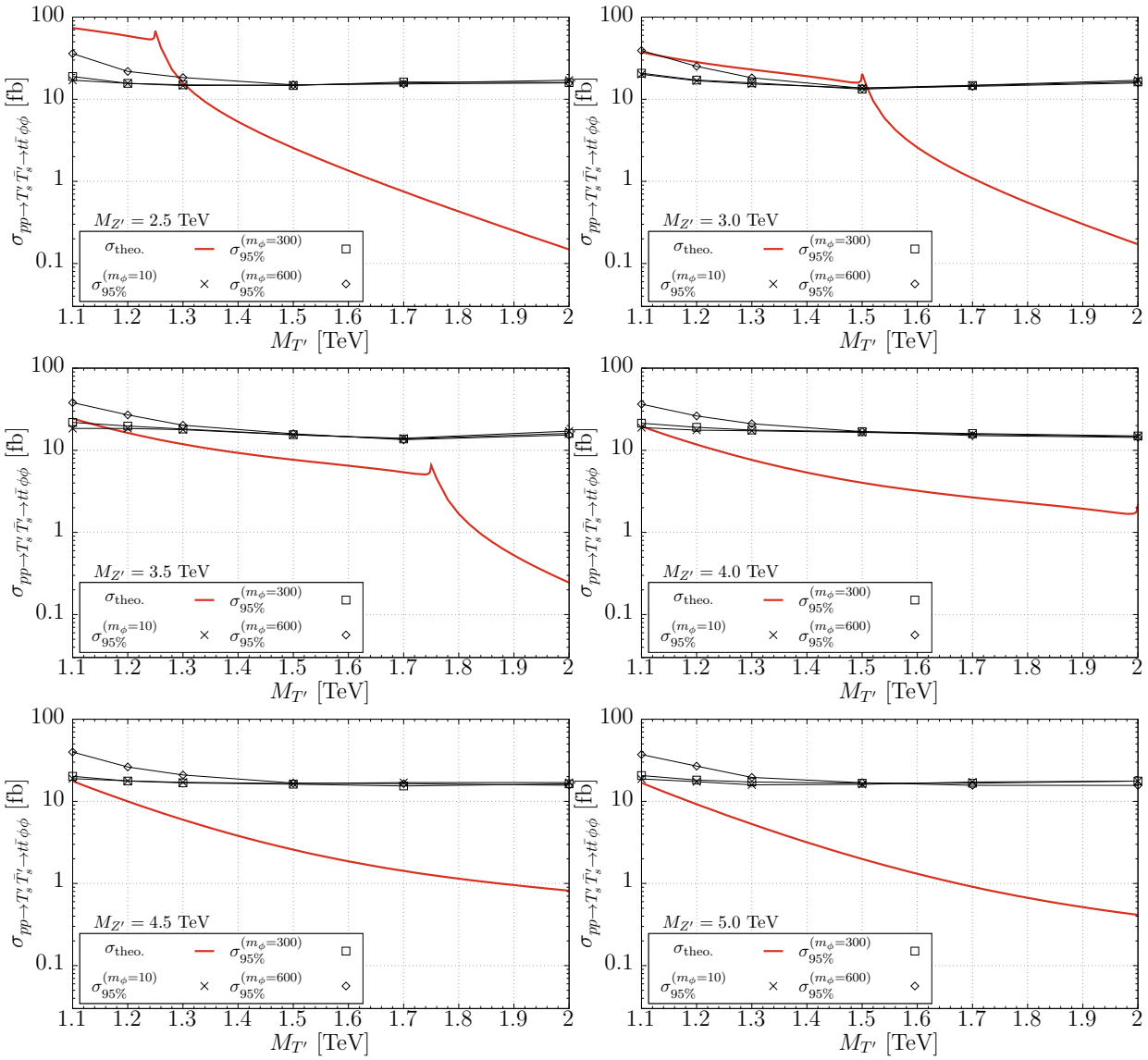

Figure 4.14: Theoretical (red) and experimental (black) cross sections for $pp \to T_s'\overline{T_s'} \to t\bar{t}\,\phi\phi$ in fb in dependence of $M_{T_s'}$ and m_ϕ for our benchmark point (same data as in figure 4.13). m_ϕ is given in GeV and the couplings read $\lambda_{Z'q\bar{q}} = 0.25 = \lambda_{Z'\ell^+\ell^-}$ and $\lambda_{Z'T_s'\overline{T_s'}} = 2.5$.

the signal exclusion easier and more precisely for each $M_{Z'}$. E.g. for $M_{Z'} = 2.5$ TeV, T'_s masses up to 1.3 TeV lead to an exclusion of the signal and hence for the entire regime of on-shell T'-pair production. Increasing $M_{Z'}$ to 3 TeV leads to similar results and the excluded region now starts at $M_{T'_s} \approx 1.51$ TeV — just slightly after off-shell T'_s-pair production starts. Further increasing $M_{Z'}$ to 3.5 TeV changes the exclusion range and now most of the on-shell T'_s-pair production regime (starting from $M_{T'_s} = 1.16$ TeV) remains unexcluded. For even heavier Z', the Z' contributions are too small to yield any new exclusion limit and all signal curves are excluded for $M_{T'_s} = 1.08$ TeV, the limit from pure QCD T'_s-pair production as shown in figure 4.8.

While the analysis performed above is only true in that detail for the particular benchmark coupling choices of equation (4.14), it is nevertheless possible to give qualitative statements for other coupling choices. On the one hand, we can expect the influence of $\lambda_{Z'T'_s\overline{T'_s}}$ to be small, as the di-jet and di-lepton bounds weaken fast for increasing $\lambda_{Z'T'_s\overline{T'_s}}$ and the $t\bar{t} + \not{E}_T$ limit also weakens with increasing $\lambda_{Z'T'_s\overline{T'_s}}$, although not that fast. On the other hand, changing $\lambda_{Z'q\bar{q}}$ only slightly can change the situation significantly, as increasing $\lambda_{Z'q\bar{q}}$ lead to rapidly growing cross sections and hence also a rapid change of the limits.

Apart from the different Z' couplings, we can also estimate the influence of the Z' contributions on the excluded $M_{T'_s}$ range for different $M_{Z'}$. To do so, we can use the fact that we observe positive and negligible interference between the Z' and QCD-induced T'_s-pair production channels (see section 4.3.2) and thus can simply add up the QCD signal cross sections and the Z' signal cross sections. Regarding the former, we see from figure 4.8 that for $M_{T'_s} \gtrsim 1.2$ TeV, the QCD signal contributions make up at most half of the experimental bound. However, when including Z' bosons with masses ≤ 3 TeV, we observe the signal to be excluded (see figure 4.14, top row), therefore indicating that the respective Z' contributions are dominating the signal cross section by far. Additionally, this behaviour would only be reinforced by increasing $\lambda_{Z'q\bar{q}}$. Once $M_{Z'}$ gets heavier, the Z' contributions shrink drastically and for $M_{Z'} \geq 4$ TeV are too small to lift the signal cross section over the experimental bound. This effectively results in a return to the QCD-only exclusion picture from figure 4.8, as if there were no Z' boson at all.

The argument stated above is also true for $M_{T'_s} \gtrsim m_t + m_\phi$ up to $M_{T'_s} \approx m_t + m_\phi + \mathcal{O}(50\text{ GeV})$ (see figure 4.8, left ends of coloured lines), as long as $m_\phi \lesssim 450$ GeV and $M_{Z'} \leq 3$ TeV. For the

remaining $M_{T_s'}$ between $m_t + m_\phi + \mathcal{O}(50\text{ GeV})$ and 1.2 TeV, it is hard to give any qualitative statement, as the signal strongly depends on m_ϕ and a dedicated benchmark analysis as the one we performed earlier needs to be done.

While this concludes the qualitative discussion of possible benchmark scenarios, let us return once more to the benchmark from equation (4.14) and put all our findings in context with the dark matter bounds presented in section 4.2. We do this by providing the exlcuded region of $\frac{M_{T_s'}}{m_\phi}$-m_ϕ parameter space when including the Z' boson in analogy to the green shape from figures 4.1 and 4.2. This is shown together with the relic density in the following figure 4.15 for the case of no Z' at all (same as the green shape in figure 4.1) as well as for a Z' of mass 2.5 TeV (red shape) and 3 TeV (blue shape). The respective DM couplings are $\lambda_{\phi H} = 0$ and $\lambda_{\phi T_s' t} = 1$.

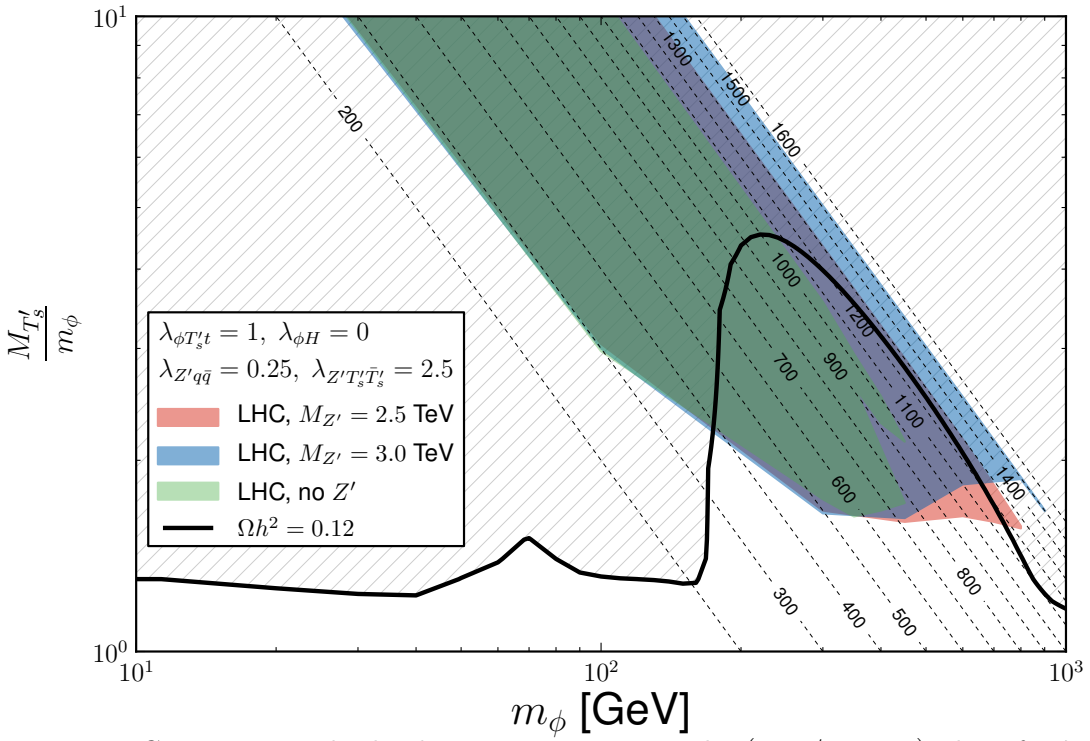

Figure 4.15: LHC, DM DD and relic density constraints in the $(M_{T_s'}/m_\phi, m_\phi)$ plane for $\lambda_{\phi H} = 0$ and $\lambda_{\phi T_s' t} = 1$. The green-shaded area indicates the current LHC exclusion region for the $t\bar{t} + \not{E}_T$ signature coming from the process $pp \to T_s'\overline{T_s'} \to t\bar{t}\,\phi\phi$ mediated by gluons (i.e. without Z' mediation). The red and blue shaded areas show the extended reach of the LHC for $M_{Z'} = 2.5$ and 3 TeV, respectively, with $\lambda_{Z' q\bar{q}} = 0.25 = \lambda_{Z'\ell^+\ell^-}$ and $\lambda_{Z' T_s' \overline{T_s'}} = 2.5$. The grey hatched parameter space above the black contour has too large relic density and the thin dashed lines indicate the iso-levels of $M_{T_s'}$ in GeV.

While the limits without Z' bosons (green) already cover a large fraction of parameter space up to $m_\phi = 450$ GeV, including the Z' contributions extends this range up to DM masses of 800 or 900 GeV for $M_{Z'} = 2.5$ or 3 TeV respectively. This in turn allows us to completely close the gap between LHC and relic density constraints along the m_ϕ axis. Once $M_{Z'} \geq 3.5$ TeV, the Z' contributions are too small to enhance the limits visibly (see paragraph above and figure 4.14, middle and bottom row) and the QCD-only limits become maximal again.

Before concluding the benchmark discussion, we provide four more benchmarks in tables A1 and A2 in appendix C in order to get a better understanding of the kinematics of different $(M_{T'_s}, m_\phi)$ mass pairs. The `CheckMATE` cutflow in the lower part of the tables shows the fraction of events surviving the respective cut (normalised to 1), while the last row in the cutflow section (bold) corresponds to the overall efficiency. The impact of the Z' can then be estimated by comparing the efficiencies between benchmarks. Supplementary, we also present in table A1 the cutflow efficicency for the BP2-RR benchmark, which is analogue to the BP2 benchmark, but with the RR Z' chiral coupling combination. It turns out that the overall efficiencies for BP2 (LL) and BP2-RR differ only by about 2 %, which confirms our initial claim from section 4.3.1 about the independence of the kinematics from the chiral coupling choices. Also, the overall efficiency when including a Z' (see table A1) is about 10 – 15 % larger compared to the case of pure QCD T'_s-pair production (see table A2) and thus non-negligible. One reason for this increase in efficiency is the larger rapidity increase of a $T'_s\overline{T'_s}$-pair coming from a Z' originating from $q\bar{q}$-fusion as compared to QCD-produced $T'_s\overline{T'_s}$-pairs. Furthermore, the $\not{E}_T$ distribution is harder when Z' bosons are present and gets harder the heavier the Z' gets. Lastly, top partners coming from Z' decays will be more boosted, resulting in more energetic but less isolated final state leptons.

4.4 Conclusions

In this chapter, we explored the phenomenology of a simplified, effective model comprising a vector resonance Z', a fermionic vector-like coloured partner of the top quark T' and a scalar DM candidate ϕ. We refer to the model as ZP-TP-DM model[9] and its particle content appears in a

[9] Publicly available implementations of the model are available at HEPMDB [169] under hepmdb:0717.0253 [170] (`CalcHEP`) and hepmdb:0717.0253 [171] (`MadGraph`).

variety of models, including Composite Higgs models (if they provide a candidate for DM).

In particular, we studied the process $pp \to Z' \to T'\overline{T'} \to t\bar{t}\,\phi\phi$ at the LHC, which to the best of our knowledge has not been studied previously. The expected final states resemble SUSY stop-pair production final states and we recasted existing ATLAS and CMS searches implemented in `CheckMATE` to determine the level of coverage or exclusion of the ZP-TP-DM model. As it turned out, the predicted $t\bar{t} + \not{E}_T$ signature via Z' bosons provides important and complementary results to those without Z' bosons (i.e. for pure QCD T'-pair production).

Another key difference between QCD and Z'-induced $T'\overline{T'}$-pair production are the underlying kinematics. In case of Z' mediation, more $\not{E}_T$ as well as larger p_T for any final state leptons can be observed, especially for heavier Z' bosons. The final state leptons also show a larger rapidity as compared to the QCD-induced final states. While larger lepton p_T and $\not{E}_T$ increase the detector efficiency at colliders, the larger lepton rapidity decreases it. Overall, however, we observe an increase in efficiency of about 10 % when including the Z'. These efficiencies are approximately identical for all possible chiral coupling choices, since we were able to show that they only marginally affect the kinematical distributions. Lastly, the interference between the QCD and Z'-induced final states is essentially independent of the Z' width and constructive, but also negligible at a level of just +3 %.

We have found that the presence of the Z' can provide an additional and even dominant contribution (about one order of magnitude larger than the QCD one) to the $t\bar{t}\,\phi\phi$ signature without conflicting with existing bounds from Z' searches in di-jet and di-lepton final states. We further showed that the $t\bar{t} + \not{E}_T$ signature at the LHC acts complementary to non-collider searches in setting limits on the ZP-TP-DM parameter space, thus making it a highly valuable tool for its further investigation. Moreover, the $t\bar{t} + \not{E}_T$ signature allows to probe all new masses of the model ($M_{Z'}$, $M_{T'}$, m_ϕ) well beyond the reach of QCD-induced $T'\overline{T'}$-pair production alone without conflicting with existing Z' searches from di-jet and di-lepton bounds. Exemplarily, a 3 TeV Z' allows to access DM masses up to 900 GeV and T' masses up to about 1.5 TeV at the LHC (see figure 4.15) — a quite remarkable increase by a factor of 2 for both masses as compared to QCD production alone. Due to these largely improved reaches, Z'-mediated top partner-pair production may play an important role in future phenomenological studies and experimental searches.

As an outlook, there is another interesting fraction of model parameter space worth studying in the future, characterised by $M_{T'} - m_\phi < m_t$. This corresponds to the case of off-shell decaying top quarks and exhibits highly different kinematics than the process we studied in this chapter. However, it is worth stressing that such a scenario can in principle be studied analogously to the SUSY scenario with degenerate stops and neutralinos.

5 | Precision Tests of Higgs Properties via VBF at Future Colliders

5.1 Introduction

In the last Chapter 4, we saw that BSM theories may very well explain a variety of issues of the SM while simultaneously providing a 125 GeV Higgs boson with a completely different nature as compared to e.g. SUSY or the SM itself. This is possible, since some of the Higgs properties have not been measured with great accuracy yet and therefore allow for a variety of different interpretations, as we have seen. Narrowing down these properties (and thus the nature) of the Higgs boson is the task of experiments, such as those performed at colliders like the LHC, and it will be the aim of this chapter to explore the potential of the LHC and possible future colliders to narrow down the properties of the Higgs boson.

One way to further specify the Higgs boson affiliation is to simply increase the collision energy of the particles colliding. This happened exemplarily in June 2015 at the LHC, where the collision energy was increased almost by a factor of two from $\sqrt{s} = 8$ TeV to $\sqrt{s} = 13$ TeV. While this increase already is anything but small, even higher energies might be necessary for various high precision measurements, such as the ones to distinctly identify the Higgs boson. For this purpose, future circular colliders (FCC) with collision energies up to 33 TeV (*High Energy Large Hadron Collider*, HE-LHC) or 100 TeV (*Very High Energy Large Hadron Collider*, VHE-LHC) are being planned [196]. Although these colliders do not exist yet, a variety of prospects and predictions for a large number of theories have been made already — including Higgs physics and supersymmetry

(see e.g. [197–202]).

In this chapter, we work with an effective field theory (EFT) based on a non-linear σ model (NLσM), where the Higgs boson arises as a field expansion in the EFT. As a consequence, the Higgs couplings to itself and the gauge bosons differ from the SM couplings by a multiplicative factor and can therefore take non-SM values. In that case, it is highly likely that the cross sections for various processes increase by a substantial amount due to the lack of unitarity cancellations at high energies. We study this potential increase in cross section based on the (non-SM) Higgs couplings for several final states containing Higgs and gauge bosons at the LHC, HE-LHC and VHE-LHC (i.e. for 13, 33 and 100 TeV respectively). After confirming that triple Higgs production benefits most from anomalous Higgs couplings (as was shown previously in Ref. [203] for 14 and 33 TeV), we perform a detailed analysis on the degree and onset of unitarity violation in the case when the three Higgs bosons arise via vector boson fusion. This together with a dedicated background analysis shows that only a 100 TeV FCC is sensible to triple Higgs production, however on the other hand with an accuracy ranging down to the permille level, provided the luminosity is large enough.

In section 5.2 of this chapter, we introduce the non-linear σ model and estimate the respective unitarity bounds. In section 5.3, we present the influence of anomalous Higgs couplings on various processes, before performing a more detailed study on triple Higgs production with a focus on unitarity violation. After further computing the expected signal strengths for triple Higgs production in dependence of the anomalous Higgs couplings and collision energies, we estimate the respective background for this signal in section 5.4. Eventually, we draw our conclusions in section 5.5.

5.2 Unitarity and the Non-linear σ Model

One of the most important quantities to describe scattering processes in particle physics are cross sections. While scattering processes with larger cross sections are more likely to occur, cross sections cannot grow arbitrarily large, but are limited by unitarity as an upper bound. For a $2 \to n$ particle scattering with collision energy s, the unitarity bound reads [204, 205] (see Appendix D

for a brief derivation)

$$\sigma(2 \to n) < \frac{4\pi}{s} \,. \tag{5.1}$$

On the other hand, the most general cross section for a $2 \to n$ scattering is proportional to

$$\sigma(2 \to n) \sim \frac{1}{s} \, |\mathcal{A}|^2(s) \, s^{n-2} \tag{5.2}$$

with $\frac{1}{s}$ being the flux factor, $|\mathcal{A}|^2(s)$ being the squared scattering amplitude and s^{n-2} giving the energy dependence of the phase space integral [204, 206]

$$R_n(s) = \int \prod_{i=1}^{n} \frac{\mathrm{d}^3 p_i}{(2\pi)^3 \, (2E_i)^3} \, (2\pi)^4 \, \delta^4 \left(\sqrt{s} - \sum_{i=1}^{n} p_i \right) = \frac{(2\pi)^{4-3n} (\frac{\pi}{2})^{n-1}}{(n-1)! \, (n-2)!} \, s^{n-2} \tag{5.3}$$

for massless particles in four dimensions. By comparing equation (5.2) and (5.1), we find that the scaling of the scattering amplitude $\mathcal{A}$ with respect to s has to fulfil

$$\mathcal{A}(2 \to n) \sim s^{1-\frac{n}{2}} \tag{5.4}$$

to not violate unitarity.

The above considerations are model-independent[1], hence allowing us to compute easily whether a scattering process violates unitarity. Consider now the Lagrangian of a non-linear σ model (NLσM), which in terms of the Callan–Coleman–Wess–Zumino (CCWZ) [207, 208] formalism is given by

$$\mathcal{L}_{\mathrm{NL}\sigma\mathrm{M}} = \frac{v^2}{4} \, \mathrm{Tr} \left[\partial_\mu U \partial^\mu U^\dagger \right] \,, \tag{5.5}$$

with $v = 246$ GeV the scale of electroweak symmetry breaking and

$$U = \mathrm{e}^{\frac{\mathrm{i}\vec{\tau} \cdot \vec{\pi}}{v}} \,. \tag{5.6}$$

with massless Goldstone bosons $\vec{\pi}$ of the (Higgs-less) theory. Via the equivalence theorem [209–214], these can be identified as the longitudinal vector bosons in the high energy limit. With naïve

[1] It is worth noting that equation (5.4) is in fact true for the SM, if it contains a Higgs boson, however not generic for other models.

power counting, the growth of scattering amplitudes in the NLσM can be estimated to be linear in s,

$$\mathcal{A}_{\mathrm{NL}\sigma\mathrm{M}}(2 \to n) \sim \frac{s}{v^n}\,. \tag{5.7}$$

As a result, any cross section in the NLσM can grow arbitrarily large and eventually will violate unitarity. The scaling of cross sections with the energy s thereby occurs much faster, the more particles n are produced, as can be seen from equation (5.4). While a $2 \to 2$ scattering requires a constant scattering amplitude, it grows as $\frac{1}{s}$ for a $2 \to 4$ scattering. Since the NLσM always grows as s, the cross sections will scale faster with s the more particles are produced. This rapid grow in cross section can be utilised to study the beginning of new physics with respect to the energy scale and is explained in detail below.

To recover unitarity, the NLσM must be completed in the ultraviolet (UV) region. In the simplest case, this can be achieved by the addition of a scalar field to the model. If this scalar then is identified as the Higgs boson with SM couplings, the newly arising Feynman diagrams cause large cancellations between amplitudes and therefore fully restore unitarity. In case the scalar does not exhibit exactly SM-like couplings, e.g. when it arises in a theory as a composite particle of a strongly coupled sector, the cancellations between amplitudes are not complete and unitarity is only partially restored. The NLσM together with such a Higgs boson can be described by an EFT, where we expand around the Higgs field. The respective Lagrangian then reads [215]

$$\begin{aligned}\mathcal{L}_{\text{eff}} = \frac{v^2}{4}\left(1 + 2a\frac{h}{v} + b\frac{h^2}{v^2} + b_3\frac{h^3}{v^3} + \cdots\right)\mathrm{Tr}\left[\partial_\mu U \partial^\mu U^\dagger\right] \\ + \frac{1}{2}(\partial_\mu h)^2 - \frac{1}{2}m_h^2 h^2 - d_3\lambda v h^3 - d_4\frac{\lambda}{4}h^4 + \cdots\,,\end{aligned} \tag{5.8}$$

where a, b, b_3, d_3 and d_4 are dimensionless parameters changing the overall coupling strength of a certain term. From this Lagrangian, the UV-complete SM can be restored by setting $a = b = d_3 = d_4 = 1$ and $b_3 = 0$ as well as redefining the Higgs field. For other values of the a, b and d parameters, the aforementioned cancellations cannot entirely be accounted for by the Higgs field and unitarity will be violated again. Since this violation of unitarity is linked to some energy scale Λ, we can infer that our EFT approach is valid only up to this scale Λ — or in other words, the EFT is valid up to the beginning of unitarity violation. This can be used as an indication for

the presence of new physics, since at or close to Λ, the effects of the 'true' theory (which the EFT approximates in the low energy limit) start to become visible, e.g. in form of some resonance unitarising the scattering amplitudes.

Before performing collider phenomenology with the above introduced model to explore the beginning of new physics, one needs to be aware that the Lagrangian (5.8) contains only longitudinally polarised gauge bosons. These are experimentally hard to separate from the transversely polarised gauge bosons and thus it is important to understand how the large longitudinal contributions can influence the full, unpolarised cross section of real vector boson scattering. This has previously been studied in Ref. [203] for a variety of final states containing Higgs and gauge bosons and we will revisit and extend their research also for possible future 100 TeV colliders in the following section. To achieve comparability and for reasons of simplicity, we choose $b = d_3 = d_4 = 1$ and $b_3 = 0$, but leave a as a free parameter. This corresponds to the SM with a modified coupling between one Higgs and two gauge bosons.

5.3 Results

5.3.1 Cross Sections for Multiple Higgs and Vector Boson Production with Two Jets

With several final states consisting of Higgs and gauge bosons benefitting from anomalous Higgs couplings, it is important to study which one benefits most of it and therefore limit the later LHC phenomenology to the dominant final state. In particular, we study the process $pp \to jj + X$ with X being W^+W^-, W^+W^-h, hh or hhh. We compute the cross sections for the SM case ($a = 1$) as well as a non-SM case with $a = 0.9$. Furthermore, we compute these cross sections with and without applied vector boson fusion (VBF) cuts, which are designed to increase the gauge or Higgs boson signal and are defined in table 5.1 below. In particular, we expect the vector bosons to be radiated off by high energetic quarks (one from each proton). Due to the high energy of the quarks (reflected in E_j), they will be nearly unscattered and continue their way back to back (reflected in large $\Delta\eta$) and close to the particle beam. From the technical side, we compute any cross sections using `Madgraph5_aMCNLO 2.2.3` [109] together with the parton density function (PDF)

Parameter	without VBF cuts	with VBF cuts
E_j [GeV]	≥ 0	≥ 1500
$\Delta\eta$	≥ 0	≥ 5

Table 5.1: Vector boson fusion (VBF) cuts.

`CTEQ611` [216] and the QCD scale set equal to M_Z. Besides the VBF cuts, we also define a set of acceptance cuts in order to avoid soft and collinear jets. These include a minimum transverse momentum of the jets, $p_{\mathrm{T}}^j \geq 50$ GeV and a minimum distance between two jets, $\Delta R(j,j) \geq 0.4$.

Finally, in table 5.2 we show the cross sections for $pp \to jj + X$ with X defined as above for the center of mass (CM) energies $\sqrt{s} = 13$, 33 and 100 TeV.

Process	VBF cuts	13 TeV		33 TeV		100 TeV	
		$a = 1.0$	$a = 0.9$	$a = 1.0$	$a = 0.9$	$a = 1.0$	$a = 0.9$
$pp \to jjW^+W^-$	×	9.88	9.88	60.56	60.48	352.14	352.49
	✓	$1.29 \cdot 10^{-2}$	$1.27 \cdot 10^{-2}$	0.48	0.47	5.49	5.47
$pp \to jjW^+W^-h$	×	$1.71 \cdot 10^{-3}$	$1.43 \cdot 10^{-3}$	$1.63 \cdot 10^{-2}$	$1.53 \cdot 10^{-3}$	0.69	0.60
	✓	$1.26 \cdot 10^{-5}$	$1.35 \cdot 10^{-5}$	$9.30 \cdot 10^{-4}$	$1.05 \cdot 10^{-3}$	0.15	0.19
$pp \to jjhh$	×	$5.11 \cdot 10^{-4}$	$3.64 \cdot 10^{-4}$	$3.49 \cdot 10^{-3}$	$2.93 \cdot 10^{-3}$	$1.70 \cdot 10^{-2}$	$1.92 \cdot 10^{-2}$
	✓	$2.13 \cdot 10^{-5}$	$1.32 \cdot 10^{-5}$	$7.65 \cdot 10^{-4}$	$7.69 \cdot 10^{-4}$	$5.56 \cdot 10^{-3}$	$9.20 \cdot 10^{-3}$
$pp \to jjhhh$	×	$2.38 \cdot 10^{-7}$	$2.50 \cdot 10^{-5}$	$1.97 \cdot 10^{-6}$	$1.37 \cdot 10^{-3}$	$1.23 \cdot 10^{-5}$	$4.60 \cdot 10^{-2}$
	✓	$6.14 \cdot 10^{-9}$	$2.06 \cdot 10^{-6}$	$4.39 \cdot 10^{-7}$	$7.48 \cdot 10^{-4}$	$4.70 \cdot 10^{-6}$	$4.10 \cdot 10^{-2}$

Table 5.2: Cross sections in pb for different Higgs and vector boson final states with variable a, $\sqrt{s}$ and VBF cuts.

As expected, all cross sections grow with the collision energy $\sqrt{s}$, independently of a or VBF cuts. In case of SM-like couplings ($a = 1$), an increase in cross section of two to three orders of magnitude is visible when going from 13 to 100 TeV. The same is true with applied VBF cuts, although their impact can be quite different for different final states. As such, the cross sections for processes involving $W^\pm$ pairs decrease by two to three orders of magnitude when VBF cuts are applied, whereas final states containing only Higgs bosons only decrease by a factor of about 30 (3) for 13 (100) TeV. This can be explained by the fact that the pure Higgs final states are produced dominantly via VBF, whereas final states involving W bosons can be produced by a larger variety of processes, e.g. via Higgs radiation from charm quark jets.

When leaving the SM and considering the case of $a = 0.9$, we note that triple Higgs production

clearly benefits most from this change. This is on the one hand due to the tri-Higgs signature being created dominantly via VBF and hence the VBF cuts do not remove much of the signature (VBF cuts decrease the $a = 0.9$ cross sections by factors of 12, 1.8 and 1.1 for 13, 33 and 100 TeV respectively), and on the other hand due to the impressive gain in cross section when increasing $\sqrt{s}$. While at 13 TeV, the change from $a = 1$ to $a = 0.9$ results in a cross section after VBF cuts about 400 times larger, the cross section at 100 TeV increased by almost a factor of 10^4. This is quite remarkable and it is worth noting that none of the other processes exhibits a similar effect. In fact, all other processes gain or lose only negligible contributions as compared to their SM cross sections. The reason for triple Higgs production standing out is the low transversal 'pollution' of the signal, whereas for the other final states, transversal contributions to the cross section dominate over the longitudinal contributions [203]. E.g. for W^+W^- production, there are only a few Feynman diagrams involving a coupling of two $W^\pm$ bosons to a longitudinal $W^\pm$ boson and therefore the cross section stays nearly constant when moving from $a = 1$ to $a = 0.9$.

In summary, triple Higgs production benefits by far the most from an anomalous Higgs coupling a and therefore offers great potential to further explore the characteristics of the Higgs boson such as its couplings to other gauge bosons (or itself) using an EFT framework. The large increase in cross section for non-SM-like couplings a could result in unitarity violations, which could be used as an indication for the beginning of new physics near the cut-off scale Λ of the considered EFT (see section 5.2).

While triple Higgs production seems to be the channel to consider for further studying the Higgs properties, it should not be forgotten, however, that the cross sections for triple Higgs production are very small as compared to the other final states and reach only a few fb, even at large collision energies. Therefore, it is of high importance to investigate the possible background for triple Higgs production and estimate the respective signal-to-background ratio. Before doing so in section 5.4, we first examine the impact and influence of different anomalous Higgs couplings a and collision energies $\sqrt{s}$ on the unitarity bounds for triple Higgs production alone in the following sections 5.3.2 and 5.3.3.

5.3.2 Unitarity Violation for Triple Higgs Production with Anomalous Higgs Couplings

The final state with two jets and three Higgs bosons is mainly produced by VBF as shown in the schematic diagram in figure 5.1. While this is the final state produced at colliders, it is nevertheless worth to also study only the VBF part of this process, i.e. $VV \to hhh$ with $V = Z, W^{\pm}$. Here,

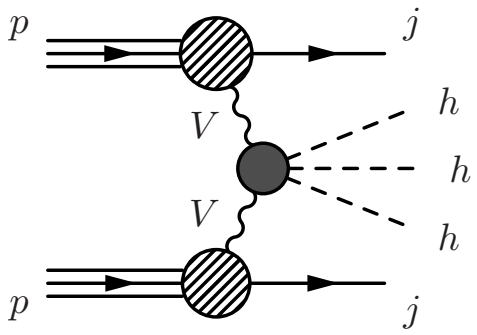

Figure 5.1: Schematic diagram for triple Higgs production with two jets via proton-proton scattering. The grey blob in the centre represents the vector boson fusion of two vector-bosons $V = Z, W^{\pm}$ to three Higgs bosons h while the hatched blobs correspond to various the parton-vector boson interactions.

the invariant mass of the three Higgs bosons, M_{hhh}, equals the VBF (denoted by a hat $\hat{}$) center-of-mass (CM) energy $\sqrt{\hat{s}_{\mathrm{VBF}}}$,

$$M_{hhh} = \sqrt{\hat{s}_{\mathrm{VBF}}}\,, \tag{5.9}$$

which poses a powerful identity for two reasons. First, it allows us to compute the unitarity bound at VBF level with high accuracy by plugging in the cross section $\sigma(VV \to hhh)$ into equation (5.1) and rearranging for $\sqrt{\hat{s}_{\mathrm{VBF}}}$, which is the minimum collision energy for which unitarity is violated. Second, equation (5.9) connects the VV and qq scatterings. Since the computed M_{hhh} at hadron level will not be a narrow peak, but a distribution easily ranging over several TeV, it is likely that parts of this distribution exceed the bound for unitarity violation. This happening is equivalent to the presence of new physics, in this case some resonance unitarising the scattering amplitudes.

Before performing this analysis at qq level, let us come back to VV level to first determine the lower limit of unitarity violation in terms of $\sqrt{\hat{s}_{\mathrm{VBF}}}$ as a function of a. To do so, we computed the cross sections for $VV \to hhh$ for various a using `CalcHEP 3.6.23` [168]. Together with the

unitarity bound from equation (5.1), this is shown in figure 5.2 below.

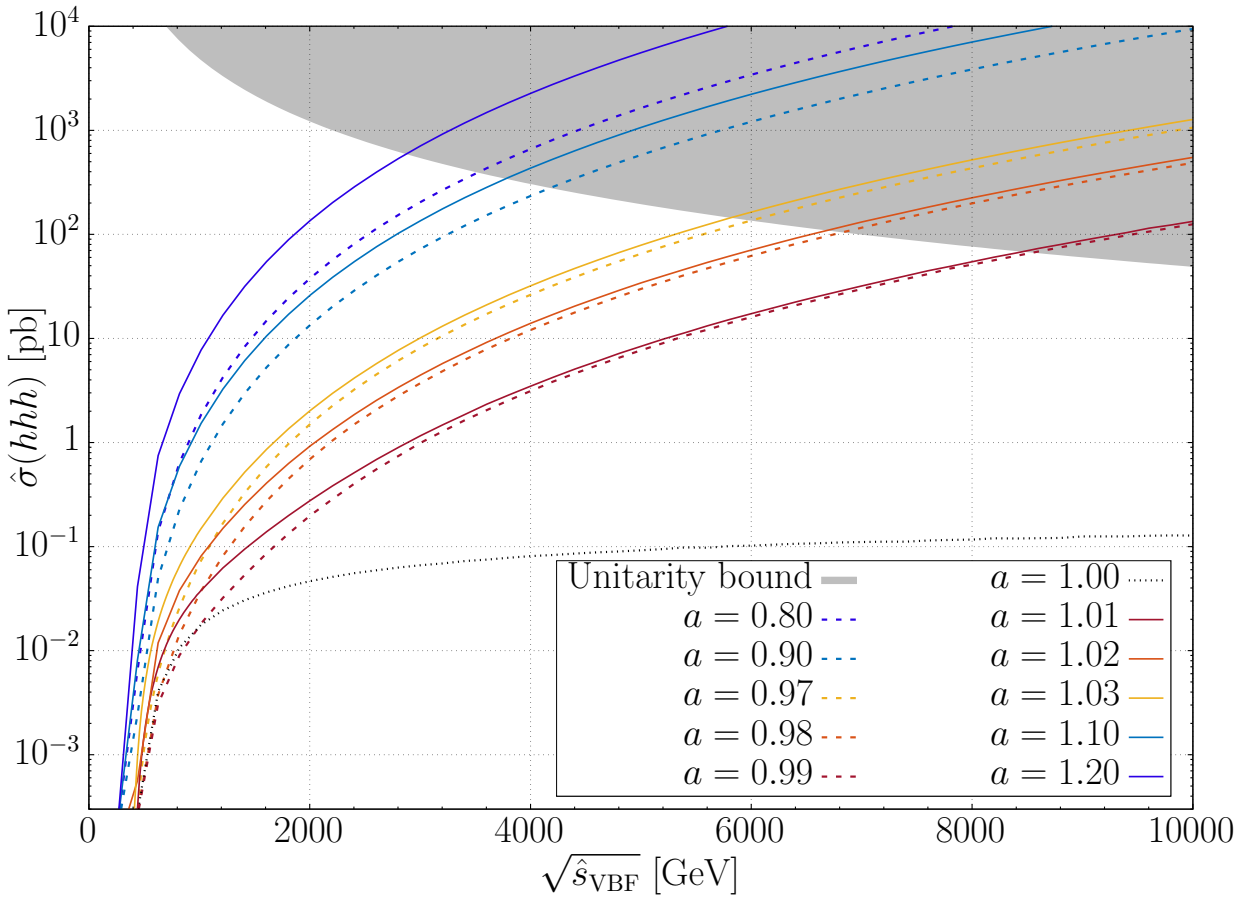

Figure 5.2: Cross sections $\hat{\sigma}$ in pb for vector boson scattering into three Higgs, $VV \to hhh$ with $V = Z, W^{\pm}$, for different values of a. The grey area marks the region of unitarity violation.

Solid coloured lines correspond to values of $a > 1$, whereas the coloured dashed lines correspond to $a < 1$. The SM case, $a = 1$ is shown as a black dotted line and the region of unitarity violation appears as a grey shape in the top right corner. For a non-SM coupling a just 1 % different to its SM value ($a = 0.99$ and $a = 1.01$), unitarity violation starts at about $\sqrt{\hat{s}_{\mathrm{VBF}}} = 8.4$ TeV. When increasing the difference in coupling to 20 % ($a = 0.8$ and $a = 1.2$), unitarity violation starts earlier at about $\sqrt{\hat{s}_{\mathrm{VBF}}} = 3.5$ and 2.8 TeV respectively. Lastly, for SM couplings ($a = 1$), unitarity is not violated, as the Higgs boson enables an exact cancellation between scattering amplitudes. This is also reflected in the overall size of cross section, as the SM cross section lies several orders

of magnitude below the cross sections for non-SM-like couplings, as explained earlier.

5.3.3 Triple Higgs Production in the SM with Anomalous Higgs Couplings

After focussing on the VBF part from figure 5.1 in the last section, we will now investigate the full process including the two hard jets. We first estimate the influence of a and $\sqrt{s}$ on the full cross section $\sigma(pp \to jjhhh)$ computed with `MadGraph` in figure 5.3, before continuing to study the unitarity violations in this scenario, visible in the M_{hhh} distributions.

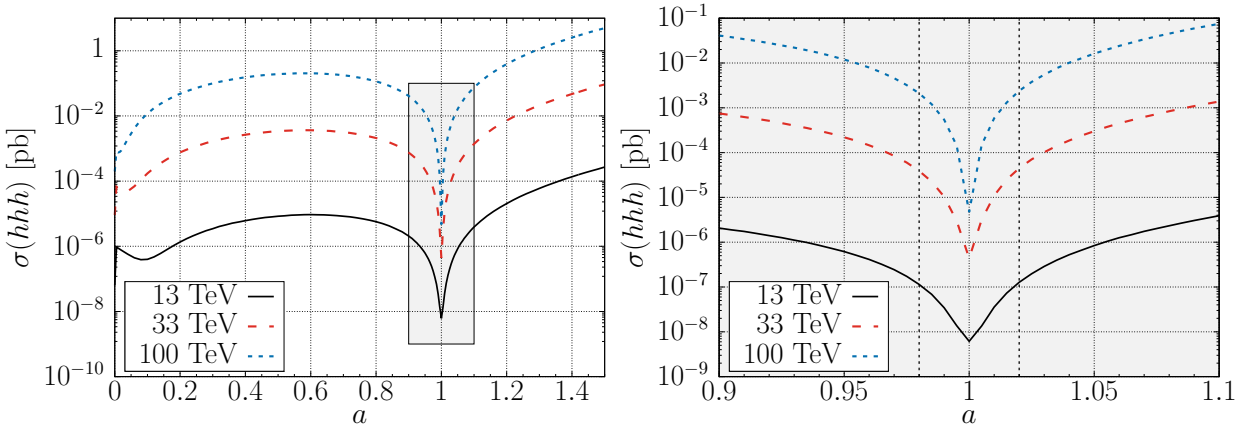

Figure 5.3: Cross sections σ in pb for $pp \to jjhhh$ with VBF cuts for $\sqrt{s} = 13$, 33, 100 TeV in dependance of a. The right panel corresponds to the grey highlighted segment with $a \in [0.9, 1.1]$ from the left panel. The vertical dotted thick black lines at $a = 0.98$ and $a = 1.02$ correspond to the 100 TeV sensitivity based on figure 5.7.

For the SM case ($a = 1$), the cross section is extremely small and ranges from 10^{-8} pb over to 10^{-6} and 10^{-5} pb for $\sqrt{s} = 13$, 33 and 100 TeV respectively. If a is just slightly different than 1, however, the cross sections grow approximately quadratically in a for $|a - 1| \lesssim 0.1$. E.g. for $a = 0.98$, the 13 TeV cross section increased by more than one order of magnitude compared to the SM one, and by more than two and three orders of magnitude for 33 and 100 TeV respectively. While moving a even further away from the SM, the increase in cross section eventually starts to peak for $a \approx 0.6$ before then decreasing again. For large $a > 1$, the cross sections just keep growing since they scale with powers of a and the multiplicative nature of a becomes dominant. However, too large deviations from the SM are already excluded experimentally and we therefore limit ourselves to changes not bigger than 20 %, i.e. for values of $a \in [0.8, 1.2]$.

To better visualise the increase in cross section compared to the SM, we show the ratio $R(\sqrt{s}, a) = \frac{\sigma^{pp\to jjhhh}(a)}{\sigma^{pp\to jjhhh}(a=1)}$ in the following figure 5.4.

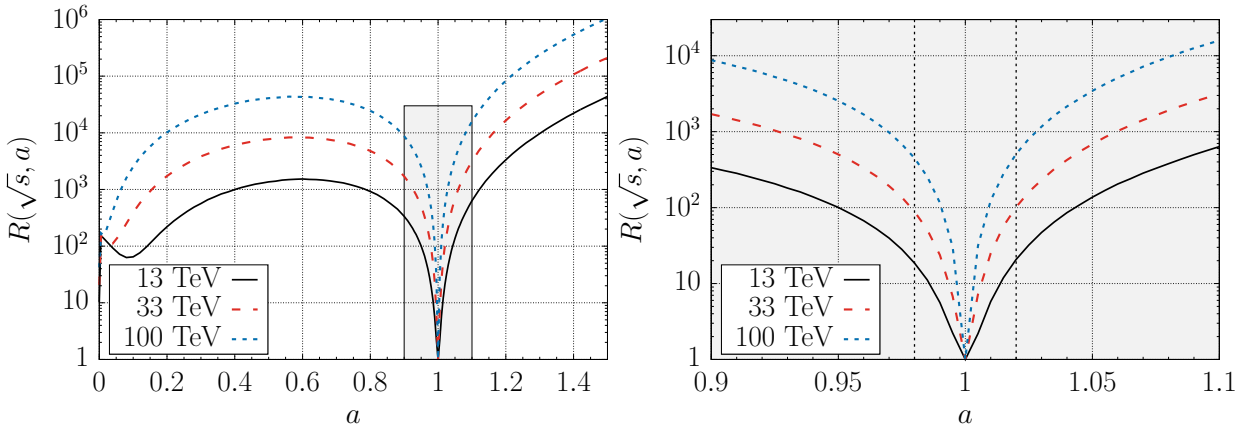

Figure 5.4: Ratio $R(\sqrt{s}, a) = \frac{\sigma^{pp\to jjhhh}(a)}{\sigma^{pp\to jjhhh}(a=1)}$ for $pp \to jjhhh$ with the data of figure 5.3. $R(\sqrt{s}, a) = 1 = R(\sqrt{s}, 1)$ corresponds to the SM cross sections. The right panel corresponds to the grey highlighted segment with $a \in [0.9, 1.1]$ from the left panel. The vertical dotted thick black lines at $a = 0.98$ and $a = 1.02$ correspond to the 100 TeV sensitivity based on figure 5.7.

It becomes apparent that the dominant increase in cross section happens for small changes of $a \in [0.9, 1.1]$, as can be seen in detail in the right panel. Regarding the collision energy $\sqrt{s}$, it also becomes obvious that larger energies lead to much larger cross sections. For a 1 % change of the SM coupling, we already see an increase by about 1, 1.5 and 2.5 orders of magnitude for 13, 33 and 100 TeV respectively and especially for 100 TeV, cross sections can grow by one order of magnitude for couplings deviating from the SM one by less than 0.5 %.

This large gain in cross section does not come without a price, however, and with larger a and large $\sqrt{s}$, we also expect large amounts of unitarity violation due to the increasingly worse Higgs cancellations in VBF processes. This is not necessarily bad, however, as the loss of unitarity is equivalent to the (slow) breakdown of the underlying EFT and it is now our goal to investigate this impact of unitarity loss on our signal. Therefore, we remind ourselves of the connection made in equation (5.9) and that we already know the energies for which unitarity is violated with respect to a. What remains now is to compute the full hadronic invariant mass of the three Higgs bosons, M_{hhh} and apply the unitarity bounds. To do so, we computed the full cross section for

$pp \to jjhhh$ using `MadGraph` and subsequently used `ROOT 5.34.25` [217] to calculate M_{hhh}. This is shown for $a = 0.9$ and $a = 0.99$ together with the unitarity violating region in grey in figures 5.5 and 5.6 respectively.

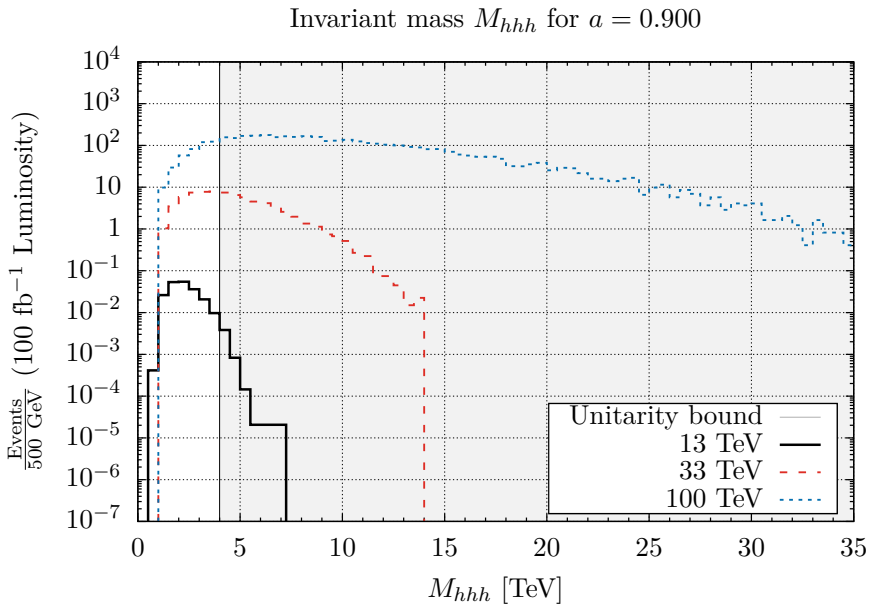

Figure 5.5: Invariant mass M_{hhh} for $pp \to jjhhh$ with $a = 0.9$ at $\sqrt{s} = 13, 33, 100$ TeV, respectively. The grey shaded area marks the region of unitarity violation.

At first glance, the distributions for M_{hhh} do not depend much on a and peak both at about 1.8 TeV for $\sqrt{s} = 13$ TeV, 3.5 TeV for $\sqrt{s} = 33$ TeV and 7 TeV for $\sqrt{s} = 100$ TeV. A more obvious difference between $= 0.9$ and $a = 0.99$ lies in the number of observable events. The closer a approaches 1, the less observable events are predicted. Another difference between the distributions is that they smear out with increasing $\sqrt{s}$ and their tail gets longer and flatter for very large M_{hhh}, which indicates the non-unitary behaviour of the scattering amplitudes as M_{hhh} increases. Apart from this, values of a closer to 1 result in larger unitarity bounds. For $a = 0.9$, the unitarity bound starts at $M_{hhh} \approx 4$ TeV, whereas for $a = 0.99$, it starts at about 8 TeV. This has severe consequences, as for $a = 0.9$, even the 13 TeV distribution violates unitarity by a non-negligible amount and for 33 and 100 TeV, the majority of events lie in the region of unitarity violation. For $a = 0.99$, on the other hand, unitarity is restored completely for the 13 TeV distribution, therefore indicating that the EFT is valid in this region. For 33 TeV, the

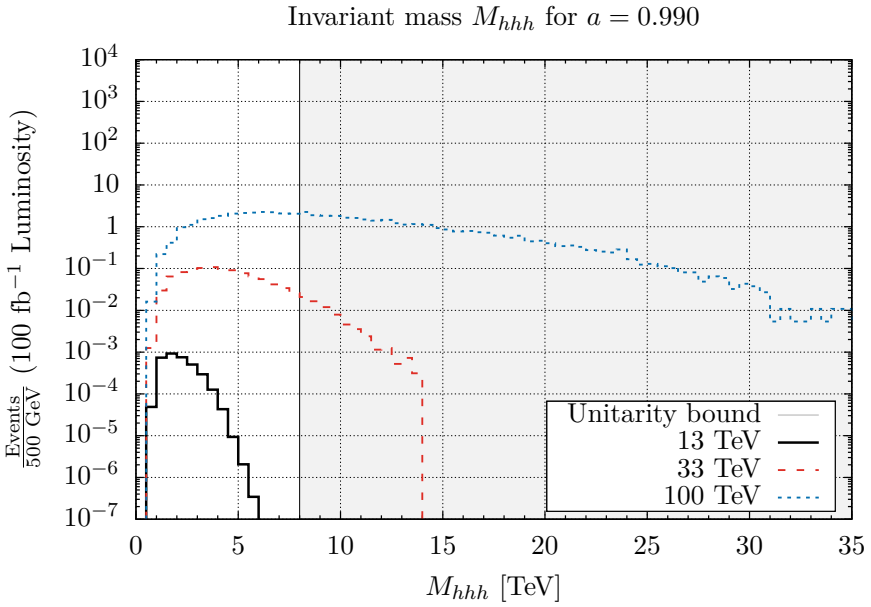

Figure 5.6: Invariant mass M_{hhh} for $pp \to jjhhh$ with $a = 0.99$ at $\sqrt{s} = 13, 33, 100$ TeV, respectively. The grey shaded area marks the region of unitarity violation.

amount of events falling into the region where unitarity is violated appears large and at 100 TeV, an even larger fraction of events exhibits unitarity violation.

Apart from comparing different values of a and the corresponding fractions of events in the unitarity violating regions, it is also worth comparing them to the SM ($a = 1$). Of particular interest thereby is the value of a, for which the SM predicts only a single event before unitarity violation starts. This is shown for $\sqrt{s} = 100$ TeV and a total integrated luminosity of 30 ab^{-1} in figure 5.7 below. It turns out that a deviation from the SM coupling by 2 % (corresponding to $a = 0.98$ or $a = 1.02$) leads to a SM prediction of just a single event before unitarity violation occurs. In case of $a = 1.02$, a total of about 3000 events is predicted[2], indicating that if a is different from 1 by not less than 2 %, a future collider with a collision energy and luminosity as stated above should be highly sensitive to this coupling.

To make the predictions of figures 5.5 and 5.6 not only qualitative but also quantitatively appealing, we count the number of events in the unitarity violating region and all available events

[2]The case of $a = 0.98$ behaves nearly identical and is therefore not shown here.

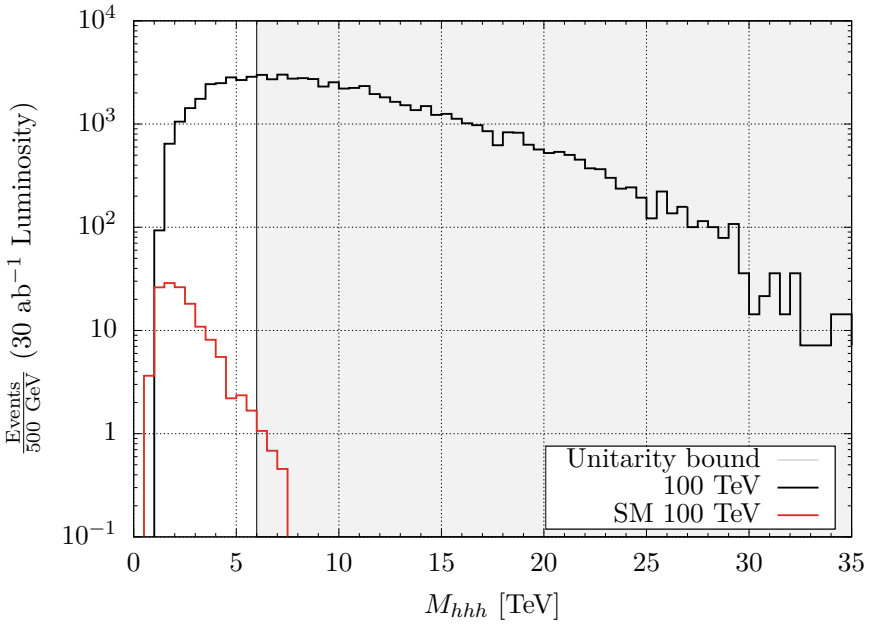

Figure 5.7: Invariant mass M_{hhh} for $pp \to jjhhh$ in the SM ($a = 1$, red) and with $a = 1.02$ (black) at $\sqrt{s} = 100$ TeV and a totel integrated luminosity of 30 ab^{-1}. The a-value was chosen such that the grey shaded area marking the region of unitarity violation starts when the SM distribution predicts only a single event.

and define the amount of unitarity violation, $\mathcal{U}$, as the ratio of the two

$$\mathcal{U} = \frac{\#\ (\text{events in region of unitarity violation})}{\#\ (\text{all events})}\,. \tag{5.10}$$

For practical reasons, however, it will be more convenient to use $\varepsilon_{\mathcal{U}} = 1 - \mathcal{U}$ rather than $\mathcal{U}$ directly, where $\varepsilon_{\mathcal{U}}$ refers to the amount of unitarity restored rather than violated.

In table 5.3, we show $\varepsilon_{\mathcal{U}}$ with respect to a and $\sqrt{s}$ for an assumed total integrated luminosity of $\mathcal{L}_{\text{int}} = 100$ fb^{-1} for all energies. This way, comparing results for different energies and comparing with other studies is simpler.

For the current LHC with $\sqrt{s} = 13$ TeV, $\varepsilon_{\mathcal{U}}$ stays above 90 % for $|a - 1| < 0.2$ and above 99 % for a change of a not larger than 10 %, indicating that the EFT is almost perfectly valid for this energy. The small degree of unitarity violation that exists, however, will be nearly impossible to detect at the current LHC, as for the entire range of a considered here, not a single event within the region of unitarity violation is expected and altogether, a maximum of only two events in the

13 TeV					33 TeV					100 TeV				
a	$\varepsilon_{\mathcal{U}}$ [%]	σ [pb]	$\mathcal{L}_{\text{int}} \cdot \sigma$	$\mathcal{L}_{\text{int}} \cdot \sigma \cdot \varepsilon_{\mathcal{U}}$	a	$\varepsilon_{\mathcal{U}}$ [%]	σ [pb]	$\mathcal{L}_{\text{int}} \cdot \sigma$	$\mathcal{L}_{\text{int}} \cdot \sigma \cdot \varepsilon_{\mathcal{U}}$	a	$\varepsilon_{\mathcal{U}}$ [%]	σ [pb]	$\mathcal{L}_{\text{int}} \cdot \sigma$	$\mathcal{L}_{\text{int}} \cdot \sigma \cdot \varepsilon_{\mathcal{U}}$
0.80	97.81	$5.70 \cdot 10^{-6}$	0.57	0.56	0.80	44.76	$2.10 \cdot 10^{-3}$	210.00	94.00	0.80	10.01	0.12	12000.00	1201.20
0.90	99.72	$2.10 \cdot 10^{-6}$	0.21	0.21	0.90	58.21	$7.50 \cdot 10^{-4}$	75.00	43.66	0.90	15.38	$4.10 \cdot 10^{-2}$	4100.00	630.58
0.92	99.30	$1.40 \cdot 10^{-6}$	0.14	0.14	0.92	62.36	$5.10 \cdot 10^{-4}$	51.00	31.80	0.92	17.48	$2.80 \cdot 10^{-2}$	2800.00	489.44
0.94	99.99	$8.50 \cdot 10^{-7}$	0.09	0.08	0.94	68.75	$3.10 \cdot 10^{-4}$	31.00	21.31	0.94	19.84	$1.70 \cdot 10^{-2}$	1700.00	337.28
0.96	100	$4.10 \cdot 10^{-7}$	0.04	0.04	0.96	76.29	$1.50 \cdot 10^{-4}$	15.00	11.44	0.96	24.76	$7.90 \cdot 10^{-3}$	790.00	195.60
0.97	100	$2.40 \cdot 10^{-7}$	0.02	0.02	0.97	82.61	$8.40 \cdot 10^{-5}$	8.40	6.94	0.97	29.97	$4.60 \cdot 10^{-3}$	460.00	137.86
0.98	100	$1.10 \cdot 10^{-7}$	0.01	0.01	0.98	89.69	$3.90 \cdot 10^{-5}$	3.90	3.50	0.98	35.53	$2.10 \cdot 10^{-3}$	210.00	74.61
0.99	100	$3.40 \cdot 10^{-8}$	0.00	0.00	0.99	96.91	$1.00 \cdot 10^{-5}$	1.00	0.97	0.99	50.34	$5.40 \cdot 10^{-4}$	54.00	27.18
1.01	100	$3.60 \cdot 10^{-8}$	0.00	0.00	1.01	96.72	$1.10 \cdot 10^{-5}$	1.10	1.06	1.01	48.88	$5.90 \cdot 10^{-4}$	59.00	28.84
1.02	100	$1.30 \cdot 10^{-7}$	0.01	0.01	1.02	88.64	$4.50 \cdot 10^{-5}$	4.50	3.99	1.02	35.10	$2.40 \cdot 10^{-3}$	240.00	84.24
1.03	100	$2.90 \cdot 10^{-7}$	0.03	0.03	1.03	81.76	$1.00 \cdot 10^{-4}$	10.00	8.18	1.03	27.59	$5.50 \cdot 10^{-3}$	550.00	151.75
1.04	99.98	$5.30 \cdot 10^{-7}$	0.05	0.05	1.04	74.37	$1.90 \cdot 10^{-4}$	19.00	14.13	1.04	23.16	$1.00 \cdot 10^{-2}$	1000.00	231.60
1.06	99.94	$1.30 \cdot 10^{-6}$	0.13	0.13	1.06	65.06	$4.50 \cdot 10^{-4}$	45.00	29.28	1.06	18.07	$2.40 \cdot 10^{-2}$	2400.00	433.68
1.08	99.56	$2.30 \cdot 10^{-6}$	0.23	0.23	1.08	56.84	$8.40 \cdot 10^{-4}$	84.00	47.75	1.08	14.94	$4.50 \cdot 10^{-2}$	4500.00	672.30
1.10	99.01	$3.90 \cdot 10^{-6}$	0.39	0.39	1.10	50.96	$1.40 \cdot 10^{-3}$	140.00	71.34	1.10	12.12	$7.50 \cdot 10^{-2}$	7500.00	909.00
1.20	91.81	$2.00 \cdot 10^{-5}$	2.00	1.84	1.20	32.60	$7.20 \cdot 10^{-3}$	720.00	234.72	1.20	7.04	0.39	39000.00	2745.60

Table 5.3: Amount of unitarity not violated $\varepsilon_{\mathcal{U}}$ in % for M_{hhh} with respect to a and $\sqrt{s}$. Also shown are the cross sections σ in pb, the total number of events $\mathcal{L}_{\text{int}} \cdot \sigma$ and the amount of events not violating unitarity $\mathcal{L}_{\text{int}} \cdot \sigma \cdot \varepsilon_{\mathcal{U}}$, where $\mathcal{L}_{\text{int}}$ is the total integrated luminosity. We assume $\mathcal{L}_{\text{int}} = 100$ fb^{-1} for all energies to allow easy comparisons between the energies.

rather extreme case of $a = 1.2$ is expected.

At $\sqrt{s} = 33$ TeV, the situation changes as deviations in a from the SM of only 1 % already lead to 4 % unitarity violation and moving a further away from 1 leads to unitarity violations up to 80 %. However, the expected number of events is still rather small and exceeds 100 again only for the extreme case of $a = 1.2$. An (expected) increase in luminosity by at least a factor of 10 may be helpful here, however if a differs by less than 10 % from the SM coupling, chances are small to detect such a signal.

For $\sqrt{s} = 100$ TeV, lastly, unitarity violations up to 90 % are expected for a 20 % deviation of a from the SM coupling and a minimum of about 50 % is expected even for deviations of about 1 %. This is a clear sign that the considered EFT based on the NLσM cannot be valid at collision energies at or beyond 100 TeV, indicating that at such energies new physics should become visible. Whether this can be observed with the triple Higgs signature depends on the number of expected (signal) events, which is comparably high[3] for 100 TeV. In the extreme case of $a = 1.2$, 39000 events are expected in total, of which 2745 events are expected to fall into the region where unitarity is violated. In more realistic scenarios where a differs from 1 only by a few %, e.g. for 1 %, still a total of 54 events is expected. Also, a future 100 TeV collider is expected to gather more than just 100 fb^{-1} of data, but already an increase by one order of magnitude may be enough to be sensible to such a signature, provided the expected background is small enough. Estimating this background for the triple Higgs signature at a 100 TeV collider is subject of the next section 5.4.

5.4 Background Estimation

The main signature we found to benefit from anomalous Higgs couplings between a Higgs and two gauge bosons is triple Higgs production via vector boson fusion at $\sqrt{s} = 100$ TeV. The expected background therefore consists of two high-energetic back-to-back jets with a large rapidity gap and the decay products of the three Higgs bosons, which we assume to decay each as $h \to b\bar{b}$. While estimating the background, we also estimate the expected signal cross section. This differs from the cross sections listed in table 5.3, since colliders will not observe the Higgs bosons, but

[3]Tagging efficiencies and Higgs branching ratios will be applied in the next section.

their decay products, and this only with a certain efficiency. The $b\bar{b}$-pairs are expected to lie in a narrow cone due to the large boost of the Higgs bosons, even for deviations to the SM coupling as small as 1 % and smallish $M_{hhh} \simeq 1$ TeV, which represents the lower edge of the distributions in figures 5.5 and 5.6. In particular, the cone size $\Delta R_{b\bar{b}}^{\text{sig}}$ is expected to be of the order

$$\Delta R_{b\bar{b}}^{\text{sig}} \approx \frac{\frac{M_h}{2}}{\frac{M_{hhh}}{3}} = \frac{\frac{125\ \text{GeV}}{2}}{\frac{1000\ \text{GeV}}{3}} \simeq 0.2\,. \tag{5.11}$$

To find the efficiency of identifying the three Higgs jets, we make use of the work done in Ref. [218]. Therein, the authors computed the efficiency of identifying two boosted Higgs bosons coming from Kaluza-Klein graviton decays including b-tagging efficiencies to be $\varepsilon_{hh} \simeq 15$ %, if the Higgs momentum is large enough. This efficiency can be related to our work and we estimate

$$\varepsilon_{hhh} = (\sqrt{\varepsilon_{hh}})^3 \simeq 0.058\,. \tag{5.12}$$

Furthermore, the branching ratio $\text{BR}\left(h \to b\bar{b}\right) \simeq 0.58$ also has to be taken into account when estimating the proper signal cross section.

Putting all of the above together, we can estimate the signal cross section $\sigma_{\text{sig}}(pp \to jjhhh)$ as a function of a to

$$\begin{aligned}\sigma_{\text{sig}}(pp \to jjhhh)\,(a) &= \sigma(pp \to jjhhh)\,(a) \times \varepsilon_{hhh} \times \text{BR}\left(h \to b\bar{b}\right)^3 \\ &\simeq \sigma(pp \to jjhhh)\,(a) \times 0.0113\,.\end{aligned} \tag{5.13}$$

Regarding the background, we assume the major part to come from QCD mediated 6 b quark final states due to the large $\text{BR}\left(h \to b\bar{b}\right) \simeq 0.58$ dominating over the other Higgs decay channels. For this reason, we assume other processes (containing e.g. $b\bar{b}\,b\bar{b}\,\gamma\gamma$ in the final state) to provide only negligible contributions to the background. Hence, the particular process we study here is $pp \to jj\,b\bar{b}\,b\bar{b}\,b\bar{b}$, however computing this process with eight particles in the final state is a challenging task and actually technically unfeasible at this time, especially if additional cuts on the phase space will be applied. Thus, neither `MadGraph` nor `CalcHEP` or other tools such as

ALPGEN [219–221] were able to compute the respective cross section or simulate events. For this reason, we relax our assumptions regarding the background and only estimate an upper bound on its cross section, which will be conservative. In particular, we leave the two back-to-back jets aside and instead focus solely on the $6b$ final state, which to compute is still a highly challenging task, as again none of the above tools is able to compute the cross sections when certain cuts are applied. However, it is possible to compute the cross section and generate events for $pp \to b\bar{b}\,b\bar{b}$ with certain cuts, and we will be able to use this cross section to estimate the cross section including three $b\bar{b}$-pairs in the final state. Before doing so, let us focus on the computation of the $4b$ final state.

To reduce any background coming from combinatorial miscalculations, we apply a mass window cut

$$\left|M^i_{bb} - M_h\right| \equiv \Delta^i_{M_h} \leq \Delta^{\text{cut}}_{M_h} = 15 \text{ GeV} \tag{5.14}$$

for $i = 1, 2, 3$, where M^i_{bb} represents the two bb or $b\bar{b}$ combinations with the lowest $\Delta^i_{M_h}$ and $\Delta^{\text{cut}}_{M_h}$ is chosen to be consistent with the jet energy resolution of less than 10 % as achieved by both ATLAS and CMS collaborations at the LHC. This resolution is expected to be roughly at the same order at future 100 TeV colliders. Besides this mass window cut, we apply the b-jet acceptance cuts

$$p^b_T \geq 50 \text{ GeV} \qquad \text{and} \qquad |\eta_b| \leq 2\,, \tag{5.15}$$

as well as a cut on the invariant mass of all $b\bar{b}$-pairs, M_{4b}. This cut is intended to further reduce the background and is set to

$$M_{4b} \geq 1 \text{ TeV}\,, \tag{5.16}$$

due to the steep drop of background[4] with increasing M_{4b} (see also the left panel of figure 5.8 below). The last cut we apply takes into account the boosted nature of the Higgs bosons and sets an upper bound on the b quark separation $\Delta R_{b\bar{b}}$ with

$$\Delta R_{b\bar{b}} = \sqrt{\Delta\phi_{b\bar{b}} + \Delta\eta_{b\bar{b}}} \leq \Delta R^{\text{cut}}_{b\bar{b}} = 0.5\,, \tag{5.17}$$

[4]The signal remains mainly unaffected by this cut due to the broad invariant mass distributions of M_{hhh} as shown in figures 5.5 and 5.6.

where, again, the signal remains unaffected by this cut due to $\Delta R_{b\bar{b}}^{\text{sig}}$ being smaller (see equation (5.11)). The importance of this cut in reducing the background is visualised in the right panel of figure 5.8 below.

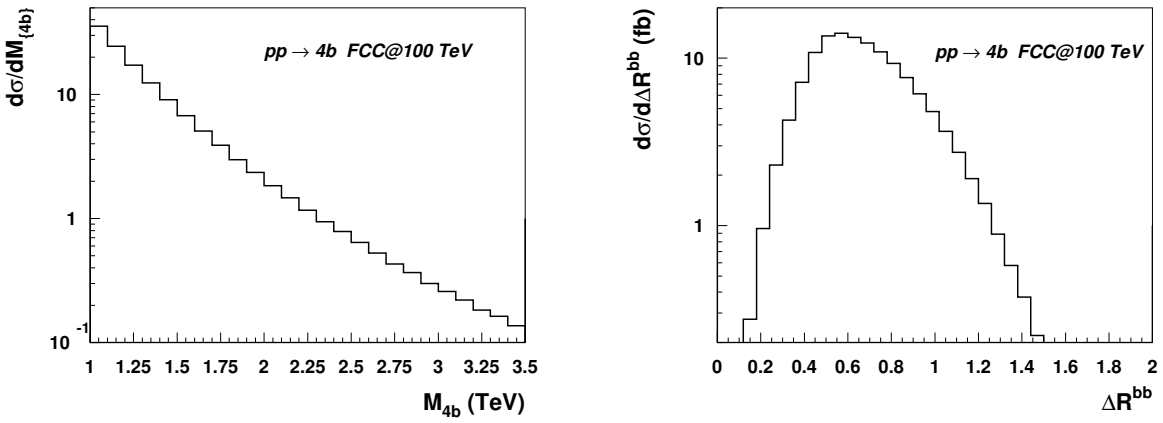

Figure 5.8: The M_{4b} (left) and $\Delta R_{b\bar{b}}$ (right) distributions for $pp \to b\bar{b}\,b\bar{b}$. The distributions were generated with the cuts from equations (5.14) to (5.15) applied at parton level.

Finally, the cross section for $pp \to b\bar{b}\,b\bar{b}$ as well as a set of 100k events can be computed using `CalcHEP` while taking into account the cuts defined in equations (5.15) to (5.17) and reads

$$\sigma(pp \to b\bar{b}\,b\bar{b}) = 19.0 \text{ fb}\,. \tag{5.18}$$

The next step now is to use this result to estimate the background cross section for $pp \to b\bar{b}\,b\bar{b}\,b\bar{b}$. To do so, we shower the 100k events for $pp \to b\bar{b}\,b\bar{b}$ using `PYTHIA 8.2.30` [140] several times and compute the probability of an additional $b\bar{b}$-pair (with properties as defined by the cuts (5.15) – (5.17) and the QCD scale set to M_{4b}) being produced via initial (ISR) and final state radiation (FSR). We validated this approach by simulating the $b\bar{b}\,b\bar{b}$ ($4b$) background as given by equation (5.18) based on a $b\bar{b}$ ($2b$) starting set of events and estimated it to be accurate up to 20 – 30 %. This is sufficient to estimate the full $6b$ background up to about an order of magnitude.

In particular, we showered a total of 500k events and estimated the probability $\omega_{b\bar{b}}$ with an uncertainty at percentage level for different values of $R_{b\bar{b}}^{\text{cut}}$, shown below in table 5.4. It becomes apparent that the background can be further reduced by reducing $R_{b\bar{b}}^{\text{cut}}$.

$\Delta R_{b\bar{b}}^{\text{cut}}$	2.0	1.5	1.0	0.5
$\omega_{b\bar{b}}$	$1.1 \cdot 10^{-3}$	$7.0 \cdot 10^{-4}$	$3.5 \cdot 10^{-4}$	$8.6 \cdot 10^{-5}$

Table 5.4: Probability $\omega_{b\bar{b}}$ to create an additional $b\bar{b}$ pair from events already containing two $b\bar{b}$-pairs with $|M_{bb} - M_h| \leq \Delta_{M_h}^{\text{cut}} = 15$ GeV for various values of $\Delta R_{b\bar{b}}^{\text{cut}}$. These numbers are based on 500k events containing two $b\bar{b}$-pairs showered via `PYTHIA`.

With these numbers in place, we can estimate the background coming from $pp \to b\bar{b}\,b\bar{b}\,b\bar{b}$, reading

$$\begin{aligned} \sigma(6b) &= \sigma(4b) \times \omega_{b\bar{b}}\,(\Delta R_{b\bar{b}} \leq 0.5) \\ &= 19.0 \text{ fb} \times 8.6 \cdot 10^{-5} \\ &\simeq 1.6 \cdot 10^{-3} \text{ fb}\,, \end{aligned} \tag{5.19}$$

and finally also the background after Higgs-jet tagging

$$\begin{aligned} \sigma_{\text{BG}}(hhh) &= \sigma(6b) \times \varepsilon_{hhh} \\ &\simeq 9.5 \cdot 10^{-5} \text{ fb}\,. \end{aligned} \tag{5.20}$$

For completeness and convenience, the signal cross section from equation (5.13) is printed here again

$$\sigma_{\text{sig}}(pp \to jjhhh)\,(a) \simeq \sigma(pp \to jjhhh)\,(a) \times 0.0113\,.$$

Before actually comparing signal and background, we can make use of equation (16) of Ref. [203] to give predictions also for sub-% deviations from the SM coupling of a Higgs to two gauge bosons. Equation(16) of Ref. [203] states that the signal cross section scales quite well as $(1-a)^2 \equiv \varepsilon_a^2$ for $|\varepsilon_a| \ll 1$ and $\sigma(pp \to jjhhh)\,(a) \gg \sigma_{\text{SM}}(pp \to jjhhh)\,(a=1)$. Using this scaling on the signal cross sections from equation (5.13) with $\sigma(pp \to jjhhh)\,(a)$ from table 5.3, we can extend the range of a down to about one permille.

In the left panel of figure 5.9, we finally compare the signal as a function of ε_a and the background for $\varepsilon_a \in [-0.01, 0.01]$, which corresponds to a maximum deviation from the SM coupling of ± 1 %. The right panel holds information on the sensitivity of a 100 TeV FCC to ε_a.

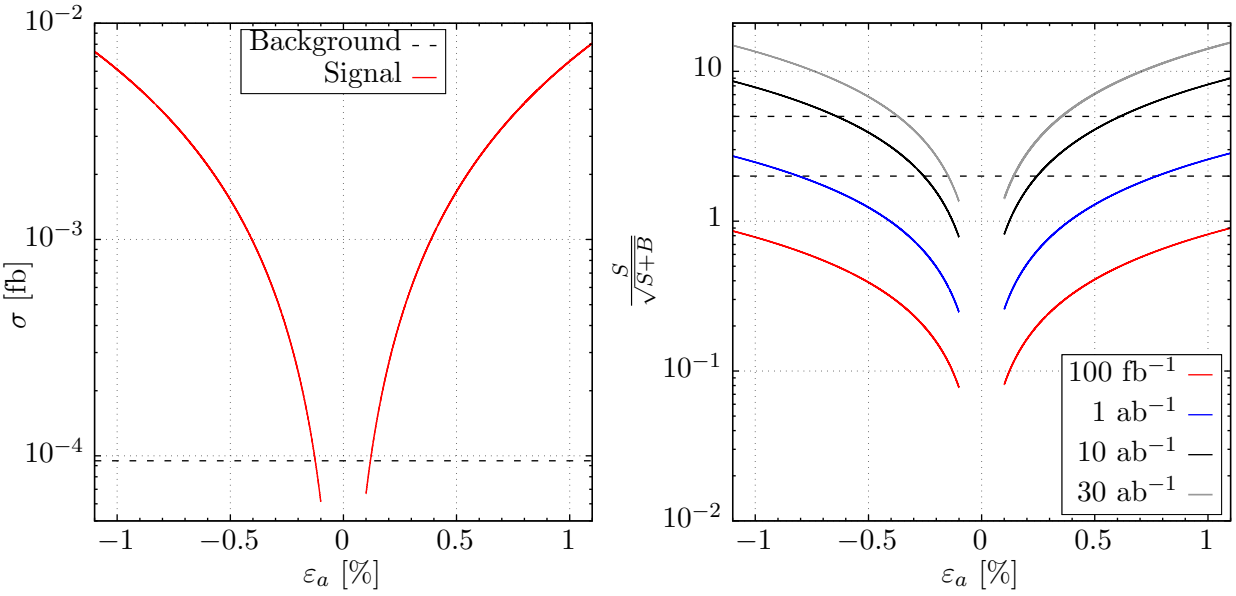

Figure 5.9: Signal and background cross sections $\sigma_{\text{sig}}(hhh)$ and $\sigma_{\text{BG}}(hhh)$ for $\varepsilon_a \in [-0.01, 0.01]$ at $\sqrt{s} = 100$ TeV (left panel) as well as the 100 TeV FCC sensitivity to ε_a (right panel) for 100 fb^{-1}, 1 ab^{-1}, 10 ab^{-1} and 30 ab^{-1} of total integrated luminosity.

It turns out that the signal clearly dominates over the background if $|\varepsilon_a|$ is larger than about 0.5 % and becomes comparable to the background only for very small $|\varepsilon_a|$ in the low permille range or below. It is worth mentioning at this place once more that the background rate we computed is conservative and acts as an upper bound, since the two omitted back-to-back VBF jets would further decrease the background by about two orders of magnitude. Therefore, it is safe to argue that the background is negligible once $|\varepsilon_a| \gtrsim 10^{-3}$ and whether such small couplings will be probable is only a question of luminosity. Exemplarily, we show the sensitivity of a 100 TeV FCC to the triple Higgs signal as a function of ε_a for the total integrated luminosities 100 fb^{-1}, 1 ab^{-1}, 10 ab^{-1} and 30 ab^{-1} in the right panel of figure 5.9 as red, blue, black and grey lines respectively. Using two standard deviations as a criterion (dashed horizontal black line at 2, discovery limit at $5\,\sigma$ shown as horizontal black line at 5), the 100 TeV FCC can probe $|\varepsilon_a| \simeq 2.5 \cdot 10^{-2}$, $|\varepsilon_a| \simeq 7.5 \cdot 10^{-3}$, $|\varepsilon_a| \simeq 2.5 \cdot 10^{-3}$ and $|\varepsilon_a| \simeq 1.3 \cdot 10^{-3}$ for 100 fb^{-1}, 1 ab^{-1}, 10 ab^{-1} and 30 ab^{-1} respectively. In summary, triple Higgs production via VBF therefore qualifies as an excellent signature to study the Higgs to two vector boson coupling with permille accuracy at a 100 TeV FCC. We find this accuracy especially remarkable, since the sensitivity of the LHC

to this coupling is about two orders of magnitude smaller.

5.5 Conclusions

In this chapter, we explored the potential of current and future hadron colliders to narrow down the properties of the Higgs-like scalar discovered in 2012. In particular, we investigated the coupling of one Higgs boson h to two gauge bosons V in a non-linear σ model combined with a Higgs boson, around which we performed a field expansion within the framework of an EFT. With this approach, the aforementioned coupling of a Higgs to two gauge bosons is extended by a multiplicative factor a and $a = 1$ restores the SM.

As was shown in the past, values of a other than 1 lead to a large increase in cross section of vector boson scattering, since the Higgs boson cannot fully account for the required cancellations in the longitudinal scattering. An important role among the possible vector boson scatterings plays triple Higgs production, which receives extraordinarily large contributions due to the absence of transversely polarised vector bosons in the final state. However, even though triple Higgs production benefits the most from anomalous Higgs couplings $a \neq 1$, the cross sections at a collision energy of $\sqrt{s} = 13$ TeV are in the sub-fb region and lead to a nearly undetectable signal. The situation is similar when increasing the collision energy to 33 TeV, but changes once 100 TeV are considered, as is planned for future pp colliders. In particular, we found that with a 100 TeV FCC, the Higgs to two gauge boson coupling can be probed effectively via triple Higgs production from vector boson fusion up to permille accuracy.

We therefore evaluated the cross sections for $pp \to jjhhh$ as a function of a with and without VBF cuts and estimated the expected background for triple Higgs production, consisting of 6 b jets. The latter turns out to be smaller than the signal if a differs not less than about one permille from its SM value $a = 1$. Furthermore, we found that a future 100 TeV FCC is sensitive enough to probe such couplings with high precision in the permille range of deviations from a to 1 (summarised in figure 5.9). This high accuracy together with the fact that the LHC with its currently operated 13 TeV collision energy is about two orders of magnitude less sensitive and therefore unable to probe such anomalous Higgs couplings, highlights the importance of future colliders with large collision energies.

6 | Conclusions

While the SM is astonishingly well tested and so far seems to be completed with the Higgs boson, the strong demand for BSM physics remains unbroken for several good reasons. On the one hand, the list of issues the SM cannot explain is long and undoubtedly requires BSM physics. On the other hand — and despite the fact that the Higgs boson discovered in 2012 so far matches the SM Higgs — some of its properties are still widely unconstrained and leave reasonable room for accommodating it in theories other than the SM. In this thesis, we addressed both of these reasons by exploring a broad range of phenomenological aspects of several BSM theories. Due to the vast amount of existing BSM theories, we focus mainly on those predicting signatures that may be observed in the near future by the LHC. In particular, we considered two supersymmetric theories (arising after symmetry breaking of a respective GUT scale model), an effective theory with particle content e.g. as in CH models, and eventually an EFT in combination with a respective simplified model.

Starting with a supersymmetric model in Chapter 2, we explored the potential of a Pati-Salam GUT scale model with distinctive $A_4 \otimes Z_5$ family symmetry to account for Δa_μ, DM as well as further experimental constraints. After breaking the Pati-Salam symmetry, the model reduces to the MSSM with novel constraints on the scalar masses. In particular, the model predicts four scalar soft masses at the GUT scale, namely m_0 (a universal left-handed scalar mass) and m_i for $i = 1, 2, 3$ (a universal right-handed scalar mass for each family i) together with non-universal gaugino and trilinear soft masses. With such soft masses, it is possible to have light smuons in order to successfully explain Δa_μ, but also heavy stops, which ensure that the Higgs mass will be large enough. We found two sets of solutions providing the desired Δa_μ and a viable DM candidate. These two sets are characterised by large μ in the TeV range as well as small $\mu \lesssim 400$

GeV respectively. While for both scenarios, the DM candidate is a bino-like neutralino $\tilde{\chi}_1^0$, the relic density constraint is satisfied for large μ via co-annihilation with the NLSPs and for small μ via resonant annihilation, if $m_{\tilde{\chi}_1^0} \approx \frac{M_Z}{2}$ or $\frac{M_h}{2}$, or co-annihilation with higgsino states for larger $m_{\tilde{\chi}_1^0}$. The model further predicts gluinos with a mass above 2 TeV, which results in heavy squarks that satisfy current LHC searches. More relevant signatures could arise from the decays of light smuons with masses around 100 – 300 GeV. We performed a `CheckMATE` analysis on the 8 TeV ATLAS and CMS searches looking for di- and tri-lepton signatures, but found them unable to probe such signals. However, the (at that time unavailable) 13 TeV LHC searches might effectively constrain the model parameter space, especially for very light mass spectra as they arise in case of small μ.

In Chapter 3, we picked up this idea and investigated the capabilities of a GUT scale $SU(5)\otimes A_4$ (also breaking down to the MSSM, but with different GUT scale conditions) to explain Δa_μ, DM and further experimental constraints. This time, however, we mainly aimed at solutions with lighter mass spectra in order to reach further into the regions where the 8 and 13 TeV LHC searches are sensitive. The soft GUT scale masses we obtain after breaking the $SU(5) \otimes A_4$ differ from the ones in Chapter 2 and, as a main difference, do not unify the left and right-handed sectors separately any longer. With these conditions, we were able to show that the desired Δa_μ in harmony with DM and other constraints can only be achieved, if the gaugino masses are non-universal and $\mu \simeq -300$ GeV. Additionally, a right-handed smuon with a mass around 100 GeV just slightly heavier than the DM candidate (which again is a bino-like LSP $\tilde{\chi}_1^0$) is required to satisfy current LHC searches and to provide the correct relic density via $\tilde{\mu}_R$-$\tilde{\chi}_1^0$ co-annihilation. Due to the small μ, DM DD experiments also set strong constraints on the model parameter space. The key finding of this chapter, however, is the requirement for gaugino mass non-universality, if Δa_μ is to be explained simultaneously with DM and current LHC data. After showing that universal and partially non-universal gaugino masses are excluded by LHC gluino and gaugino searches, we performed dedicated benchmark analyses for the case of fully non-universal gaugino masses, i.e. $M_1 < M_2 \ll M_3$. This case is still allowed if $M_1 \simeq 250$ GeV $< M_2 \ll M_3$ and leads to higgsino-like $\tilde{\chi}_2^0$ and $\tilde{\chi}_1^\pm$ due to the inevitable model prediction of $\mu \simeq -300$ GeV. Together with the almost mass-degenerate LSP and right-handed smuon, the LHC may be able to explore

this parameter space entirely via di- and tri-lepton signatures, once its luminosity reaches about 3 ab^{-1}. Lastly, we found that DM DD experiments may also explore the entire model parameter space independent of the LHC searches, once their sensitivity is increased by a factor of about two, which is expected to take place in the next few years.

As an alternative to SUSY, we studied the BSM phenomenology of a simplified model with a heavy resonance Z', top partners T' and DM ϕ in Chapter 4. Such a particle content is typical e.g. for CH models, where the Higgs boson arises as the bound state of some new strong dynamics. The most interesting process of our proposed model is $T'\overline{T'}$-pair production via Z'-mediation with the top partners further decaying as $T' \to t\phi$, resulting in the final state signature $t\bar{t} + \not{E}_T$. After determining the LHC constraints on this model for QCD-induced $T'_s\overline{T'_s}$-pair production as well as di-jet and di-lepton searches, we found that the presence of the Z' can greatly improve the $t\bar{t} + \not{E}_T$ signature without conflicting with existing Z' bounds and may even provide the dominant contribution to it. Additionally, we found that the $t\bar{t} + \not{E}_T$ signature covers parts of the model parameter space widely unconstrained by non-collider searches, therefore making it a highly valuable addition to constrain models involving Z' bosons, top partners and DM. Furthermore, the presence of the Z' allows to probe the masses of the Z' boson, the top partner T'_s and DM with the $t\bar{t} + \not{E}_T$ signature well beyond the limits coming from QCD-mediated $T'\overline{T'}$-pair production alone, which by itself already seems quite remarkable. Lastly, the model parameter space can be further explored by considering off-shell top quark decays, i.e. when $M_{T'} - m_\phi < m_t$. In this case, the underlying kinematics are completely different, but nevertheless can in principle be studied with similar methods as in the SUSY scenario with degenerate stops and neutralinos.

Finally, in Chapter 5 we addressed the potential of current and future hadron colliders to determine the nature of the Higgs boson by investigating its coupling to two gauge bosons (labelled hVV) via a non-linear σ model. The Higgs field is added to the NLσM as a field expansion in an EFT and results in an extension of the hVV coupling in form of a multiplicative factor a, hence restoring the SM coupling for $a = 1$. If $a \neq 1$, we confirmed that such anomalous Higgs couplings greatly increase the cross sections of vector boson scattering due to the lack of cancellation between scattering amplitudes of longitudinal vector bosons. Eventually, if either a or $\sqrt{s}$ becomes large enough, the cross sections start exceeding the unitarity bound, indicating that the EFT reached its

limit of validity and the high energy theory, which can be any new physics, has to be considered. A secondary aim of this chapter therefore was to identify when and to what degree unitarity will be violated in dependence of the anomalous Higgs coupling a and the collider energy $\sqrt{s}$. For both this and the question whether the hVV coupling is SM-like or not, we investigated the process $pp \to jj\,hhh$ (triple Higgs production via vector boson fusion), which stands out with an especially large growth in cross section due to the complete absence of transversely polarised gauge bosons in the final state. We found that while the LHC with $\sqrt{s} = 13$ TeV is not sensitive to such a signal, a 100 TeV FCC on the other hand can be sensitive to anomalous Higgs couplings differing only by a few permille from the SM coupling. To reinforce this argument, we estimated the respective background for a triple Higgs signal (6 b jets) and found that it becomes comparable to the signal only when a differs not more than a few permille from its SM value $a = 1$. Lastly, we found that already 1 ab^{-1} of total integrated luminosity is sufficient to probe anomalous Higgs couplings with a permille accuracy, which highlights the importance of developing and upgrading experimental setups in the search for new physics.

Overall, in this thesis we studied the phenomenology of several BSM theories at the LHC. We found that supersymmetric as well as Composite Higgs or Technicolor theories provide viable explanations for several issues of the SM, such as dark matter or $(g-2)_\mu$, and lead to new physics predictions that may be probed experimentally in the near future. Due to the vastly different origins of the Higgs boson in these BSM theories, we further explored the capability of the LHC and future colliders to determine its nature by precisely measuring its couplings to gauge bosons and hence provide another option to shed light on new physics. We found that future colliders have great potential to address this question with an accuracy to a change in couplings in the permille range. Hence, in the (hopefully very unlikely) case that no sign of new physics will be found in the current era of the LHC, its successors will clearly have the potential to change this.

Appendix

A Details about the Hierarchy Problem in the SM

In this appendix, we exemplarily show the hierarchy problem in the SM based on the Higgs-loop Higgs self energy, as depicted in figure A.1 below. Before computing the contribution of this

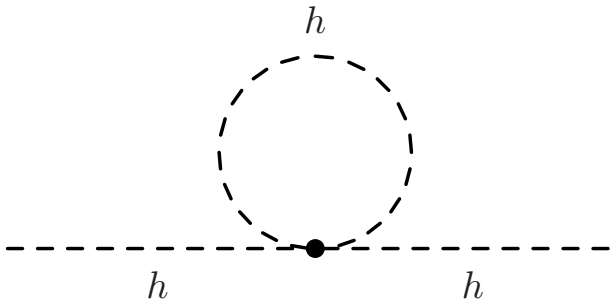

Figure A.1: Feynman diagram for the Higgs one-loop self-energy.

diagram, let us briefly review the Higgs sector of the SM. The Higgs potential reads

$$V = -\mu^2 \, \phi^\dagger \phi + \frac{\lambda}{4} \left(\phi^\dagger \phi \right)^2 \tag{A.1}$$

with $\phi = \left(\phi^+, \phi^0\right)^T$ being the $SU(2)$ Higgs doublet as well as $\lambda > 0$ and $\mu^2 > 0$ to ensure spontaneous symmetry breaking. Minimising V yields the vacuum expectation value (vev)

$$\langle 0 | \phi^0 | 0 \rangle = 2 \sqrt{\frac{\mu^2}{\lambda}} \equiv v \tag{A.2}$$

with $v \approx 246$ GeV. Since v is related to all masses in the SM, one could say it sets the general mass scale of the theory. For example, the Higgs and electron mass read $m_h = v\sqrt{\frac{\lambda}{2}}$ and $m_e = g_f \frac{v}{\sqrt{2}}$ with g_f being the coupling of a Higgs to a fermion anti-fermion pair $f\bar{f}$. So far, all considerations took place at tree level and loop-induced contributions were neglected. If taken into account, the picture changes drastically. Consider now the one-loop self-energy of the Higgs boson shown in figure A.1, which is proportional to

$$\lambda \int^{\Lambda} \frac{\mathrm{d}^4 k}{k^2 - m_h^2} \tag{A.3}$$

with k being the internal loop momentum and Λ being some cut-off scale up to which the SM is valid[1], e.g. the Planck scale M_P. This integral diverges quadratically in k and yields a positive correction to μ^2 proportional to [222]

$$\lambda \Lambda^2 \, \phi^\dagger \phi \, . \tag{A.4}$$

With this correction, the physical mass now reads

$$\mu_{\text{phys}}^2 \approx \mu^2 - \lambda \Lambda^2 \tag{A.5}$$

instead of just the 'bare' mass μ^2.

Reminimising the Higgs potential V with μ_{phys} then leads to equation (A.2) with μ_{phys} instead of just μ, connecting μ_{phys} and λ as follows

$$\mu_{\text{phys}} \approx \sqrt{\lambda} \cdot 123 \, \text{GeV} \, . \tag{A.6}$$

This implies $\mu_{\text{phys}} \sim \mathcal{O}(100)$ GeV in order for a perturbative treatment of the Higgs boson to be possible. However, since $\Lambda \sim M_P \approx 10^{19}$ GeV, equation (A.5) implies μ_{phys} to be of order 10^{19} GeV. Now the only way to retain a λ small enough for perturbation theory to still work is to either have $\mu^2 \sim M_P^2$, or to have some new physics arising at a scale much lower than the Planck scale and not much larger than v, i.e. at the order of a few TeV. While the first solution is usually disfavoured for its large amount of fine tuning necessary, the second solution offers a more general (and maybe more natural) perspective to solve the hierarchy problem.

[1] Since the SM is renormalisable, Λ could go all the way up to infinity, implying that the SM remains valid for all energy scales. This, however, is a highly uncommon belief among physicists.

B The Groups A_4 and Z_5

B.1 The Alternating Group A_4

The group A_4 represents the alternating group on four letters (or *of degree 4*), which corresponds to the orientation-preserving rotations of a tetrahedron. These rotations comprise angles of $\frac{\pi}{2}$ and $\frac{\pi}{3}$, and a total of two generators is sufficient to generate the group. The two generators, commonly denoted as S (for the $\frac{\pi}{2}$ rotations) and T (for the $\frac{\pi}{3}$ rotations) can be written explicitely in block-diagonal form as

$$S = \begin{pmatrix} 1 & 0 & 0 & 0 \\ 0 & 1 & 0 & 0 \\ 0 & 0 & -1 & 0 \\ 0 & 0 & 0 & -1 \end{pmatrix}, \qquad T = \begin{pmatrix} 1 & 0 & 0 & 0 \\ 0 & 0 & 1 & 0 \\ 0 & 0 & 0 & 1 \\ 0 & 1 & 0 & 0 \end{pmatrix}. \tag{B.1}$$

The generators satisfy $S^2 = T^3 = \mathbb{1}$ as well as $(ST)^3 = \mathbb{1}$ and result in a total of 12 group elements. Due to the block-diagonal structure of S and T, an irreducible representation of A_4 consists of a singlet and a triplet, $\mathbf{4} \to \mathbf{1} \oplus \mathbf{3}$. This can also be understood geometrically, when rotating the tetrahedron around a fixed vertex. The fixed vertex then represents the singlet, while the remaining three vertices correspond to the triplet. Lastly, due to $T^3 = 1$, there are two more singlets denoted as $\mathbf{1}'$ and $\mathbf{1}''$, which do not have a geometric interpretation in terms of a tetrahedron.

B.2 The Cyclic Group Z_5

Cyclic groups are generated by a single element g. All other elements of the group can be obtained by repeatedly applying the group operation or its inverse to g. Exemplarily, the roots of unity

$$z^n = 1\,, \tag{B.2}$$

with $z \in \mathbb{C}$ and $n \in \mathbb{N}$ form the cyclic group Z_n under multiplication and a specific representation of the generating group element is e.g.

$$g = \mathrm{e}^{\frac{2\pi \mathrm{i}}{n}}\,. \tag{B.3}$$

In this manner, the group Z_5 therefore contains the five elements (sometimes also referred to as *charges*) $1 = \alpha^0$, $\alpha = \alpha^1$, α^2, α^3, α^4, given by

$$\alpha^k = \mathrm{e}^{\frac{2\pi \mathrm{i} k}{5}} \,. \tag{B.4}$$

with $k = 0, 1, 2, 3, 4$.

C ZP-TP-DM Benchmark Cutflows

In the following two tables A1 and A2, we provide four benchmarks for the full process of figure 4.3 and its QCD induced production respectively. Additionally, the `CheckMATE` cutflows for each benchmark are also shown. The couplings of all benchmark points read $\lambda_{Z'q\bar{q}} = \lambda_{Z'\ell^+\ell^-} = 0.25$, $\lambda_{Z'T_s'\overline{T_s'}} = 2.5$, $\lambda_{\phi H} = 0$ and $\lambda_{\phi T_s' t} = 0.1$. We also provide the benchmark "BP2-RR", which is the chiral counterpart to the LL choice we used in this thesis (see section 4.3.1) and has $\lambda_{Z'q\bar{q},R} = \lambda_{Z'\ell^+\ell^-,R} = 0.25$, $\lambda_{Z'T_s'\overline{T_s'},R} = 2.5$ and $\lambda_{Z'q\bar{q},L} = 0 = \lambda_{Z'\ell^+\ell^-,L}$, $\lambda_{Z'T_s'\overline{T_s'},L} = 0$.

	Parameter	BP1	BP2	BP2-RR	BP3	BP4
Input	$M_{Z'}$ [GeV]	2500	3000	3000	3000	3500
	$M_{T'_s}$ [GeV]	1150	1200	1200	1500	1700
	m_ϕ [GeV]	600	300	300	300	500
	$\Gamma_{Z'}$ [GeV]	241.75	435.61	435.61	59.61	227.40
	$\frac{\Gamma_{Z'}}{M_{Z'}}$ [%]	16.11	14.52	14.52	1.99	6.50
	σ [fb]	66.24	28.29	28.29	20.46	5.40
Cutflow	0_trigger_etmiss	0.81518	0.90046	0.89952	0.92820	0.93820
	1_lepton_onelepton	0.17616	0.18460	0.18678	0.18566	0.18072
	2_mt	0.17184	0.17992	0.18190	0.18166	0.17734
	3_jets	0.16436	0.16782	0.17030	0.17042	0.16630
	tN_high_01_tauVeto	0.14892	0.15640	0.15716	0.16108	0.15782
	tN_high_02_nJets	0.08944	0.08940	0.09160	0.08970	0.08618
	tN_high_03_JetsPT	0.07292	0.07766	0.07934	0.08020	0.07594
	tN_high_04_etmiss	0.03268	0.05156	0.05208	0.06118	0.06030
	tN_high_05_etmissVcal	0.03268	0.05156	0.05208	0.06118	0.06030
	tN_high_06_htmiss	0.03250	0.05118	0.05162	0.06092	0.05970
	tN_high_07_mt	0.02930	0.04672	0.04706	0.05612	0.05526
	tN_high_08_amt2	0.02872	0.04578	0.04626	0.05542	0.05456
	tN_high_09_no	0.02872	0.04578	0.04626	0.05542	0.05456
	tN_high_10_no	0.02872	0.04578	0.04626	0.05542	0.05456
	tN_high_11_dR	0.02638	0.04082	0.04046	0.05090	0.04934
	tN_high_12_LRJET_PT	0.02354	0.03846	0.03808	0.04888	0.04766
	tN_high_13_LRJET_M	0.02146	0.03530	0.03480	0.04580	0.04412
	tN_high_14_dphi	**0.02030**	**0.03334**	**0.03250**	**0.04272**	**0.04104**

Table A1: Benchmarks for the full process (see figure 4.3) together with the CheckMATE cutflow efficiencies (fraction of events surviving a certain cut, normalised to 1). The couplings for all points read $\lambda_{Z'q\bar{q}} = \lambda_{Z'\ell^+\ell^-} = 0.25$, $\lambda_{Z'T'_s\overline{T'_s}} = 2.5$, $\lambda_{\phi H} = 0$ and $\lambda_{\phi T'_s t} = 0.1$. The cutflow corresponds to the SR tN_high from ATLAS_CONF_2016_050, which yields the best limits.

	Parameter	BP1-QCD	BP2-QCD	BP3-QCD	BP4-QCD
Input	$M_{Z'}$ [GeV]	-	-	-	-
	$M_{T'_s}$ [GeV]	1150	1200	1500	1700
	m_ϕ [GeV]	600	300	300	500
	$\Gamma_{Z'}$ [GeV]	-	-	-	-
	$\frac{\Gamma_{Z'}}{M_{Z'}}$ [%]	-	-	-	-
	σ [fb]	11.62	8.49	1.49	0.51
Cutflow	0_trigger_etmiss	0.81470	0.88948	0.93012	0.93932
	1_lepton_onelepton	0.17338	0.18490	0.17670	0.17674
	2_mt	0.16814	0.17936	0.17280	0.17274
	3_jets	0.15880	0.16744	0.16024	0.15952
	tN_high_01_tauVeto	0.14244	0.15376	0.15060	0.15032
	tN_high_02_nJets	0.09092	0.09196	0.08616	0.08528
	tN_high_03_JetsPT	0.07704	0.08022	0.07682	0.07574
	tN_high_04_etmiss	0.03576	0.05076	0.05804	0.05862
	tN_high_05_etmissVcal	0.03576	0.05076	0.05804	0.05862
	tN_high_06_htmiss	0.03550	0.05028	0.05714	0.05772
	tN_high_07_mt	0.03136	0.04468	0.05164	0.05316
	tN_high_08_amt2	0.03036	0.04368	0.05060	0.05240
	tN_high_09_no	0.03036	0.04368	0.05060	0.05240
	tN_high_10_no	0.03036	0.04368	0.05060	0.05240
	tN_high_11_dR	0.02664	0.03830	0.04402	0.04580
	tN_high_12_LRJET_PT	0.02330	0.03596	0.04244	0.04444
	tN_high_13_LRJET_M	0.02082	0.03284	0.03910	0.04080
	tN_high_14_dphi	**0.01976**	**0.03062**	**0.03662**	**0.03844**

Table A2: QCD benchmarks (see figure 4.3, centre and right) together with the CheckMATE cutflow efficiencies (fraction of events surviving a certain cut, normalised to 1). The couplings for all points read $\lambda_{Z'q\bar{q}} = \lambda_{Z'\ell^+\ell^-} = 0.25$, $\lambda_{Z'T'_s\overline{T'_s}} = 2.5$, $\lambda_{\phi H} = 0$ and $\lambda_{\phi T'_s t} = 0.1$. The cutflow corresponds to the SR tN_high from ATLAS_CONF_2016_050, which yields the best limits.

D Derivation of the Unitarity Bound

The below derivation of the unitarity bound closely follows the reasoning in Ref. [204]. The unitarity bound is a consequence of the unitarity condition of the S matrix, $S^\dagger S = \mathbb{1}$. Expressing $S = \mathbb{1} + \mathrm{i}T$ leads to $T^\dagger T = 2\,\mathrm{Im}\,T$. When taking the matrix element of both sides between identical two-body states and inserting a complete set of intermediate states into the left-hand

side, one gets

$$\int \mathrm{dPS}_2 \; |T_{\mathrm{el}}(2 \to 2)|^2 + \sum_n \int \mathrm{dPS}_n \; |T_{\mathrm{inel}}(2 \to n)|^2 = 2 \, \mathrm{Im} \, T_{\mathrm{el}}(2 \to 2) \tag{D.1}$$

with the n-body phase space dPS_n and the sum runs over all inelastic intermediate states with $n \geq 2$. Now define the $2 \to 2$ elastic scattering amplitude via the partial wave expansion as

$$T_{\mathrm{el}} \, (2 \to 2) = 16\pi \sum_j (2j+1) \, P_j \, (\cos\theta) \; a_j^{\mathrm{el}} \tag{D.2}$$

with

$$a_j^{\mathrm{el}} = \frac{1}{32\pi} \int_{-1}^{1} \mathrm{d} \cos\theta \, P_j \, (\cos\theta) \; T_{\mathrm{el}} \, (2 \to 2) \; , \tag{D.3}$$

where $P_j(x)$ are the Legendre polynomials, θ is the scattering angle and the incoming and outgoing particles are assumed to have the same helicities. With equations (D.2) and (D.3), one can compute

$$\int \mathrm{dPS}_2 \; |T_{\mathrm{el}} \, (2 \to 2)|^2 = 32\pi \sum_j (2j+1) \, |a_j^{\mathrm{el}}|^2 \tag{D.4}$$

and further rephrase equation (D.1) to

$$\sum_j (2j+1) \left(\frac{1}{4} - \left(\mathrm{Re} \, a_j^{\mathrm{el}} \right)^2 - \left(\mathrm{Im} \, a_j^{\mathrm{el}} - \frac{1}{2} \right)^2 \right) = \frac{1}{32\pi} \sum_n \int \mathrm{dPS}_n \; |T_{\mathrm{inel}}(2 \to n)|^2 \geq 0 \, . \tag{D.5}$$

Since the right-hand side of equation (D.5) is positive, there exists a consistent solution for each value of j,

$$\left(\mathrm{Re} \, a_j^{\mathrm{el}} \right)^2 + \left(\mathrm{Im} \, a_j^{\mathrm{el}} - \frac{1}{2} \right)^2 \leq \frac{1}{4} \, , \tag{D.6}$$

leading to

$$\left| \mathrm{Re} \, a_j^{\mathrm{el}} \right| \leq \frac{1}{2} \, , \tag{D.7}$$

$$\left| a_j^{\mathrm{el}} \right| \leq 1 \, . \tag{D.8}$$

Lastly, by assuming s-wave dominance (i.e. the $j = 0$ contribution to be dominant in the elastic channel), an upper bound for the inelastic cross section $\sigma_{\mathrm{inel}} \, (2 \to n)$ can be derived using equa-

tion (D.5),

$$\sigma_{\text{inel}}(2 \to n) \quad \leq \quad \frac{4\pi}{s}\,, \tag{D.9}$$

which is the desired unitarity bound.

Bibliography

[1] U. le Verrier, "Lettre de M. Le Verrier à M. Faye sur la théorie de Mercure et sur le movement du périhélie de cette planète." `https://archive.org/stream/comptesrendusheb49acad/#page/378/mode/2up`, 1859. Online; accessed 16/10/2017.

[2] G. Arnison *et al.*, "Experimental Observation of Isolated Large Transverse Energy Electrons with Associated Missing Energy at s**(1/2) = 540-GeV," *Phys. Lett.*, vol. 122B, pp. 103–116, 1983. [,611(1983)].

[3] M. Banner *et al.*, "Observation of Single Isolated Electrons of High Transverse Momentum in Events with Missing Transverse Energy at the CERN anti-p p Collider," *Phys. Lett.*, vol. 122B, pp. 476–485, 1983.

[4] G. Arnison *et al.*, "Experimental Observation of Lepton Pairs of Invariant Mass Around 95-GeV/c**2 at the CERN SPS Collider," *Phys. Lett.*, vol. 126B, pp. 398–410, 1983.

[5] S. Schael *et al.*, "Precision electroweak measurements on the Z resonance," *Phys. Rept.*, vol. 427, pp. 257–454, 2006.

[6] R. Barate *et al.*, "Search for the standard model Higgs boson at LEP," *Phys. Lett.*, vol. B565, pp. 61–75, 2003.

[7] G. Aad *et al.*, "Observation of a new particle in the search for the Standard Model Higgs boson with the ATLAS detector at the LHC," *Phys. Lett.*, vol. B716, pp. 1–29, 2012.

[8] S. Chatrchyan *et al.*, "Observation of a new boson at a mass of 125 GeV with the CMS experiment at the LHC," *Phys. Lett.*, vol. B716, pp. 30–61, 2012.

[9] K. Kodama *et al.*, "Observation of tau neutrino interactions," *Phys. Lett.*, vol. B504, pp. 218–224, 2001.

[10] S. Abachi *et al.*, "Observation of the top quark," *Phys. Rev. Lett.*, vol. 74, pp. 2632–2637, 1995.

[11] S. L. Glashow, J. Iliopoulos, and L. Maiani, "Weak Interactions with Lepton-Hadron Symmetry," *Phys. Rev.*, vol. D2, pp. 1285–1292, 1970.

[12] S. W. Herb *et al.*, "Observation of a Dimuon Resonance at 9.5-GeV in 400-GeV Proton-Nucleus Collisions," *Phys. Rev. Lett.*, vol. 39, pp. 252–255, 1977.

[13] D. Hanneke, S. F. Hoogerheide, and G. Gabrielse, "Cavity Control of a Single-Electron Quantum Cyclotron: Measuring the Electron Magnetic Moment," *Phys. Rev.*, vol. A83, p. 052122, 2011.

[14] F. Zwicky, "On the Masses of Nebulae and of Clusters of Nebulae," *Astrophys. J.*, vol. 86, pp. 217–246, 1937.

[15] D. Clowe, M. Bradac, A. H. Gonzalez, M. Markevitch, S. W. Randall, C. Jones, and D. Zaritsky, "A direct empirical proof of the existence of dark matter," *Astrophys. J.*, vol. 648, pp. L109–L113, 2006.

[16] P. A. R. Ade *et al.*, "Planck 2015 results. XIII. Cosmological parameters," *Astron. Astrophys.*, vol. 594, p. A13, 2016.

[17] M. R. Lovell, V. Eke, C. S. Frenk, L. Gao, A. Jenkins, T. Theuns, J. Wang, D. M. White, A. Boyarsky, and O. Ruchayskiy, "The Haloes of Bright Satellite Galaxies in a Warm Dark Matter Universe," *Mon. Not. Roy. Astron. Soc.*, vol. 420, pp. 2318–2324, 2012.

[18] Y. Fukuda *et al.*, "Evidence for oscillation of atmospheric neutrinos," *Phys. Rev. Lett.*, vol. 81, pp. 1562–1567, 1998.

[19] J. M. Pendlebury *et al.*, "Revised experimental upper limit on the electric dipole moment of the neutron," *Phys. Rev.*, vol. D92, no. 9, p. 092003, 2015.

[20] D. Baumann, "Inflation," in *Physics of the large and the small, TASI 09, proceedings of the Theoretical Advanced Study Institute in Elementary Particle Physics, Boulder, Colorado, USA, 1-26 June 2009*, pp. 523–686, 2011.

[21] A. D. Sakharov, "Violation of CP Invariance, c Asymmetry, and Baryon Asymmetry of the Universe," *Pisma Zh. Eksp. Teor. Fiz.*, vol. 5, pp. 32–35, 1967. [Usp. Fiz. Nauk161,61(1991)].

[22] J. H. Christenson, J. W. Cronin, V. L. Fitch, and R. Turlay, "Evidence for the 2π Decay of the K_2^0 Meson," *Phys. Rev. Lett.*, vol. 13, pp. 138–140, 1964.

[23] S. R. Coleman and J. Mandula, "All Possible Symmetries of the S Matrix," *Phys. Rev.*, vol. 159, pp. 1251–1256, 1967.

[24] R. Haag, J. T. Lopuszanski, and M. Sohnius, "All Possible Generators of Supersymmetries of the s Matrix," *Nucl. Phys.*, vol. B88, p. 257, 1975.

[25] L. Girardello and M. T. Grisaru, "Soft Breaking of Supersymmetry," *Nucl. Phys.*, vol. B194, p. 65, 1982.

[26] S. P. Martin, "A Supersymmetry primer," 1997. [Adv. Ser. Direct. High Energy Phys.18,1(1998)].

[27] S. Dimopoulos and D. W. Sutter, "The Supersymmetric flavor problem," *Nucl. Phys.*, vol. B452, pp. 496–512, 1995.

[28] D. J. H. Chung, L. L. Everett, G. L. Kane, S. F. King, J. D. Lykken, and L.-T. Wang, "The Soft supersymmetry breaking Lagrangian: Theory and applications," *Phys. Rept.*, vol. 407, pp. 1–203, 2005.

[29] A. S. Belyaev, J. E. Camargo-Molina, S. F. King, D. J. Miller, A. P. Morais, and P. B. Schaefers, "A to Z of the Muon Anomalous Magnetic Moment in the MSSM with Pati-Salam at the GUT scale," *JHEP*, vol. 06, p. 142, 2016.

[30] A. S. Belyaev, S. F. King, and P. B. Schaefers, "Muon g-2 and Dark Matter suggest Non-Universal Gaugino Masses: $\mathbf{SU(5)} \times \mathbf{A_4}$ case study at the LHC," 2018.

[31] A. S. Belyaev, T. Flacke, B. Jain, and P. B. Schaefers, "LHC Dark Matter Signals from Vector Resonances and Top Partners," 2017.

[32] A. S. Belyaev, P. B. Schaefers, and M. C. Thomas, "Precise test of Higgs properties via triple Higgs production in VBF at future colliders," 2018.

[33] P. Bechtle *et al.*, "Constrained Supersymmetry after two years of LHC data: a global view with Fittino," *JHEP*, vol. 06, p. 098, 2012.

[34] O. Buchmueller *et al.*, "The CMSSM and NUHM1 in Light of 7 TeV LHC, $B_s \to \mu^+\mu^-$ and XENON100 Data," *Eur. Phys. J.*, vol. C72, p. 2243, 2012.

[35] C. Balazs, A. Buckley, D. Carter, B. Farmer, and M. White, "Should we still believe in constrained supersymmetry?," *Eur. Phys. J.*, vol. C73, p. 2563, 2013.

[36] M. Ibe, T. T. Yanagida, and N. Yokozaki, "Muon g-2 and 125 GeV Higgs in Split-Family Supersymmetry," *JHEP*, vol. 08, p. 067, 2013.

[37] M. Endo, K. Hamaguchi, S. Iwamoto, and T. Yoshinaga, "Muon g-2 vs LHC in Supersymmetric Models," *JHEP*, vol. 01, p. 123, 2014.

[38] D. J. Miller and A. P. Morais, "Supersymmetric SU(5) Grand Unification for a Post Higgs Boson Era," *JHEP*, vol. 10, p. 226, 2013.

[39] D. J. Miller and A. P. Morais, "Supersymmetric SO(10) Grand Unification at the LHC and Beyond," *JHEP*, vol. 12, p. 132, 2014.

[40] H. Baer, A. Belyaev, T. Krupovnickas, and A. Mustafayev, "SUSY normal scalar mass hierarchy reconciles (g-2)(mu), b $\to$ s gamma and relic density," *JHEP*, vol. 06, p. 044, 2004.

[41] A. Djouadi *et al.*, "The Minimal supersymmetric standard model: Group summary report," in *GDR (Groupement De Recherche) - Supersymetrie Montpellier, France, April 15-17, 1998*, 1998.

[42] S. F. King, "A to Z of Flavour with Pati-Salam," *JHEP*, vol. 08, p. 130, 2014.

[43] G. W. Bennett *et al.*, "Final Report of the Muon E821 Anomalous Magnetic Moment Measurement at BNL," *Phys. Rev.*, vol. D73, p. 072003, 2006.

[44] K. A. Olive *et al.*, "Review of Particle Physics," *Chin. Phys.*, vol. C38, p. 090001, 2014.

[45] J. Grange *et al.*, "Muon (g-2) Technical Design Report," 2015.

[46] N. Saito, "A novel precision measurement of muon g-2 and EDM at J-PARC," *AIP Conf. Proc.*, vol. 1467, pp. 45–56, 2012.

[47] F. Jegerlehner and A. Nyffeler, "The Muon g-2," *Phys. Rept.*, vol. 477, pp. 1–110, 2009.

[48] T. Blum, A. Denig, I. Logashenko, E. de Rafael, B. Lee Roberts, T. Teubner, and G. Venanzoni, "The Muon (g-2) Theory Value: Present and Future," 2013.

[49] M. Benayoun *et al.*, "Hadronic contributions to the muon anomalous magnetic moment Workshop. $(g-2)_\mu$: Quo vadis? Workshop. Mini proceedings," 2014.

[50] M. Knecht, "The Muon Anomalous Magnetic Moment," *Nucl. Part. Phys. Proc.*, vol. 258-259, pp. 235–240, 2015.

[51] T. Aoyama, M. Hayakawa, T. Kinoshita, and M. Nio, "Complete Tenth-Order QED Contribution to the Muon g-2," *Phys. Rev. Lett.*, vol. 109, p. 111808, 2012.

[52] A. L. Kataev, "Analytical eighth-order light-by-light QED contributions from leptons with heavier masses to the anomalous magnetic moment of electron," *Phys. Rev.*, vol. D86, p. 013010, 2012.

[53] R. Lee, P. Marquard, A. V. Smirnov, V. A. Smirnov, and M. Steinhauser, "Four-loop corrections with two closed fermion loops to fermion self energies and the lepton anomalous magnetic moment," *JHEP*, vol. 03, p. 162, 2013.

[54] A. Kurz, T. Liu, P. Marquard, and M. Steinhauser, "Anomalous magnetic moment with heavy virtual leptons," *Nucl. Phys.*, vol. B879, pp. 1–18, 2014.

[55] A. Kurz, T. Liu, P. Marquard, A. V. Smirnov, V. A. Smirnov, and M. Steinhauser, "Light-by-light-type corrections to the muon anomalous magnetic moment at four-loop order," *Phys. Rev.*, vol. D92, no. 7, p. 073019, 2015.

[56] A. Czarnecki, W. J. Marciano, and A. Vainshtein, "Refinements in electroweak contributions to the muon anomalous magnetic moment," *Phys. Rev.*, vol. D67, p. 073006, 2003. [Erratum: Phys. Rev.D73,119901(2006)].

[57] C. Gnendiger, D. Stöckinger, and H. Stöckinger-Kim, "The electroweak contributions to $(g-2)_\mu$ after the Higgs boson mass measurement," *Phys. Rev.*, vol. D88, p. 053005, 2013.

[58] A. Nyffeler, "Hadronic light-by-light scattering in the muon g-2: A New short-distance constraint on pion-exchange," *Phys. Rev.*, vol. D79, p. 073012, 2009.

[59] M. Davier, A. Hoecker, B. Malaescu, and Z. Zhang, "Reevaluation of the Hadronic Contributions to the Muon g-2 and to alpha(MZ)," *Eur. Phys. J.*, vol. C71, p. 1515, 2011. [Erratum: Eur. Phys. J.C72,1874(2012)].

[60] K. Hagiwara, R. Liao, A. D. Martin, D. Nomura, and T. Teubner, "$(g-2)_\mu$ and $\alpha(M_Z^2)$ re-evaluated using new precise data," *J. Phys.*, vol. G38, p. 085003, 2011.

[61] M. Benayoun, P. David, L. DelBuono, and F. Jegerlehner, "An Update of the HLS Estimate of the Muon g-2," *Eur. Phys. J.*, vol. C73, p. 2453, 2013.

[62] G. Colangelo, M. Hoferichter, M. Procura, and P. Stoffer, "Dispersive approach to hadronic light-by-light scattering," *JHEP*, vol. 09, p. 091, 2014.

[63] A. Kurz, T. Liu, P. Marquard, and M. Steinhauser, "Hadronic contribution to the muon anomalous magnetic moment to next-to-next-to-leading order," *Phys. Lett.*, vol. B734, pp. 144–147, 2014.

[64] G. Colangelo, M. Hoferichter, A. Nyffeler, M. Passera, and P. Stoffer, "Remarks on higher-order hadronic corrections to the muon g-2," *Phys. Lett.*, vol. B735, pp. 90–91, 2014.

[65] G. Colangelo, M. Hoferichter, B. Kubis, M. Procura, and P. Stoffer, "Towards a data-driven analysis of hadronic light-by-light scattering," *Phys. Lett.*, vol. B738, pp. 6–12, 2014.

[66] V. Pauk and M. Vanderhaeghen, "Anomalous magnetic moment of the muon in a dispersive approach," *Phys. Rev.*, vol. D90, no. 11, p. 113012, 2014.

[67] G. Colangelo, M. Hoferichter, M. Procura, and P. Stoffer, "Dispersion relation for hadronic light-by-light scattering: theoretical foundations," *JHEP*, vol. 09, p. 074, 2015.

[68] M. Benayoun, P. David, L. DelBuono, and F. Jegerlehner, "Muon $g-2$ estimates: can one trust effective Lagrangians and global fits?," *Eur. Phys. J.*, vol. C75, no. 12, p. 613, 2015.

[69] T. Blum, S. Chowdhury, M. Hayakawa, and T. Izubuchi, "Hadronic light-by-light scattering contribution to the muon anomalous magnetic moment from lattice QCD," *Phys. Rev. Lett.*, vol. 114, no. 1, p. 012001, 2015.

[70] L. Jin, T. Blum, N. Christ, M. Hayakawa, T. Izubuchi, and C. Lehner, "Lattice Calculation of the Connected Hadronic Light-by-Light Contribution to the Muon Anomalous Magnetic Moment," in *12th Conference on the Intersections of Particle and Nuclear Physics (CIPANP 2015) Vail, Colorado, USA, May 19-24, 2015*, 2015.

[71] B. Chakraborty, C. T. H. Davies, J. Koponen, G. P. Lepage, M. J. Peardon, and S. M. Ryan, "An estimate of the hadronic vacuum polarization disconnected contribution to the anomalous magnetic moment of the muon from lattice QCD," 2015.

[72] C. Aubin, T. Blum, P. Chau, M. Golterman, S. Peris, and C. Tu, "Finite-volume effects in the muon anomalous magnetic moment on the lattice," 2015.

[73] T. Blum, P. A. Boyle, T. Izubuchi, L. Jin, A. Jüttner, C. Lehner, K. Maltman, M. Marinkovic, A. Portelli, and M. Spraggs, "Calculation of the hadronic vacuum polarization disconnected contribution to the muon anomalous magnetic moment," 2015.

[74] J. A. Grifols and A. Mendez, "Constraints on Supersymmetric Particle Masses From $(g-2)$ μ," *Phys. Rev.*, vol. D26, p. 1809, 1982.

[75] J. R. Ellis, J. S. Hagelin, and D. V. Nanopoulos, "Spin 0 Leptons and the Anomalous Magnetic Moment of the Muon," *Phys. Lett.*, vol. B116, p. 283, 1982.

[76] J. Chakrabortty, S. Mohanty, and S. Rao, "Non-universal gaugino mass GUT models in the light of dark matter and LHC constraints," *JHEP*, vol. 02, p. 074, 2014.

[77] J. Chakrabortty, A. Choudhury, and S. Mondal, "Non-universal Gaugino mass models under the lamppost of muon (g-2)," *JHEP*, vol. 07, p. 038, 2015.

[78] R. Barbieri and L. Maiani, "The Muon Anomalous Magnetic Moment in Broken Supersymmetric Theories," *Phys. Lett.*, vol. B117, p. 203, 1982.

[79] D. A. Kosower, L. M. Krauss, and N. Sakai, "Low-Energy Supergravity and the Anomalous Magnetic Moment of the Muon," *Phys. Lett.*, vol. B133, p. 305, 1983.

[80] T. C. Yuan, R. L. Arnowitt, A. H. Chamseddine, and P. Nath, "Supersymmetric Electroweak Effects on G-2 (mu)," *Z. Phys.*, vol. C26, p. 407, 1984.

[81] J. C. Romao, A. Barroso, M. C. Bento, and G. C. Branco, "Flavor Violation in Supersymmetric Theories," *Nucl. Phys.*, vol. B250, p. 295, 1985.

[82] J. L. Lopez, D. V. Nanopoulos, and X. Wang, "Large (g-2)-mu in SU(5) x U(1) supergravity models," *Phys. Rev.*, vol. D49, pp. 366–372, 1994.

[83] T. Moroi, "The Muon anomalous magnetic dipole moment in the minimal supersymmetric standard model," *Phys. Rev.*, vol. D53, pp. 6565–6575, 1996. [Erratum: Phys. Rev.D56,4424(1997)].

[84] S. P. Martin and J. D. Wells, "Constraints on ultraviolet stable fixed points in supersymmetric gauge theories," *Phys. Rev.*, vol. D64, p. 036010, 2001.

[85] A. Czarnecki and W. J. Marciano, "The Muon anomalous magnetic moment: A Harbinger for 'new physics'," *Phys. Rev.*, vol. D64, p. 013014, 2001.

[86] G.-C. Cho, K. Hagiwara, Y. Matsumoto, and D. Nomura, "The MSSM confronts the precision electroweak data and the muon g-2," *JHEP*, vol. 11, p. 068, 2011.

[87] M. Endo, K. Hamaguchi, S. Iwamoto, and N. Yokozaki, "Higgs Mass and Muon Anomalous Magnetic Moment in Supersymmetric Models with Vector-Like Matters," *Phys. Rev.*, vol. D84, p. 075017, 2011.

[88] M. Endo, K. Hamaguchi, S. Iwamoto, and N. Yokozaki, "Higgs mass, muon g-2, and LHC prospects in gauge mediation models with vector-like matters," *Phys. Rev.*, vol. D85, p. 095012, 2012.

[89] M. Endo, K. Hamaguchi, S. Iwamoto, K. Nakayama, and N. Yokozaki, "Higgs mass and muon anomalous magnetic moment in the U(1) extended MSSM," *Phys. Rev.*, vol. D85, p. 095006, 2012.

[90] J. L. Evans, M. Ibe, S. Shirai, and T. T. Yanagida, "A 125GeV Higgs Boson and Muon g-2 in More Generic Gauge Mediation," *Phys. Rev.*, vol. D85, p. 095004, 2012.

[91] S. Mohanty, S. Rao, and D. P. Roy, "Reconciling the muon $g-2$ and dark matter relic density with the LHC results in nonuniversal gaugino mass models," *JHEP*, vol. 09, p. 027, 2013.

[92] S. Akula and P. Nath, "Gluino-driven radiative breaking, Higgs boson mass, muon g-2, and the Higgs diphoton decay in supergravity unification," *Phys. Rev.*, vol. D87, no. 11, p. 115022, 2013.

[93] N. Okada, S. Raza, and Q. Shafi, "Particle Spectroscopy of Supersymmetric SU(5) in Light of 125 GeV Higgs and Muon g-2 Data," *Phys. Rev.*, vol. D90, no. 1, p. 015020, 2014.

[94] M. Endo, K. Hamaguchi, T. Kitahara, and T. Yoshinaga, "Probing Bino contribution to muon $g-2$," *JHEP*, vol. 11, p. 013, 2013.

[95] G. Bhattacharyya, B. Bhattacherjee, T. T. Yanagida, and N. Yokozaki, "A practical GMSB model for explaining the muon (g-2) with gauge coupling unification," *Phys. Lett.*, vol. B730, pp. 231–235, 2014.

[96] I. Gogoladze, F. Nasir, Q. Shafi, and C. S. Un, "Nonuniversal Gaugino Masses and Muon g-2," *Phys. Rev.*, vol. D90, no. 3, p. 035008, 2014.

[97] J. Kersten, J.-h. Park, D. Stöckinger, and L. Velasco-Sevilla, "Understanding the correlation between $(g-2)_\mu$ and $\mu \to e\gamma$ in the MSSM," *JHEP*, vol. 08, p. 118, 2014.

[98] T. Li and S. Raza, "Electroweak supersymmetry from the generalized minimal supergravity model in the MSSM," *Phys. Rev.*, vol. D91, no. 5, p. 055016, 2015.

[99] W.-C. Chiu, C.-Q. Geng, and D. Huang, "Correlation Between Muon $g-2$ and $\mu \to e\gamma$," *Phys. Rev.*, vol. D91, no. 1, p. 013006, 2015.

[100] M. Badziak, Z. Lalak, M. Lewicki, M. Olechowski, and S. Pokorski, "Upper bounds on sparticle masses from muon g - 2 and the Higgs mass and the complementarity of future colliders," *JHEP*, vol. 03, p. 003, 2015.

[101] L. Calibbi, I. Galon, A. Masiero, P. Paradisi, and Y. Shadmi, "Charged Slepton Flavor post the 8 TeV LHC: A Simplified Model Analysis of Low-Energy Constraints and LHC SUSY Searches," *JHEP*, vol. 10, p. 043, 2015.

[102] K. Kowalska, L. Roszkowski, E. M. Sessolo, and A. J. Williams, "GUT-inspired SUSY and the muon g - 2 anomaly: prospects for LHC 14 TeV," *JHEP*, vol. 06, p. 020, 2015.

[103] F. Wang, W. Wang, and J. M. Yang, "Reconcile muon g-2 anomaly with LHC data in SUGRA with generalized gravity mediation," *JHEP*, vol. 06, p. 079, 2015.

[104] P. A. R. Ade *et al.*, "Planck 2013 results. XVI. Cosmological parameters," *Astron. Astrophys.*, vol. 571, p. A16, 2014.

[105] D. S. Akerib *et al.*, "First results from the LUX dark matter experiment at the Sanford Underground Research Facility," *Phys. Rev. Lett.*, vol. 112, p. 091303, 2014.

[106] G. Aad *et al.*, "Combined Measurement of the Higgs Boson Mass in pp Collisions at $\sqrt{s} = 7$ and 8 TeV with the ATLAS and CMS Experiments," *Phys. Rev. Lett.*, vol. 114, p. 191803, 2015.

[107] J. P. Lees *et al.*, "Exclusive Measurements of $b \to s\gamma$ Transition Rate and Photon Energy Spectrum," *Phys. Rev.*, vol. D86, p. 052012, 2012.

[108] S. Chatrchyan *et al.*, "Measurement of the B(s) to mu+ mu- branching fraction and search for B0 to mu+ mu- with the CMS Experiment," *Phys. Rev. Lett.*, vol. 111, p. 101804, 2013.

[109] J. Alwall, R. Frederix, S. Frixione, V. Hirschi, F. Maltoni, *et al.*, "The automated computation of tree-level and next-to-leading order differential cross sections, and their matching to parton shower simulations," *JHEP*, vol. 1407, p. 079, 2014.

[110] T. Sjostrand, S. Mrenna, and P. Z. Skands, "PYTHIA 6.4 Physics and Manual," *JHEP*, vol. 05, p. 026, 2006.

[111] J. de Favereau, C. Delaere, P. Demin, A. Giammanco, V. Lemaître, A. Mertens, and M. Selvaggi, "DELPHES 3, A modular framework for fast simulation of a generic collider experiment," *JHEP*, vol. 02, p. 057, 2014.

[112] M. Drees, H. Dreiner, D. Schmeier, J. Tattersall, and J. S. Kim, "CheckMATE: Confronting your Favourite New Physics Model with LHC Data," *Comput. Phys. Commun.*, vol. 187, pp. 227–265, 2014.

[113] G. Aad *et al.*, "Search for direct production of charginos and neutralinos in events with three leptons and missing transverse momentum in $\sqrt{s} = 8$TeV pp collisions with the ATLAS detector," *JHEP*, vol. 04, p. 169, 2014.

[114] "Search for direct production of charginos and neutralinos in events with three leptons and missing transverse momentum in $21\,\text{fb}^{-1}$ of pp collisions at $\sqrt{s} = 8\,\text{TeV}$ with the ATLAS detector," 2013.

[115] B. C. Allanach, "SOFTSUSY: a program for calculating supersymmetric spectra," *Comput. Phys. Commun.*, vol. 143, pp. 305–331, 2002.

[116] G. Belanger, F. Boudjema, A. Pukhov, and A. Semenov, "micrOMEGAs_3: A program for calculating dark matter observables," *Comput. Phys. Commun.*, vol. 185, pp. 960–985, 2014.

[117] J. E. Camargo-Molina, B. O'Leary, W. Porod, and F. Staub, "**Vevacious**: A Tool For Finding The Global Minima Of One-Loop Effective Potentials With Many Scalars," *Eur. Phys. J.*, vol. C73, no. 10, p. 2588, 2013.

[118] J. E. Camargo-Molina, B. O'Leary, W. Porod, and F. Staub, "Stability of the CMSSM against sfermion VEVs," *JHEP*, vol. 12, p. 103, 2013.

[119] A. Corsetti and P. Nath, "Gaugino mass nonuniversality and dark matter in SUGRA, strings and D-brane models," *Phys. Rev.*, vol. D64, p. 125010, 2001.

[120] S. F. King, J. P. Roberts, and D. P. Roy, "Natural dark matter in SUSY GUTs with non-universal gaugino masses," *JHEP*, vol. 10, p. 106, 2007.

[121] U. Chattopadhyay, D. Das, and D. P. Roy, "Mixed Neutralino Dark Matter in Nonuniversal Gaugino Mass Models," *Phys. Rev.*, vol. D79, p. 095013, 2009.

[122] B. Ananthanarayan and P. N. Pandita, "Sparticle Mass Spectrum in Grand Unified Theories," *Int. J. Mod. Phys.*, vol. A22, pp. 3229–3259, 2007.

[123] S. Bhattacharya, A. Datta, and B. Mukhopadhyaya, "Non-universal gaugino masses: A Signal-based analysis for the Large Hadron Collider," *JHEP*, vol. 10, p. 080, 2007.

[124] S. P. Martin, "Non-universal gaugino masses from non-singlet F-terms in non-minimal unified models," *Phys. Rev.*, vol. D79, p. 095019, 2009.

[125] S. P. Martin, "Nonuniversal gaugino masses and seminatural supersymmetry in view of the Higgs boson discovery," *Phys. Rev.*, vol. D89, no. 3, p. 035011, 2014.

[126] A. Anandakrishnan and S. Raby, "Yukawa Unification Predictions with effective "Mirage" Mediation," *Phys. Rev. Lett.*, vol. 111, no. 21, p. 211801, 2013.

[127] M. A. Ajaib, "SU(5) with Non-Universal Gaugino Masses," 2017.

[128] B. D. Callen and R. R. Volkas, "Large lepton mixing angles from a 4+1-dimensional SU(5) x A(4) domain-wall braneworld model," *Phys. Rev.*, vol. D86, p. 056007, 2012.

[129] S. Antusch, S. F. King, and M. Spinrath, "Spontaneous CP violation in $A_4 \times SU(5)$ with Constrained Sequential Dominance 2," *Phys. Rev.*, vol. D87, no. 9, p. 096018, 2013.

[130] I. K. Cooper, S. F. King, and C. Luhn, "A4xSU(5) SUSY GUT of Flavour with Trimaximal Neutrino Mixing," *JHEP*, vol. 06, p. 130, 2012.

[131] I. K. Cooper, S. F. King, and C. Luhn, "SUSY SU(5) with singlet plus adjoint matter and A4 family symmetry," *Phys. Lett.*, vol. B690, pp. 396–402, 2010.

[132] F. Björkeroth, F. J. de Anda, I. de Medeiros Varzielas, and S. F. King, "Towards a complete $A_4\times$ SU(5) SUSY GUT," *JHEP*, vol. 06, p. 141, 2015.

[133] E. Aprile *et al.*, "First Dark Matter Search Results from the XENON1T Experiment," 2017.

[134] W. Porod, "SPheno, a program for calculating supersymmetric spectra, SUSY particle decays and SUSY particle production at e+ e- colliders," *Comput. Phys. Commun.*, vol. 153, pp. 275–315, 2003.

[135] W. Porod and F. Staub, "SPheno 3.1: Extensions including flavour, CP-phases and models beyond the MSSM," *Comput. Phys. Commun.*, vol. 183, pp. 2458–2469, 2012.

[136] "Search for pair-production of gluinos decaying via stop and sbottom in events with b-jets and large missing transverse momentum in $\sqrt{s} = 13$ TeV pp collisions with the ATLAS detector," 2015.

[137] A. M. Sirunyan *et al.*, "Search for new phenomena with the M_{T2} variable in the all-hadronic final state produced in proton–proton collisions at $\sqrt{s} = 13$ TeV," *Eur. Phys. J.*, vol. C77, no. 10, p. 710, 2017.

[138] G. Pasztor, "Search for gauginos and gauge mediated SUSY breaking scenarios at LEP," *PoS*, vol. HEP2005, p. 346, 2006.

[139] D. Dercks, N. Desai, J. S. Kim, K. Rolbiecki, J. Tattersall, and T. Weber, "CheckMATE 2: From the model to the limit," 2016.

[140] T. Sjostrand, S. Mrenna, and P. Z. Skands, "A Brief Introduction to PYTHIA 8.1," *Comput. Phys. Commun.*, vol. 178, pp. 852–867, 2008.

[141] T. A. collaboration, "Search for supersymmetry with two and three leptons and missing transverse momentum in the final state at $\sqrt{s} = 13$ TeV with the ATLAS detector," 2016.

[142] S. Weinberg, "Implications of Dynamical Symmetry Breaking," *Phys. Rev.*, vol. D13, pp. 974–996, 1976.

[143] L. Susskind, "Dynamics of Spontaneous Symmetry Breaking in the Weinberg-Salam Theory," *Phys. Rev.*, vol. D20, pp. 2619–2625, 1979.

[144] A. Belyaev, M. S. Brown, R. Foadi, and M. T. Frandsen, "The Technicolor Higgs in the Light of LHC Data," *Phys. Rev.*, vol. D90, p. 035012, 2014.

[145] D. B. Kaplan, H. Georgi, and S. Dimopoulos, "Composite Higgs Scalars," *Phys. Lett.*, vol. B136, pp. 187–190, 1984.

[146] H. Georgi, D. B. Kaplan, and P. Galison, "Calculation of the Composite Higgs Mass," *Phys. Lett.*, vol. B143, pp. 152–154, 1984.

[147] M. J. Dugan, H. Georgi, and D. B. Kaplan, "Anatomy of a Composite Higgs Model," *Nucl. Phys.*, vol. B254, pp. 299–326, 1985.

[148] K. Agashe, R. Contino, and A. Pomarol, "The Minimal composite Higgs model," *Nucl. Phys.*, vol. B719, pp. 165–187, 2005.

[149] G. Cacciapaglia and F. Sannino, "Fundamental Composite (Goldstone) Higgs Dynamics," *JHEP*, vol. 04, p. 111, 2014.

[150] L. Randall and R. Sundrum, "A Large mass hierarchy from a small extra dimension," *Phys. Rev. Lett.*, vol. 83, pp. 3370–3373, 1999.

[151] T. Gherghetta and A. Pomarol, "Bulk fields and supersymmetry in a slice of AdS," *Nucl. Phys.*, vol. B586, pp. 141–162, 2000.

[152] N. Arkani-Hamed, A. G. Cohen, E. Katz, A. E. Nelson, T. Gregoire, and J. G. Wacker, "The Minimal moose for a little Higgs," *JHEP*, vol. 08, p. 021, 2002.

[153] N. Arkani-Hamed, A. G. Cohen, E. Katz, and A. E. Nelson, "The Littlest Higgs," *JHEP*, vol. 07, p. 034, 2002.

[154] M. Schmaltz and D. Tucker-Smith, "Little Higgs review," *Ann. Rev. Nucl. Part. Sci.*, vol. 55, pp. 229–270, 2005.

[155] Z. Chacko, H.-S. Goh, and R. Harnik, "The Twin Higgs: Natural electroweak breaking from mirror symmetry," *Phys. Rev. Lett.*, vol. 96, p. 231802, 2006.

[156] N. Craig, S. Knapen, and P. Longhi, "Neutral Naturalness from Orbifold Higgs Models," *Phys. Rev. Lett.*, vol. 114, no. 6, p. 061803, 2015.

[157] T. Han, R. Mahbubani, D. G. E. Walker, and L.-T. Wang, "Top Quark Pair plus Large Missing Energy at the LHC," *JHEP*, vol. 05, p. 117, 2009.

[158] S. Kraml, U. Laa, L. Panizzi, and H. Prager, "Scalar versus fermionic top partner interpretations of $t\bar{t} + E_T^{\rm miss}$ searches at the LHC," *JHEP*, vol. 11, p. 107, 2016.

[159] S. Baek, P. Ko, and P. Wu, "Top-philic Scalar Dark Matter with a Vector-like Fermionic Top Partner," *JHEP*, vol. 10, p. 117, 2016.

[160] D. Barducci and C. Delaunay, "Bounding wide composite vector resonances at the LHC," *JHEP*, vol. 02, p. 055, 2016.

[161] B. A. Dobrescu, K. Kong, and R. Mahbubani, "Prospects for top-prime quark discovery at the Tevatron," *JHEP*, vol. 06, p. 001, 2009.

[162] F. Giacchino, A. Ibarra, L. Lopez Honorez, M. H. G. Tytgat, and S. Wild, "Signatures from Scalar Dark Matter with a Vector-like Quark Mediator," *JCAP*, vol. 1602, no. 02, p. 002, 2016.

[163] A. Semenov, "LanHEP: A package for automatic generation of Feynman rules from the Lagrangian," *Comput.Phys.Commun.*, vol. 115, pp. 124–139, 1998.

[164] A. Semenov, "LanHEP - a package for the automatic generation of Feynman rules in field theory. Version 3.0," *Comput. Phys. Commun.*, vol. 180, pp. 431–454, 2009.

[165] A. Semenov, "LanHEP - a package for automatic generation of Feynman rules from the Lagrangian. Updated version 3.1," 2010.

[166] N. D. Christensen and C. Duhr, "FeynRules - Feynman rules made easy," *Comput.Phys.Commun.*, vol. 180, pp. 1614–1641, 2009.

[167] A. Alloul, N. D. Christensen, C. Degrande, C. Duhr, and B. Fuks, "FeynRules 2.0 - A complete toolbox for tree-level phenomenology," *Comput. Phys. Commun.*, vol. 185, pp. 2250–2300, 2014.

[168] A. Belyaev, N. D. Christensen, and A. Pukhov, "CalcHEP 3.4 for collider physics within and beyond the Standard Model," *Comput. Phys. Commun.*, vol. 184, pp. 1729–1769, 2013.

[169] M. Bondarenko, A. Belyaev, L. Basso, E. Boos, V. Bunichev, *et al.*, "High Energy Physics Model Database : Towards decoding of the underlying theory (within Les Houches 2011: Physics at TeV Colliders New Physics Working Group Report)," 2012.

[170] `http://hepmdb.soton.ac.uk/hepmdb:0717.0253`.

[171] `http://hepmdb.soton.ac.uk/hepmdb:0717.0254`.

[172] R. D. Ball, V. Bertone, S. Carrazza, L. Del Debbio, S. Forte, A. Guffanti, N. P. Hartland, and J. Rojo, "Parton distributions with QED corrections," *Nucl. Phys.*, vol. B877, pp. 290–320, 2013.

[173] M. Cacciari and G. P. Salam, "Dispelling the N^3 myth for the k_t jet-finder," *Phys. Lett.*, vol. B641, pp. 57–61, 2006.

[174] M. Cacciari, G. P. Salam, and G. Soyez, "FastJet User Manual," *Eur. Phys. J.*, vol. C72, p. 1896, 2012.

[175] G. Aad *et al.*, "Search for supersymmetry at $\sqrt{s} = 13$ TeV in final states with jets and two same-sign leptons or three leptons with the ATLAS detector," *Eur. Phys. J.*, vol. C76, no. 5, p. 259, 2016.

[176] M. Aaboud *et al.*, "Search for new phenomena in events with a photon and missing transverse momentum in pp collisions at $\sqrt{s} = 13$ TeV with the ATLAS detector," *JHEP*, vol. 06, p. 059, 2016.

[177] M. Aaboud *et al.*, "Search for new phenomena in final states with an energetic jet and large missing transverse momentum in pp collisions at $\sqrt{s} = 13$ TeV using the ATLAS detector," *Phys. Rev.*, vol. D94, no. 3, p. 032005, 2016.

[178] M. Aaboud *et al.*, "Search for squarks and gluinos in final states with jets and missing transverse momentum at $\sqrt{s} = 13$ TeV with the ATLAS detector," *Eur. Phys. J.*, vol. C76, no. 7, p. 392, 2016.

[179] G. Aad *et al.*, "Search for gluinos in events with an isolated lepton, jets and missing transverse momentum at $\sqrt{s} = 13$ Te V with the ATLAS detector," *Eur. Phys. J.*, vol. C76, no. 10, p. 565, 2016.

[180] G. Aad *et al.*, "Search for pair production of gluinos decaying via stop and sbottom in events with b-jets and large missing transverse momentum in pp collisions at $\sqrt{s} = 13$ TeV with the ATLAS detector," *Phys. Rev.*, vol. D94, no. 3, p. 032003, 2016.

[181] M. Aaboud *et al.*, "Search for top squarks in final states with one isolated lepton, jets, and missing transverse momentum in $\sqrt{s} = 13$ TeV pp collisions with the ATLAS detector," *Phys. Rev.*, vol. D94, no. 5, p. 052009, 2016.

[182] "A search for Supersymmetry in events containing a leptonically decaying Z boson, jets and missing transverse momentum in $\sqrt{s} = 13$ TeV pp collisions with the ATLAS detector," Tech. Rep. ATLAS-CONF-2015-082, CERN, Geneva, 2015.

[183] "Search for production of vector-like top quark pairs and of four top quarks in the lepton-plus-jets final state in pp collisions at $\sqrt{s} = 13$ TeV with the ATLAS detector," Tech. Rep. ATLAS-CONF-2016-013, CERN, Geneva, 2016.

[184] "Search for direct top squark pair production and dark matter production in final states with two leptons in $\sqrt{s} = 13$ TeV pp collisions using 13.3 fb^{-1} of ATLAS data," tech. rep., CERN, Geneva, 2016.

[185] "Search for top squarks in final states with one isolated lepton, jets, and missing transverse momentum in $\sqrt{s} = 13$ TeV pp collisions with the ATLAS detector," Tech. Rep. ATLAS-CONF-2016-050, CERN, Geneva, 2016.

[186] "Search for new physics in final states with two opposite-sign same-flavor leptons, jets and missing transverse momentum in pp collisions at sqrt(s)=13 TeV," Tech. Rep. CMS-PAS-SUS-15-011, CERN, Geneva, 2015.

[187] G. Belanger, F. Boudjema, A. Pukhov, and A. Semenov, "MicrOMEGAs 2.0: A Program to calculate the relic density of dark matter in a generic model," *Comput. Phys. Commun.*, vol. 176, pp. 367–382, 2007.

[188] G. Belanger, F. Boudjema, P. Brun, A. Pukhov, S. Rosier-Lees, P. Salati, and A. Semenov, "Indirect search for dark matter with micrOMEGAs2.4," *Comput. Phys. Commun.*, vol. 182, pp. 842–856, 2011.

[189] `https://hepmdb.soton.ac.uk/phenodata/view.php?id=595e239abb817586383e929d`.

[190] P. Ade *et al.*, "Planck 2015 results. XIII. Cosmological parameters," 2015.

[191] G. Aad *et al.*, "Search for invisible decays of a Higgs boson using vector-boson fusion in *pp* collisions at $\sqrt{s} = 8$ TeV with the ATLAS detector," *CERN-PH-EP-2015-186*, 2015.

[192] "Search for New Phenomena in Dijet Events with the ATLAS Detector at $\sqrt{s}$=13 TeV with 2015 and 2016 data," Tech. Rep. ATLAS-CONF-2016-069, CERN, Geneva, 2016.

[193] A. M. Sirunyan *et al.*, "Search for dijet resonances in proton-proton collisions at $\sqrt{s} = 13$ TeV and constraints on dark matter and other models," *Submitted to: Phys. Lett. B*, 2016.

[194] "Search for new high-mass resonances in the dilepton final state using proton-proton collisions at $\sqrt{s} = 13$ TeV with the ATLAS detector," Tech. Rep. ATLAS-CONF-2016-045, CERN, Geneva, 2016.

[195] "Search for a high-mass resonance decaying into a dilepton final state in 13 fb^{-1} of pp collisions at $\sqrt{s} = 13$ TeV," Tech. Rep. CMS-PAS-EXO-16-031, CERN, Geneva, 2016.

[196] A. Ball, M. Benedikt, L. Bottura, O. Dominguez, F. Gianotti, *et al.*, "Future Circular Collider Study Hadron Collider Parameters," *FCC-ACC-SPC-0001*, 2014.

[197] X.-G. He, G.-N. Li, and Y.-J. Zheng, "Probing Higgs Boson CP Properties with $t\bar{t}H$ at the LHC and the 100 TeV pp Collider," 2014.

[198] A. J. Barr, M. J. Dolan, C. Englert, D. E. Ferreira de Lima, and M. Spannowsky, "Higgs Self-Coupling Measurements at a 100 TeV Hadron Collider," *JHEP*, vol. 1502, p. 016, 2015.

[199] M. Low and L.-T. Wang, "Neutralino dark matter at 14 TeV and 100 TeV," *JHEP*, vol. 1408, p. 161, 2014.

[200] B. S. Acharya, K. Bożek, C. Pongkitivanichkul, and K. Sakurai, "Prospects for observing charginos and neutralinos at a 100 TeV proton-proton collider," *JHEP*, vol. 1502, p. 181, 2015.

[201] B. Auerbach, S. Chekanov, J. Love, J. Proudfoot, and A. Kotwal, "Sensitivity to new high-mass states decaying to $t\bar{t}$ at a 100 TeV collider," *Phys.Rev.*, vol. D91, no. 3, p. 034014, 2015.

[202] A. Fowlie and M. Raidal, "Prospects for constrained supersymmetry at $\sqrt{s} = 33\,\text{TeV}$ and $\sqrt{s} = 100\,\text{TeV}$ proton-proton super-colliders," *Eur.Phys.J.*, vol. C74, p. 2948, 2014.

[203] A. Belyaev, A. Oliveira, R. Rosenfeld, and M. C. Thomas, "Multi Higgs and Vector boson production beyond the Standard Model," *JHEP*, vol. 1305, p. 005, 2013.

[204] D. A. Dicus and H.-J. He, "Scales of fermion mass generation and electroweak symmetry breaking," *Phys.Rev.*, vol. D71, p. 093009, 2005.

[205] F. Maltoni, J. Niczyporuk, and S. Willenbrock, "The Scale of fermion mass generation," *Phys.Rev.*, vol. D65, p. 033004, 2002.

[206] B. E. and K. Kajantie, "Particle Kinematics," *John Wiley & Sons Ltd.*, 1973.

[207] S. R. Coleman, J. Wess, and B. Zumino, "Structure of phenomenological Lagrangians. 1.," *Phys. Rev.*, vol. 177, pp. 2239–2247, 1969.

[208] C. G. Callan, Jr., S. R. Coleman, J. Wess, and B. Zumino, "Structure of phenomenological Lagrangians. 2.," *Phys. Rev.*, vol. 177, pp. 2247–2250, 1969.

[209] J. M. Cornwall, D. N. Levin, and G. Tiktopoulos, "Derivation of Gauge Invariance from High-Energy Unitarity Bounds on the s Matrix," *Phys. Rev.*, vol. D10, p. 1145, 1974. [Erratum: Phys. Rev.D11,972(1975)].

[210] B. W. Lee, C. Quigg, and H. B. Thacker, "Weak Interactions at Very High-Energies: The Role of the Higgs Boson Mass," *Phys. Rev.*, vol. D16, p. 1519, 1977.

[211] M. S. Chanowitz and M. K. Gaillard, "The TeV Physics of Strongly Interacting W's and Z's," *Nucl. Phys.*, vol. B261, p. 379, 1985.

[212] S. S. D. Willenbrock, "Pair Production of W and Z Bosons and the Goldstone Boson Equivalence Theorem," *Annals Phys.*, vol. 186, p. 15, 1988.

[213] J. Bagger and C. Schmidt, "Equivalence Theorem Redux," *Phys. Rev.*, vol. D41, p. 264, 1990.

[214] H. G. J. Veltman, "The Equivalence Theorem," *Phys. Rev.*, vol. D41, p. 2294, 1990.

[215] G. Giudice, C. Grojean, A. Pomarol, and R. Rattazzi, "The Strongly-Interacting Light Higgs," *JHEP*, vol. 0706, p. 045, 2007.

[216] J. Pumplin, D. Stump, J. Huston, H. Lai, P. M. Nadolsky, *et al.*, "New generation of parton distributions with uncertainties from global QCD analysis," *JHEP*, vol. 0207, p. 012, 2002.

[217] R. Brun and F. Rademakers, "ROOT - An Object Oriented Data Analysis Framework," *Nucl. Inst. & Meth. in Phys. Res.*, vol. A 389, pp. 81–86, 1997.

[218] M. Gouzevitch, A. Oliveira, J. Rojo, R. Rosenfeld, G. P. Salam, and V. Sanz, "Scale-invariant resonance tagging in multijet events and new physics in Higgs pair production," *JHEP*, vol. 07, p. 148, 2013.

[219] M. L. Mangano, M. Moretti, F. Piccinini, R. Pittau, and A. D. Polosa, "ALPGEN, a generator for hard multiparton processes in hadronic collisions," *JHEP*, vol. 07, p. 001, 2003.

[220] M. L. Mangano, M. Moretti, and R. Pittau, "Multijet matrix elements and shower evolution in hadronic collisions: $Wb\bar{b} + n$ jets as a case study," *Nucl. Phys.*, vol. B632, pp. 343–362, 2002.

[221] F. Caravaglios, M. L. Mangano, M. Moretti, and R. Pittau, "A New approach to multijet calculations in hadron collisions," *Nucl. Phys.*, vol. B539, pp. 215–232, 1999.

[222] I. J. R. Aitchison, *Supersymmetry in Particle Physics. An Elementary Introduction.* 2007.